# An Improved Gain Wing-Integrated Antenna Design for Meridian UAS and Sensor-Driven Wing Sizing Approach

By,

**Ankur Santaji Patil**

Submitted to the graduate degree program in Aerospace Engineering and the Graduate Faculty of the University of Kansas in partial fulfillment of the requirements for the Degree of Master of Science

Dr. Emily Arnold ……..

Chairperson

Dr. Ron Barrett ……...

Committee Member

Dr. Richard Hale ……...

Committee Member

Date Defended ……

The Thesis Committee of Ankur Patil certifies that this is the approved version of the following thesis:

# An Improved Gain Wing-Integrated Antenna Design for Meridian UAS and Sensor-Driven Wing Sizing Approach

……

Chairperson Dr. Emily Arnold

Date Approved: …….

# Abstract

Ice sheets in Antarctic and Arctic regions are undergoing rapid changes, causing a rise in sea level with direct impacts on society and the global system. Airborne remote sensing offers a robust way to study changes occurring in this region and the effects on climate. The Center for Remote Sensing of Ice Sheets (CReSIS) has flown many missions in polar regions to collect data on bed topography, basal conditions, and deep internal layers by using high-sensitivity radar and advanced processing algorithms. The goal of the current study is two-fold. First, a new wing-integrated antenna concept is developed for the Meridian, an Unmanned Aerial System (UAS) designed at the University of Kansas. Second, preliminary wing-sizing equations are derived from wing-integrated antenna performance analyses. The purpose of both studies is to improve both current and future UAS sensor-platforms used for remote sensing applications, such as those currently supported by CReSIS.

An improved design of a wing-integrated airborne antenna array is presented by performing an antenna trade study for three low-profile antennas. This study seeks to improve not only the gain of the antenna system but the aircraft performance by developing a structurally-embedded design. Three candidate antenna designs are carried forward to the detailed design stage. These designs include a planar dipole embedded in the lower wing skin of the vehicle, a planar dipole offset a quarter-wavelength from the conductive lower wing-skin via a custom support structure, and a quarter-wave patch antenna integrated inside the wing. Considering the existing wing size limitations for antenna array integration into the Meridian wing, two different designs are recommended—the first design strictly optimizing antenna performance for the given wing size limitations and the second design improving both the electrical and vehicle performance over the original design. The planar dipole antenna offset from a ground plane offers the best results in terms of antenna performance within aircraft's dimensional constraint.

In the first design, when antenna performance is given priority, the final offset array design results in a gain improvement of about 6 dB over existing Vivaldi system. Since the ratio of received power to transmitted power is proportional to square of the gain (by Friis equation), for an antenna acting as a transmitter and receiver, the gain is actually doubled (i.e. about 12 dB improvement in gain) in decibel (dB) scale. However, this design significantly increased drag, which is expected to reduce the vehicle range by ~31% compared to the Vivaldi system. This design also adds a total additional weight of 84 lbs. due to the antenna supporting structure and modifications made to the existing Meridian wing. The second design, a dipole array embedded in the wing (bay) skin, offers advantages for both aircraft and sensor performance. The advantages, particularly from a sensor perspective, are relatively small. When compared to the existing Vivaldi system, the embedded antenna design results in ~6% increase in aircraft range, and about 2.5 dB (actually about 5 dB by Friis equation) increase in gain. This design adds an extra weight of 9.5 lbs. per wing due to composite material modifications. The results of these two systems illustrate the constant compromise that occurs between vehicle and sensor performance, and the difficulty to optimize both systems simultaneously.

This study then extends toward a sensor-driven wing sizing study, in which sensor performance requirements are considered in the preliminary design process of wing sizing. The conclusions drawn based on this study are specifically applicable to dipole (half wavelength)

antenna design. Considering the higher electrical performance offered by a ground plane, a single planar dipole antenna was simulated with a ground plane. The ground plane is assumed to be the lower skin of an aircraft. The ground plane length, width, and offset from the antenna were varied. For ground plane length sizing, the width and offset parameters are kept constant, while the ground plane extension outside of the antenna edge is varied. The ground plane width and offset sizing were performed in a similar manner by keeping all other variables constant. It is determined that ground plane length and width should be 50% of the wavelength extended outside the antenna edges and the ground plane-antenna offset should be kept at 15% of the wavelength for maximum dipole antenna performance. Relationships for wing ground plane span, wing chord, and thickness are derived from extensive parametric electromagnetic simulations that provide optimum antenna performance for generic planar dipole antenna. The relationships derived are for the ground plane (conductive) portion of the wing. These equations provide a useful tool that can inform the designer of expected sensor performance while determining the wing parameters.

# Acknowledgements

Words cannot describe how grateful I am to Dr. Arnold for her support and guidance at every step for last two years. I appreciate her kindness and patience. I want to thank Dr. Barrett for guiding me in the first year of my Master's and pushing me in the right direction. I also want to thank Dr. Hale for passing valuable knowledge through the 'structural composites' class, it certainly helped me in the structural analysis part of my study.

I want to thank my dad (Santaji Patil) and my mom (Mangal Patil) for their courageous decision to send me abroad for education. I want to thank my elder sister for inspiring me for higher education in Aeronautical Engineering. I also want to thank my siblings and friends for their help and support.

# Table of Contents

# List of Symbols

## Latin

| Symbol | Description | Units |
|---|---|---|
| C | Feed probe offset | in |
| E | Modulus of elasticity | psi |
| f | Frequency | Hz |
| F | Stress allowable | psi |
| G | Shear modulus | psi |
| I | Moment of Inertia | $in^4$ |
| M | Moment | lbf.in |
| P | Patch length | in |
| t | Thickness of lamina | in |
| t/c | Thickness to chord ratio | ~ |
| V | Wave speed | m/s |
| y | Fairing spar height | in |

## Greek

| Symbol | Description | Units |
|---|---|---|
| $\alpha$ | Coefficient of thermal expansion | in/in/°F |
| $\Delta$ | Step size | ~ |
| $\lambda$ | Wavelength | in |
| $\nu$ | Poisson's ratio | ~ |
| $\rho$ | Density | $lb_f/in^3$ |
| $\sigma$ | Stress | ksi |
| $\phi$ | Azimuth angle | Degree |

# Subscripts and Superscripts

| Symbol | Description |
|---|---|
| 1 | Primary material axis |
| 12 | Shear axis |
| 2 | Secondary material axis |
| C | Compressive |
| nom | Nominal |
| SU | Shear Ultimate |
| T | Tensile |
| TU | Tensile Ultimate |
| x | X axis |
| y | Y axis |

# List of Abbreviations

| Acronym | Description |
|---|---|
| CAD | Computer-Aided Design |
| CFRP | Carbon Fiber Reinforced Plastic |
| CReSIS | Center for Remote Sensing of Ice Sheets |
| EM | Electromagnetic |
| F.S. | Factor of Safety |
| FEA | Finite Element Analysis |
| FEM | Finite Element Model |
| FHS | Flexible Hybrid System |
| GP | Ground Plane |
| GFRP | Glass Fiber-Reinforced Plastic |
| HFSS | High Frequency Structural Simulator |
| ISM | Industrial, Scientific and Medical |
| KUAE | University of Kansas Aerospace Engineering |
| M.S. | Margin of Safety |
| MAS | Multifunctional Aircraft Structures |
| MCoRDS | Multichannel Coherent Radar Depth Sounder |
| NASA | National Aeronautics and Space Administration |
| NSF | National Science Foundation |
| PA | Patch Antenna |
| PEC | Perfect electrical conductor |
| QW | Quarter-Wave |

| Acronym | Description |
|---|---|
| RF | Radio Frequency |
| SFC | Specific Fuel Consumption |
| STC | Science and Technology Center |
| UAS | Unmanned Aircraft System |
| UHF | Ultra-High Frequency |
| UWB | Ultra-wideband |
| VHF | Very High Frequency |

# List of Figures

**Page #**

# List of Tables

**Page #**

# 1. Introduction

It is the consensus of the scientific community that climate change is anthropogenic and is a multifaceted threat to humans as well as all other living things on the earth. Scientists have been measuring, analyzing, and predicting the accelerating trend of global temperature and global sea-level rise due to ocean warming and ice loss by glaciers in polar regions [1], [2]. The Center for Remote Sensing of Ice Sheets (CReSIS), a Science and Technology Center (STC) funded by National Science Foundation (NSF), supports cryospheric research by developing new technologies (specifically ice penetrating radar) to conduct measurements in polar regions (both Arctic and Antarctic). Radars developed at CReSIS are used to collect data to determine the bedrock topography, thickness of ice, basal characteristics, shallow and deep internal layers, and snow accumulation over land and ice. The University of Kansas, leading this research, developed a medium-range Unmanned Aircraft System (UAS) called the Meridian, which carries an antenna array for CReSIS's Very High Frequency (VHF) depth sounding radar. The Meridian is a propeller driven, low altitude, medium-range UAS designed specifically for cryospheric research. UASs offer the advantage of collecting data over a large region efficiently without risking human lives. A detailed description of the current vehicle and radar is included in Section 1.2.

This work entails a two-part study. The aim of the first part of the study is to develop an improved wing-integrated antenna array for cryospheric remote sensing. An integrated system that could optimize electrical and vehicle (i.e. aircraft) performance was proposed. Considering the existing wing size limitations for an antenna array integrated inside the Meridian wing, two different designs were studied: the first design strictly optimized antenna performance given the wing size limitations, and the second design improved both the electrical and vehicle performance over the original design. This design study further motivated the second part of the study: the development of preliminary wing sizing equations that take into account sensor performance. Using these sizing equations, the ideal wing span, chord, t/c ratio, and ground plane aspect ratios could be determined for future vehicle design.

## 1.1. Motivation

### 1.1.1. Improving Existing Meridian System

The motivation of this study is to improve the existing radar antenna design of the Meridian UAS, and potentially improve aircraft performance by reducing the drag with the new antenna design. An integrated system that optimizes both electrical and vehicle (i.e. aircraft) performance was the goal. The current Meridian Vivaldi antenna design has less than 0 dB gain over the frequency range of interest. In addition, these flat plate-like antennas are mounted externally to the underside of the wing. With eight antennas installed on Meridian, the range is reduced to 932.5 nmi from the clean aircraft range of 1000 nmi without fuel reserve, i.e. about 7% decrease in range [3]. Keeping this in mind, a secondary motivation was to improve aircraft performance by developing a low drag design for an antenna array.

### 1.1.2. Developing Relationships between Sensor Performance and Wing Sizing

This Meridian design case study further motivated the development of a preliminary wing sizing approach that takes into account integrated-sensor performance. By developing wing-sensor relationships relating ideal wing span, chord, t/c ratio, and ground plane aspect ratios for the conductive portion of the wing, sensor performance can be integrated into the design process of future platforms. This is especially relevant to UAS applications as the primary purpose of the

vehicle is to carry the sensor. Since the upper or lower wing skin of an aircraft could be used as a potential ground plane, cost and weight of the system could be reduced.

To establish wing size-sensor performance relationships, the behavior and performance of an antenna in the presence of the conductive ground plane are studied. Then the ground plane size and offset from the antenna are related to the various wing parameters. The trade-off between the antenna performance and ground plane size (i.e. wing parameters) are predicted. The developed relationships could help designers determine whether a smaller wing could be chosen at the expense of the antenna performance and this degradation in the antenna performance could be estimated. An ideal ground plane size (i.e. wing span, chord and thickness or offset from an antenna) can be determined in terms of wavelength to maximize array performance at any operating frequency.

## 1.2. Background

This section includes a detailed description of the Meridian and the existing Vivaldi antenna (including its inadequate electrical performance, which was the motivation for a new antenna design).

### 1.2.1. Meridian UAS

Meridian is a low-wing, propeller-driven medium range vehicle. This UAS was designed and manufactured by the faculty and students in the University of Kansas Aerospace Engineering (KUAE) department. Selection of material for the wing is one of the main considerations to improve antenna performance. The Meridian wings were made of carbon fiber composite material, and since the Vivaldi antennas were integrated below the wing, the existing wing was acting as a ground plane to a Vivaldi array. For an embedded design, carbon fibers cause coupling with the antenna elements, distortion of the radiation pattern, and in turn degradation of the antenna performance, since the carbon fibers are conductive. Hence for a wing embedded antenna design, the existing wing material needs to be replaced with low-loss dielectric material (e.g. fiberglass), which has a fairly low dielectric constant of around 3.4 [4]. Structural design, analysis and testing of the original Vivaldi antenna is documented in [5], and structural loads considered in the analysis include the skin friction drag, inertial loads, and aerodynamic lift on the plate. As the Vivaldi antennas are attached to the lower surface of the wing, they cause additional drag and weight that affects the range of the Meridian. For the worst case scenario, the drag coefficient of the turbulent flat plate ($c_d$ = 0.005) is used to calculate the drag due to the antennas parallel to flow [6], and resulting drag force for eight Vivaldi antennas is estimated to be 10.4 lbs, for a cruise speed of 133 kts and antenna planform area of 2.2 $ft^2$.

The Meridian was designed to house an ice-sounding radar and a large cross-track antenna array for sounding ice thickness and bedrock topography in the cryosphere. Prior to the unexpected loss of the vehicle in 2011, the Meridian had been flown in both Antarctica and Greenland. Table 1 summarizes the salient vehicle characteristics [3].

**Table 1: Salient characteristics of Meridian UAS**

| Meridian UAS | | | |
|---|---|---|---|
| Wing Span | 26.4 ft | Wing Dihedral | 5° |
| Takeoff Weight | 1100 lbs. | V-Tail Dihedral | 50° |
| Fuel Capacity | 120 lbs. | Range | 950 nmi |
| Payload Capacity | 165 lbs. | L/D | 13.9 |

### 1.2.2. MCoRDS Radar Antennas

The Multichannel Coherent Radar Depth Sounder System (MCoRDS), developed at the University of Kansas, has been used to measure ice thickness, bedrock topography, and deep internal layers. This system has been installed on a variety of platforms and these various systems typically operate from 160-230 MHz. The MCoRDS system is capable of measuring depths to about 13,000 ft (4 km) with a vertical resolution of 6 m in ice [7]. Previously the MCoRDS system has been implemented with dipole arrays on the following platforms: Twin Otter, NASA P-3 and NASA DC-8.

The Vivaldi antenna, shown in Figure 1, was originally designed for the Meridian MCoRDS system, and it was chosen for its wide bandwidth and moderate gain. The antennas were mounted below the wing with custom brackets and stiffeners. The antenna measures 15.75 inch (40 cm) long, 20.1 inch (51 cm) wide and 0.125 inch (0.32 cm) thick with weight of 3.2 lbs., with 29.5 inch (75 cm) center to center spacing [8]. A four-element array is integrated on each wing, one array of four elements for transmitting the signal, and the other four for receiving the signal. Figure 1 shows a single Vivaldi antenna element as well as an installed partial array [8, 9].


**Figure 1: Vivaldi Antenna [8] (left) and Meridian UAS with four antennas integrated below wing [9] (right)**

Figure 2 and Figure 3 show the return loss and gain, respectively, of the Meridian Vivaldi antenna. These measurements were conducting in the anechoic chamber located at the University of Kansas. The bandwidth of the Vivaldi antenna was found to be 960 MHz, and it operates from the frequency of 162 MHz to 1.12 GHz. The gain measurement test was performed by taking a C3142 log-periodic antenna as a reference, then the Vivaldi antenna gains were measured both

with and without the ground plane. From Figure 2, it is clear that the Vivaldi antenna has a wide bandwidth but poor gain properties at low frequencies of about 200 MHz. The maximum gain of the Vivaldi antenna with ground plane is shown in Figure 3 to be 5.1 dB. However, the gain of the Vivaldi antenna is less than 2 dB at the desired operating frequency of 180-210 MHz. This is less than the typical gain of a dipole without a ground plane. The low gain performance is due to the dissipation of a significant amount of energy, thus the low radiated power. While the antenna design seems to exhibit wideband performance from the return loss measurement, the poor gain performance is the motivation behind the antenna re-design efforts in this document.

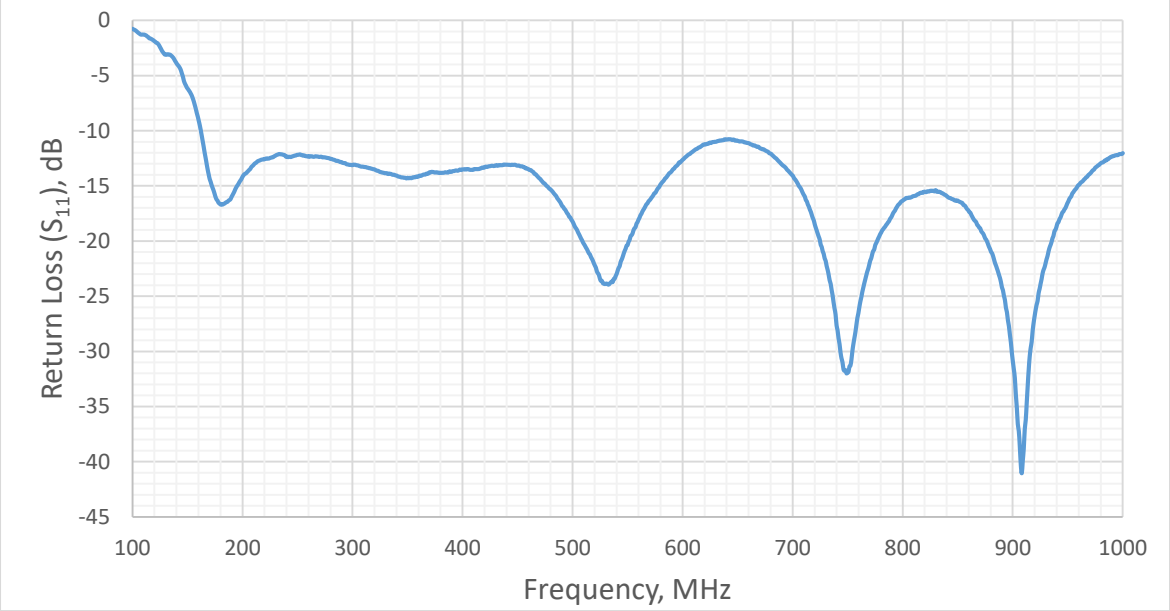


**Figure 2: Frequency vs Return loss ($S_{11}$) plot for Vivaldi Antenna**

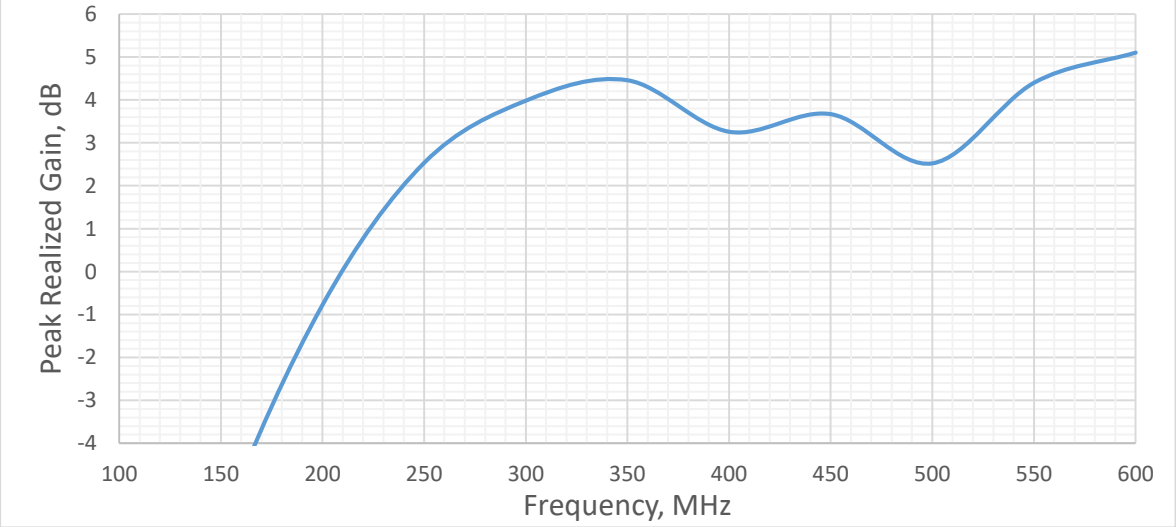


**Figure 3: Frequency vs Gain plot for Vivaldi Antenna**

## 1.3. Sensor-Wing Sizing Study

It is well known that sensor performance is very sensitive to the ground plane size. To better understand the sensor performance sensitivity to the size of a wing being utilized as a ground plane, the relations between the sensor performance and wing parameters are determined using a series of parametric analyses in an Electromagnetic (EM) analysis software tool. In this study, the conductive (and flat) portion of wing is sized in terms of the wavelength, from which ideal wing parameters (in terms of sensor performance) such as wing span, wing chord and wing-antenna offset can be estimated for a particular operating frequency to achieve desired sensor performance. Sensor performance could also be predicted based on available wing size. During preliminary wing sizing, once ground plane aspect ratio is known wing span and wing chord could be chosen such that it delivers the best possible sensor performance. If the antenna array has been designed, then based on these sensor-wing sizing relations an aircraft satisfying these relations can be selected. The development of a sensor-driven wing sizing approach could be used as a guide for future vehicle development.

## 1.4. Following Chapter Summary

Chapter 2 provides a survey of wing-integrated sensors and platforms, as well as a review of related work. Chapter 3 presents the high-level antenna design trade study. In the trade study, potential Meridian antenna designs are presented and simulated with the help of ANSYS HFSS software, and then candidate designs are assessed in more details in Chapter 4. The detailed analysis includes candidate designs simulated as a linear array, assuming they would be integrated either below the wing or inside the wing bay, as well as the preliminary structural design and analysis of the antenna structures. Chapter 5 includes the preliminary wing-sizing relationships driven by sensor performance, and trade-offs between sensor performance and wing size for a general dipole antenna are assessed. Finally, Chapter 6 contains the conclusions and recommendations for this study.

# 2. Related Work

Since the 1960s, radio echo sounding has been used to measure the ice thickness of polar regions [10]. This section provides an overview of the various (mainly) CReSIS radars and platforms used for cryospheric surveying of polar regions to collect the data on bedrock topography, deep internal layering and basal characteristics, etc. The platforms are: P-3, DHC-6 Twin Otter, Basler BT-67 and G1X. Each platform has a custom radar antenna-array due to its installation, size, and mission type. Specific focus is given to the wing-mounted systems that CReSIS uses for its MCoRDS system. This section also gives an overview of Multifunctional Aircraft Structures (MAS), where antennas are typically embedded into the structure to improve the sensor and vehicle performance simultaneously.

## 2.1. Wing-Integrated Sensors

CReSIS has developed various radar systems operating over a range of frequency bands to support a variety of snow and ice measurements. These radar systems with their operating frequency range are: MCoRDS (180-210 MHz), Ku-band radar (12-18 GHz), Snow radar (2-8 GHz), Accumulation radar (600-900 MHz), Very High Frequency (VHF) /High Frequency (HF) radar (14 and 35 MHz), Ultra-wideband (UWB) ice radar (150-600 MHz) [11], and UWB snow radar (2-18 GHz). The primary system that CReSIS has integrated into the wings of an aircraft is the MCoRDS system, though most recently the UWB-ICE system was integrated onto the wings of a Basler BT-67. The MCoRDS radar antenna system is a VHF depth sounder with a frequency band of 180-210 MHz and supports up to total 15 channels with seven antennas transmitting and all 15 antennas receiving. This radar system has been flown on Meridian UAS, NASA P-3B, NASA DC-8, and Twin Otter. All of the antenna arrays for these systems are integrated onto the wing with the exception of the DC-8. The wing-integrated systems and platforms are described in detail below.

The NASA P-3B, a four engine turboprop aircraft, has flown the MCoRDS, Snow, Ku-band, and accumulation radars simultaneously by installing these sensors at multiple locations including the bomb bay and ten hard points along the wing [11]. These radars were installed on the aircraft, as shown in Figure 4 [11], and the 15-element MCoRDS array was installed on the wings with the help of custom pylons and fairings. The P-3 aircraft has a range of about 3000 nmi, nominal cruise speed range of 240-400 kts [6], and an operation ceiling of 28,000 ft [12]. It has been used for low altitude, long duration missions. However, compared to UAS, this aircraft is less fuel efficient, which makes it less preferable when considering the environmental impact of the system. Also, due to high speed, this aircraft has a higher turn radius and becomes challenging to achieve closely spaces gridlines

The Twin Otter, a twin turboprop aircraft, has a cruise speed of 120 kts, and a range of about 780 nmi [12]. The aircraft can be landed on wheels or skis, and it is suitable for low-altitude surveying of ice sheets. A MCoRDS array of 12 folded dipoles were attached via custom hard points on the wings, as shown in Figure 5. This aircraft has a smaller range as comparted to the P-3 which limits the extent of the surveys it can conduct. However, the low altitude and low speed are advantageous for sensor performance, as the smaller turn radius allows for more closely spaced ground track patterns.

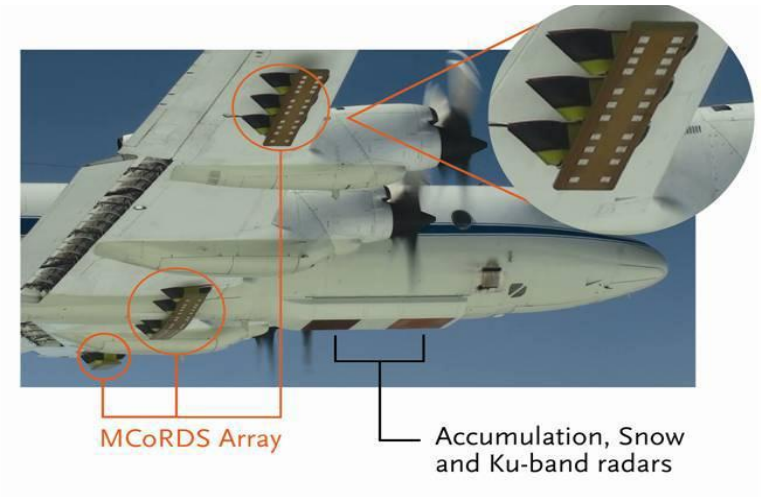


**Figure 4: NASA P-3 with all sensors installed [11]**

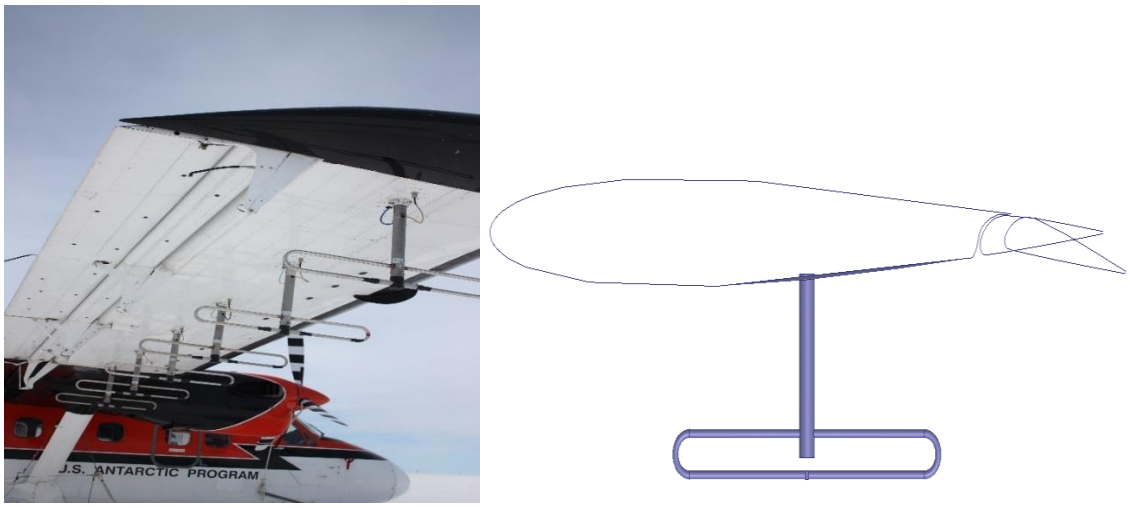


**Figure 5: Twin Otter Wing with dipole array (left) (Credit: Dr. Shawn Keshmiri, KUAE) and cross-section of assembly (right) [11]**

CReSIS has also developed a multichannel VHF/UHF UWB radar for polar ice sheets measurement, the UWB-ICE system was integrated into a Basler BT-67 aircraft for airborne mapping and imaging of glaciers and ice sheets at Greenland. This radar has an operating frequency range of 150-600 MHz with eight transmitting and 24 receiving channels. This radar system was designed to provide a 10 km wide ice bed image. The Basler B-67 is a twin turboprop cargo aircraft. It cruises at a speed of 210 kts with a range of 2,140 nmi, and has a service ceiling of 25,000 ft. This aircraft has carried UWB-ICE conducted two field deployments in Greenland [14], and one in Antarctica. This custom antenna–support structure consist of three 13.12 ft (4 m) long fairings each containing an eight-element antenna subarray. One of the fairings was integrated below the fuselage and the other two were integrated below the starboard and port wings, as shown in Figure 6. This aircraft has a comparable range to the P-3. It has a 95 ft long wing span, yet only one subarray per wing was integrated. Due to higher payload capacity, the power required for the radar is less of a concern in this case.


**Figure 6: Basler BT-67 with wing integrated sensors [14]**

There are many advantages of favoring UASs over manned aircraft, including that they do not risk the pilot and radar operator. Also the UAS is very fuel efficient compared to manned aircraft. The UAS can also fly closely spaced gridlines to provide higher spatial resolution measurements, and has the potential for more accurate flight path tracking. However, civilian-accessible UAS have limited range and payload capacity. A compact radar system, developed by CReSIS, was integrated on KU's G1X UAS [15], as shown in Figure 7. This UAS has a wing span of 208.7 in (5.3 m), weighs 85 lbs and has a range of about 62 miles. Two separate dipole-based antennas with operating frequency of 14 MHz and 35 MHz were integrated into the wings of this UAS. Similar to the MCoRDS system this system was designed for sounding temperate ice, measuring polar ice sheet thickness. This system is ideal for conducting tightly spaced grid line measurements, however, the range of this UAS is small and thus it can survey only a few science targets per deployment. Also, at lower operating frequency, the antennas are larger than the spatial limitations of the wing, making it difficult to design a highly efficient antenna.


**Figure 7: The G1X UAS in flight (left) (Credit: Dr. Shawn Keshmiri, KUAE) and antennas integrated on the wing (right) [15]**

Apart from the CReSIS radar systems, a few other wing integrated sensor designs were also studied. The Small Unmanned Aerial Vehicle (SUAV) with wing integrated sensors has been used for exploration, surveillance and military applications. These SUAV are equipped with sensors for remote sensing of specific region (especially on land), and they typically have a short range. There has been an attempt to fly an antenna array on SUAV, where a printed antenna array was embedded into the wing structure of a small UAV [16]. This eliminates the aerodynamic drag caused by externally mounted sensors and offers improved aircraft range. An L-shaped four-element antenna array, operating in the 2.4 GHz Industrial, Scientific and Medical (ISM) band, was embedded into the wing structure. This mini-Telemaster UAV has a wing span of 45 in, and fuselage length of 32.5 in. It is made of Balsa wood (dielectric constant of 1.2) and has a payload capacity of 20 oz. This L-shaped antenna is 1.3 in (33 mm) long with arm length of 0.34 in (8.5 mm), and the ground plane has size of 0.69 in X 0.82 in (17.5 mm X 20.8 mm). This UAV has small range, hence can be used for limited applications.


**Figure 8: Printed antenna array into wing structure [16]**

Similar to CReSIS radar systems, a Very High Frequency (VHF) ice penetrating radar system, called High Capability Radar Sounder (HiCARS), was developed by University of Texas, Institute of Geophysics (UTIG) [12], for remote sensing of ice in polar regions. Various aircraft have been equipped with wing-integrated HiCARS sensors. It operates in the frequency range of 52.5-67.5 MHz, has been used extensively in Antarctica (2009-20012) and Greenland, and penetrates ice up to 2.2 nmi (4 km) thick. This sounder has been used to build the ice-sheet profile showing ice thickness, deep internal layers and ice-bedrock interface. This sounder has been flown on both a Twin Otter and a Basler, and consists of two dipoles integrated below the wing with the supporting structures, as shown in Figure 9 [12]. The dipole antennas operate as transmitter and receiver individually. This system is also capable of sounding deep ice, but it does not provide advanced cross-track beam forming capabilities hence they are unable to suppress off-nadir clutter. The gain of this sounder is comparatively low due to the limited antenna elements.


**Figure 9: HiCARS installed on Basler (Photo courtesy of UTIG) [12]**

## 2.2. Multifunctional Aircraft Structures (MAS)

In addition to developing an improved wing-integrated system, a secondary motivation of this work was to develop sensor-wing sizing relationships. For the systems described in the previous section, the design of the platform and antennas were developed separately, which is largely a result of using existing platforms. While the simultaneous design of both platform and sensor is a somewhat unique approach, there are a few examples in literature that highlight applications of a multi-disciplinary sensor-structure design.

The multi-disciplinary optimization (MDO) system described in [17] is an example of a design methodology that considers both aircraft and sensor performance. The program was designed to optimize the aircraft flight performance and antenna system performance simultaneously by performing a series of parametric trade studies. The MDO system varies the parameters of the aircraft geometry and antenna system configuration for each iteration, and each iteration of the MDO system was controlled by a parameterized CAD model. The combined performance index value, a single number depicting the aircraft and antenna performance, was found which defines fitness of each analysis module [17]. This fitness parameter is determined by user specified aircraft performance characteristics, such as wing area (S) and wing chord (c). Conventional configurations with favorable stability characteristics (typically lateral and longitudinal stability) received higher fitness, while an unstable vehicle and/or poor antenna performance is given lower fitness. This system does not consider the interference of metal components of the UAS and delivers lower fitness for larger UAVs and antennas operating at low frequency. Also this system was only used for detailed design.

A heavy or bulky antenna system can degrade the speed, range, endurance and payload of an aircraft. Conformal Load-bearing Antenna Structures (CLAS) combine the aircraft structures and antenna components and forms an embedded antenna structure design, which improves structural efficiency, damage resistance, and antenna performance. This system offers synergies that can reduce weight added and aircraft drag. The CLAS system presented in [18] utilized the Flexible Hybrid System (FHS), that combines printed electronics with FleX ICs (see Figure 10), and creates a very thin, very flexible, lightweight conformal system. The FleX ICs offers localized signal

processing and control, which reduces the signal loss due to long transmission lines. In this CLAS system, the flexible antenna was embedded into the structural laminate with a dielectric material between the antenna and ground plane. It offers reduction in drag and eliminates unwanted protrusion in aircraft for sensors. This technology has been widely used for military applications.

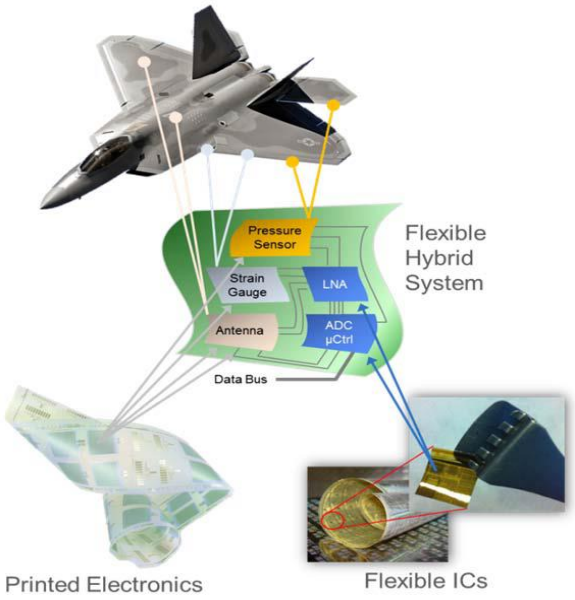


**Figure 10: CLAS flexible hybrid system [18]**

The Composite Smart Structure (CSS) presented in [19] describes electrically and structurally effective antenna structures. The study was aimed for improved electrical performance by focusing on higher gain and wide bandwidth, and improved structural efficiency by selecting materials with higher strength and stiffness. Wide bandwidth and high stiffness was achieved by stacking microstrip patch antennas and sandwich structure with organic composite material and honeycomb. The microstrip antennas were inserted into multilayer sandwich panels, as shown in Figure 11. These antennas are low profile, conformal, simple and inexpensive to manufacture. The materials used for the sandwich structures (fiberglass) have low dielectric constants, to improve antenna efficiency. The two stiff facesheets carry axial loads while the core (honeycomb) sustains shear stress. With the CSS concept, it is possible to achieve antenna efficiency as well as structural efficiency. However, this study was limited to a microstrip antenna, and maintenance of such embedded antennas might be a problem in the future.

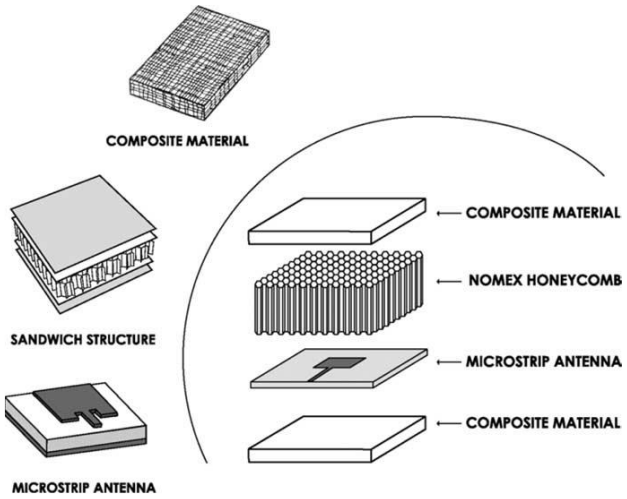


**Figure 11: Composite Smart Structure [19]**

## 2.3. Summary

The multifunctional aircraft systems have focused on optimizing aircraft performance by finding efficient ways to integrate sensors onto aircraft. CReSIS has installed radars on many aircraft but those aircraft designs were not sensor oriented. The sensors were designed to fit onto suitable aircraft, which often resulted in externally mounted antenna arrays that added extra weight and drag. In this study, effort was made to optimize the Meridian UAS and sensor performance, by proposing two separate design approaches. Later in this study, design rules for aircraft wing ground planes are presented that take into account the sensor performance. A ground plane size is directly related to the antenna operating frequency (or wavelength). Keeping that in mind, wing ground plane parameters are predicted that would deliver better sensor performance. This way a more optimal balance in both aircraft and antenna performance could be identified.

# 3. Antenna Design Trade Study

To start the investigation of an improved antenna concept for the Meridian UAS, a high-level trade study was performed to determine the most suitable antenna type. This trade study was driven by both electrical (i.e. antenna) performance and the dimensional constraints of the aircraft (i.e. Meridian wing), and the objective of this study was to identify the antenna type that will maximize electrical performance while minimizing vehicle performance degradation. The electrical performance requirements from the MCoRDS system that formed the basis of this trade study include: gain > 2 dBi, bandwidth > 30 MHz, operating frequency range between 150 - 230 MHz, a center frequency of about 200 MHz, and maximum directivity of the antenna directed normal to the plane of the antenna. In addition, if the antenna is to be integrated below the wings, the antenna array should be no longer than 140" per wing. Figure 12 shows the port side wing of the Meridian UAS (original CAD model by Bill Donovan) with its major dimensions. If the antenna were assumed to be integrated into the existing Meridian wing, the space available in a wing bay for the antenna is 18.5 in X 14 in X 2.8 in. It was determined that the chord and height dimensional constraints of the wing would be maintained, but that the span constraint was flexible assuming the rib locations and/or designs could be modified to accommodate a longer antenna design. Table 2 provides a summary of the antenna designs considered for the trade study, as well as the pros and cons of the various low-profile VHF antenna designs.

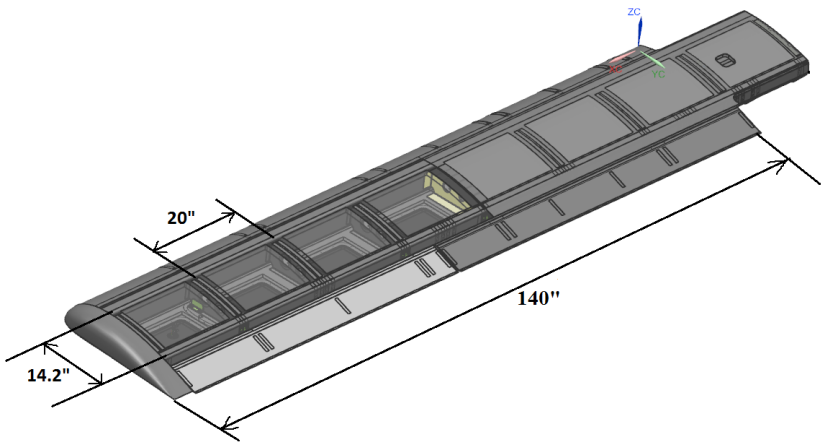


**Figure 12: Meridian Wing with Wing Bay dimensional constraints for antenna integration**

**Table 2: Comparison of low profile antennas**

| Antenna types | Pros | Cons |
|---|---|---|
| Dipole Antenna | Wide bandwidth, planar design, easy installation | Lower gain typically 2-3 dBi |
| Half-wave Patch Antenna | Higher gain typically 6-8 dBi, | Narrow bandwidth typically <10%, expensive, complex design |
| Quarter-wave Patch Antenna | Moderate gain of 4-6 dBi | Narrow bandwidth typically <10%, expensive, complex design |

All the antenna designs throughout this document were simulated with the help of ANSYS HFSS software [21]. Figure 13 shows a simulation setup for an antenna with ground plane, a typical setup includes antenna element(s), substrate, ground plane (depending on design), radiation boundary box and feed. Perfect Electrical Conductor (PEC) properties were given to all the conducting (or radiating) components of an antenna design, such as an antenna conductor and ground plane. A typical antenna element was supported with a substrate, and depending on design they were given material properties of FR-4, fiberglass, Rohacell foam or air. The frequency range (sweep) of simulations were set according to antenna operating frequency and bandwidth, typically between 100-300 MHz. The 'Discrete' sweep type was used with step size of ~5 MHz. The solution frequency of 200 MHz was used for these simulations with maximum passes of 20. The simulation solution space was defined with an air box with vacuum properties and radiating boundary conditions. To avoid the interference from the radiation boundary, the radiation box was maintained at least $\lambda/4$ away from the radiating (any conductive) surface (including ground plane). Also it could be noted that no additional conductive parts, such as cables, metallic components of surrounding structure, etc., were included in these simulations, and their effect on antenna performance is left for future study. While simulating, these antennas were excited by a feed of 50-ohm impedance (with lumped port). The reader should note that the half-wave and quarter-wave patch antennas are radiating in the z-direction (i.e. nadir is in z-direction) and the dipole antennas are radiating in opposite of z-direction due to the ground plane position with respect to the radiating conductor.

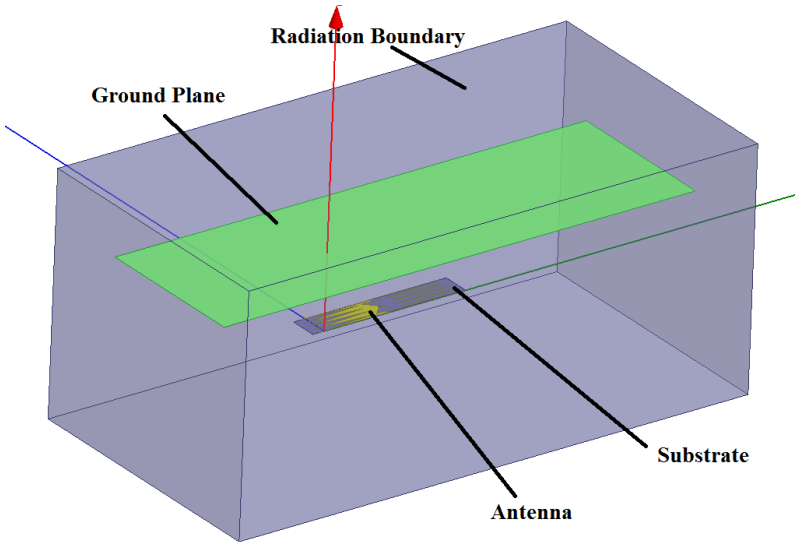


**Figure 13: A simulation setup for an antenna with ground plane**

## 3.1. Dipole Antenna

The dipole antenna was studied as it has wide bandwidth and a planar design which could be readily integrated into the lower wing skin of the Meridian UAS. CReSIS has used this type of antenna on previous installs such as the NASA DC-8 and NASA P-3 MCoRDS systems [6]. **Error! Reference source not found.** shows the dipole antenna used on NASA P-3 Orion aircraft. T

his antenna has a size of 27.2 in X 5.51 in and was originally designed by Harish and Joshi [22] and later modified by Byers [23]. The yellow surfaces in **Error! Reference source not found.** are t he radiating arms of the dipole antenna and the substrate (black surface) was given FR-4 properties. The resonant frequency varies with the length of the dipole arms, hence to lower the resonant frequency to 200 MHz and to increase the bandwidth, the original antenna size was modified to 29.2 in X 5.51 in from 27.2 in X 5.51 in by lengthening the dipole arms. The modified design of the dipole antenna developed by the author through the use of ANSYS HFSS software [21] was used in the trade study. The dipole antenna was simulated with and without the ground plane. For ground plane simulations, antenna was offset quarter wavelength (14.76 in) from ground plane. As expected, the dipole antenna with ground plane has higher gain and results in about double the gain at nadir. The dipole without the ground plane can be installed inside the wing bay, which avoids the complications of the supporting structure (hence less weight) and also avoids the additional drag due to antenna array assembly offset at quarter wavelength distance offset from the lower wing skin.

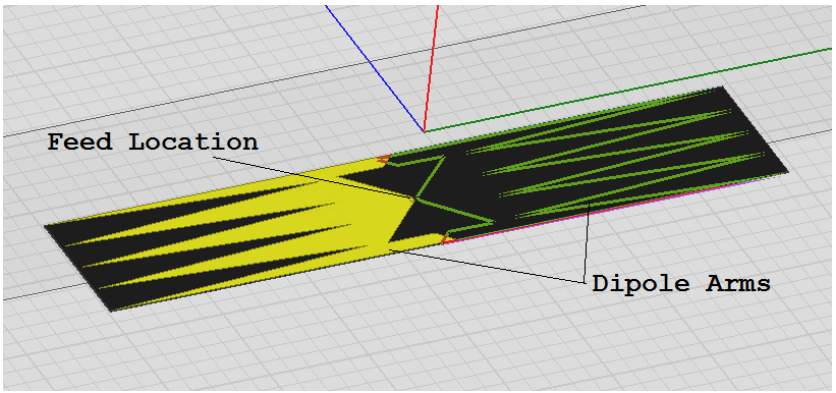


**Figure 14: Original Dipole Antenna**

### 3.1.1. Dipole Antenna without Ground Plane

Though the dipole antenna offset a quarter wavelength from the ground plane has higher gain since the reflected electromagnetic waves add constructively with the forward radiated energy, the dipole antenna without a ground plane is easy to incorporate inside the wing bay, and could be integrated into the lower wing skin. Hence the dipole antenna integrated into a dielectric S2-glass wing skin is considered as a potential design. For this initial simulation, the effects of the dielectric panel (wing skin) were ignored and only the antenna element is simulated. The simulated return loss versus frequency plot for both the original and modified dipole antennas are shown in Figure 15. The original dipole antenna resonates at 225 MHz with a bandwidth of 82 MHz and frequency range of 178-260 MHz. Then this dipole antenna was modified by extending its dipole arms by the author to lower the resonant frequency and increase the antenna bandwidth. This change in antenna geometry shifts the resonant frequency to 195 MHz, and it gives a frequency range of 163-260 MHz with a bandwidth of 97 MHz. The results obtained are tabulated in Table 3. It is noticed that due to antenna modification, the resonant frequency is dropped by 30 MHz but the peak gain is also dropped by 0.5 dB.

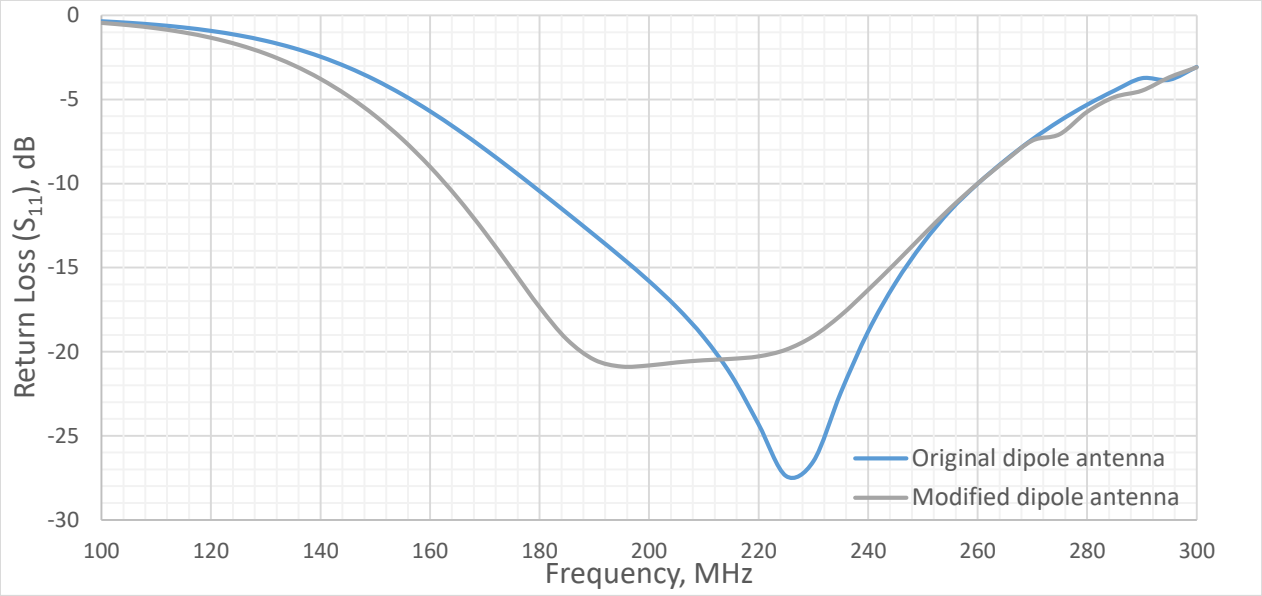


**Figure 15: Return loss vs frequency plot comparison between original and modified dipole antenna**

**Table 3: Comparison of original and modified dipole antenna results**

| Antenna Type | Resonant Frequency, MHz | Bandwidth, MHz | Frequency Range, MHz | Peak Realized Gain at Resonant frequency, dB |
|---|---|---|---|---|
| Original dipole antenna [23] | 225 | 82 | 178-260 | 2.79 |
| Modified dipole antenna | 195 | 97 | 163-260 | 2.32 |

### 3.1.2. Dipole Antenna with the Ground Plane

From the previous section, it was found that the modified dipole antenna had a lower resonant frequency and wider bandwidth, thus only the modified dipole antenna design was then simulated with the ground plane. For the simulation, it was assumed that the lower surface of the wing (flat surface with size of 140 in X 16.5 in) is a perfect conductor and acts as a ground plane, and the antenna operating at a frequency of 200 MHz is located at a quarter wavelength (14.76 in) offset from the lower wing surface, as shown in Figure 16. The return loss result is shown in Figure 17. This design has a bandwidth of 98 MHz and a peak realized gain of 6.76 dB at 175 MHz, which is more than twice that of the dipole antenna without the ground plane. Due to the lower resonant frequency, attenuation and scattering in the ice is expected to be slightly lesser. The lower resonant frequency and higher gain are both desired to meet the objectives of this study.

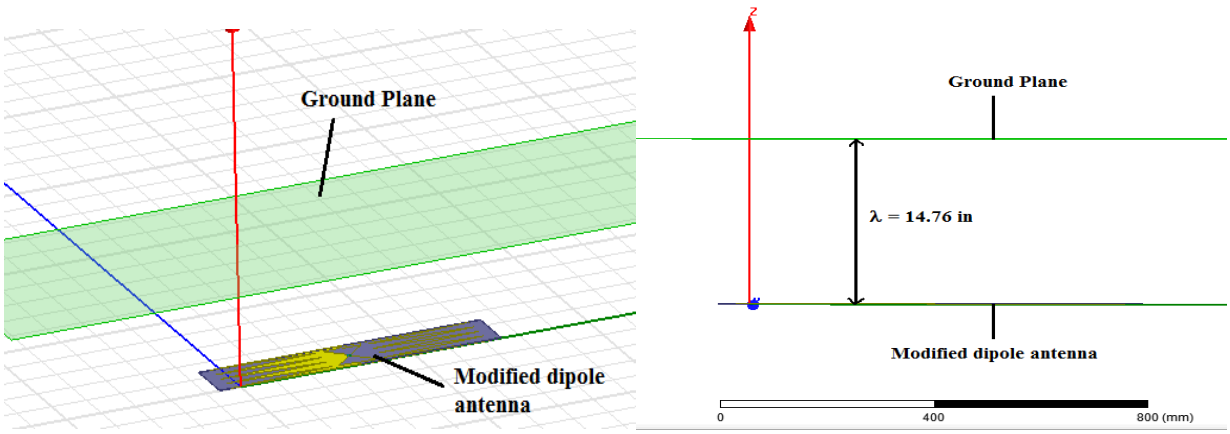


**Figure 16: Isometric view (left) and front view (right) of the modified dipole antenna with the ground plane at a quarter wavelength offset**

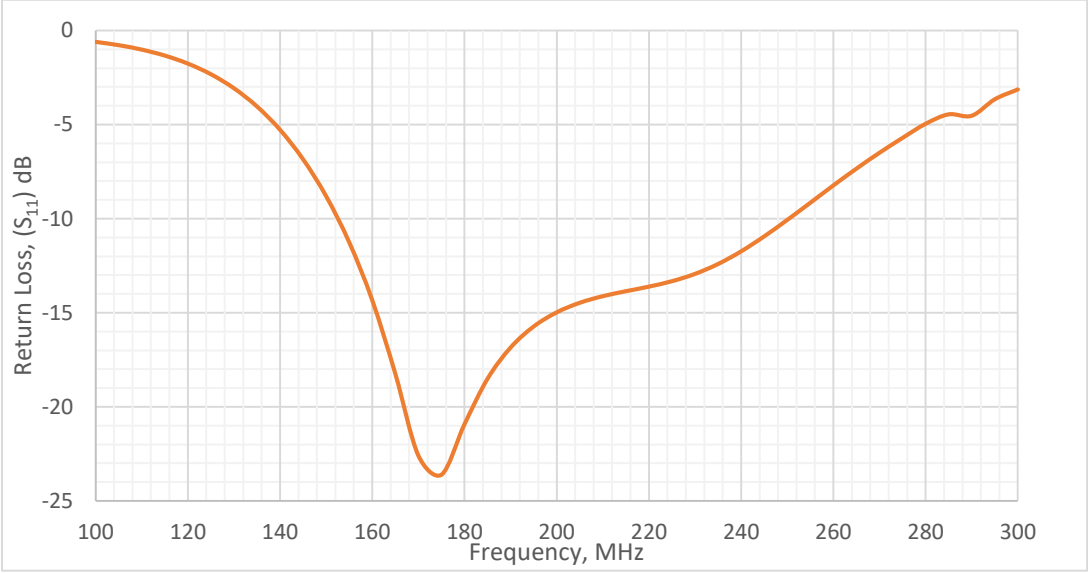


**Figure 17: Return loss plot for modified dipole antenna with ground plane**

## 3.2. Patch Antenna

The patch antenna was considered for its higher gain as compared to the dipole antenna at the expense of narrower bandwidth. The patch antenna was studied from [24], and designed with the help of [25]. In this design, the square patch antenna was excited by a capacitive patch and a constant 0.03 in (0.75 mm) of offset was maintained between them. This approach was taken in favor of a direct probe excitation in an effort to minimize the inductive impedance of the feed probe which is caused by the relatively large offset of the ground plane due to the low frequency of operation. The diameter of this feed probe was kept 0.08 in (2 mm), Figure 18 shows the details of the patch antenna. ROHACELL® foam is used as the substrate between the radiating patch and capacitive feed patch, and also between the ground plane and capacitive feed patch. PEC properties were given to radiating patch, excitation patch, feed probe, and ground plane. Initially, radiating square patch size was set to half wavelength (~ 30 in), ground plane was set to ~ 37 in, height 'H'

(between radiating patch and ground plane) was set to 2.6 in, and feed probe was located at (8 in, 16 in) in X and Y direction respectively.

A parametric analysis was completed to find the patch size for the antenna that can meet desired electrical requirements by varying patch dimensions along the X and Y axis (i.e. Px and Py), feed location along the X- and Y-axis (i.e. Cx and Cy), and distance between radiating patch and ground plane (H) (parameters are defined in Figure 18). The patch dimensions (Px and Py) varied from 15.75 in to 25.6 in (400 mm to 650 mm) to find a patch size that meets frequency requirements, and subsequently the feed location, Cx and Cy, were varied to find an ideal feed location. Also the distance between the patch and ground plane (H) was varied from 2.16 in to 2.56 in (55 mm to 65 mm). Later, the total height of the antenna assembly was restricted to the maximum height of 2.56 in (65 mm) per the dimensional constraints of the wing bay described in the beginning of this section. As shown in Figure 19 and Figure 20, the only antenna designs that meet the frequency range requirements are Patch Antennas (PA) with patch size of 23.62 in X 23.62 in (600 mm X 600 mm) and 25.6 in X 25.6 in (650 mm X 650 mm), named as PA 600 and PA 650 respectively; however, these antennas are larger than the available wing bay area. The peak realized gain of about 8.2 dB was achieved from these antennas, which is three times more than that of the modified dipole antenna without ground plane. The return loss versus frequency plot for different square patch sizes are provided in Figure 19, and the peak realized gain versus frequency plot is shown in Figure 20, with their respective square patch dimensions. Dielectric (S2) material properties (dielectric constant of 3.4) were given to the uppermost layer skin.

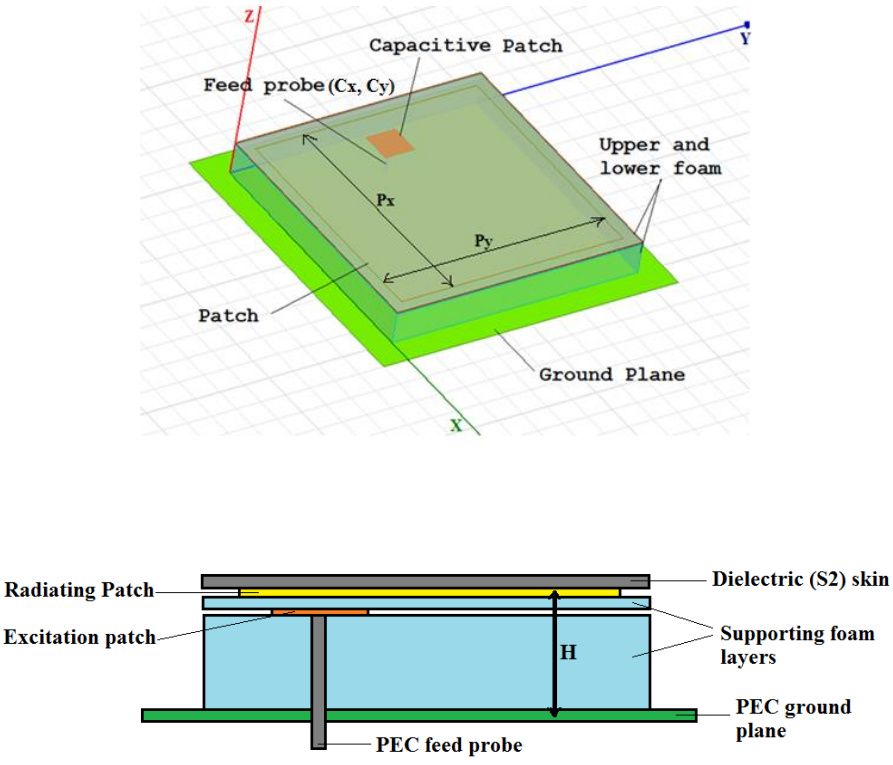


**Figure 18: 3-D view (above) and front view (below, not drawn to scale) of the patch antenna**

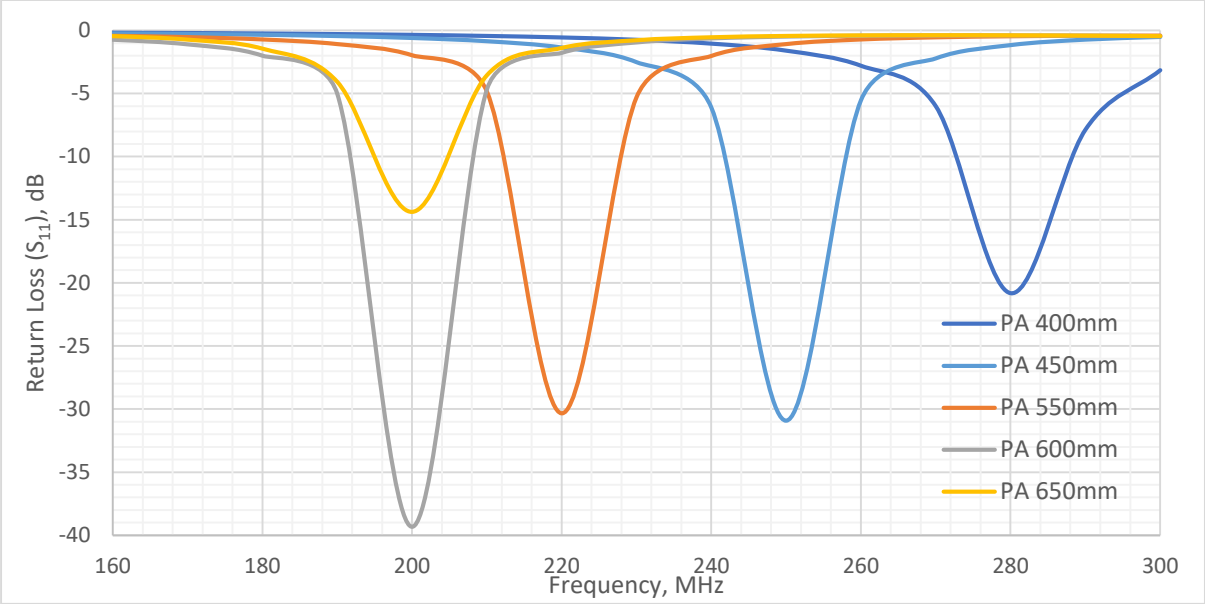


**Figure 19: Return loss vs frequency plot for various square patch antennas**

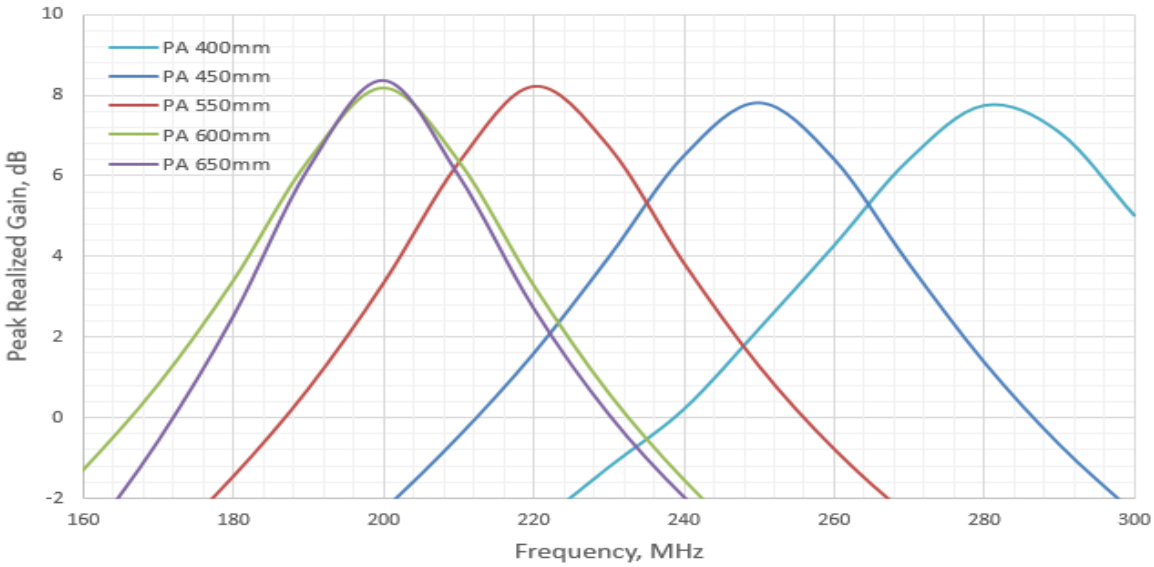


**Figure 20: Antenna gain vs frequency plot for various square patch antennas**

While this design demonstrates a significant gain improvement over the dipoles in Section 3.1, a standard patch antenna is not a viable choice, as it violates the dimensional constraints of the wing bay (length) to meet the frequency range requirements. Also it was found that resonant frequency is incredibly sensitive to the offset between the capacitive patch and the antenna patch. Also, a long feed probe is not ideal for a flexing and vibrating aircraft as the fragile feed probe would likely fracture in the presence of vibration.

## 3.3. Quarter-wave Patch Antenna

The quarter-wave patch antenna was investigated due to its low-profile design and low resonant frequency at the cost of narrow bandwidth. In this design, the square patch is excited by a feed probe, and it is supported by a foam substrate with an edge shorted to the ground plane as shown in Figure 21. Theoretically the effective (i.e. total) length of the quarter-wave patch antenna is half the wavelength at the operating frequency (i.e. the addition of the patch length and shorting wall height is equal to half the wavelength). The size of this antenna is constrained by the rear spar height and spar spacing. The volume of the space available for the antenna in the wing bay is 18.5 in X 14.2 in X 2.8 in (470 mm X 355 mm X 71 mm). Thus a wing bay can accommodate a square patch of 14 in X 14 in and a shorting wall height of 2.8 in (70mm).

PEC properties were given to radiating quarter-wave patch, shorting wall, feed probe, and ground plane. The substrate was given the foam (dielectric constant of 1.07) material properties. Initially, radiating square quarter-wave patch size was set to quarter wavelength (~ 15 in), ground plane was set to ~ 18 in, height 'h' (between radiating quarter-wave patch and ground plane) was set to 2.6 in, and feed probe was located at (8 in, 14 in) in X and Y direction respectively. The diameter of this feed probe was kept 0.08 in (2 mm). To find an antenna that resonates at 200 MHz and considering the dimensional constraints mentioned above, parametric analyses using HFSS were performed for different square patch sizes, height of shorting wall (h), and feed location (Cx and Cy). The return loss for the various designs are shown in Figure 22. The quarter-wave (QW) Patch antenna designs with patch size of 12.8 in X 12.8 in (325 mm X 325 mm) and 13.2 in X 13.2 in (335 mm X 335 mm), named as QW 325 and QW 335 respectively, resonate at 195 MHz and 190 MHz with bandwidths of 9-10 dB and peak realized gains of about 4.3 dB, as show in Figure 22 and Figure 23, respectively. The antenna designs QW 325 and QW 335 satisfy the operating frequency requirements (i.e. resonating about 200 MHz) with higher gain, and also these designs satisfy the dimensional constraints of the wing bay. Hence these designs are considered as candidate designs and are studied in detail in Chapter 4.

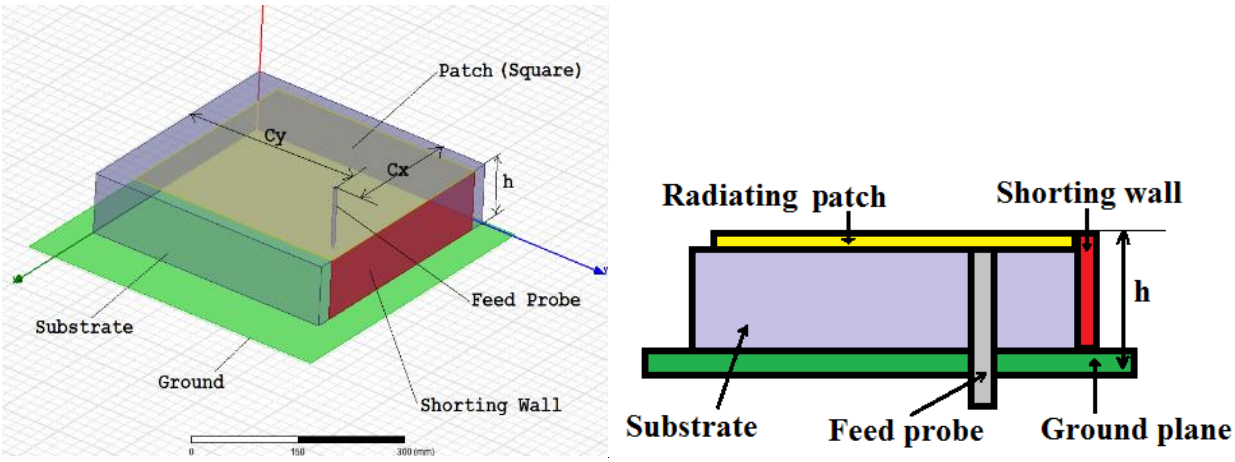


**Figure 21: 3-D view (left) and side view (right, not to scale) of quarter-wave patch antenna**

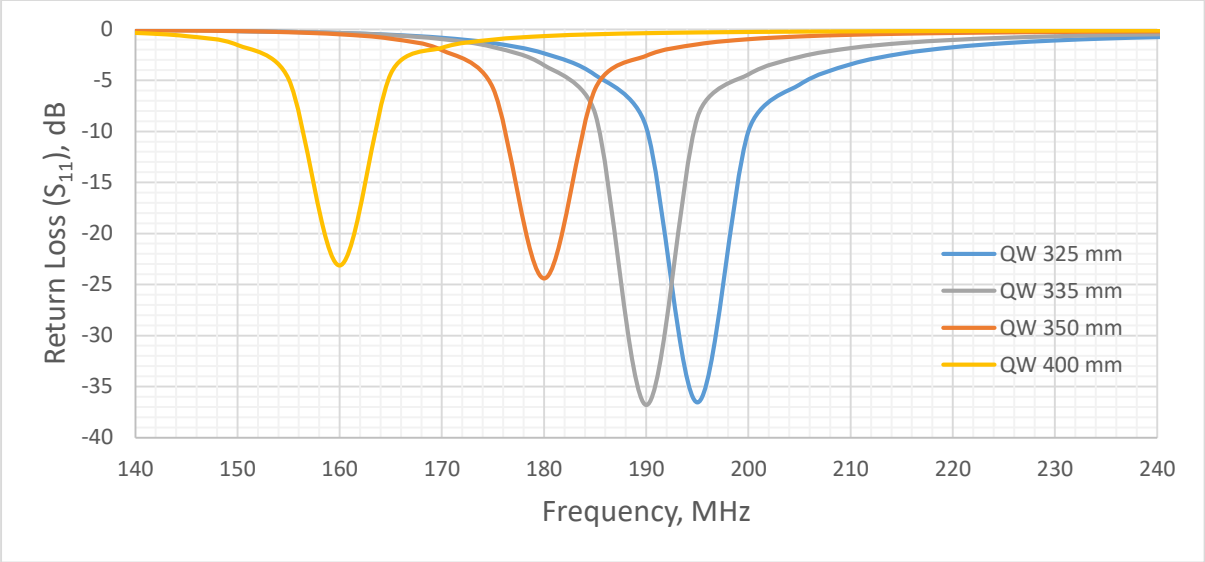


**Figure 22: Return loss vs frequency plot for various quarter-wave patch antenna sizes**

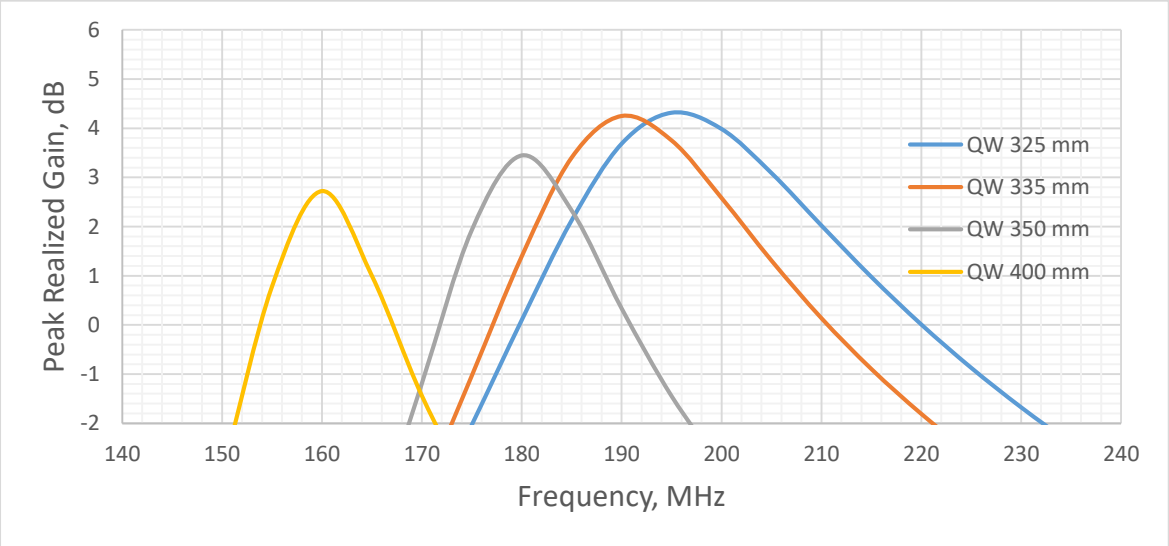


**Figure 23: Gain vs frequency plot for various quarter-wave patch antennas**

## 3.4. Summary of Antenna Design Trade Study

From the trade study, it was found that designs for the dipole antenna (without ground plane) and quarter-wave patch antenna could meet electrical performance requirements like resonant frequency, as well as dimensional constraints of the wing bay, hence these two designs were included in the detailed analysis in the next section. In addition, due to the superior electrical performance of the dipole with ground plane, this design was also carried forward while recognizing its implications on the aircraft performance. The electrical performances of the

candidate designs are compared in Table 4. While the electrical performance of the half-wave patch antenna is acceptable (high gain of 8.2 dB), it has lower bandwidth of 16 MHz, but it was primarily eliminated due to its violation of dimensional constraints. In addition, to locate the larger patch antenna below the wing, the supporting structure would add more weight and drag (possibly lift depending on fairing cross-section), as compared to the planar dipole integrated in the same manor. The patch antenna (~ 2.56 in) is much thicker compared to the dipole antenna (~ 0.06 in), hence the patch antenna will need thicker (hence more drag) and heavier supporting structure than the dipole antenna. Also, the dipole antenna design is simple, more robust, thinner to integrate, and lighter. The patch antenna has more components, and it is more complex than the dipole antenna. Also, the patch antenna and quarter-wave patch antenna were found to be very sensitive to the probe offset from patch (change of 0.04 inch in probe offset would shift resonating frequency by 5-10 MHz), which means their performance will deteriorate in the presence of vibration. The quarter-wave patch antenna fits inside the wing bay and has moderate gain of 4.3 dB. Hence assuming a more robust design of this antenna would be achievable in the future with advanced design technique, this design was studied further. Due to the violation of the size constraints and the lack of robustness in the half-wave patch design, only the planar dipole and the quarter-wave patch designs were considered in the detailed analysis in the Chapter 4.

**Table 4: Electrical performance comparison of candidate designs**

| Antenna Type | Resonant / Center Frequency, MHz | Bandwidth, MHz | Frequency Range, MHz | Peak Realized Gain, dB |
|---|---|---|---|---|
| Vivaldi Antenna | 750 | 960 | 162-1121 | -0.80 (at 200 MHz) |
| Modified dipole antenna without GP | 195 | 97 | 163-260 | 2.32 |
| Modified dipole antenna with GP | 175 | 98 | 152-250 | 6.76 |
| Half-wave patch | 200 | 16 | 192-208 | 8.2 |
| Quarter-wave patch antenna | 190 | 9 | 185-194 | 4.3 |

# 4. Detailed Analysis of the Candidate Antenna Designs

In this section, the candidate designs for the dipole antenna and quarter-wave patch antenna are described in terms of their electrical performance such as return loss, gain, and radiation pattern. An identical simulation setup (same as Section 3) was used for all array designs of this section with additional antenna elements and excitation ports. The purpose of this section is to identify the ideal antenna design from the candidate design pool. This section also includes the array performance of these candidate antenna designs when integrated into the Meridian UAS. The final antenna design was chosen based on its electrical performance. A wing integrated antenna array was then structurally sized with the help of Finite Element Analysis (FEA) to estimate the weight added to the aircraft due to the new radar system.

## 4.1. Antenna Performance

### 4.1.1. Dipole Antenna without Ground Plane

The electrical performance of the modified dipole antenna without ground plane is described in Section 3.1.1. The antenna return loss and peak realized gain properties are plotted against frequency in Figure 15 and Figure 24, respectively. The electrical performance of this antenna is described in Table 3. This design has comparably lower gain, but it has steady gain in the frequency range of our interest.

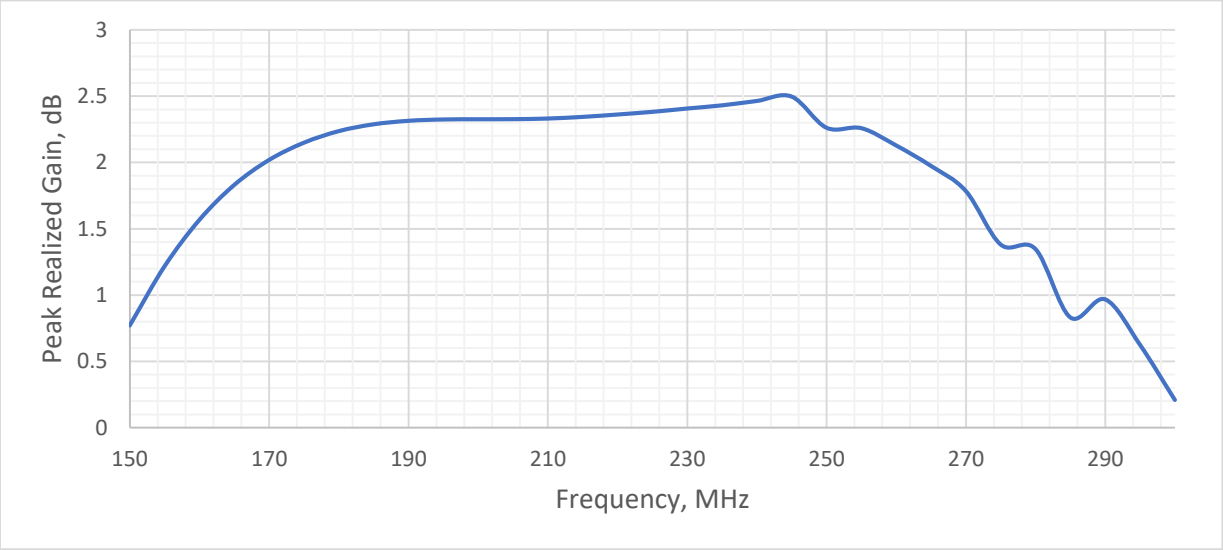


**Figure 24: Peak realized gain plot for modified dipole antenna**

The coordinate system for the simulations is shown in Figure 25, where $\phi$ is the azimuth angle (the angle from the x-axis) and $\theta$ is the elevation angle (angle from the z-axis). The radiation patterns for modified dipole design at $\phi = 0^o$ and $90^o$ are shown in Figure 26, where it can be seen that modified dipole antenna radiates energy in a doughnut shaped pattern. For ice sounding applications, energy radiated in zenith direction is wasted. The modified dipole has a beamwidth of about $70^o$ in the $\phi = 0^o$ plane. The next subsection presents the design that mitigates this problem (i.e. wide beamwidth). In the $\phi = 90^o$ plane, an oblong radiation pattern at nadir can be noticed, due to this unusual pattern radiating power at nadir is reduced by 10 % in the $\phi = 90^o$ plane.

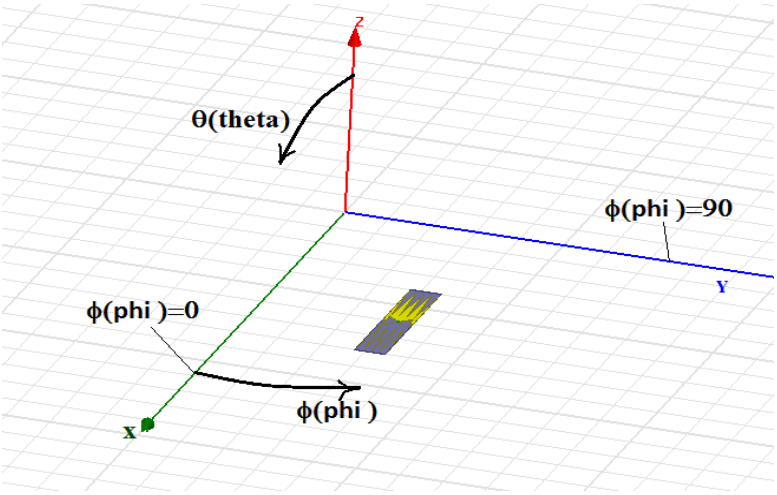


**Figure 25: Coordinate system angle definition**

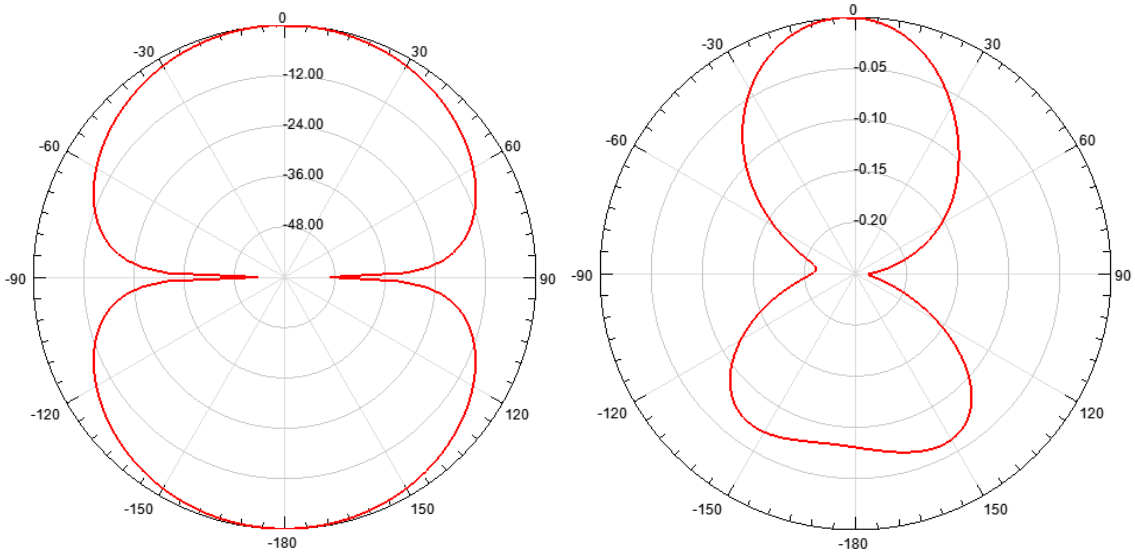


**Figure 26: Radiation Pattern of a modified dipole antenna at ϕ = 0º (left) and 90º (right).**

### 4.1.2. Dipole Antenna with Ground Plane

Since the modified dipole antenna with ground plane (GP) is expected to have higher gain compared to the modified dipole alone, it was also examined as part of the detailed study. The upper or lower skin of the wing can potentially be used as a ground plane, which could save the weight and cost required to design and integrate a separate ground plane; therefore, two GP configurations were considered for the dipole—one with the upper skin as the ground plane and one with the lower skin of the wing as a ground plane (both assume quarter wavelength offset from the antenna at an assumed resonant frequency of 200 MHz). Though Meridian wing is made of carbon fiber composite material, PEC properties were applied to skins due to conductive properties that are similar enough to make this assumption for early studies. The performances of the configurations are compared in Table 5. The antenna return loss and peak realized gain for these

two configurations are compared in Figure 27 and Figure 28. The realized gain is relatively constant across the desired frequency range of 180-210 MHz, also the antenna gain and bandwidth is slightly higher when the flat lower skin is utilized as the ground plane.

**Table 5: Dipole antenna performance at quarter wavelength offset**

| Antenna Type | Resonant Frequency, MHz | Bandwidth, MHz | Frequency Range, MHz | Peak Realized Gain, dB |
|---|---|---|---|---|
| Dipole antenna with upper skin as GP | 175 | 90 | 156-246 | 6.72 |
| Dipole antenna with lower skin as GP | 175 | 98 | 152-250 | 6.76 |

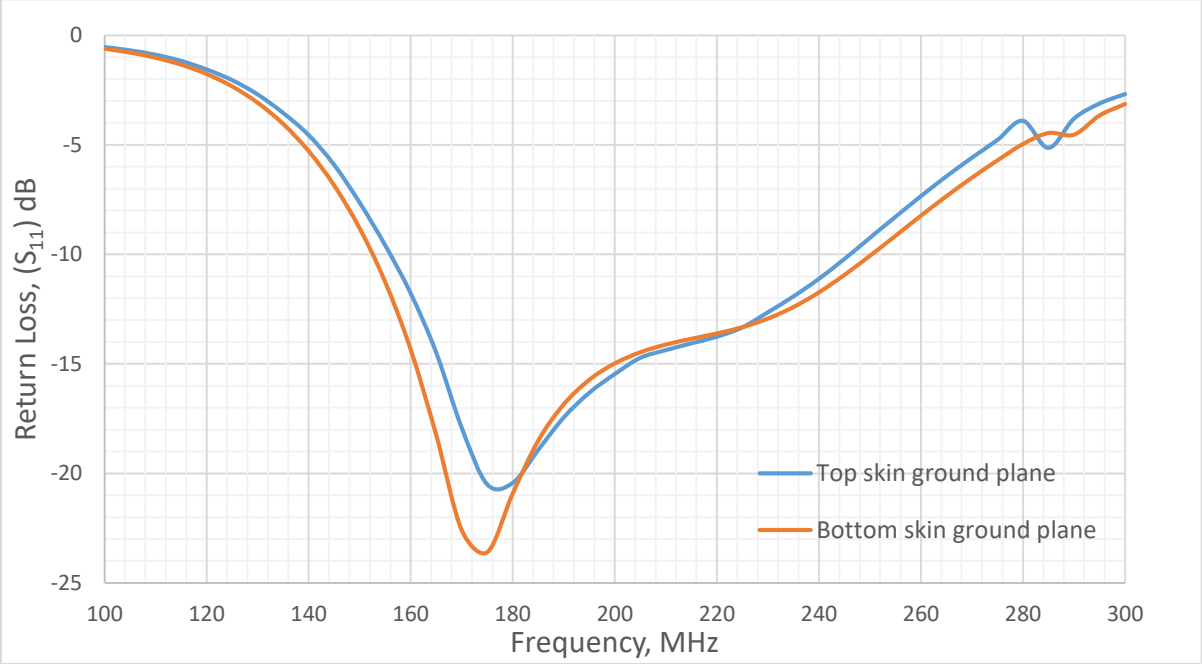


**Figure 27: Return loss comparison for the antenna with upper and lower skin as a ground plane at a quarter wavelength offset**

The antenna with lower skin as the ground plane gives almost constant peak gain of about 6.5 dB over the frequency range of interest. It also produces a uniform radiation pattern in the nadir direction. If the upper skin was used as a ground plane, there would be possible adverse flow interactions between the required support structure and the control surfaces due to the reduced vertical separation. This would also require the use of dielectric material for the lower skin and control surfaces, which greatly increases manufacturing complexity, and the thermal coefficient of expansion mismatch over the entire span of the wing will increase stress. With these considerations it was determined that the carbon fiber composite lower skin as a ground plane was preferred.

The radiation pattern for both designs at ϕ= 0º and 90º are shown in Figure 29 and Figure 30, where it can be seen that the antenna with the upper skin as a ground plane has a tilted radiation pattern by about 5°. Both of these designs have a wide beamwidth of about 60º.

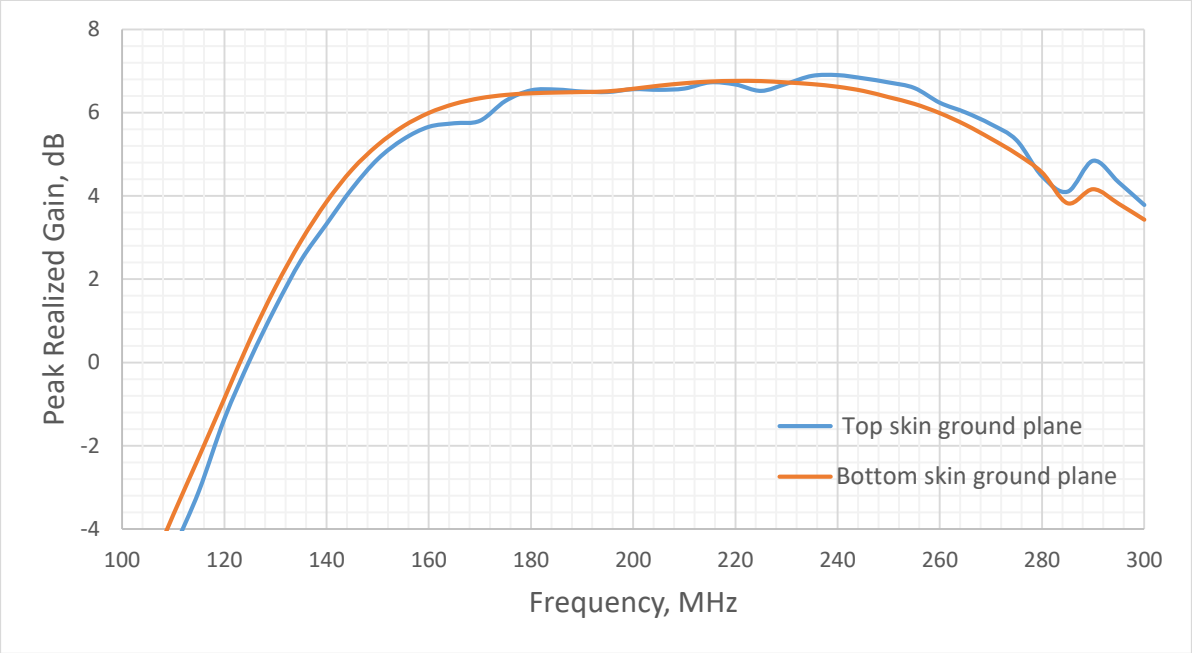


**Figure 28: Gain comparison for the antenna with upper and lower skin as a ground plane at a quarter wavelength offset**

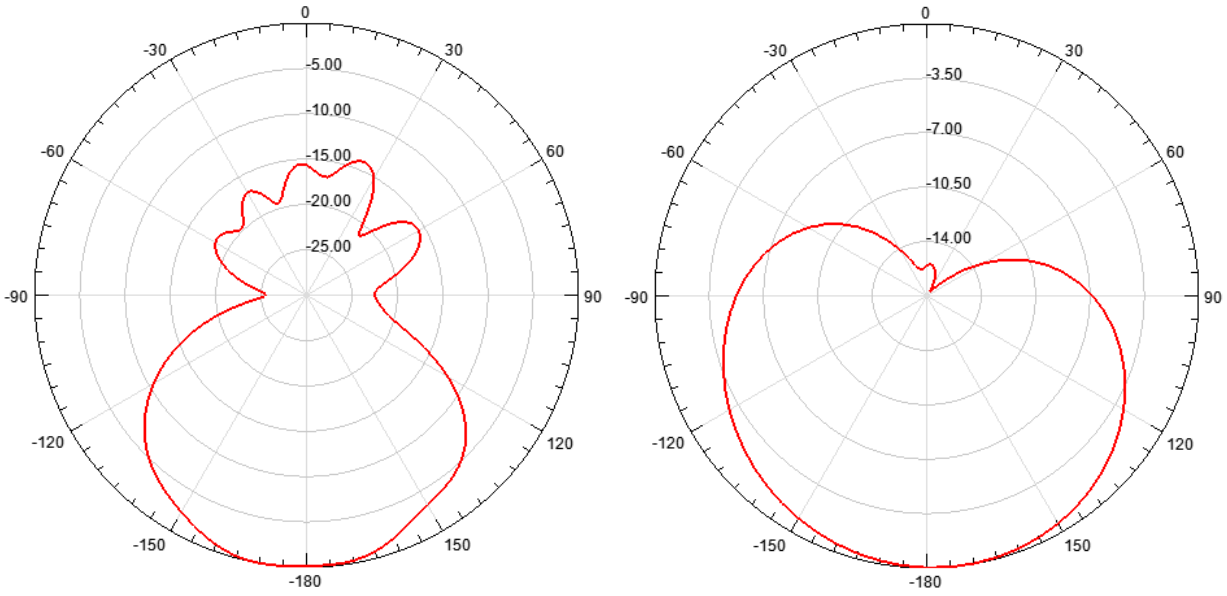


**Figure 29: Radiation Pattern of an antenna with upper skin as a ground plane at ϕ = 0º (left) and 90º (right).**

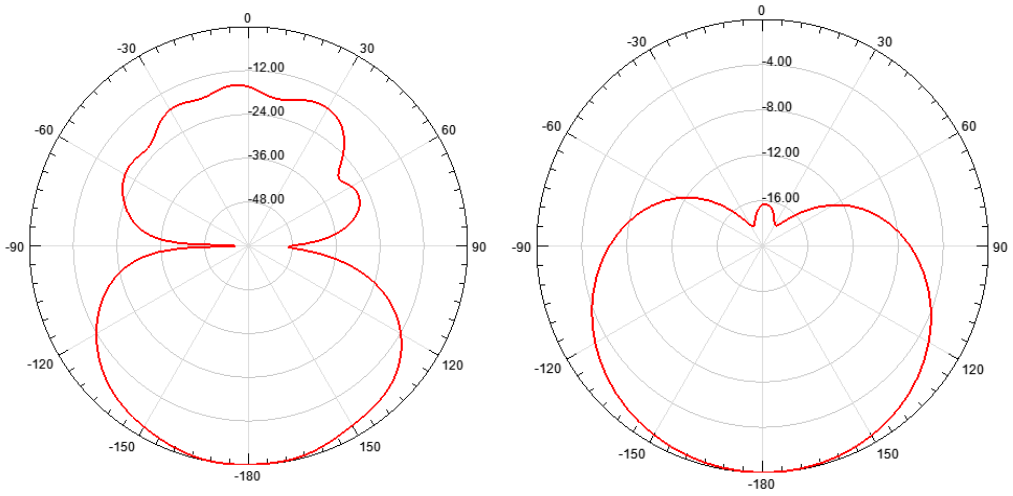


**Figure 30: Radiation Pattern of an antenna with lower skin as a ground plane at ϕ = 0º (left) and 90º right.**

### 4.1.3. Quarter-wave Patch Antenna

After the preliminary analysis, a patch size of 13.2 in X 13.2 in (335 mm X 335 mm) was selected from Section 3.3 as a candidate design for this antenna type due to its lower return loss and higher gain. In the detailed analysis, a parametric analysis was performed to optimize the design with regards to the return loss and gain performance. During this analysis, the location of the feed (Cx and Cy) were varied simultaneously with small steps of ΔCx and ΔCy along the x- and y-axis, respectively, along with offset between the patch and ground plane (i.e. shorting wall height). The parameters are shown in Figure 21 and Figure 31, along with offset between the patch and ground plane (i.e. shorting wall height). The step size of 5 MHz was used during frequency sweep. Cx was then kept constant at 8.46 in (215 mm) and Cy was varied from 11 in to 13.4 in (280-340 mm). At the same time, the shorting wall height (h) was varied from 1.97 in to 2.56 in (50-65 mm). The diameter of feed probe was kept 0.08 in. The optimal design determined from the parametric analysis has a resonant frequency of 190 MHz, bandwidth of 9 dB, and a gain of 4.25 dB as shown in Figure 32 and Figure 33, respectively. This design has radiating patch size of 13.2 in X 13.2 in, height 'h' (between radiating quarter-wave patch and ground plane) is 2 in, and feed probe was located at (8.6 in, 14 in) in X and Y direction respectively.

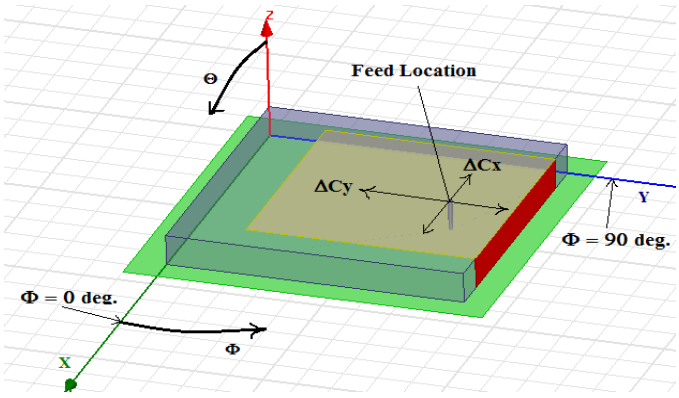


**Figure 31: Parametric analysis with different feed locations**

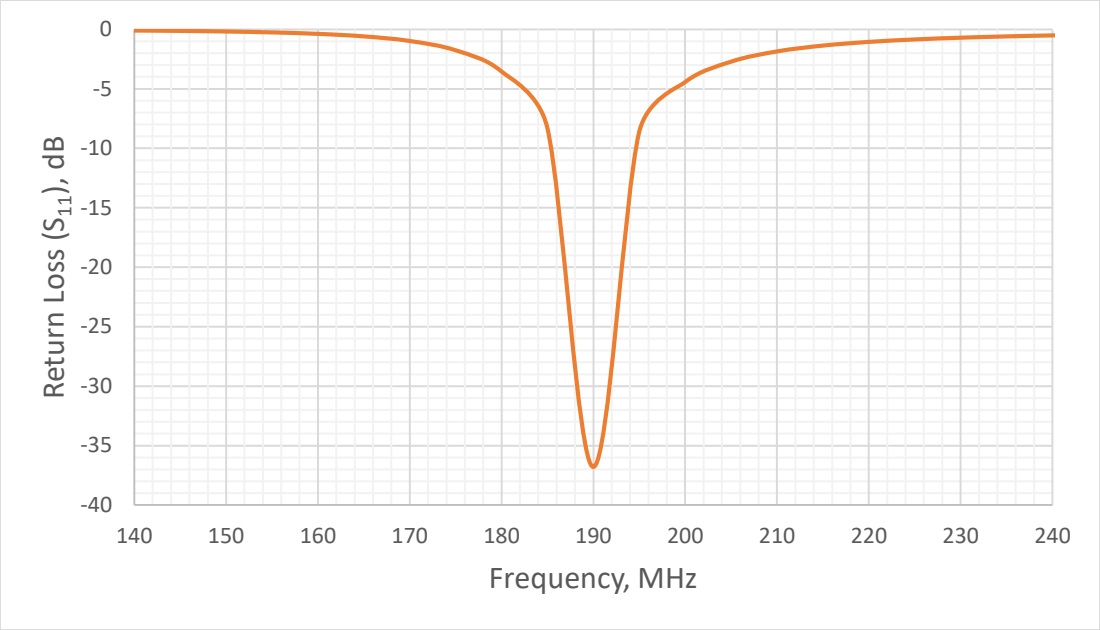


**Figure 32: Return loss plot for the quarter-wave patch antenna with ground plane**

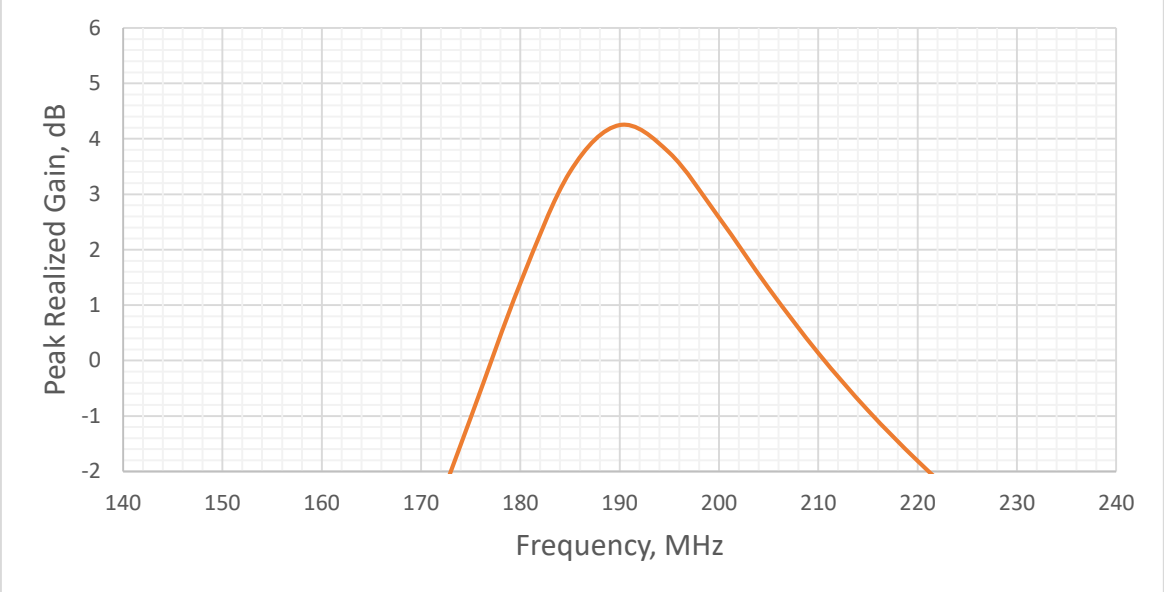


**Figure 33: Gain plot for the quarter-wave patch antenna**

The radiation pattern for the quarter-wave antenna is shown in Figure 34 for angles $\phi = 0^{o}$ and $90^{o}$. This antenna satisfies the dimensional constraints of the Meridian wing and resonates at a frequency of 190 MHz. Unlike the dipole with ground plane design, this antenna could be integrated inside the wing bay with ground plane, and this design has about 2 dB higher gain compared to dipole without ground plane design. The following sub-section describes the array performance of the three designs.

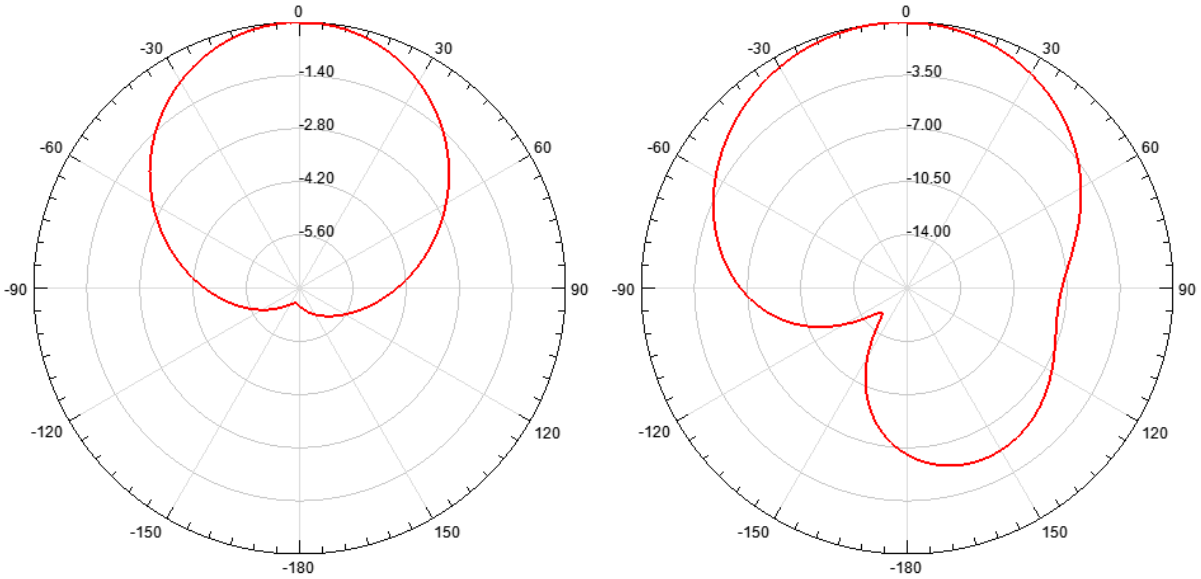


**Figure 34: Radiation Pattern of an antenna at ϕ = 0 (left) and 90 deg. (right).**

## 4.2. Array Performance

The three antenna designs were modeled in linear arrays to assess the as-installed performance. To sufficiently suppress surface clutter and image the bedrock topography deep below the ice sheet, large cross-track antenna arrays with high gains in the nadir direction are required. For this study, number of elements in the array was limited by the dimensional constraints imposed by the wing. If the antenna is to integrate below the wings (as in the case of the dipole with ground plane), the antenna array should be no longer than 140 inches per wing. The dipole antenna array with ground plane was assumed to be installed below the wing with the help of a custom fairing while the lower skin of the Meridian acts as a ground plane. The antenna design with the upper skin as a ground plane was not assessed due to its reduction in bandwidth and asymmetric radiation pattern towards nadir. The quarter-wave patch antenna array and the dipole without ground plane designs were assumed to be installed inside Meridian wing bays. An array of seven quarter-wave patch antennas could be installed into seven out of the eight wing boxes of each wing. The root wing box was excluded, as it is not located outside the fuselage mold line. In the array performance study, cross coupling between antennas was taken into account by the simulations. Based on the array performance and practicality of these designs, the final antenna design to be integrated into the Meridian UAS could be selected. Again these simulations did not include the conductive components, such as cables and metallic parts of the wing, and it is left for detailed study in future. The simulation set-ups for each case was the same as observed for the individual elements except the radiation box was extended to accommodate the array and maintain at least quarter wavelength offset between an array and box.

### 4.2.1. Dipole Antenna Array of the Four Antennas

#### 4.2.1.1. Dipole Antenna Array without Ground Plane

The dipole antennas are placed in a uniform linear array configuration to improve cross-track beam performance as shown in Figure 35. The element center-to-center spacing of 32.4 in is maintained, which is slightly higher than half the wavelength at 200 MHz ($\lambda/2$ = 29.5 in), to avoid grating lobes and to minimize the cross coupling between antennas. This spacing results in a gap of 2 in between adjacent antennas. Table 6 summarizes the results of the dipole array performance.

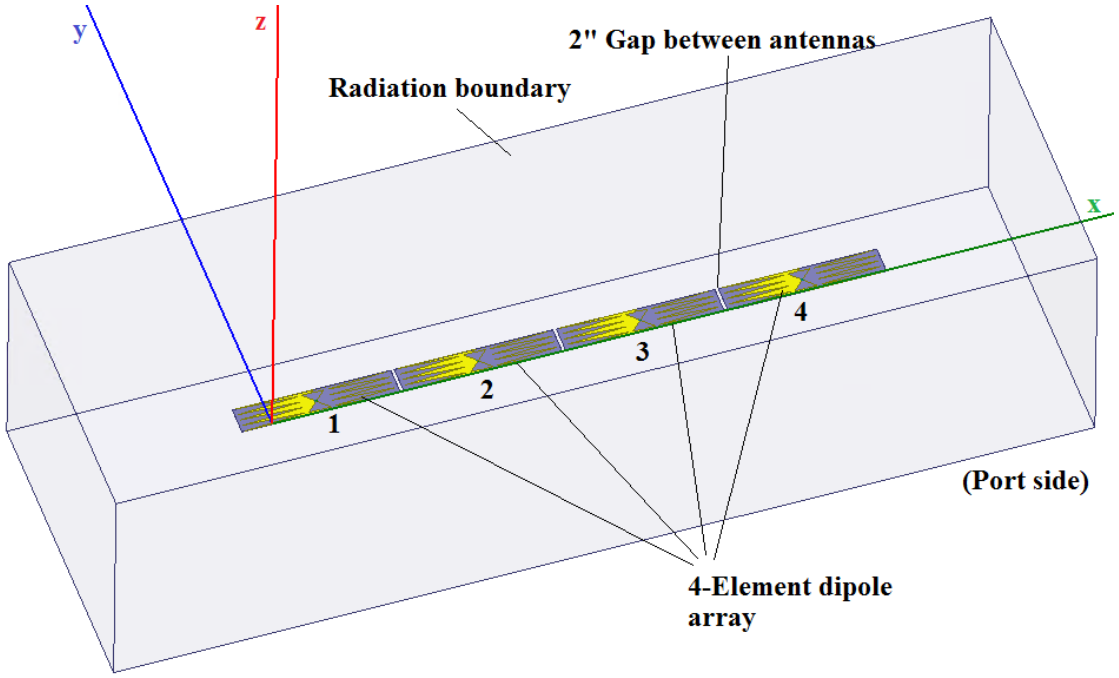


**Figure 35: 3-D View of four dipole element array without ground plane from HFSS design**

**Table 6: Four-element dipole antenna array performance**

| Antenna Type | Resonant Frequency, MHz | Bandwidth, MHz | Frequency Range, MHz | Peak Realized Gain at 205 MHz, dB |
|---|---|---|---|---|
| Four-element Dipole antenna array | 205 | 88 | 166-254 | 6.5 |

Figure 36 and Figure 37 shows the return loss of each element ($S_{11}$ indicates return loss of Element 1, $S_{22}$ is the return loss of Element 2, etc) and the array gain, respectively. The peak gain of the array (7.05 dB) occurs at 240 MHz. Also it can be noticed that the peak gain varies by

about1.5 dB over the antenna bandwidth which will be taken into account in the design of the radar waveform.

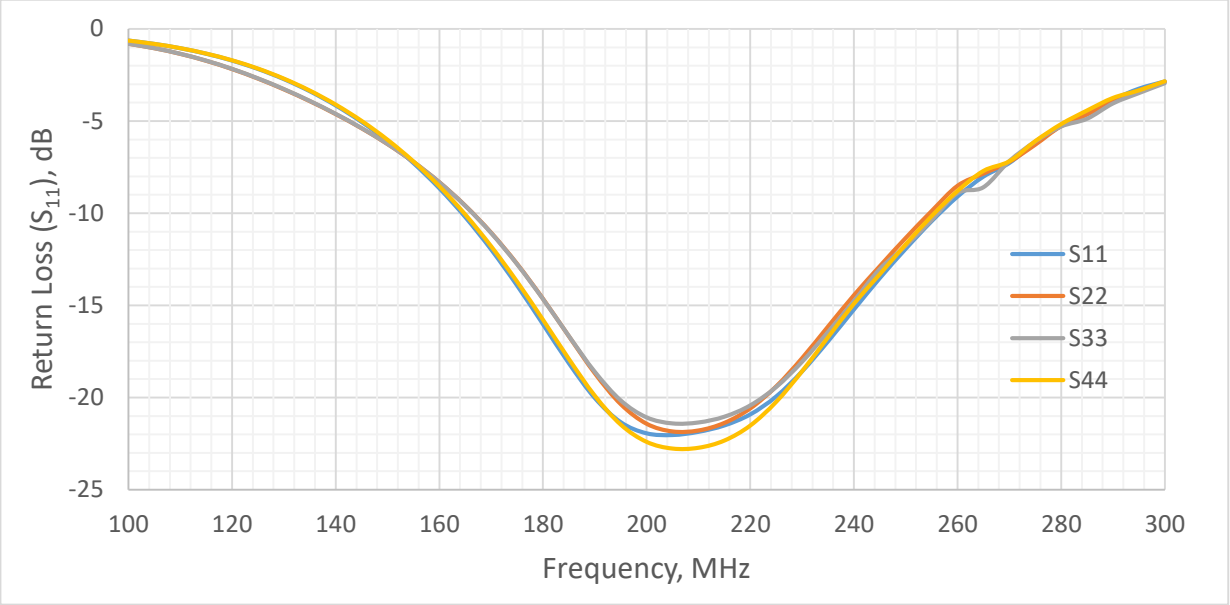


**Figure 36: Return loss of each dipole antenna versus frequency**

Comparing the radiation pattern of a single dipole element which resembles standard dipole radiation pattern, with a four-element dipole array without ground plane in Figure 38 (left), it can be noticed that the array has two primary lobes with much narrower beam widths in the cross-track direction. The main beam lobes of the array are symmetric and they are in the zenith and nadir direction as there is no ground plane. This design has a sidelobe level of ~12dB. The 3-dB beamwidth is about 25° for the four-element dipole array design, as shown in Figure 38 (left). This array design could be embedded into a Meridian wing as a transmitter, with another array on the other wing as a receiver.

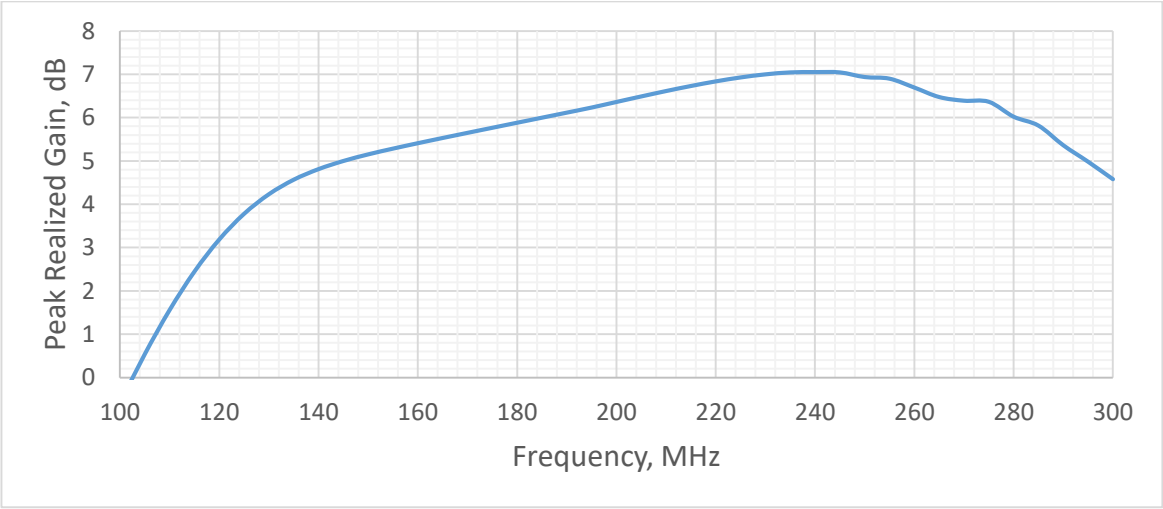


**Figure 37: Peak gain of the dipole antenna array**

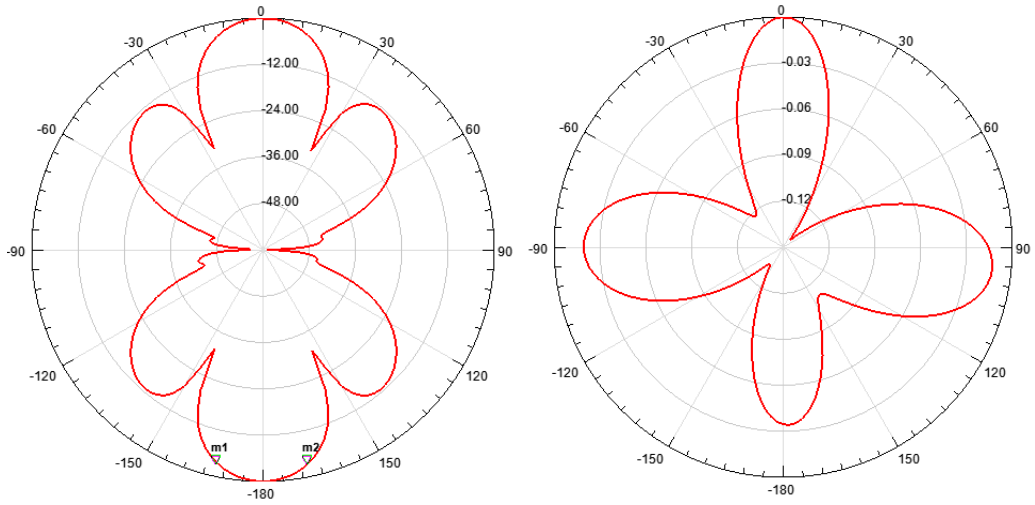


**Figure 38: Radiation Pattern of a four-element dipole array at ϕ = 0º (left) and 90º (right).**

#### 4.2.1.2. Dipole Antenna Array with Ground Plane

Similar to the previous study, in this sub-section the dipole antennas were placed in a uniform linear array configuration to improve cross-track beam performance as shown in Figure 39; however, in this simulation a ground plane representing the wing was included. The ground plane used was 150 in long and 32 in wide, and was maintained 14.8 in (quarter wavelength) above the array. Table 7 summarizes the results of the dipole array performance. Figure 40 and Figure 41 show the return loss of each element and the array gain, assuming the lower wing skin acts as ground plane for this four element array. The peak gain of an array (10.74 dB) occurs at 220 MHz. The peak gain variation in the bandwidth is small (varies by 0.75 dB). This array delivers about 4 dB higher gain than the array without ground plane, and more than twice the power is now radiated in the nadir direction. Also this array resonates at 180 MHz, 25 MHz lower than the array without ground plane. It can also be noticed that the ground plane reduces the bandwidth of an array by 5 MHz, which is not significant for this design.

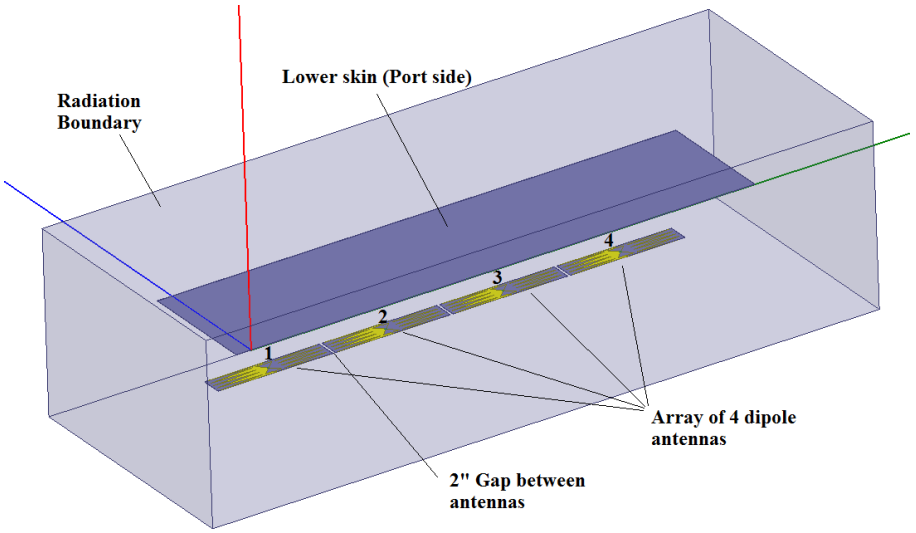


**Figure 39: 3-D View of four-element dipole array with lower wing skin from HFSS design**

**Table 7: Four-element dipole antenna array performance at quarter wavelength offset**

| Antenna Type | Resonant Frequency, MHz | Bandwidth, MHz | Frequency Range, MHz | Nadir Realized Gain at 180 MHz, dB |
|---|---|---|---|---|
| Dipole antenna array with lower skin as GP | 180 | 83 | 155-238 | 10.34 |

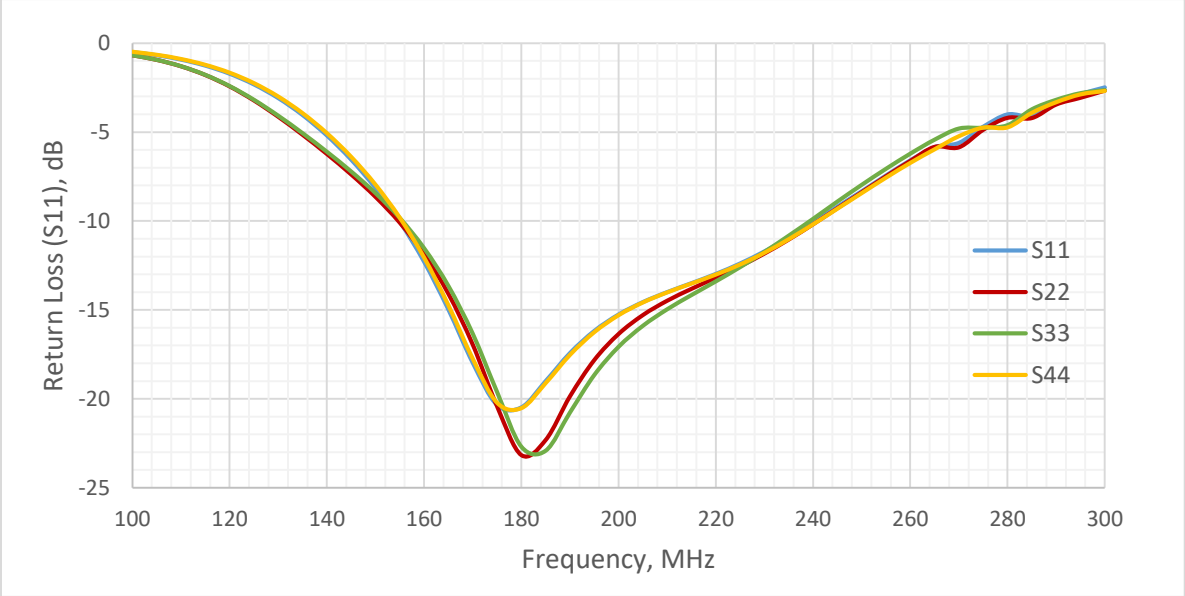


**Figure 40: Return loss of each dipole antenna versus frequency with lower skin as a ground plane at quarter wavelength offset**

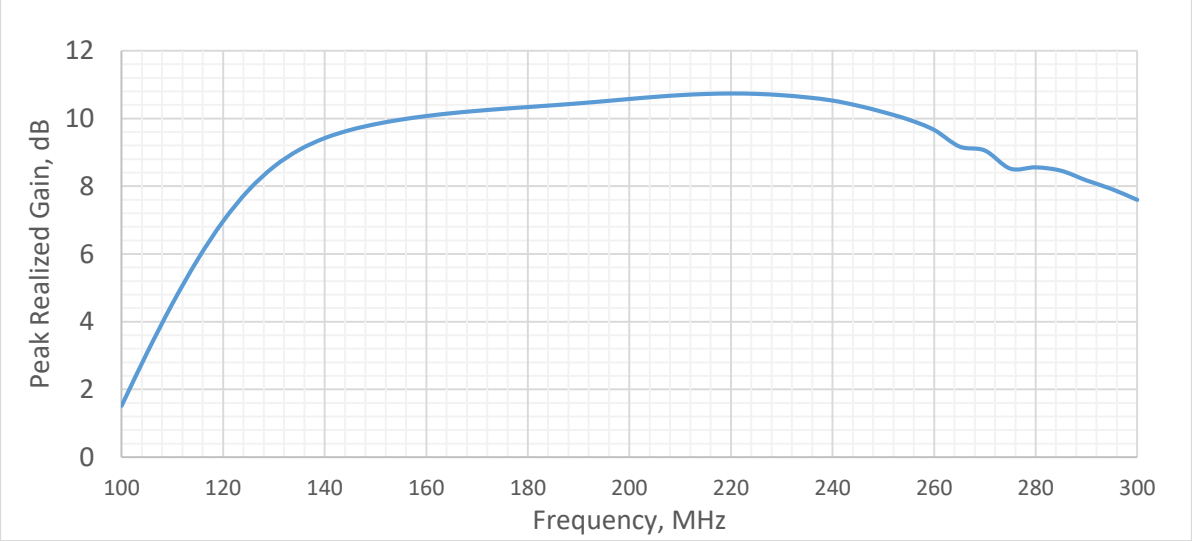


**Figure 41: Peak gain of the dipole antenna array with lower skin as a ground plane at quarter wavelength offset**

Comparing the radiation pattern of a dipole array without ground plane in Figure 38 (left) with the four-element array with ground plane in Figure 42 (left), it can be noticed that main beam lobe is only in the nadir direction and is sharper (i.e. narrower). A sidelobe level of ~12dB is achieved. The 3-dB beam width is about 22° for the four-element dipole array design, and the back lobe is ~16 dB below the forward lobe power. This array design could be installed below the Meridian wings with the help of custom fairing and pylon structures. This design is later studied in detail, where the implications of weight and drag are further examined.

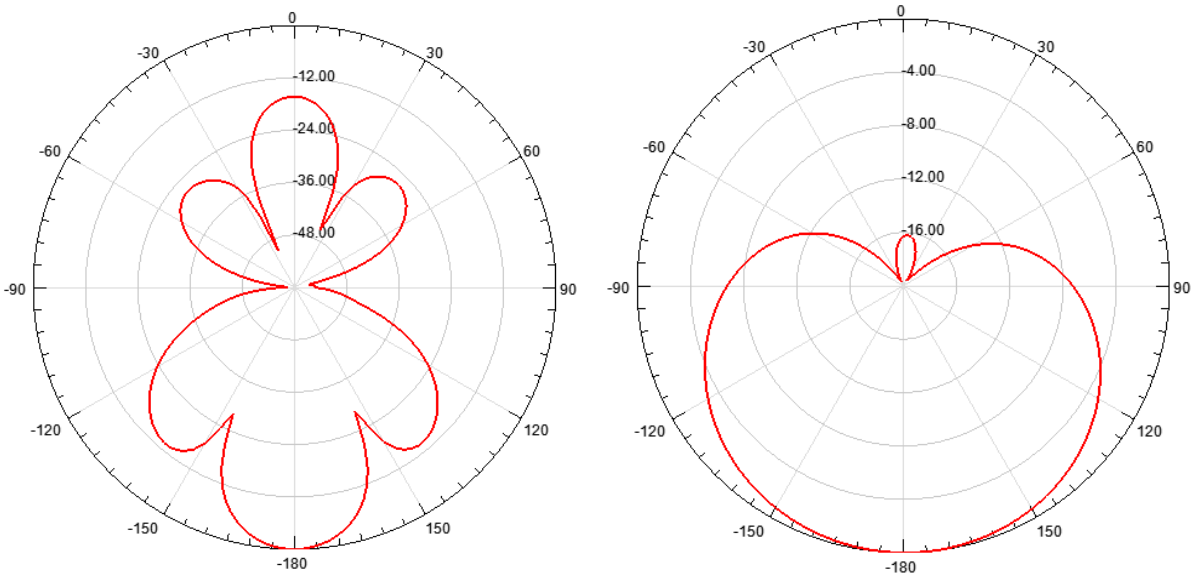


**Figure 42: Radiation Pattern of a four-element dipole array with lower skin as a ground plane at $\phi$ = 0º (left) and 90º (right).**

### 4.2.2. Dipole Antenna Array of the Eight Antennas

#### 4.2.2.1. Dipole Antenna Array without Ground Plane

This section shows the performance of an eight-element dipole array spanning both the starboard and port wings. A gap (72 in) was maintained between the middle elements of the array to account for the presence of fuselage and landing gear (and skis) structure, as shown in Figure 43. In this preliminary study, these structures were not included into this array simulation, but it is noted that these elements will interact with the array and need to be accounted for in future detailed studies. The element center-to-center spacing of 32.4 in is maintained, except between the middle elements (element 1 and 5) where it is 72 in. Table 8 summarizes the array performance results with the array offset a quarter wavelength from the lower wing skin. In Figure 44 and Figure 45, the return loss plot of each antenna element and the array gain is shown for the eight-element array, respectively. The return loss plots of the elements seem identical. The elements of the array resonate from 200–210 MHz, and the array has a bandwidth of 87 MHz and average peak gain of about 9 dB over this bandwidth. This array shows that all eight antenna elements could be used as transmitter and receivers, while also increasing the gain by 3 dB over that achieved by the four-element array (without ground plane). Hence if the number of antennas increased from four to

eight, the power could be doubled and better array performance could be achieved. Each array could be integrated into lower skins of the Meridian wing by two possible ways. It could be embedded into the lower wing skin (i.e. load bearing antenna), or it could be integrated onto the lower skin by modifying the wing ribs, such that they hop over the antenna elements. The latter approach would change the load path for the lower wing skin, however these details (and corresponding structural analysis) of array integration are left for future study.

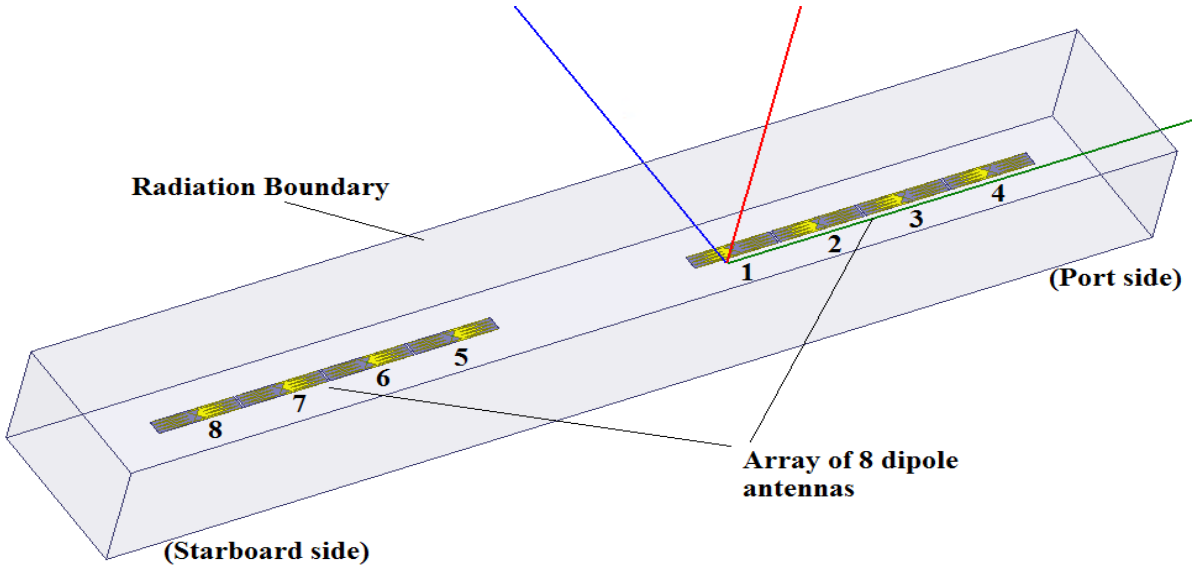


**Figure 43: 3-D View of an eight-element array from HFSS design**

**Table 8: Eight-element Dipole antenna array performance**

| Antenna Type | Resonant Frequency, MHz | Bandwidth, MHz | Frequency Range, MHz | Peak Realized Gain at 205 MHz, dB |
|---|---|---|---|---|
| Dipole antenna array without GP | 200-210 | 87 | 167-254 | 9.5 |

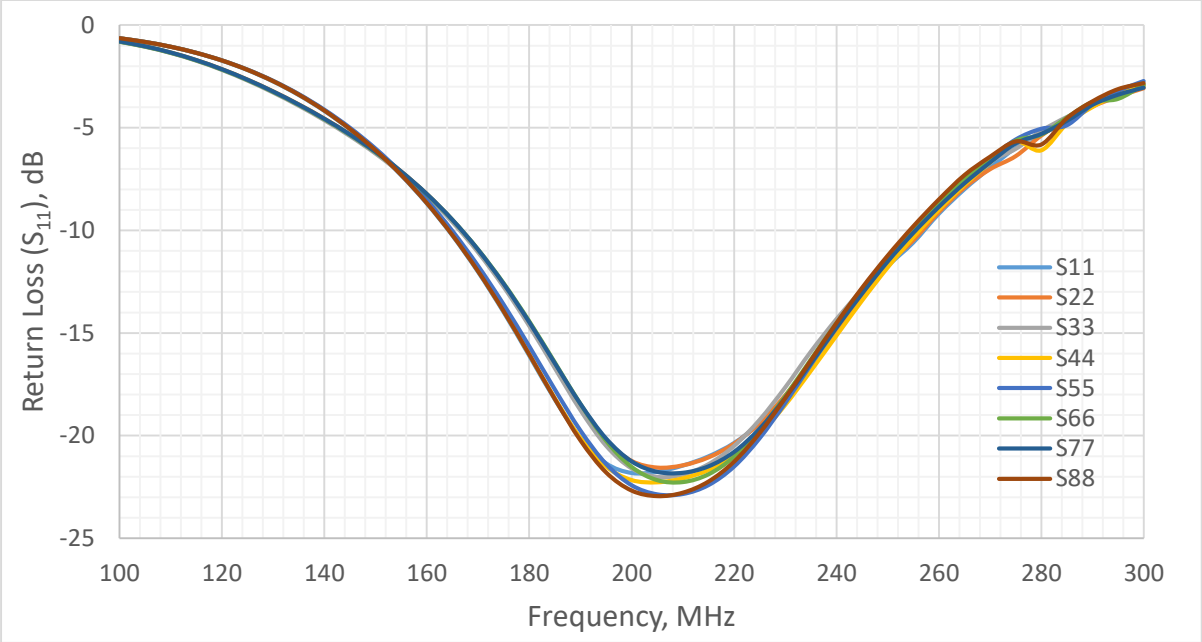


**Figure 44: Return loss of each dipole antenna versus frequency**

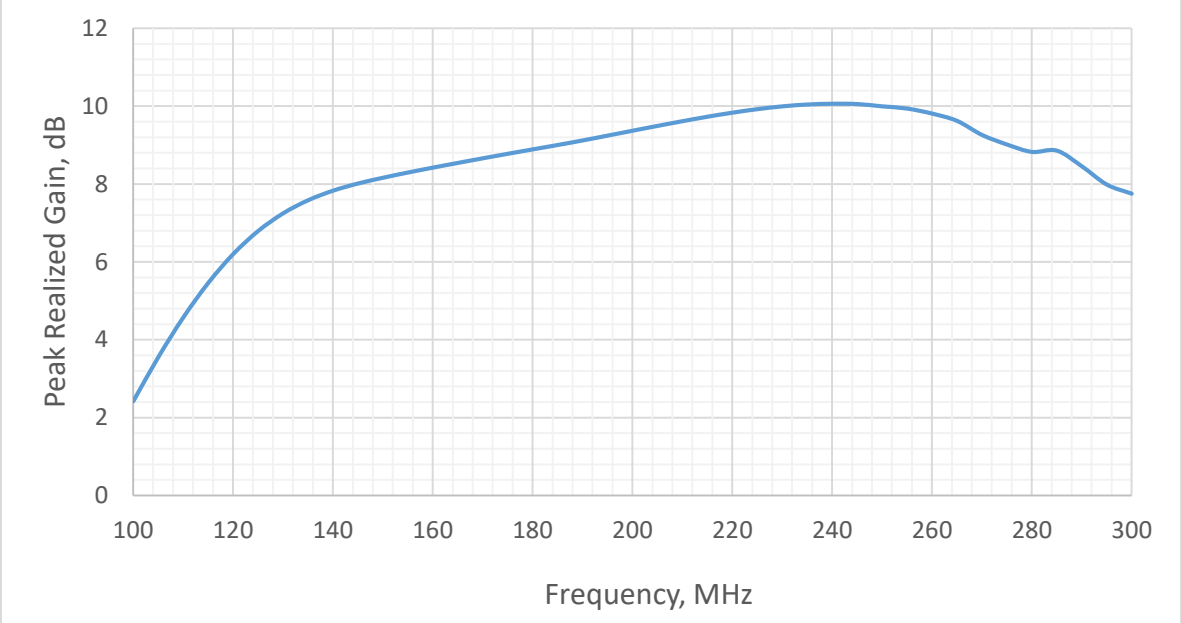


**Figure 45: Gain of an eight-element dipole antenna array**

The radiation pattern for this array is shown in Figure 46 at ϕ angle of 0º and 90º. The 3-dB cross-track beam width is about 10° for this eight-element dipole array design, as can be seen in Figure 46 (left). This array has a sidelobe level of about ~7 dB and has no significant grating lobes. This antenna array directs half of its energy into the zenith direction and the other half into the nadir direction. This array has negligible beam rotation in either direction, as can be seen in Figure 46 (right). With this array design, all antenna elements could be used to transmit and receive the radio signals to collect more data.

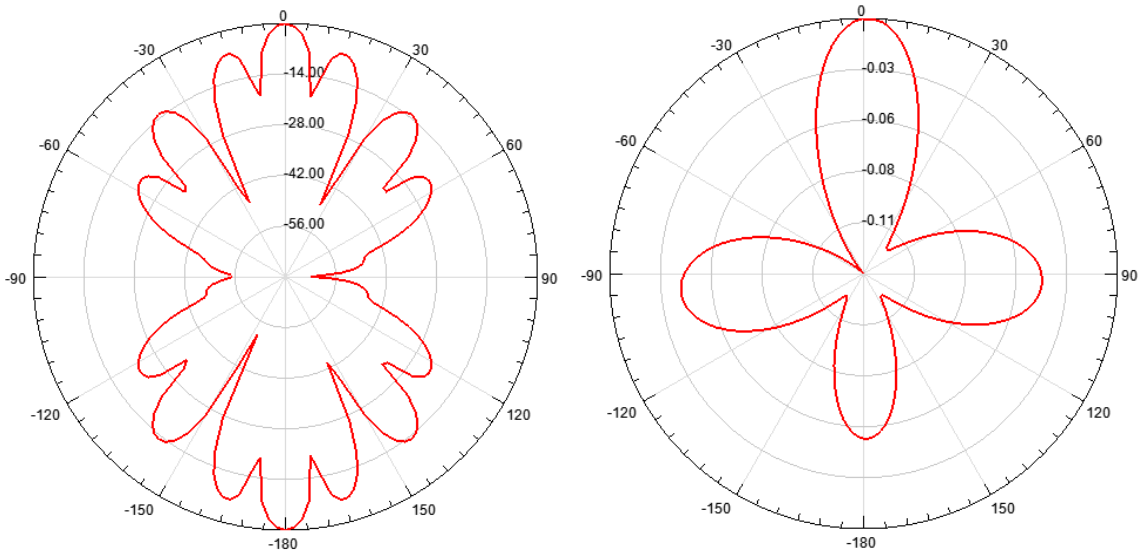


**Figure 46: Radiation Pattern of an eight-element dipole antenna array at ϕ = 0º (left) and 90º (right).**

#### 4.2.2.2. Dipole Antenna Array with Ground Plane

Similar to the previous section, an eight-element dipole array spanning both the starboard and port wings was simulated along with a ground plane (lower wing skin) located at quarter wavelength offset, as shown in Figure 47. Table 9 summarizes the array performance results with an array offset of a quarter wavelength from the lower wing skin. In Figure 48 and Figure 49, the return loss plot of each antenna element and array gain are shown for an eight-element array with ground plane. The array elements resonate between 175–180 MHz, and the array provides a bandwidth of 87 MHz. The average peak gain is about 13.5 dB over this bandwidth. This array shows that all eight antenna elements could be used as transmitter and receiver, while also increasing the gain by 3 dB over the four element dipole array. This array also delivers almost 4 dB higher gain than the eight-element dipole array without ground plane. Hence this array design radiates twice the power than that of the four-element dipole array with ground plane and the eight-element dipole array without ground plane. It can also be noticed that the array bandwidth of the eight-element dipole array remains constant with or without ground plane, but the frequency range of the array with ground plane is lowered by 12 MHz versus the array without ground plane. Also the resonant frequency of this array is reduced by more than 20 MHz as compared to the eight-element dipole array without ground plane.

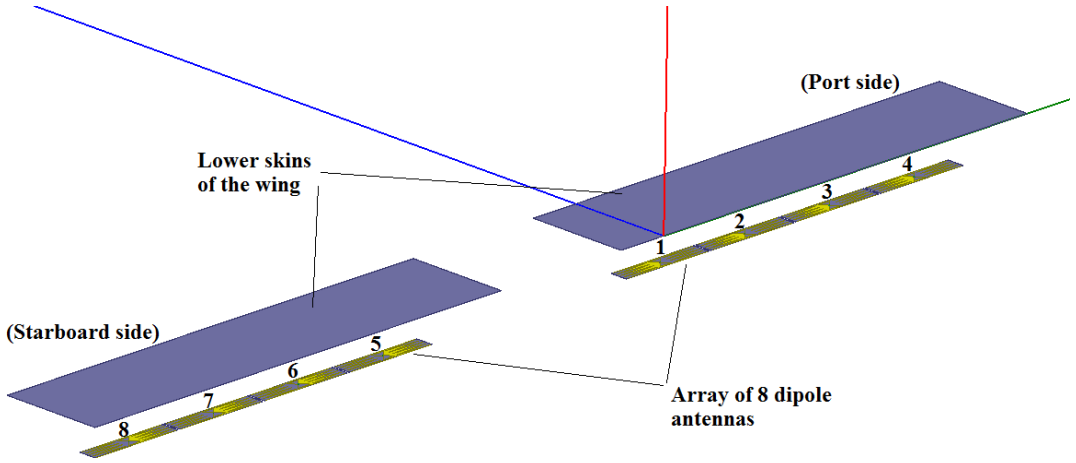


**Figure 47: 3-D View of an eight-element array with lower wing skins from HFSS design**

**Table 9: Eight-element antenna array performance at quarter wavelength offset**

| Antenna Type | Resonant Frequency, MHz | Bandwidth, MHz | Frequency Range, MHz | Nadir Realized Gain at 180 MHz, dB |
|---|---|---|---|---|
| Dipole antenna array with lower skin as GP | 175-180 | 87 | 155-242 | 13.3 |

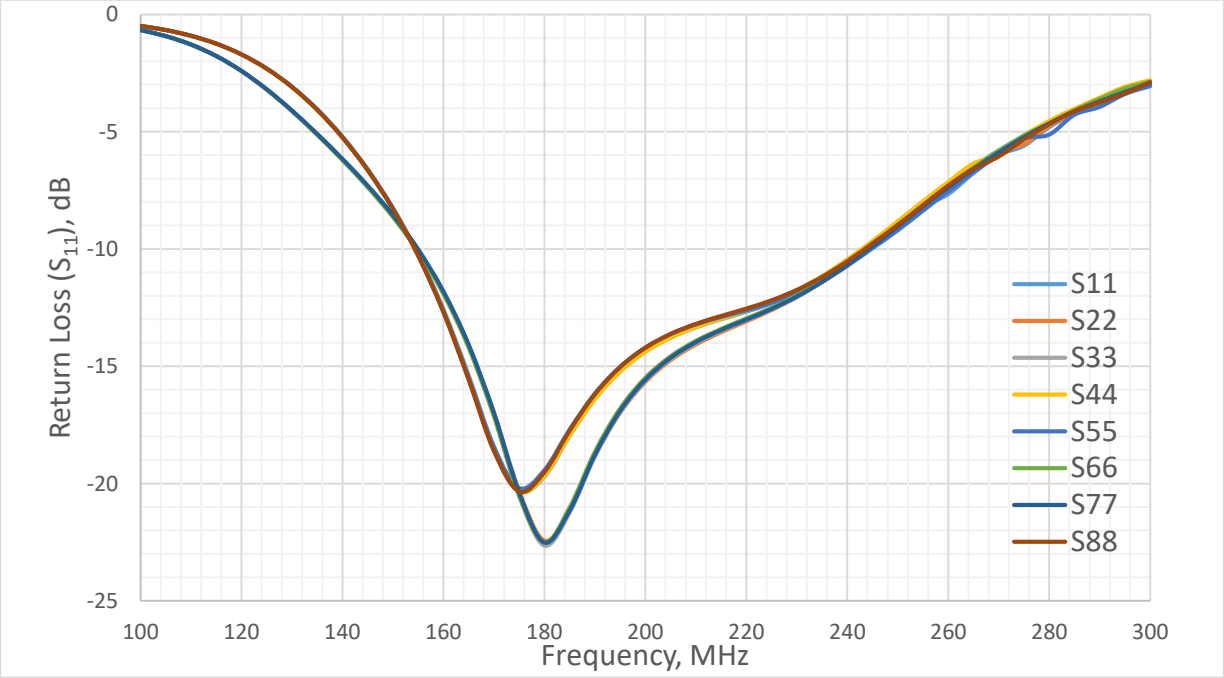


**Figure 48: Return loss of each dipole antenna versus frequency with lower skin as a ground plane at quarter wavelength offset**

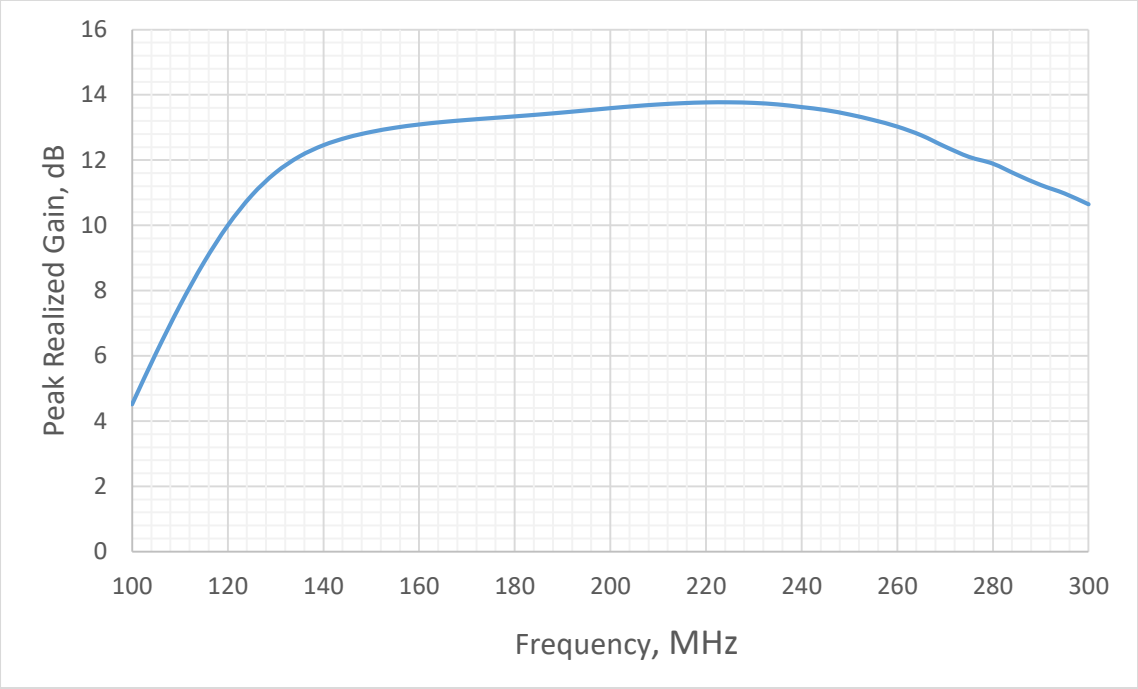


**Figure 49: Gain of an eight-element dipole antenna array with lower skin as a ground plane at quarter wavelength offset**

The radiation pattern for this array is shown in Figure 50 at $\phi$=0º and 90º. The 3-dB beam width is narrower than the single dipole and four element dipole designs, and it is about 10° for this eight-element dipole array design, as can be seen in Figure 50 (left). This antenna array directs most of its energy into a narrow beam (at $\phi$ = 0º plane) in nadir direction with higher gain, and it also radiates a small amount of power (-16.2 dB) in the zenith direction (i.e. smaller back lobe and side lobes in zenith direction as compared to the eight-element dipole array without ground plane). This array has a sidelobe level of about ~7 dB, while this sidelobe level is not ideal for polar remote sensing, it can be managed by advanced beamforming techniques. This array has negligible beam rotation, as can be seen in Figure 50 (right). This array design could be used when all antenna elements need to transmit and/or receive the radio signals. This array delivers better electrical performance, such as resonant frequency, bandwidth, radiation pattern and gain, than all the arrays that have been discussed so far. This array could be installed below the wing with the help of a custom fairing and pylon structure, however this will have major weight and drag implications which will be discussed in detail in Section 4.3.

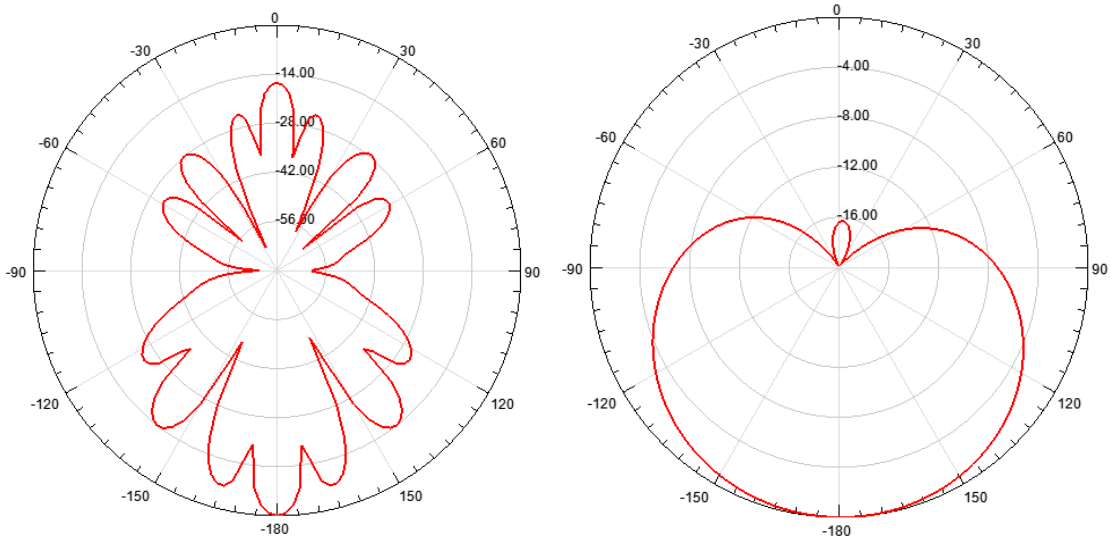


**Figure 50: Radiation Pattern of an eight-element dipole antenna array with lower skin as a ground plane at ϕ = 0º (left) and 90º (right).**

### 4.2.3. Quarter-wave Patch Antenna Array of Seven Antennas

In this section, the array performance of a linear seven-element array of quarter-wave patch antenna was studied. The array is shown in Figure 51, the element spacing of ~21 in was maintained, the ground plane (green) of 146 in long and 32 in was modeled, and similar (as single quarter-wave patch antenna) simulation set-up was created. Table 10 shows the electrical performance of the quarter-wave patch antenna array. In Figure 52 and Figure 53, the return loss of each quarter-wave patch antenna and the array gain are shown, respectively. All seven elements resonate at a frequency of 190 MHz. It can be noticed that return loss properties of the Elements 3, 4 and 5 are deteriorated due to cross-coupling between adjacent antennas, the bandwidth of the array was reduced to 6 MHz as compared to the 9 MHz bandwidth of single quarter-wave patch antenna. The peak realized gain of 11.5 dB was achieved at resonant frequency of 190 MHz.

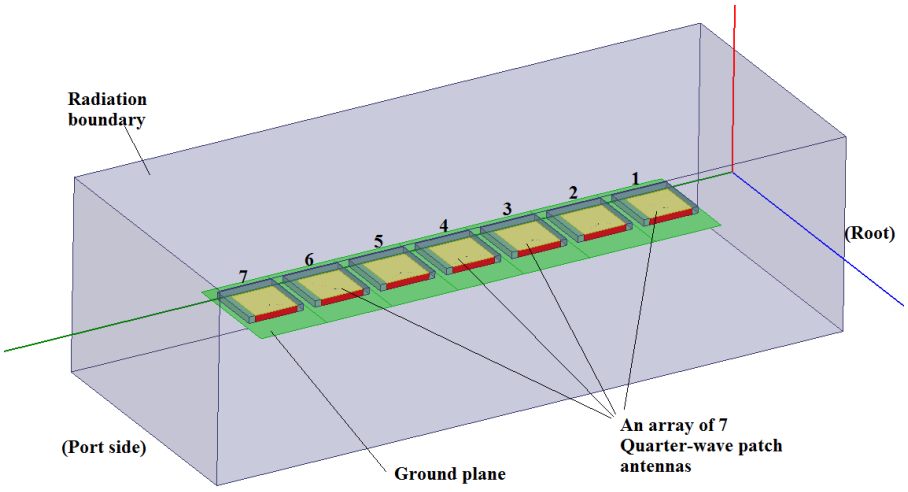


**Figure 51: 3-D Array View of seven quarter-wave antenna array from HFSS design**

**Table 10: Quarter-wave patch antenna array (seven) performance**

| Antenna Type | Resonant Frequency, MHz | Bandwidth, MHz | Frequency Range, MHz | Peak Realized Gain at 190 MHz, dB |
|---|---|---|---|---|
| QW antenna array of seven antennas | 190 | 6 | 187-193 | 11.5 |

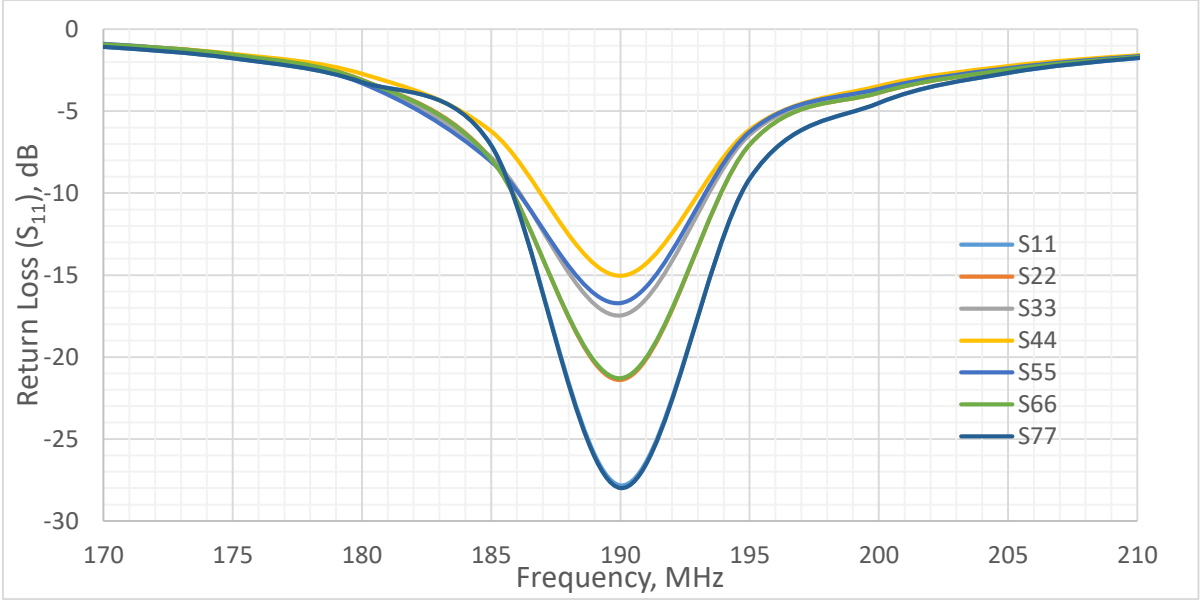


**Figure 52: Return loss of each Quarter-wave antenna versus frequency**

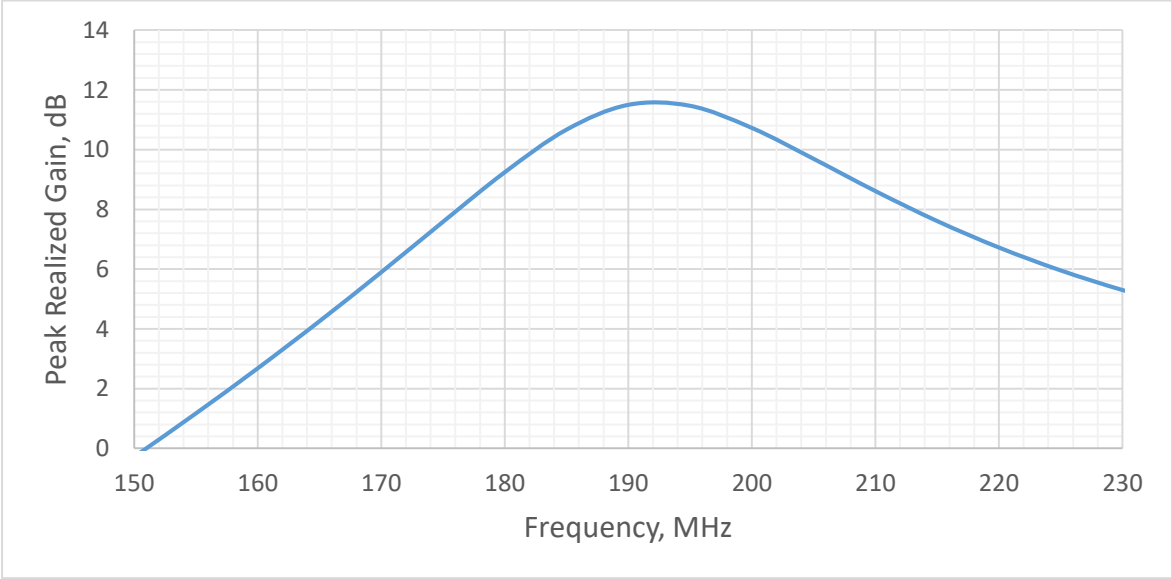


**Figure 53: Gain plot of a seven quarter-wave patch antenna array**

The seven-element array has about 1 dB higher gain compared to the four-element dipole array (with GP), however it has small bandwidth of 6 MHz as compared to 83 MHz bandwidth of four-element dipole array (with GP). The radiation pattern for this configuration is shown in Figure 54 at $\phi = 0^{o}$ and $90^{o}$. The 3-dB beamwidth ($\phi = 0^{o}$ plane) of this array is about 20°, and the array has directed most of its energy in the z-direction, as shown in Figure 54 (left). This array has a sidelobe level of ~14dB, and it has back lobe level of ~12 dB . This array has beam rotation of about 15° ($\phi = 90^{o}$ plane), as can be seen in Figure 54 (right), which is likely shorting wall effect.

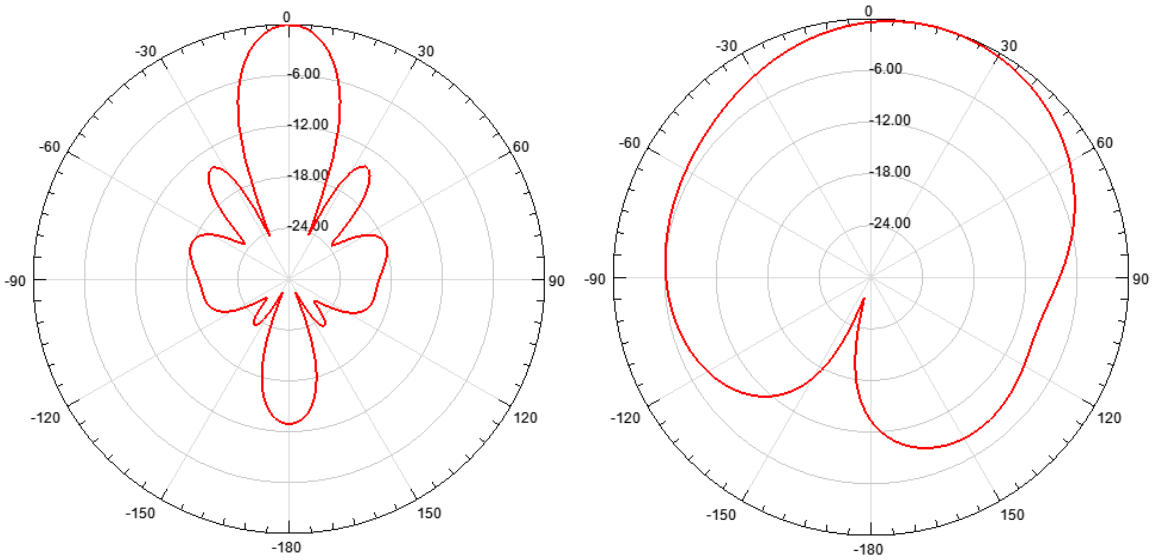


**Figure 54: Radiation Pattern of a seven quarter-wave patch antenna array at $\phi = 0^{o}$ (left) and $90^{o}$ (right).**

### 4.2.4. Quarter-wave Patch Antenna Array of 14 Antennas

In this section, the array performance of 14 quarter-wave patch antennas is studied, which were placed in uniform linear array spanning both wings as shown in Figure 55, similar to seven element QW array a simulation set-up was created. The gap of about 80" is maintained between two wing arrays (i.e. starboard side and port side) due to fuselage structure, landing gear and skis. The simulation set-up does not include cables or any conductive aircraft components. Table 11 summarizes the quarter-wave patch antenna array performance. Figure 56 and Figure 57 show the simulated return loss for each antenna element) and peak realized gain of an array, respectively.

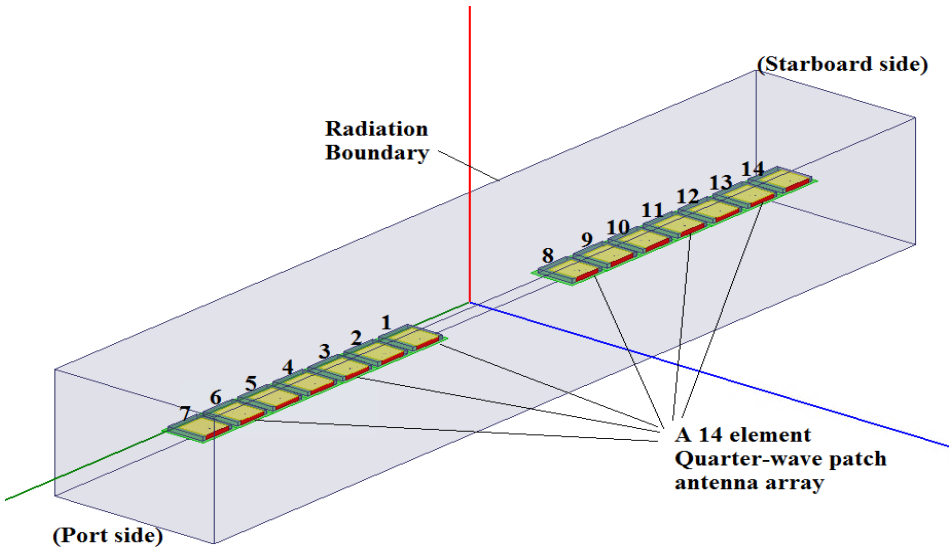


**Figure 55: 3-D Array View of 14 quarter-wave antenna array from HFSS design**

**Table 11: Quarter-wave patch antenna array (14) performance**

| Antenna Type | Resonant Frequency, MHz | Bandwidth, MHz | Frequency Range, MHz | Peak Realized Gain at 190 MHz, dB |
|---|---|---|---|---|
| QW antenna array of 14 antennas | 190 | 6 | 186.5-192.5 | 13.4 |

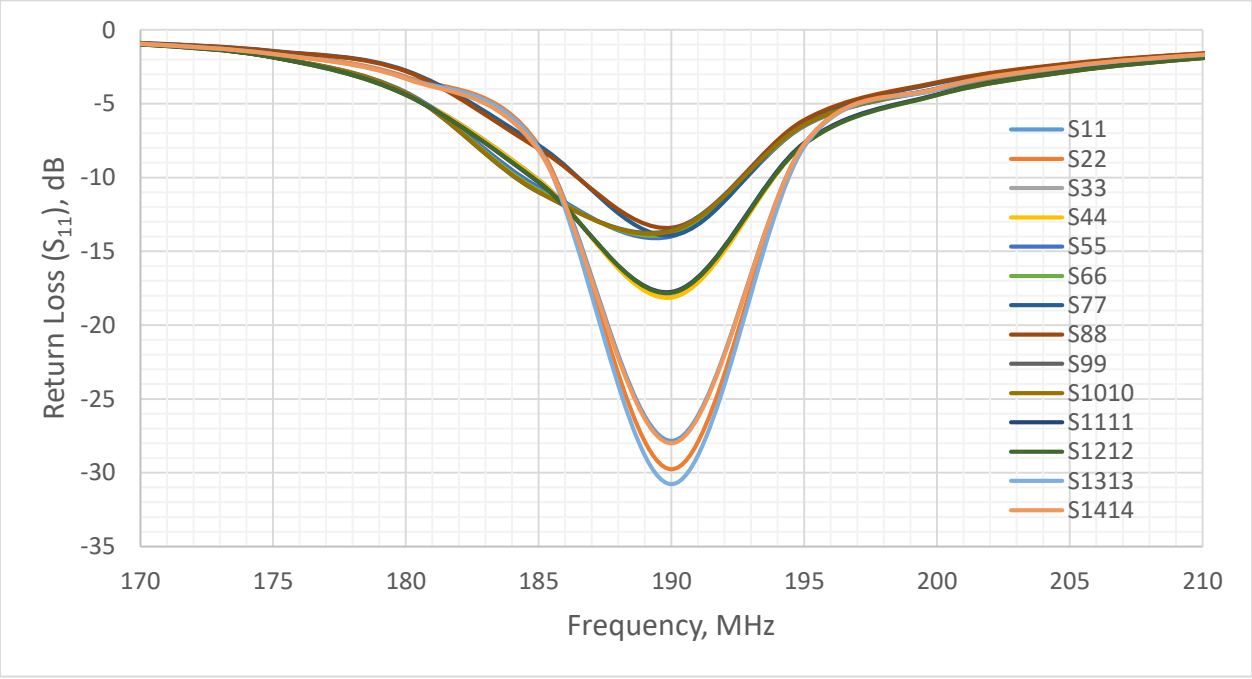


**Figure 56: Return loss plot for the quarter-wave patch 14-element array**

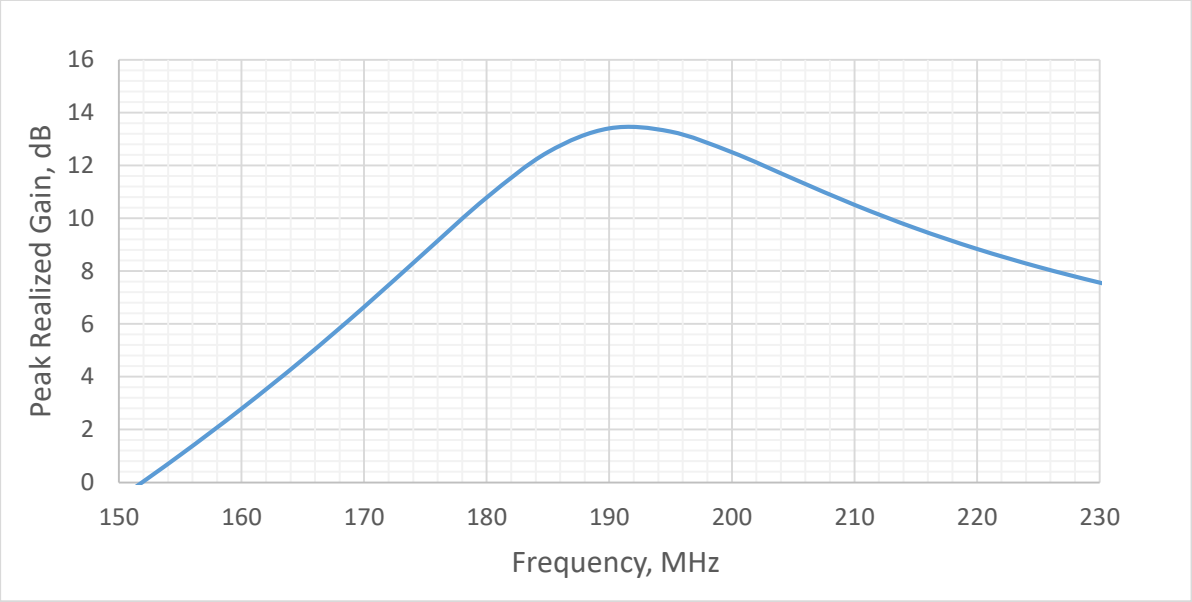


**Figure 57: Gain plot for a 14 quarter-wave patch antenna array**

All 14 elements resonate at a frequency of 190 MHz with narrower bandwidth of 6 MHz. The array delivers a peak gain of 13.4 dB at 190 MHz. This array delivers almost equal gain that could be achieved by an eight-element dipole array with ground plane, but the bandwidth of this array is small as compared to the 87 MHz bandwidth of the eight-element dipole array. The radiation pattern for this configuration is shown in Figure 58 for $\phi$=0º and 90º. The array beam has rotated about 5° (Figure 58, right). Also large back lobe level and sidelobe of ~6dB can be seen in Figure 58 (left). This array has 3-dB beamwidth of about ~6° (narrowest) and could be used as a single continuous array for both transmit and receive.

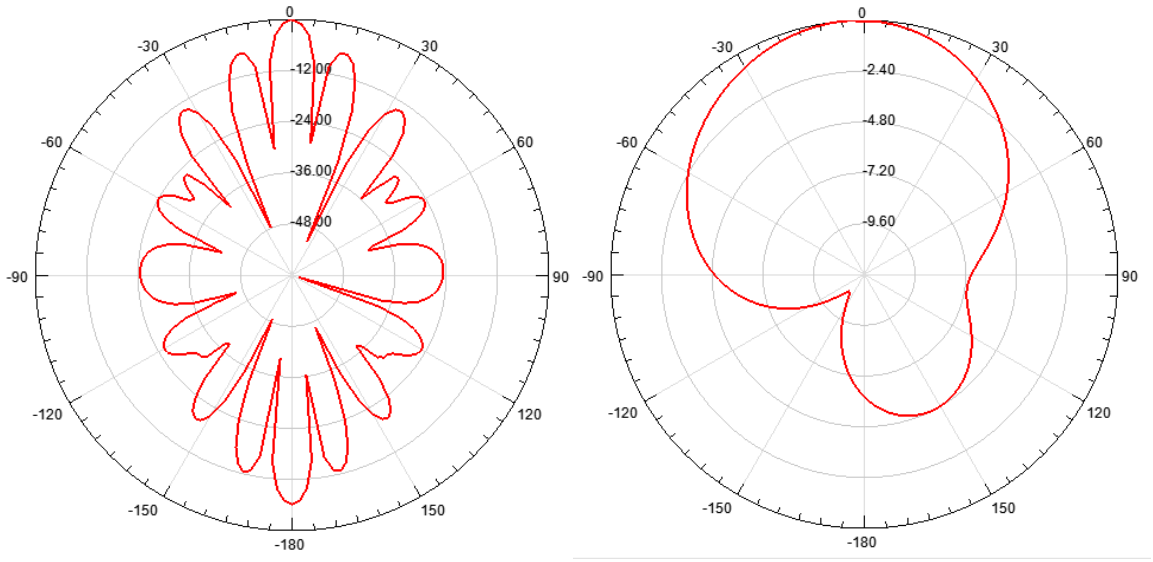


**Figure 58: Radiation Pattern of a 14 quarter-wave patch antenna array (14) at $\phi$ = 0º (left) and 90º (right).**

### 4.2.5. Summary of Antenna Detailed Design and Array Results

Table 12 summarizes the array performance of the dipole and quarter-wave patch antenna.

**Table 12: Array performance comparison**

| Antenna Type | Resonant Frequency, MHz | Bandwidth, MHz | Frequency Range, MHz | Peak Realized Gain at 190 MHz, dB | 3-dB beamwidth |
|---|---|---|---|---|---|
| Four-element Dipole array | 205 | 88 | 166-254 | 6.5 | 25° |
| Four-element Dipole array with GP | 200-210 | 87 | 167-254 | 9.5 | 22° |
| Eight-element Dipole array | 180 | 83 | 155-238 | 10.34 | 10° |
| Eight-element Dipole array with GP | 175-180 | 87 | 155-242 | 13.3 | 10° |
| Seven-element QW antenna array | 190 | 6 | 187-193 | 11.5 | 20° |
| Fourteen-element QW antenna array | 190 | 6 | 186.5-192.5 | 13.4 | 6° |

The dipole antenna array with ground plane has the best electrical performance to include a wide bandwidth, better radiation pattern, and higher gain for fewer number of antenna elements. However, it needs a custom external structure to house the arrays. Obviously the addition of an external structure increases the weight and aerodynamic drag thus reducing the range of the Meridian. It is noted that the quarter-wave patch array had equal gain as the dipole antenna array, but it requires almost twice the number of antenna elements. Also this array has significantly narrower bandwidth, tilted radiation pattern, and large back and side lobes. An advantage of the quarter-wave patch antenna array is that it could be installed into the wing bay, which eliminates the significant drag penalty; however, it was found that the quarter-wave patch antenna is incredibly sensitive to feed height (i.e. shorting wall height). A change of 0.1 inch (3 mm) in feed height could shift the resonant frequency by 5 MHz. When considering the effects of vibrations caused by airplane maneuvers and air turbulence, this antenna requires a more robust design. Also the quarter-wave patch antenna design is more complex and would be more complex to integrate and maintain inside the wing bay as compared to the dipole antenna array with ground plane. Therefore, the current QW patch antenna is not recommended.

From the detailed trade study of antenna performance, one of the dipole design could be chosen depending on the antenna and aircraft performance requirements of a mission. Of course, the dipole with ground plane has the obvious negative impacts on the vehicle performance, but the design represents the optimal antenna gain and it is recommended in exceptional cases where higher gain and deeper ice penetration (~5 km) is the paramount goal. On the other hand, the dipole without ground plane design offers both vehicle and sensor advantages compared to existing performance. Because of the advantages of both designs, in the next section, two solutions for a modified wing

that could accommodate the arrays are presented along with their trade-off with aircraft performance (specifically range). While it is recognized that aircraft handling qualities, and take-off and landing distances will also be affected, examination of these effects will be left for future studies. The first design is a fiber glass version of the Meridian wing, and could house the dipole without ground plane (or even the quarter-wave patch) design. The second design includes an external custom fairing to house the antenna array as well as modifications to the original Meridian wing design.

## 4.3. Structural Design and Sizing

In this section, two wing designs that could be used to integrate the antenna arrays into the Meridian wing were structurally sized with the help of Finite Element Analysis (FEA) software, MSC PATRAN/NASTRAN (version 2013). This study was performed to estimate the added weight to aircraft. Figure 59 shows the major components of the existing Meridian wing, which include the upper and lower wing skins, front and rear spars, spar inserts, leading edge and leading edge inserts, wing ribs and wing root attachments. The spar inserts and wing root attachments were used to ease the stress concentration at the wing root. The two proposed wing designs include one for the dipole antenna array without ground plane that could be embedded into the lower wing skin and the other one for the dipole antenna array with ground plane which could be integrated below the Meridian wing at a quarter-wavelength offset. While the former wing design is considering the embedded dipole array, it could also accommodate a quarter wave patch array—assuming a more robust antenna design could be determined that can withstand the aircraft loads and vibrations. The latter wing design uses a custom fairing and pylon to offset the antenna array at quarter-wavelength away. For both structural analyses, the original (i.e. existing) FEA Meridian wing model was used. For the internal antenna wing design, the material of the existing FEA wing model (Carbon Fiber Reinforced Plastic (CFRP) composite) was modified to Glass Fiber-Reinforced Plastic (GFRP) composite material properties presented in Section 4.3.3, while the external antenna structure design maintains the original wing materials. These wing designs are discussed in detail in the sub-sections below.

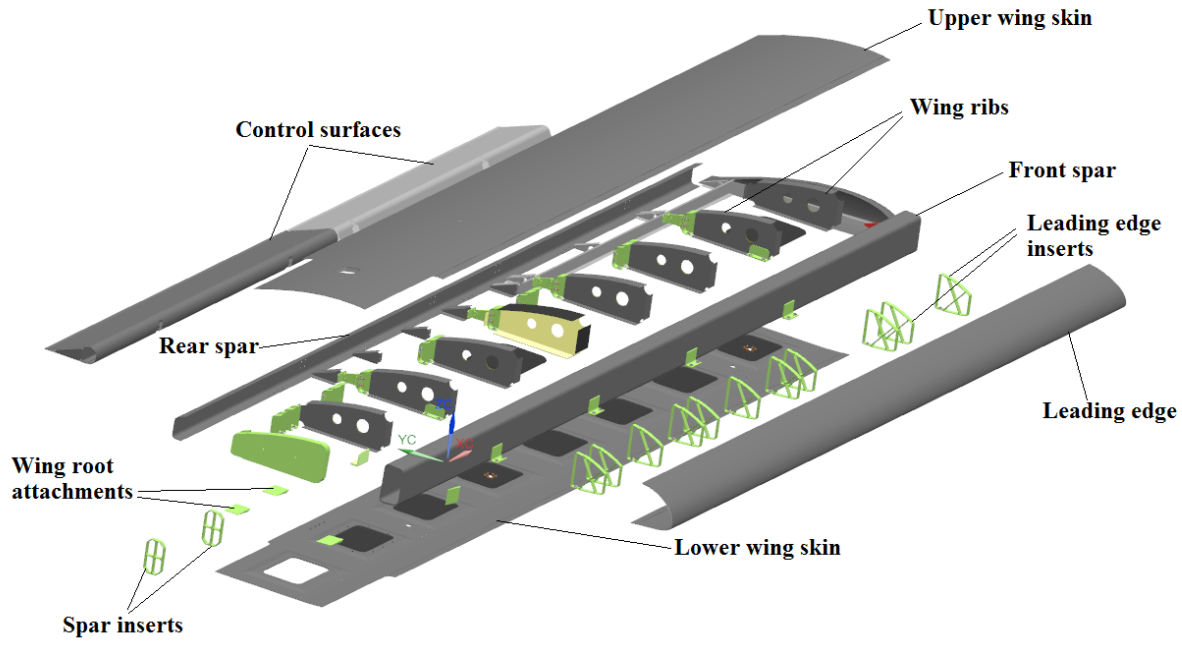


**Figure 59: Exploded view of the Meridian wing**

### 4.3.1. Geometry of Wing Designs and Fairing-Pylon Structure

This section includes the geometry and layups of the critical components of the wing designs and fairing-pylon structure. The geometry presented in this section is a result of sizing, which is covered in Section 4.3.7.

#### 4.3.1.1. Wing Design I

For Wing Design I, the antenna array is assumed to be integrated within the wing box (see Figure 12), as shown in Figure 60. It is noted that to integrate the dipole antenna array inside the wing, the wing ribs may need to be modified such that they hop over the dipole antenna due to longer length of dipole antenna (31.2”) than the wing rib spacing (20”), however these changes were not made in the FEM for this preliminary sizing analysis. This will change the load path and thus will add more weight. The major components of the Meridian wing are made up of Carbon Fiber Reinforced Plastic (CFRP) composite materials, which is semi-conductive and electrically-lossy. Therefore, for this design Glass Fiber-Reinforced Plastic (GFRP) composite is considered as the material for fabrication of the Meridian wing components due to its Radio Frequency (RF) transparency, relatively low dielectric constant, and aerospace grade structural properties. All the major components of the wing, such as the upper skin, lower skin, front spar, rear spar, wing ribs and leading edge, are considered to be fabricated using GFRP.

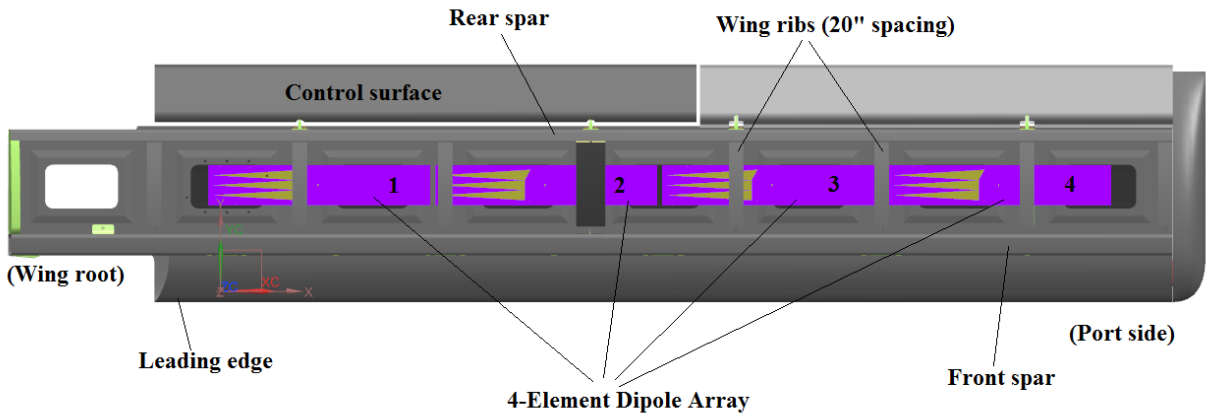


**Figure 60: Wing design I design overview**

During the analysis, it was found that the critical elements lie in the inboard most section of the front wing spar inside the fuselage. Since no antenna is present in that region, eight layers of carbon fiber cloth were added to the front spar cap section for the first 25” at the wing root to strengthen the critical area. After modifying the FEM’s material to Glass Fiber-Reinforced Plastic (GFRP), to alleviate the stress concentration near the root three additional spar inserts at the wing root section were added, as shown in Figure 61. Also additional layers of fiberglass composite were also added to the spar cap and spar web section at the root. Although wing root attachments (added for bearing loads) are present on Meridian, they were missing in Meridian’s FEM, hence they were also added. These modifications to the original Meridian wing are summarized in Table 13.

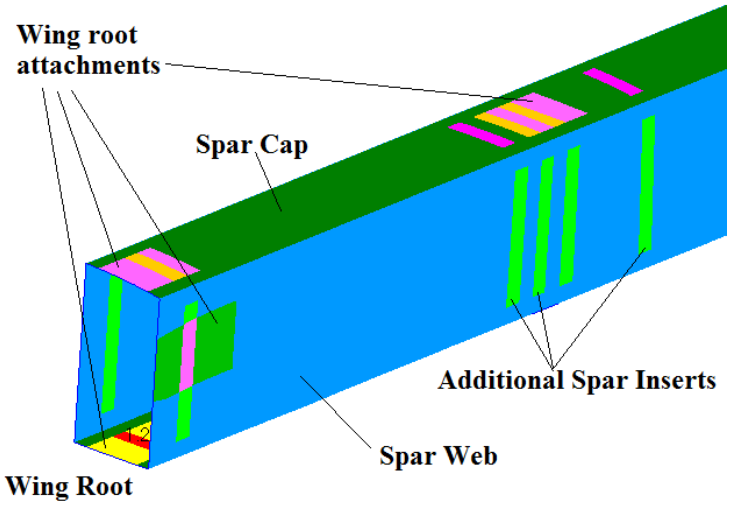


**Figure 61: Additional inserts added to inboard section of front spar of Meridian Wing**

**Table 13: Modifications made in Meridian FEM**

| Component | Color | Number of components added | Location |
|---|---|---|---|
| Spar inserts | Light Green | 3 | Front spar at wing root |
| Wing root attachments | Green, Yellow, Light Pink | 4 | Front spar and wing skin at wing root |

The front spar cap, as shown in Figure 62, has tapered laminate sections with the red color section being the thickest at the root (0.42 in) to the white color section being the thinnest at the tip of the wing (0.07 in). The empty cutouts have different laminate layups, as spar inserts and wing root attachments are made up of 7075-T651 aluminum alloy. The different colors in Figure 62, identify laminates with different layups and thickness which are summarized in Table 14. In the table, C and T represents fiberglass cloth and tape material respectively, $C_C$ represents the carbon fiber cloth material, and the subscript S indicates the laminate symmetry. It is noted that the laminate summarized in Table 14 is an extreme laminate as it contains no +/- 45 plies. Since the sizing performed is preliminary and is simply to serve as a feasibility study, it is recommended that the laminate be re-examined should this concept be pursued. In addition, the inboard laminates in Figure 62 are relatively thick, more significant inserts in either the laminate or structure should also be considered in a final design.

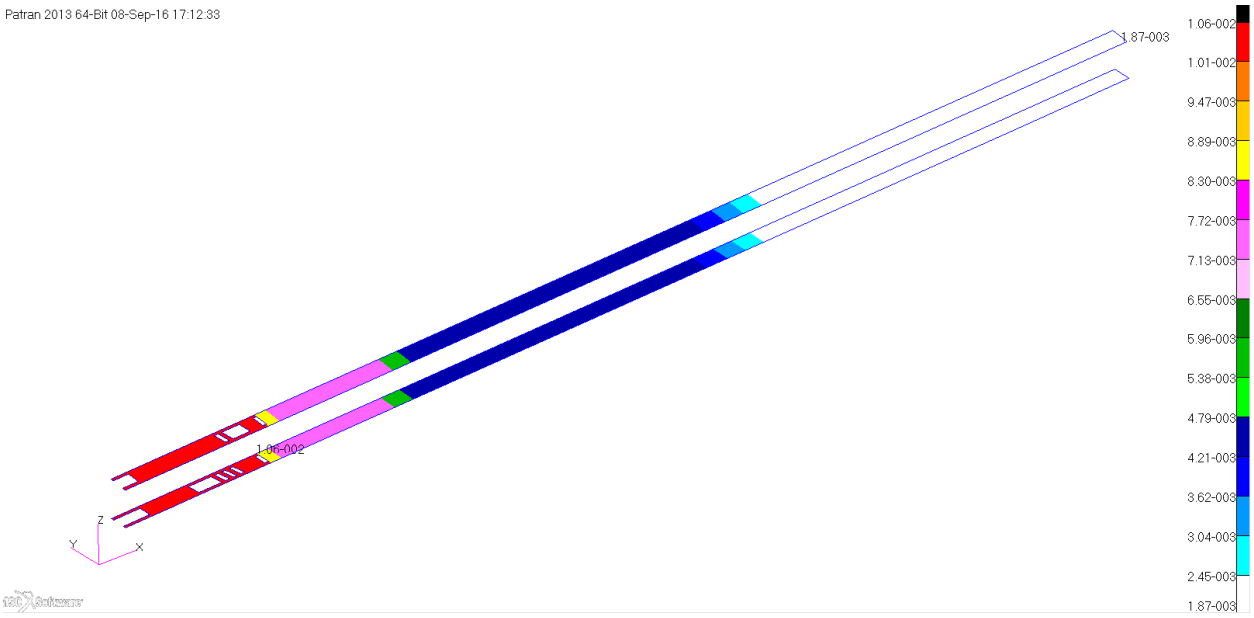


**Figure 62: Front spar cap laminates (Wing Design I) thickness plot**

**Table 14: Front Spar cap laminate layups and their thicknesses (Wing Design I)**

| Laminate Color | Laminate Layup | Laminate Thickness, (inch) |
|---|---|---|
| Red | $[C,C_C,C_C,T,T,T,T,T,C,T,T,T,T,C,\ C_C,C_C,T,T,C,T,T,T,T,C]_S$ | 0.42 |
| Yellow | $[C,\ C_C,C_C,T,T,T,T,C,T,T,T,T,C,T,T,C,T,T,T,T,C]_S$ | 0.35 |
| Pink | $[C,\ T,T,T,T,C,T,T,T,T,C,T,T,C,T,T,T,T,C]_S$ | 0.29 |
| Green | $[C,\ T,T,T,T,C,T,T,T,T,C,T,T,T,C]_S$ | 0.23 |
| Dark blue | $[C,\ T,T,T,T,C,T,T,T,T,C]_S$ | 0.17 |
| Blue | $[C,\ T,T,T,T,C,T,T,T,\ C]_S$ | 0.15 |
| Light blue | $[C,\ T,T,T,T,C,T,\ T,\ C]_S$ | 0.14 |
| Cyan | $[C,\ T,T,C,T,\ T,\ C]_S$ | 0.11 |
| White | $[C,\ T,T,\ T,\ C]_S$ | 0.07 |

The increase in weight due to modifications made in material, layups, and inserts was estimated, and compared to the existing FEM of Meridian wing. The increase in weight was found to be 4.7 lbs per wing, as shown in Table 15, and the justification for the added weight will be addressed in the analysis section, Section 4.3.7.

**Table 15: Estimation of the increase in weight per wing (Wing Design I)**

| No | Component | Original Weight (lbs) | Modified Weight (lbs) | Change in Weight (lbs) |
|---|---|---|---|---|
| 1 | Front Spar cap | 6.9 | 10.6 | +3.7 |
| 2 | Front Spar web | 6.4 | 8.3 | +1.9 |
| 3 | Lower Skin panel intersection | 0.2 | 0.4 | +0.2 |
| 4 | Front Spar inserts (3) | 0 | 0.3 | +0.3 |
| 5 | Upper skin | 9.4 | 8.4 | -1.2 |
| 6 | Lower skin | 6.1 | 5.2 | -0.9 |
| 7 | Rib | 1.0 | 1.5 | +0.5 |
| 8 | Leading edge | 4.1 | 4.0 | -0.1 |
| 9 | Rear spar | 3.7 | 4.0 | +0.3 |
| **Total Weight added per wing (lbs)** | | | | **+4.7** |

#### 4.3.1.2. Wing Design II

In this design, the dipole antennas are assumed to be integrated into a custom fairing structure, supported by custom pylons which would be fastened to the Meridian wing. Due to the addition of the antenna fairing, the original carbon fiber Meridian wing was analyzed and sized to reaction loads imposed by the fairing-pylon structure in addition to the dynamic pressure. These reaction loads will be discussed in detail in Section 4.3.2. To reduce the increased stress concentration at the root, three additional spar inserts at the wing root section were added same as previous design and additional layers of carbon fiber composite were also added to the spar cap and spar web section at the root.

The front spar web, as shown in Figure 63, has tapered laminate sections with the red color section being the thickest at the root (0.13 in or 3.2 mm) to the white color section being the thinnest at the tip of the wing (0.04 in or 1.1 mm). The empty cutouts have different laminate layups due to spar inserts and attachments (made of 7075-T651 aluminum alloy). The different colors in Figure 63 identify laminates with different layups and thickness, and Table 16 summarizes the laminate layups, where $C_C$ represents the carbon fiber cloth material. The laminate summarized in Table 16 contains +/- 45 plies.

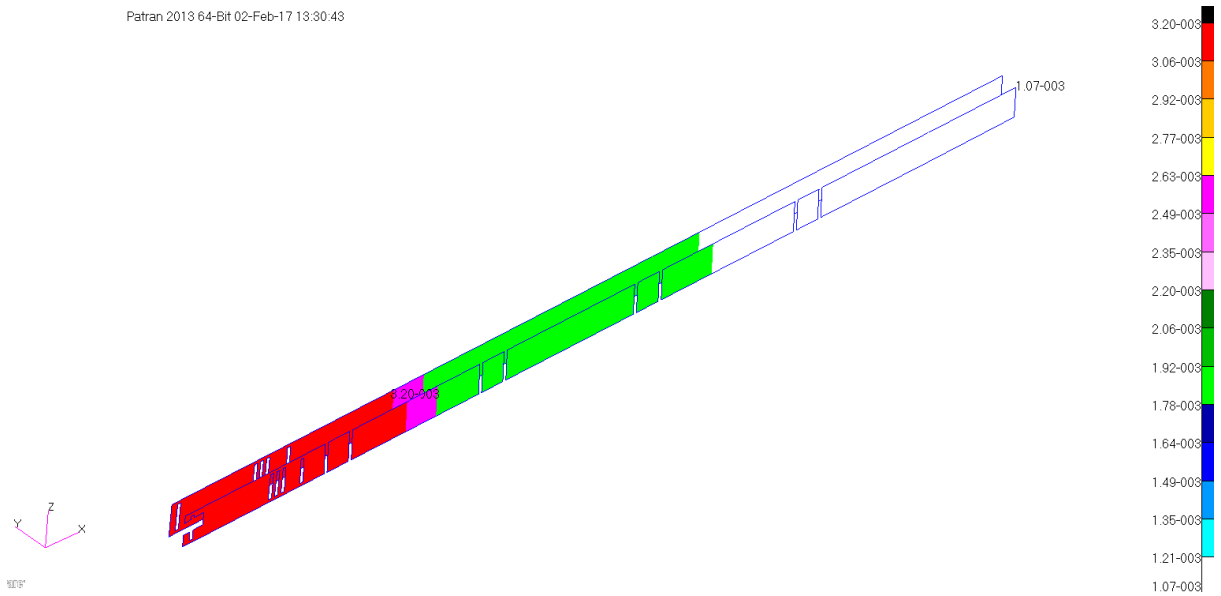


**Figure 63: Front spar web laminates (Wing Design II) thickness plot**

**Table 16: Front spar web laminate layups and their thicknesses (Wing Design II)**

| Laminate Color | Laminate Layup | Orientation | Laminate Thickness, (inch) |
|---|---|---|---|
| Red | [$C_C$,$C_C$,$C_C$,$C_C$,$C_C$,$C_C$,$C_C$,$C_C$,$C_C$] | [45,45,0,0,0,0,0,45,45] | 0.13 |
| Pink | [$C_C$,$C_C$,$C_C$,$C_C$,$C_C$,$C_C$,$C_C$] | [45,45,0,0,0,45,45] | 0.10 |
| Green | [$C_C$,$C_C$,$C_C$,$C_C$,$C_C$] | [45,45,0, 45,45] | 0.07 |
| White | [$C_C$,$C_C$,$C_C$] | [45,0, 45] | 0.04 |

The front spar cap, as shown in Figure 64, also has tapered laminate sections with the red color section being the thickest at the root (0.29 in or 7.3 mm) to the white color section being the thinnest at the tip of the wing (0.07 in or 1.83 mm). Table 17 shows the laminate layups according to color assigned to the laminates and their thicknesses, where $C_C$ represents the carbon fiber cloth material and $C_T$ represents the carbon fiber unidirectional tape material.

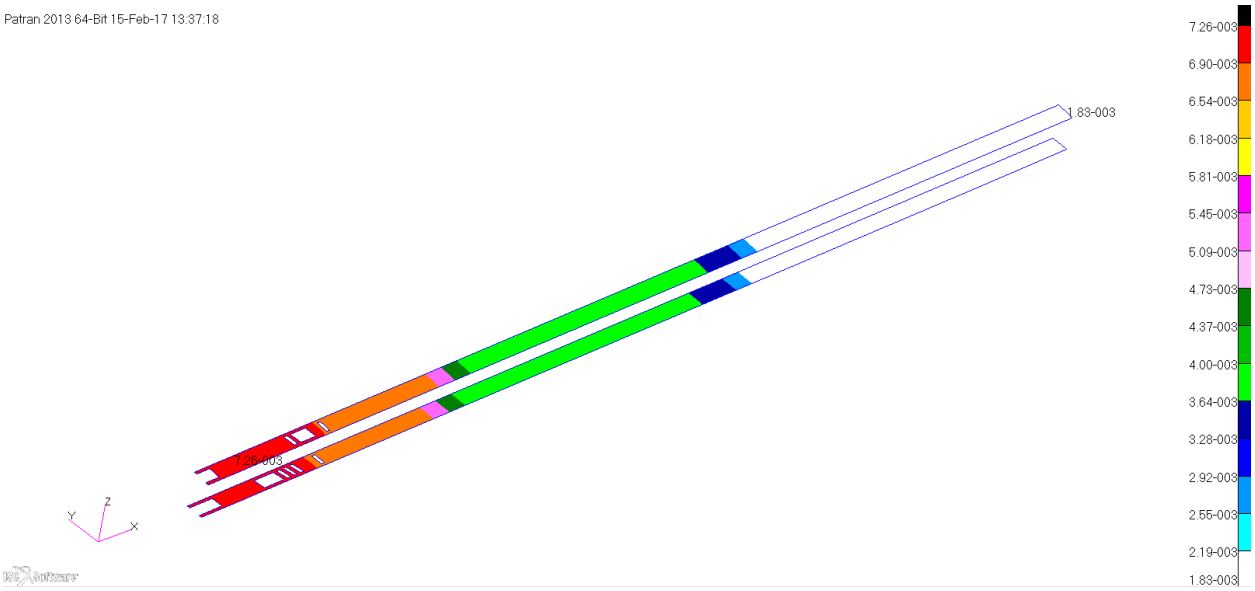


**Figure 64: Front spar cap laminates (Wing Design II) thickness plot**

**Table 17: Front spar cap laminate layups and their thicknesses (Wing Design II)**

| Laminate Color | Laminate Layup | Laminate Thicknes, (inch) |
|---|---|---|
| Red | $[C_C,C_T,C_T,C_T,C_T,C_C,C_T,C_T,C_T,C_T,C_C,C_T,C_T,C_T,C_T,C_C,C_T,C_T,C_T,C_T,\overline{C_C}]_S$ | 0.29 |
| Orange | $[C_C,C_T,C_T,C_T,C_T,C_C,C_T,C_T,C_T,C_T,C_C,C_T,C_T,C_C,C_T,C_T,C_T,C_T,\overline{C_C}]_S$ | 0.27 |
| Pink | $[C_C,C_T,C_T,C_T,C_T,C_C,C_T,C_T,C_T,C_T,C_C,C_T,C_T,C_T,\overline{C_C}]_S$ | 0.21 |
| Dark green | $[C_C,C_T,C_T,C_T,C_T,C_C,C_T,C_T,C_C,C_T,C_T,\overline{C_C}]_S$ | 0.18 |
| Light green | $[C_C,C_T,C_T,C_T,C_T,C_C,C_T,C_T,C_T,C_T,\overline{C_C}]_S$ | 0.15 |
| Dark blue | $[C_C,C_T,C_T,C_T,C_T,C_C,C_T,C_T,C_T,\overline{C_C}]_S$ | 0.14 |
| Dark blue | $[C_C,C_T,C_T,C_T,C_T,C_C,C_T,C_T,\overline{C_C}]_S$ | 0.13 |
| Light blue | $[C_C,C_T,C_T,C_C,C_T,C_T,\overline{C_C}]_S$ | 0.11 |
| White | $[C_C,C_T,C_T,C_T,\overline{C_C}]_S$ | 0.07 |

Table 18 estimates the increased weight of the wing to be 3.7 lbs per wing, due to added composite layers and spar inserts to the wing.

**Table 18: Estimation of the increase in weight per wing (Wing Design II)**

| No | Component | Original Weight (lbs) | Modified Weight (lbs) | Increase in Weight (lbs) |
|---|---|---|---|---|
| 1 | Front Spar cap | 6.9 | 8.6 | 1.7 |
| 2 | Front Spar web | 6.4 | 7.9 | 1.5 |
| 3 | Lower Skin panel intersection | 0.2 | 0.4 | 0.2 |
| 4 | Front Spar inserts (3) | 0.0 | 0.3 | 0.3 |
| **Total Weight added per wing (lbs)** | | | | **3.7** |

#### 4.3.1.3. Fairing-Pylon Structure

The preliminary concept for the custom support structure is shown in Figure 65. The fairing and pylons were designed with Siemens NX Unigraphics 8.5 [26]. The offset geometry of this support structure with lower wing skin was examined to make sure that there is no flow separation over the wing control surfaces.

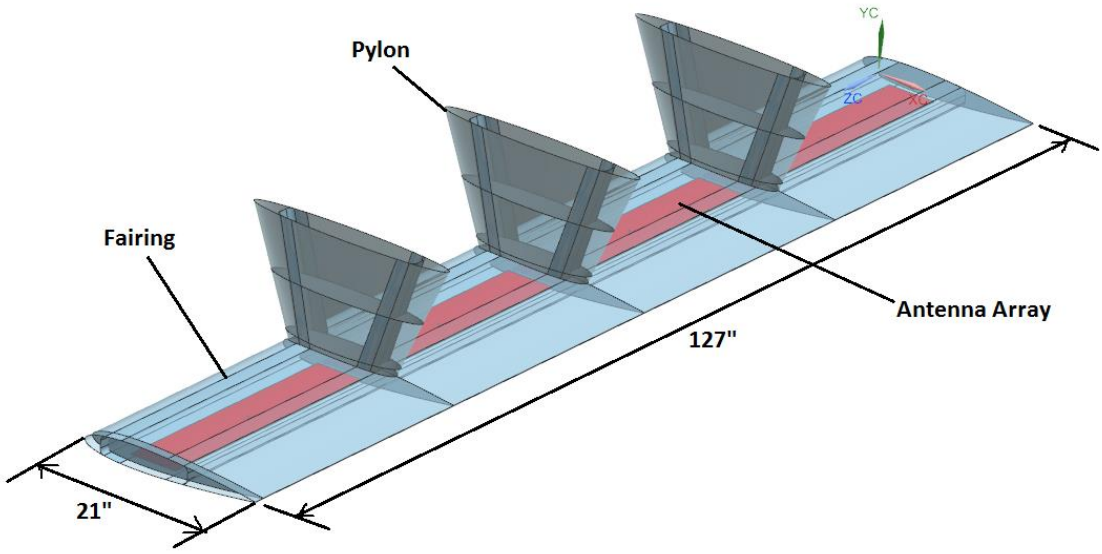


**Figure 65: Fairing and Pylon support assembly with four-element dipole array**

The pylon and fairing structure assemblies each have the following major components: skin, spars, and ribs. The fairing structure has a planform of 127 in X 21 in with a maximum thickness of 2.5 in. The NACA 0012 airfoil (Figure 65) was chosen for the fairing cross-section due to its low drag coefficient ($c_d$= 0.04) and zero lift at zero angle of attack. An added advantage is the availability of the airfoil's historical data. The NACA 0012 airfoil has a maximum thickness of 12% at 30% of chord and no camber, it also provides sufficient thickness of 2.5 in to accommodate the antenna connector and cable assembly in this design. Figure 66 shows the fairing spars and their cross section. The spar cross-section (C-channel) was modified such that it could be bonded to the fairing skin. Note that due to the airfoil section of the fairing skin, the cross-sections of the forward spar and aft spar are slightly different. A total of five fairing ribs supporting the fairing skin are spaced 31.2 in apart from each other, and four dipole antennas are integrated between the fairing ribs.

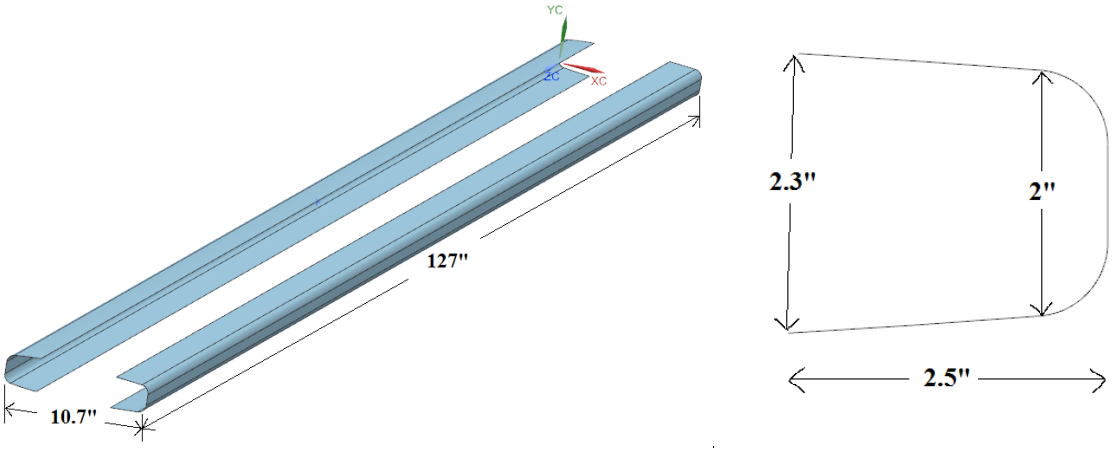


**Figure 66: Fairing forward and aft spar (left) with cross-section of forward spar (right)**

The fairing structure is attached to the lower wing skin via three pylons. The pylon height is chosen such that it creates the quarter-wavelength offset between the antenna array and the wing bottom skin which serves as ground plane. An elliptical cross section is chosen for the pylon for ease of manufacturing.

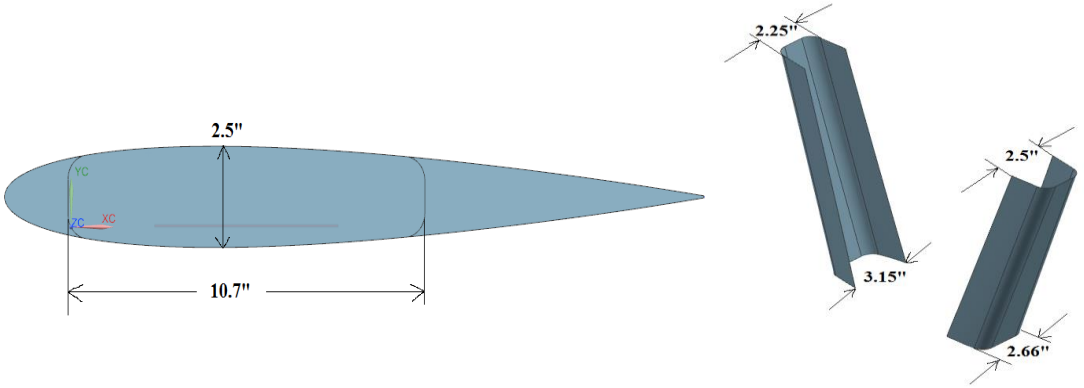


**Figure 67: Fairing cross-section (left) and tapered pylon spar (right)**

To determine the height of fairing spars in a preliminary sizing exercise, the Meridian wing maximum pressure distribution was used from which average pressure was calculated and converted into a uniformly distributed load. This load was then applied to a rectangular beam representing the fairing. This beam was modeled such that its length is identical to the fairing span (140") and simply supported at three hardpoints (where the three pylons would be attached). The maximum moment (~56,000 in-lbs) was found for this model. Using the calculated moment and assuming the fiberglass stress allowable (presented in Section 4.3.3), the minimum height of the fairing spar web was determined to be 1.44", using the following stress relation:

$$\sigma_{min} = \frac{M_{max} * y}{I}$$

Where, $\sigma_{min}$ is the fiberglass stress allowable, $M_{max}$ is the maximum moment acting on the fairing beam, y is the fairing spar height, I is the moment of inertia (rectangular approximation I = $b*y^3/12 = 2.6\ in^4$), and b is the distance between front and rear fairing spar (10.5”). From the value obtained for minimum height of the spar web, initial spar web height was chosen to be 2”.

During the linear static analysis of fairing and pylon structure, spar inserts were added to alleviate the stress concentration at the spar intersections, as shown in Figure 68. These spar inserts are made of 7075-T651 Aluminum Alloy. Also, four glass cloth plies were added in the red section of the fairing spar to minimize the critical stress in the fairing spar. The thicknesses of the fairing and pylon spars are summarized in Table 19. The ‘C’ represents the fiberglass cloth and ‘A’ represents the 7075-T651 aluminum alloy plate. Again, it is noted that the laminate summarized in Table 19 is an extreme laminate, as no +/- 45 plies were included in this preliminary sizing.

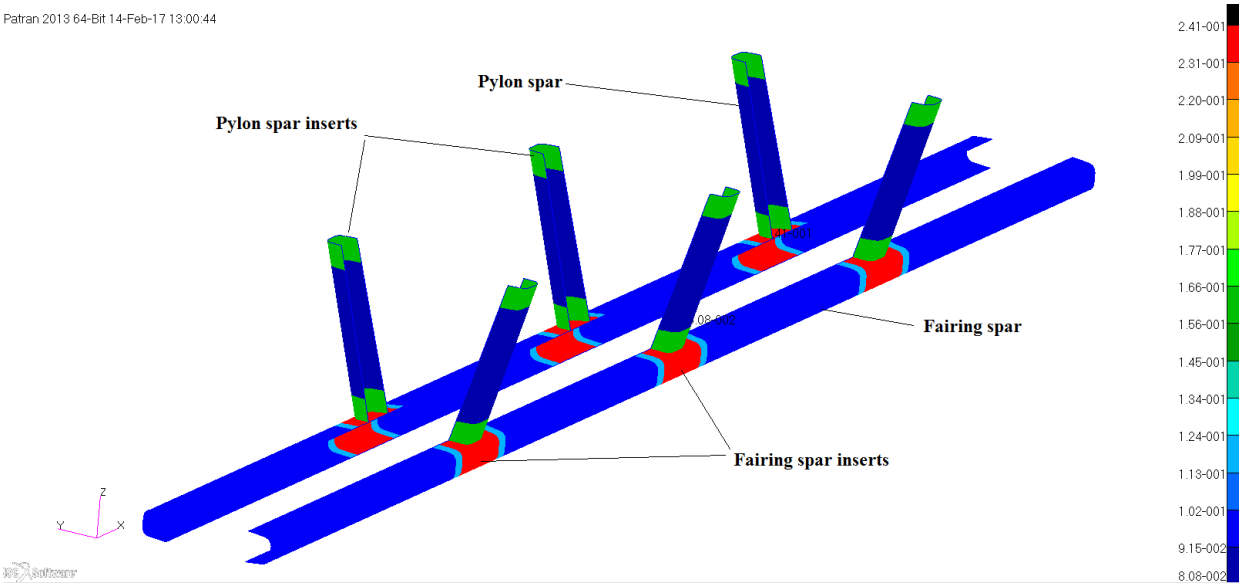


**Figure 68: Fairing and pylon spar inserts thickness plot**

**Table 19: Fairing and pylon spar laminate layups and laminate thicknesses**

| Laminate Color | Component | Laminate Layup | Laminate Thickness, (inch) |
|---|---|---|---|
| Red | Fairing spar insert | [C,C,C,C,C,C,C,C,C,C,C,C,C,A] | 0.24 |
| Green | Pylon spar insert | [C,C,C,C,C,C,C,C,A] | 0.16 |
| Blue | Fairing spar | [C,C,C,C,C,C,C,C,C,C] | 0.10 |
| Dark Blue | Pylon spar | [C,C,C,C,C,C,C,C] | 0.08 |

Rohacell 71 IG foam was added to the fairing skin (upper and lower) and pylon skin to mitigate the buckling stress. The foam was added to the red and yellow part of the pylon and fairing skin respectively, as shown in Figure 69. The fairing and pylon skin laminate thicknesses are shown in Table 20, where C and F represents fiberglass cloth material and foam respectively.

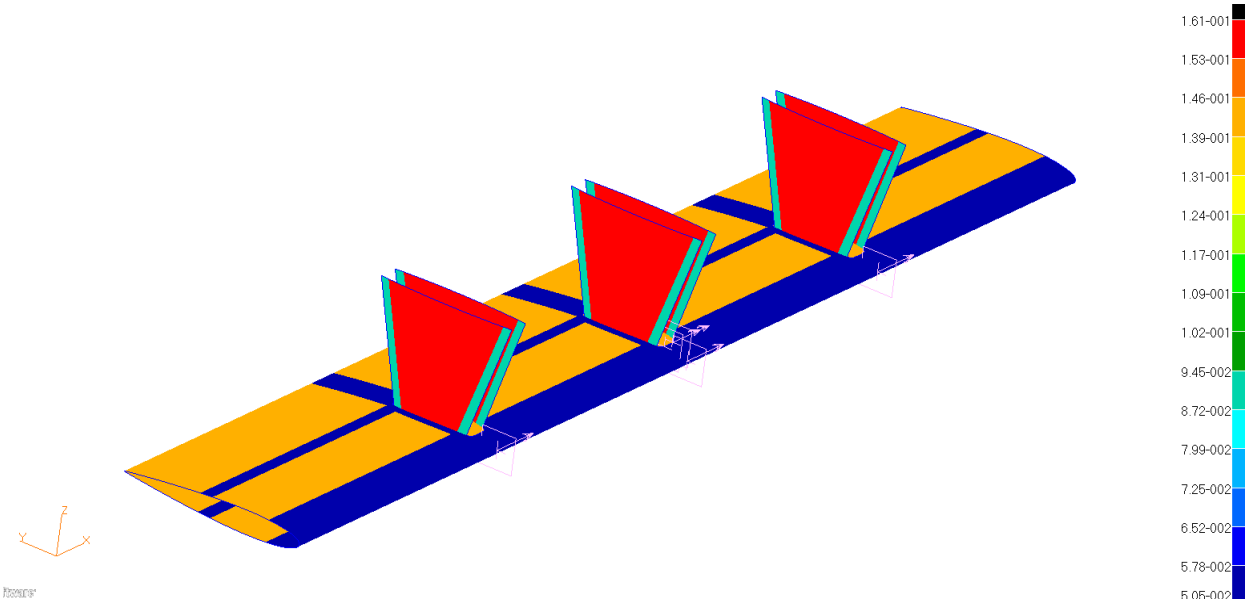


**Figure 69: Fairing and pylon skin thickness plot**

**Table 20: Fairing and pylon skin laminate layups and laminate thicknesses**

| Laminate Color | Component | Laminate Layup | Laminate Thickness, (inch) |
|---|---|---|---|
| Red | Pylon skin | [C,C,C,F,C,C,C] | 0.16 |
| Yellow | Fairing skin | [C,C,F,C,C] | 0.14 |
| Cyan | Pylon skin | [C,C,C,C,C,C,C,C,C] | 0.09 |
| Dark Blue | Fairing skin | [C,C,C,C,C] | 0.05 |

### 4.3.2. Overview of Load Cases

MSC PATRAN/NASTRAN (2013) was used to analyze the existing Meridian FEA wing model and replace the carbon fiber composite material with the fiberglass composite material. A factor of safety of 1.5 (same as existing carbon fiber wing model) was used. Note that original Meridian FEM was created in SI units, so all image outputs are in SI units, but they are converted where necessary. In addition, open hole strength allowables were used so that the design is more conservative. The analyzed load cases for the glass-wing with embedded array (Wing Design I), the carbon wing with external support structure (Wing Design II), and the antenna fairing for Wing

Design II are summarized in Table 21. The existing load case defined in the original FEM [31] was determined to be the critical load case for all wing components. This load case includes the maximum dynamic pressure load at dive speed of 290 ft/s and an inertial load (boundary conditions are in section 4.3.5).

**Table 21: Summary of the load cases**

| Name | Applicable Design | Description |
|---|---|---|
| **Case 1** | Wing Design I | Max Dynamic pressure at dive speed (290 ft/s) with thermal gradient of $\Delta T = -142°$ F |
| **Case 2** | Wing Design II | Max Dynamic pressure at dive speed (290 ft/s) and fairing reaction loads at stall speed (96 ft/s) |
| **Case 3** | Fairing and pylon assembly | Max Dynamic pressure at dive speed (290 ft/s), No displacement at pylon and wing intersection |
| **Case 4** | Fairing and pylon assembly | Dynamic pressure at stall speed (96 ft/s) with max displacement from wing dive case at pylon and wing intersection from Meridian FEA model |
| **Case 5** | Fairing and pylon assembly | Dynamic pressure at cruise speed (220 ft/s) with corresponding displacement at pylon and wing intersection from Meridian FEA model |

Load Case 1 defined for Wing Design I, used the original FEM's critical load case along with the additional thermal loads. The Meridian wing was analyzed for maximum dynamic pressure at the dive speed. During analysis, front wing spar was found critical in root section, hence eight carbon fiber cloth layers were added to this critical section. Due to the addition of carbon fiber cloth, thermal loads ($\Delta T=142°F$) were also applied considering a mixed lay up of fiberglass and carbon fiber composites and their different coefficients of thermal expansion. During the FEM analysis, the operational (analysis) temperature was set to be -75° F and assuming wet layup cured at room temperature the reference (i.e. room) temperature was applied to the material properties.

For Load Case 2, the Meridian wing was also analyzed for maximum dynamic pressure at the dive speed along with reaction load imposed by the fairing-pylon structure. To be more conservative, the highest reaction load from the fairing-pylon load cases (Load Case 3, 4 and 5) was chosen. Load Case 4 was found to have the highest reaction loads. In the fairing model, nodes shared by the pylon spar and wing bottom skin were fixed, and a total reaction load of 2120 lbs (9430 N) in the z-direction was applied to the fairing as verified in the .f06 file shown in Figure 70. The external forces were distributed among the six hard points, three on the front spar and three on the rear spar. Each hard point was given 353.33 lbs (1571.7 N) of reaction load, this total load per hard point is distributed among the nodes shared by the pylon spar and wing bottom skin, as shown in Figure 71. With these reaction loads, the Meridian wing was reanalyzed for the Meridian critical load case and the reaction loads.

| SUBCASE/ DAREA | ID | LOAD TYPE | T1 | T2 | T3 | R1 | R2 | R3 |
|---|---|---|---|---|---|---|---|---|
| 0 | 1 | FX | -4.779505E-03 | ---- | ---- | ---- | -3.116770E-01 | -1.688848E-03 |
| | | FY | ---- | -6.910225E+02 | ---- | 4.463198E+04 | ---- | -6.227397E+02 |
| | | FZ | ---- | ---- | 2.119660E+03 | 4.057606E+03 | -1.909988E+03 | ---- |
| | | MX | ---- | ---- | ---- | 0.000000E+00 | ---- | ---- |
| | | MY | ---- | ---- | ---- | ---- | 0.000000E+00 | ---- |
| | | MZ | ---- | ---- | ---- | ---- | ---- | 0.000000E+00 |
| | | TOTALS | -4.779505E-03 | -6.910225E+02 | 2.119660E+03 | 4.868958E+04 | -1.910300E+03 | -6.227414E+02 |

1 MSC.NASTRAN JOB CREATED ON 29-APR-16 AT 11:02:29 JULY 27, 2016 MSC Nastran 3/14/14

**Figure 70: Reaction loads from structure Load Case 4**

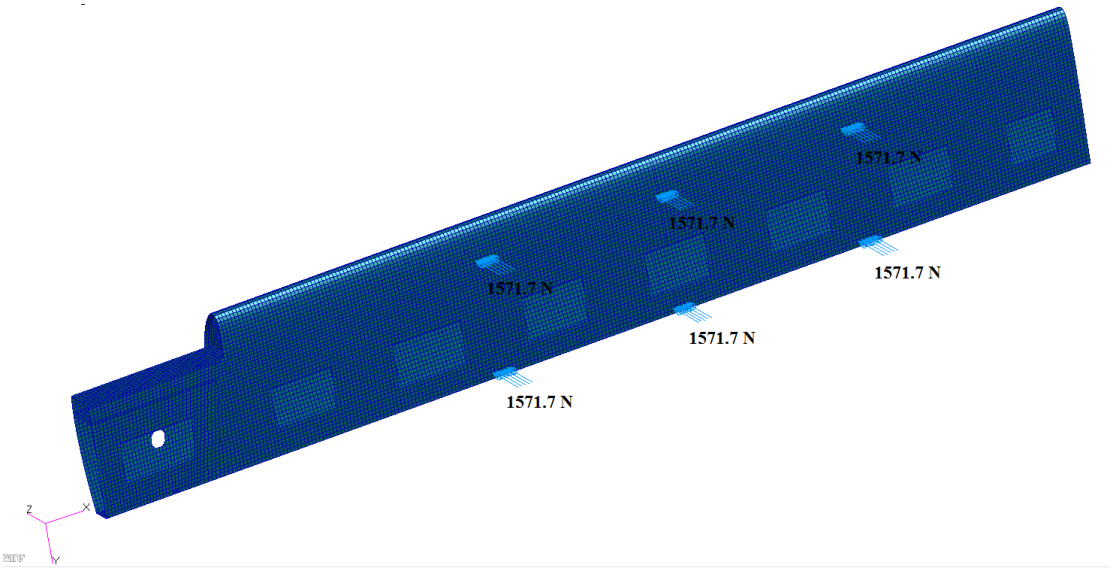


**Figure 71: Structure reaction loads applied at bottom skin**

For Load Case 3, the Meridian dive speed (290 ft/s) and its corresponding dynamic pressure of (0.7 lbf/in$^2$) was used to determine the pressure distribution around the NACA 0012 airfoil with the help of XFLR5 software [32], an analysis tool for airfoils. To design the fairing section, dive speed conditions, such as Reynolds number (3.23*10$^6$), speed (290 ft/s), and angle of attack of 14°, were applied to the model. The stall angle of attack (14°) was taken from Meridian specifications. The author found pressure coefficients for the upper and lower surface of a NACA 0012 airfoil with respect to the chord length. The plot of the pressure coefficient ($c_p$) versus the position along the chord ($x/\bar{c}$) for all three fairing load cases are compared in Figure 72. The data was obtained from XFLR5 analysis software. The pressure coefficient ($c_p$) vs position along the chord ($x/\bar{c}$) plot for Gregory pressure data [33] was also included at a Reynolds number of 3*10$^6$ and an angle of attack of 15°, to compare the pressure distribution and assure that data obtained from XFLR5 software is comparable to other published results. From Figure 72, it is concluded that the results from XFLR5 are in good agreement with Gregory. These pressure coefficients were then applied to the upper and lower skin of the fairing as a pressure load by multiplying them by the associated dynamic pressure. Translational constraints were given to the nodes shared by the pylon spars and wing bottom skin and the details of the boundary conditions are discussed in Section 4.3.5.

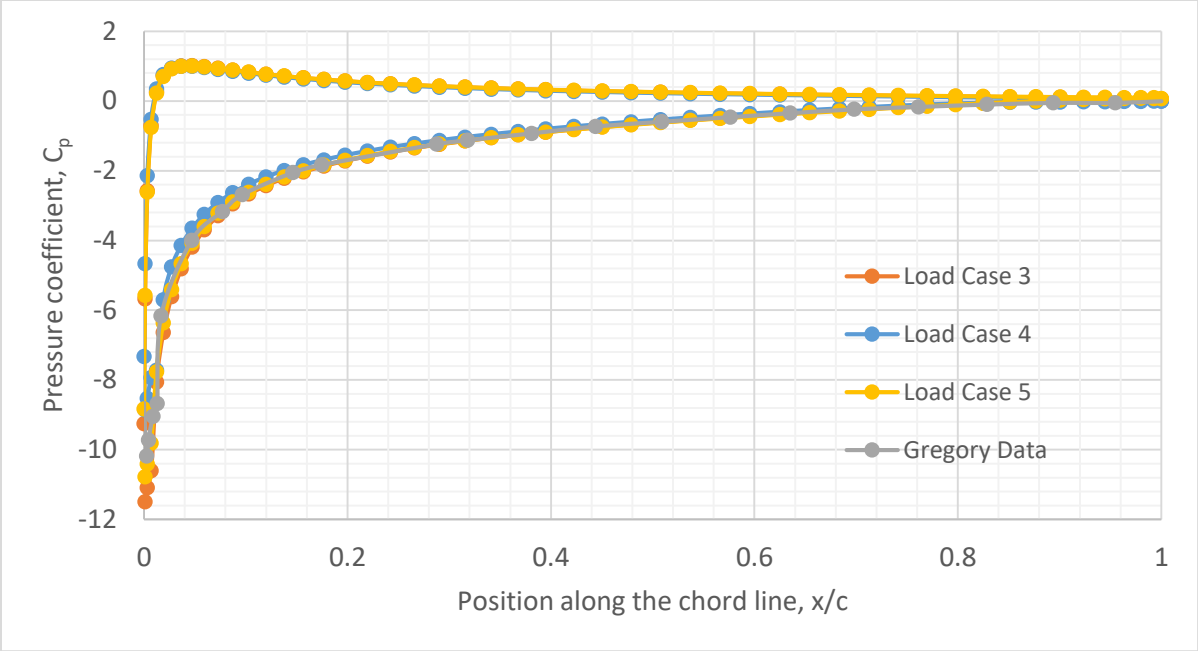


**Figure 72: Pressure coefficient data point comparison**

For Load Case 4, the pressure distribution on the fairing was determined for a Meridian stall speed of 96 ft/s and Reynolds number of $1.07*10^6$ using the same method described for Load Case 3. Nodal displacements generated from the original Meridian FEA model for the dive load case were applied to the nodes shared by the pylon spar and wing bottom skin. It was noted that these deflections drive the critical load case for the fairing and pylon structure.

For Load Case 5, the fairing pressure distribution was found for a cruise speed of 220 ft/s, using XFLR5 software [32]. The Meridian critical load case (existing) was analyzed for cruise speed to get the relative displacement of the wing spar hard point locations, and these displacements constraints were then given to the nodes shared by the pylon spar and wing bottom skin in structure FEM.

### 4.3.3. Material Properties

The material assigned to the Meridian wing components, for both wing designs are summarized in the Table 22. In Wing Design I, the antenna array is embedded into the lower wing skin, and the material of the wing components are modified from carbon fiber. In Wing Design II, the antenna array is supported below the wing with the help of the fairing-pylon structure, and the material of wing components are left unchanged. The materials of the spar inserts, leading edge inserts and wing root attachments are also left unchanged (aluminum alloy). All the components of the fairing-pylon structure are made of fiberglass material.

**Table 22: Summary of material assigned**

| Wing component | Type of material | |
|---|---|---|
| | Wing Design I | Wing Design II |
| Wing skins | Fiberglass | Carbon Fiber |
| Wing spars | Fiberglass | Carbon Fiber |
| Wing ribs | Fiberglass, Rohacell 71 IG | Carbon Fiber, Rohacell 71 IG |
| Spar and leading edge inserts | 7075-T651 plate 0.25-0.499 | 7075-T651 plate 0.25-0.499 |
| Wing root attachments | 2024-T3 sheet 0.01-0.128 | 2024-T3 sheet 0.01-0.128 |

The properties of the aluminum alloys [27] used are tabulated in Table 23 and Table 24. The Rohacell foam [28] properties are given in Table 25. The properties of the GFRP [29] are tabulated in Table 26. The properties of the CFRP cloth and tape [29] [30] are taken from original Meridian FEA model and they are tabulated in Table 27.

**Table 23: 2024-T3 sheet 0.01-0.128 [27]**

| Property | Value | Unit |
|---|---|---|
| E | 10600 | ksi |
| $\alpha$ | $2.34*10^{-5}$ | in/in/°F |
| $\rho$ | 0.1 | lbf /$in^3$ |
| $\nu$ | 0.33 | ~ |
| $F_{tu}$ | 64 | ksi |
| $F_{su}$ | 39 | ksi |

**Table 24:7075-T651 plate 0.25-0.499 [27]**

| Property | Value | Unit |
|---|---|---|
| E | 10,450 | ksi |
| $\alpha$ | 2.34*10-5 | in/in/°F |
| $\rho$ | 0.101 | lbf /$in^3$ |
| $\nu$ | 0.33 | ~ |
| $F_{tu}$ | 77 | ksi |
| $F_{su}$ | 43 | ksi |

**Table 25: Rohacell 71 IG Properties [28]**

| Property | Value | Unit |
|---|---|---|
| E | 13.34 | ksi |
| G | 4.205 | ksi |
| $\rho$ | 0.0027 | lbf /in$^3$ |
| $F_{tu}$ | 406 | psi |
| $F_{cu}$ | 217 | psi |
| $F_{su}$ | 188 | psi |

**Table 26: Fiberglass (GFRP) material properties [29]**

| Property | Fiberglass Cloth 75F, RTD | Fiberglass Tape 75F, RTD | Unit | Fiberglass Cloth 75F, RTD | Fiberglass Tape 75F, RTD | Unit |
|---|---|---|---|---|---|---|
| $E_{1T}$ | 4,220 | 13,150 | ksi | 29.1 | 90.7 | GPa |
| $E_{1C}$ | 4,220 | 11,900 | ksi | 29.1 | 82 | GPa |
| $E_{2T}$ | 4,070 | 1,300 | ksi | 28.1 | 8.96 | GPa |
| $E_{2C}$ | 4,020 | 1,410 | ksi | 27.7 | 9.72 | GPa |
| $G_{12}$ | 550 | 680 | ksi | 3.8 | 4.69 | GPa |
| $\nu_{12}$ | 0.14 | 0.423 | ~ | 0.14 | 0.423 | ~ |
| $t_{nom}$ | 0.0101 | 0.0072 | in | 0.257 | 0.183 | mm |
| $\alpha_1$ | $9*10^{-6}$ | $9*10^{-6}$ | in/in/°F | $9*10^{-6}$ | $9*10^{-6}$ | m/m/°F |
| $\alpha_2$ | $9*10^{-6}$ | $9*10^{-6}$ | in/in/°F | $9*10^{-6}$ | $9*10^{-6}$ | m/m/°F |
| $\rho$ | 0.065 | 0.057 | lbf / in$^3$ | 1,799 | 1,580.4 | kg / m$^3$ |
| $F_{1T}$ | 32.1 | 155.4 | ksi | 221 | 1,072 | MPa |
| $F_{1C}$ | 37 | 105.8 | ksi | 255 | 730 | MPa |
| $F_{2T}$ | 30.8 | 7.6 | ksi | 212 | 52 | MPa |
| $F_{2C}$ | 31.6 | 34.1 | ksi | 218 | 235 | MPa |
| $F_{12}$ | 9.2 | 100.9 | ksi | 63 | 696 | MPa |

**Table 27: Carbon Fiber (CFRP) material properties [29] [30]**

| Property | Carbon Fiber Cloth 75F, RTD | Carbon Fiber Tape 75F, RTD | Unit | Carbon Fiber Cloth 75F, RTD | Carbon Fiber Tape 75F, RTD | Unit |
|---|---|---|---|---|---|---|
| $E_{11}$ | 10,000 | 18,700 | ksi | 68.95 | 128.93 | GPa |
| $E_{22}$ | 10,000 | 1,900 | ksi | 68.95 | 13.1 | GPa |
| $G_{12}$ | 800 | 850 | ksi | 5.52 | 5.86 | GPa |
| $\nu_{12}$ | 0.058 | 0.3 | ~ | 0.058 | 0.3 | ~ |
| tnom | 0.014 | 0.005 | in | 0.3556 | 0.127 | mm |
| $\alpha_1$ | $1.836*10^{-5}$ | $7.2*10^{-7}$ | in/in/°F | $1.836*10^{-5}$ | $7.2*10^{-7}$ | m/m/°F |
| $\alpha_2$ | $1.836*10^{-5}$ | $3.6*10^{-5}$ | in/in/°F | $1.836*10^{-5}$ | $3.6*10^{-5}$ | m/m/°F |
| $\rho$ | 0.0571 | 0.0571 | $lbf / in^3$ | 1,580.4 | 1,580.4 | $kg / m^3$ |
| $F_{1T}$ | 112 | 274 | ksi | 772 | 1,889 | MPa |
| $F_{1C}$ | 82 | 279.6 | ksi | 565 | 1,928 | MPa |
| $F_{2T}$ | 112 | 9.5 | ksi | 772 | 66 | MPa |
| $F_{2C}$ | 82 | 38.9 | ksi | 565 | 268 | MPa |
| $F_{12}$ | 13 | 19.55 | ksi | 92 | 135 | MPa |

### 4.3.4. Finite Elements Used

The existing Meridian's FEM was modified and analyzed. The elements representing the spar inserts were modified from 1D beam (bar) elements to 2D shell elements, for better and more accurate stress predictions. The finite elements used for the wing components and fairing-pylon structure are given below.

**Wing Design I and II**

For Wing Design I and II, the same existing wing FEM with different material properties and loads were analyzed. The finite elements assigned for each wing component are as follows:

- Wing skins were modeled with 2D shell elements to withstand axial, shear and bending loads.
- Wing spars were modeled with 2D shell elements, so spar caps and spar webs can withstand axial, shear and bending loads.
- Wing ribs were modeled with 2D shell elements, so rib caps and rib webs can withstand axial, shear and bending loads.
- Wing leading edge was modeled with 2D shell elements to withstand axial, shear and bending loads.
- Wing leading edge inserts and spar inserts were also modeled with 2D shell elements to withstand axial, shear and bending loads.

Figure 73 shows FEM of the Meridian wing, the FEM mesh density of the Meridian wing with universal node spacing is about 0.5 in.

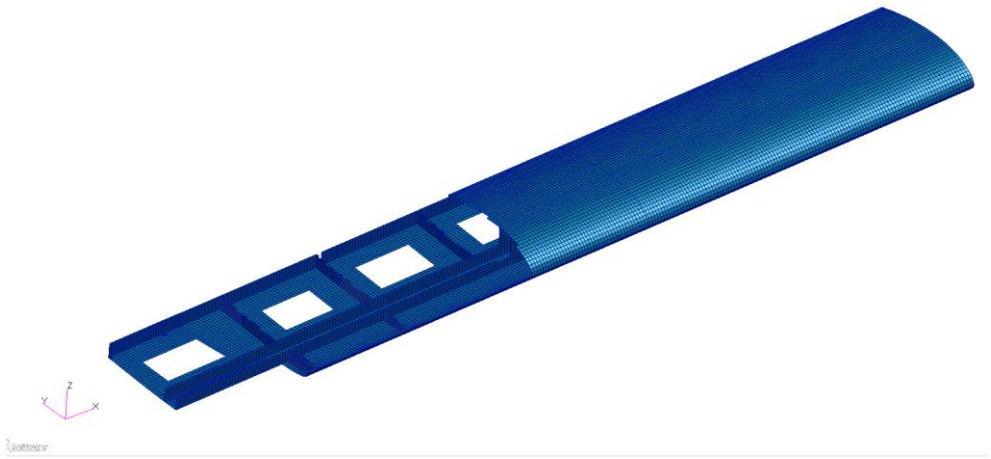

**Figure 73: Fiberglass FEM for the Meridian wing with half cut section**

**Fairing-Pylon Structure**

The finite elements assigned for each of the fairing-pylon structure components are as follows:

- Fairing and pylon skins were modeled with 2D shell elements to withstand axial, shear and bending loads.
- Fairing and pylon spars were modeled with 2D shell elements, so spar caps and spar webs can withstand axial, shear and bending loads.
- Fairing and pylon ribs were modeled with 2D shell elements, so rib caps and rib webs can withstand axial, shear and bending loads.
- Fairing and pylon spar inserts were also modeled with 2D shell elements to withstand axial, shear and bending loads.

For all the FEM's, the 2D shell elements were meshed as quad elements, while paying attention to skewing and warping of the elements. A few triangular elements were necessary where it was difficult to mesh with quad elements. No triangular elements were used critical stress regions.

### 4.3.5. Boundary Conditions

**Wing Design I and II**

The displacement constraints of the existing Meridian FEM were not modified. The existing Meridian FEM has three displacement constraints. The Meridian's fuselage was constrained along its centerline, as shown in Figure 74, and spanwise (X) translations were constrained.

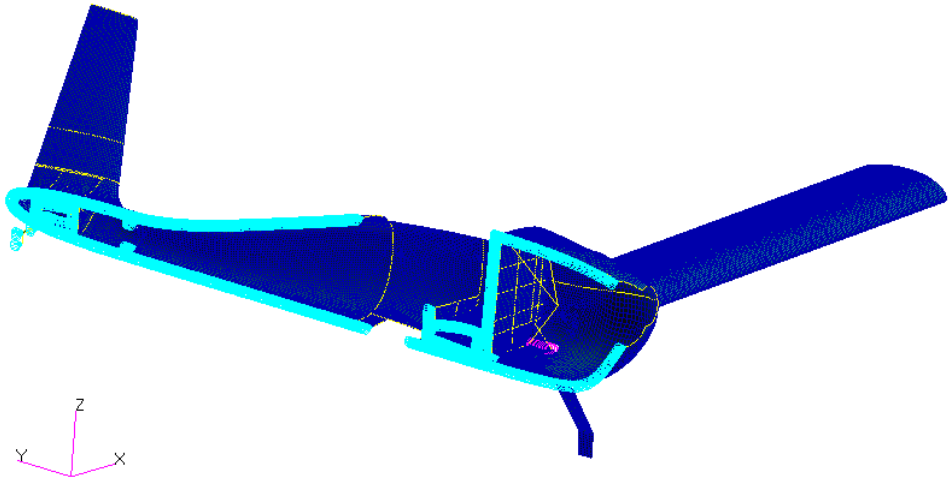


**Figure 74: Meridian's fuselage (centerline) constraint**

The Meridian's firewall was constrained at the intersecting corners of firewall and wing spars, as shown in Figure 75 (left), and spanwise (X) and chordwise (Y) translations were constrained. This resulted in high local stress but provides more realistic boundary condition for the wing. The Meridian's landing gear was given translational and rotational constraints at the fuselage and landing gear intersection, as shown in Figure 75 (right). The spanwise (X) translations were constrained and spanwise (X), chordwise (Y) and heightwise (Z) rotations were also constrained.

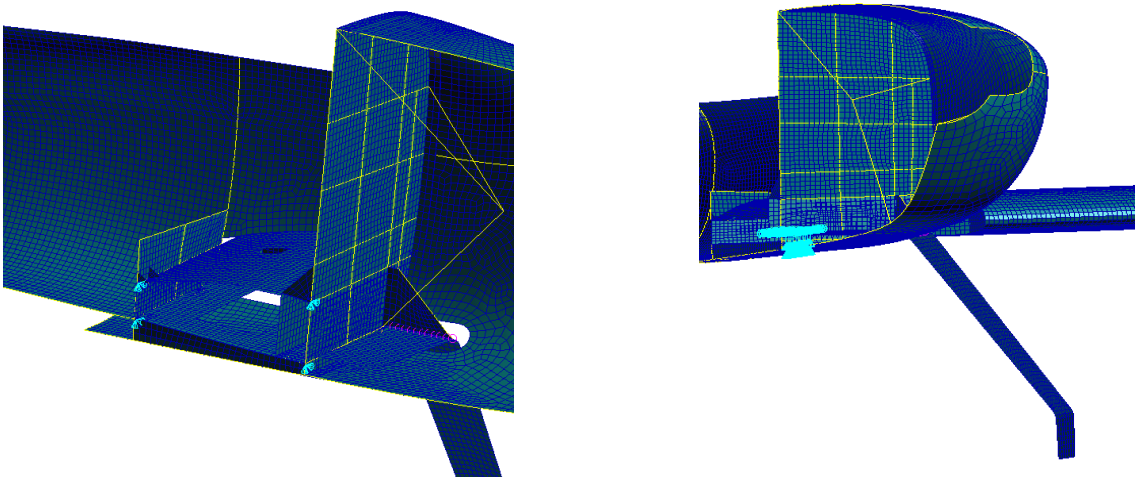

**Figure 75: Meridian's firewall constraint (left) and landing gear constraint (right)**

**Fairing-pylon structure**

This fairing-pylon structure was modeled separately, and the boundary conditions (displacement constraints) were extracted from original wing FEM. The displacement constraints were applied to the wing-pylon intersection, as shown in Figure 76. Spanwise (X), chordwise (Y) and heightwise (Z) translations of these nodes were constrained. Different heightwise (Z)

translational constraints were given for Load Cases 3, 4 and 5 (see Table 28), and they were described in their respective sections.

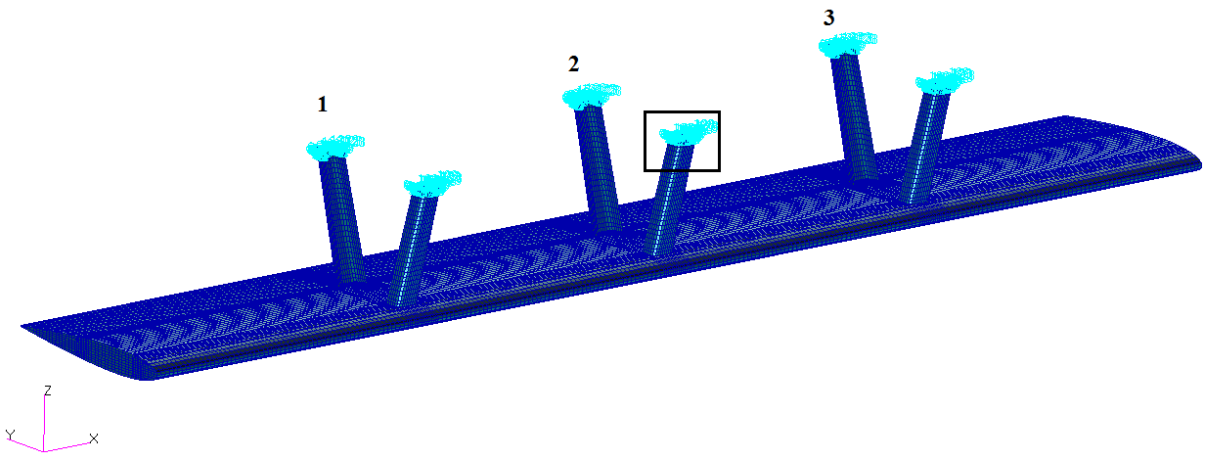


**Figure 76: Translational constraints of fairing-pylon structure**

**Table 28: Summary of the fairing translational constraints**

| Load case | Pylon spar 1, in | Pylon spar 2, in | Pylon spar 3, in |
|---|---|---|---|
| **Load Case 3** | (0, 0, 0) | (0, 0, 0) | (0, 0, 0) |
| **Load Case 4** | (0, 0, 0) | (0, 0, 1.29) | (0, 0, 2.75) |
| **Load Case 5** | (0, 0, 0) | (0, 0, 0.63) | (0, 0, 1.32) |

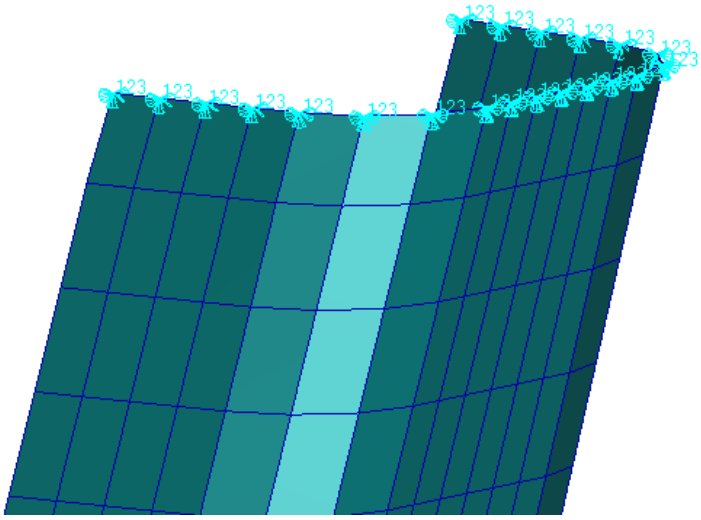

**Figure 77: Enlarged view of translational constraints of fairing-pylon structure**

### 4.3.6. Degrees of Freedom

The existing Meridian FEM used for Wing Design I and II, have about 61502 shell elements and about 6769 beam elements [30]. The total degrees of freedom estimated by PATRAN are about 440500. The fairing-pylon's FEM have about 76200 shell elements, and the total degrees of freedom estimated by PATRAN are 335572.

### 4.3.7. Structure Sizing and FEM Analysis

The maximum stress criterion was used to determine the critical components of the Meridian wing and fairing-pylon substructure.

#### 4.3.7.1. Wing Design I

In this section, only the most critical component is documented and all other components are provided in Appendix A- Wing Design I. The Wing Design I was found to be the most critical in longitudinal compression in the front spar cap (layer - 47, material - fiberglass, orientation - 0°), where a margin of safety of +0.04 was achieved with factor of safety of 1.5. The critical element is identified in Figure 78 with an enlarged section shown in Figure 79. The .f06 file results are shown in Figure 80. The same element was critical for carbon fiber cloth at layer 46, where a M.S. of +0.43 was achieved at ultimate load. Also for spar inserts an M.S. of +0.09 was achieved at ultimate load. The buckling analysis of this wing design was left for future study.

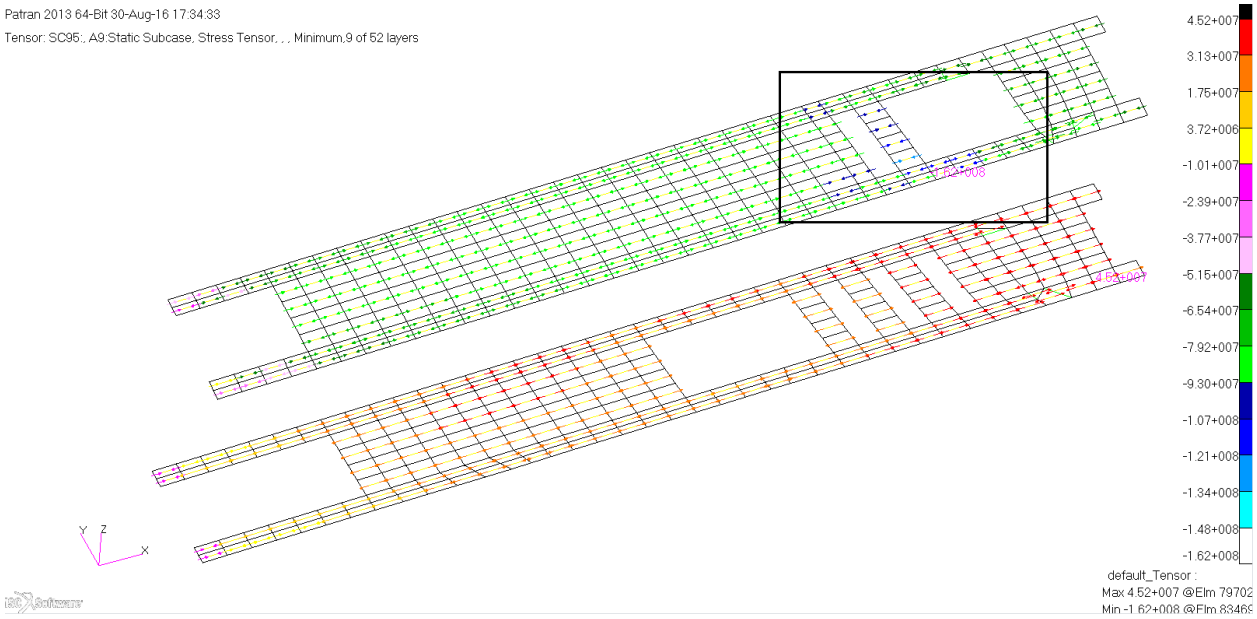


**Figure 78: Critical red section of the front spar cap**

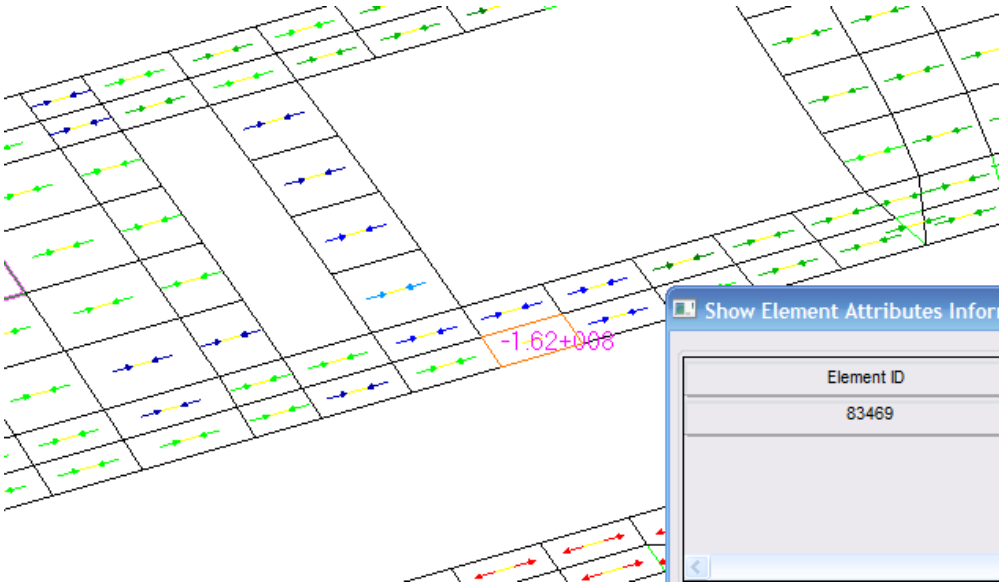


**Figure 79: Enlarged critical section of front spar cap**

| | | | STRESSES IN LAYERED COMPOSITE ELEMENTS (QUAD4) | | | | | | | | | |
|---|---|---|---|---|---|---|---|---|---|---|---|---|
| | ELEMENT ID | PLY ID | STRESSES IN FIBER AND MATRIX DIRECTIONS NORMAL-1 | NORMAL-2 | SHEAR-12 | INTER-LAMINAR STRESSES SHEAR XZ-MAT | SHEAR YZ-MAT | PRINCIPAL STRESSES (ZERO SHEAR) ANGLE | MAJOR | MINOR | MAX SHEAR |
| 0 | 83469 | 43 | -4.06086E+08 | -3.12947E+07 | -1.00572E-03 | -6.06271E+06 | -6.67996E+06 | -90.00 | -3.12947E+07 | -4.06086E+08 | 1.87395E+08 |
| 0 | 83469 | 44 | -4.12545E+08 | -3.19592E+07 | -1.02321E-03 | -4.88727E+06 | -6.50779E+06 | -90.00 | -3.19592E+07 | -4.12545E+08 | 1.90293E+08 |
| 0 | 83469 | 45 | -2.52851E+08 | -2.63662E+07 | -1.23409E+07 | -2.87840E+06 | -3.81423E+06 | -86.89 | -2.56957E+07 | -2.53522E+08 | 1.13913E+08 |
| 0 | 83469 | 46 | -2.63300E+08 | -3.24464E+07 | -1.27412E+07 | -7.11844E+05 | -9.09233E+05 | -86.85 | -3.17454E+07 | -2.64001E+08 | 1.16128E+08 |
| 0 | 83469 | 47 | -1.62072E+08 | -6.72524E+07 | -8.99644E+06 | -1.61323E-07 | -3.64029E-08 | -84.63 | -6.64064E+07 | -1.62918E+08 | 4.82560E+07 |
| 0 | 83470 | 1 | -2.99840E+07 | 1.68970E+07 | -4.47252E+06 | 9.58438E+05 | -7.25430E+04 | -84.60 | 1.73198E+07 | -3.04069E+07 | 2.38634E+07 |
| 0 | 83470 | 2 | 1.83554E+07 | 1.40242E+08 | -6.26171E+06 | 3.87552E+06 | -3.04318E+05 | -87.07 | 1.40563E+08 | 1.80345E+07 | 6.12642E+07 |
| 0 | 83470 | 3 | 1.25057E+07 | 1.34742E+08 | -5.97848E+06 | 6.58028E+06 | -5.19223E+05 | -87.21 | 1.35034E+08 | 1.22140E+07 | 6.14100E+07 |
| 0 | 83470 | 4 | -1.08457E+08 | -1.07011E+04 | -4.89942E-04 | 8.16292E+06 | -5.32960E+05 | -90.00 | -1.07011E+04 | -1.08457E+08 | 5.42230E+07 |
| 0 | 83470 | 5 | -1.12058E+08 | -5.22127E+05 | -4.77561E-04 | 9.67762E+06 | -5.46108E+05 | -90.00 | -5.22127E+05 | -1.12058E+08 | 5.57679E+07 |
| 0 | 83470 | 6 | -1.15659E+08 | -1.03355E+06 | -4.65180E-04 | 1.11244E+07 | -5.58665E+05 | -90.00 | -1.03355E+06 | -1.15659E+08 | 5.73127E+07 |
| 0 | 83470 | 7 | -1.19260E+08 | -1.54498E+06 | -4.52798E-04 | 1.25032E+07 | -5.70634E+05 | -90.00 | -1.54498E+06 | -1.19260E+08 | 5.88575E+07 |
| 0 | 83470 | 8 | -1.22861E+08 | -2.05641E+06 | -4.40417E-04 | 1.38142E+07 | -5.82012E+05 | -90.00 | -2.05641E+06 | -1.22861E+08 | 6.04024E+07 |
| 0 | 83470 | 9 | -4.41387E+07 | 4.02897E+06 | -3.44188E+06 | 1.44251E+07 | -6.28257E+05 | -85.93 | 4.27367E+06 | -4.43834E+07 | 2.43285E+07 |
| 0 | 83470 | 10 | -1.31514E+08 | -3.28525E+06 | -4.10668E-04 | 1.55728E+07 | -6.38219E+05 | -90.00 | -3.28525E+06 | -1.31514E+08 | 6.41142E+07 |
| 0 | 83470 | 11 | -1.35115E+08 | -3.79668E+06 | -3.98287E-04 | 1.66526E+07 | -6.47591E+05 | -90.00 | -3.79668E+06 | -1.35115E+08 | 6.56591E+07 |

**Figure 80: Element and ply ID of critical element from .f06 file**

The minor principal stress in the fiberglass lamina 47 is higher than normal stress in the longitudinal fiber direction, hence to be more conservative the former stress was used in the M.S. calculations. The corresponding margin of safety (M.S.) for compressive stress of the front spar is as follow: the allowable compressive stress used to calculate the M.S. is 37 ksi (255 MPa) (see Table 26) and actual tensile stress is found to be 23.63 ksi (162.92 MPa).

$$MS = \frac{\sigma_{allowable}}{FS * \sigma_{actual}} - 1 = \frac{-37\ ksi}{1.5 * (-23.63\ ksi)} - 1 = +0.04$$

Table 29 shows the M.S. and critical mode found for each major component of the Meridian wing made up of fiberglass composite material. It can be noticed that the wing is most critical in longitudinal compression in the front spar.

**Table 29: Critical modes and Margin of safety of Meridian wing components**

| Meridian Component | Margin of Safety | Critical Mode |
|---|---|---|
| Upper Skin | +0.36 | Longitudinal Compression |
| Lower Skin | +0.08 | Longitudinal Tension |
| Front Spar | +0.04 | Longitudinal Compression |
| Rear Spar | +0.12 | Longitudinal Tension |
| Ribs | +1.87 | Transverse Compression |
| Leading Edge | +0.15 | Shear |

#### 4.3.7.2. Wing Design II

Once again only the most critical component of the wing is documented in this section. The rest of the components are documented in Appendix B- Wing Design II. The Wing Design II was found to be most critical in transverse compression in the front spar web at the wing root (layer - 9, material – carbon fiber, orientation - 0°), and a margin of safety of +0.06 was achieved with factor of safety of 1.5. The critical element is identified in Figure 81 with its enlarged section shown in Figure 82 and .f06 file results are shown in Figure 83. For carbon fiber tape (in front spar cap), M.S. of +0.39 was achieved with F.S. of 1.5 and for spar inserts M.S. of +0.32 was achieved with F.S. of 1.5.

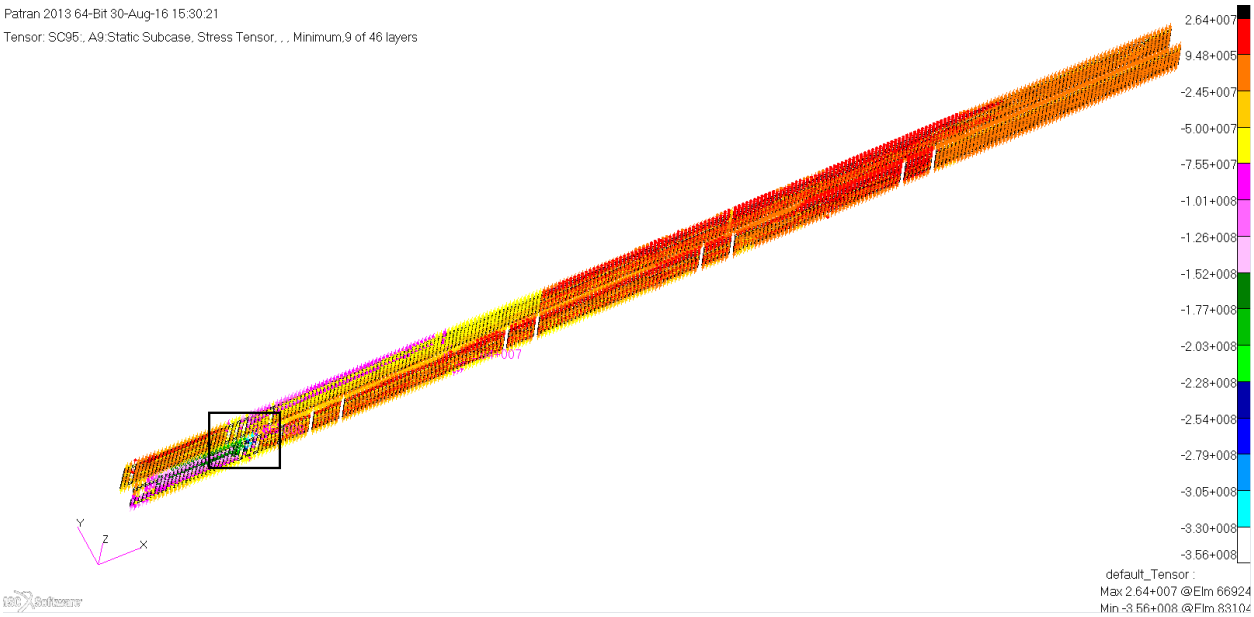


**Figure 81: Critical red section of the front spar web**

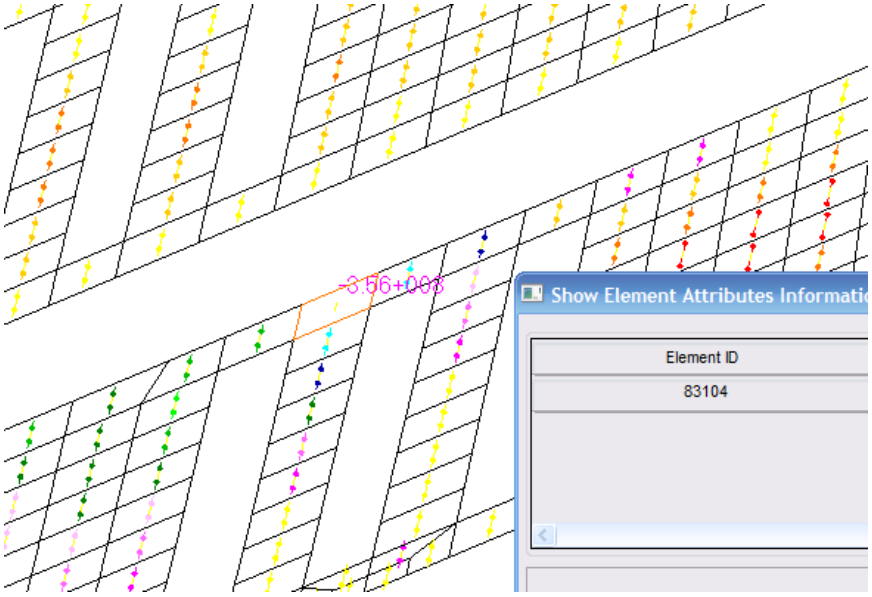


**Figure 82: Enlarged critical section of front spar web**

The corresponding margin of safety (MS) for compressive stress of the front spar is as follows, and the allowable compressive stress used to calculate the M.S. is 82 ksi (565.4 MPa) (see Table 26) and actual compressive stress is found to be 51.62 ksi (355.89 MPa).

$$MS = \frac{\sigma_{allowable}}{FS * \sigma_{actual}} - 1 = \frac{-82\ ksi}{1.5 * (-51.62\ ksi)} - 1 = +0.06$$

| | | | | | | | | | | | |
|---|---|---|---|---|---|---|---|---|---|---|---|
| 0 | 83104 | 6 | -2.16314E+08 | -1.66696E+08 | 2.78121E+07 | -2.66862E+06 | 1.73847E+06 | 65.87 | -1.54236E+08 | -2.28775E+08 | 3.72693E+07 |
| 0 | 83104 | 7 | -2.16675E+08 | -1.60230E+08 | 2.83342E+07 | -1.81618E+06 | 1.18315E+06 | 67.44 | -1.48461E+08 | -2.28444E+08 | 3.99917E+07 |
| 0 | 83104 | 8 | -1.49341E+07 | -3.55865E+08 | 5.35533E+06 | -1.03782E+06 | 6.76084E+05 | 0.90 | -1.48500E+07 | -3.55949E+08 | 1.70549E+08 |
| 0 | 83104 | 9 | -8.79654E+06 | -3.55896E+08 | 5.93317E+06 | 1.24076E-09 | -8.08291E-10 | 0.98 | -8.69514E+06 | -3.55998E+08 | 1.73651E+08 |
| 0 | 83105 | 1 | -1.90950E+08 | -3.22718E+08 | -1.42347E+07 | 5.05236E+05 | 1.74251E+05 | -6.10 | -1.89430E+08 | -3.24238E+08 | 6.74044E+07 |
| 0 | 83105 | 2 | -1.84351E+08 | -3.16960E+08 | -1.38561E+07 | 8.84164E+05 | 3.04939E+05 | -5.90 | -1.82919E+08 | -3.18392E+08 | 6.77366E+07 |
| 0 | 83105 | 3 | -1.64860E+08 | -3.24094E+08 | 1.12951E+07 | 1.29916E+06 | 4.48066E+05 | 4.04 | -1.64063E+08 | -3.24891E+08 | 8.04141E+07 |
| 0 | 83105 | 4 | -1.60918E+08 | -3.15679E+08 | 1.13662E+07 | 1.50665E+06 | 5.19629E+05 | 4.18 | -1.60087E+08 | -3.16509E+08 | 7.82109E+07 |
| 0 | 83105 | 5 | -1.56975E+08 | -3.07264E+08 | 1.14373E+07 | 1.50665E+06 | 5.19629E+05 | 4.33 | -1.56110E+08 | -3.08129E+08 | 7.60096E+07 |

1 THIS IS A DEFAULT SUBCASE. AUGUST 8, 2016 MSC Nastran 3/14/14 PAGE 13242

0 SUBCASE 95

S T R E S S E S I N L A Y E R E D C O M P O S I T E E L E M E N T S ( Q U A D 4 )

| | ELEMENT ID | PLY ID | STRESSES IN FIBER AND MATRIX DIRECTIONS NORMAL-1 | NORMAL-2 | SHEAR-12 | INTER-LAMINAR STRESSES SHEAR XZ-MAT | SHEAR YZ-MAT | PRINCIPAL STRESSES (ZERO SHEAR) ANGLE | MAJOR | MINOR | MAX SHEAR |
|---|---|---|---|---|---|---|---|---|---|---|---|
| 0 | 83105 | 6 | -1.53033E+08 | -2.98849E+08 | 1.15084E+07 | 1.29916E+06 | 4.48066E+05 | 4.49 | -1.52130E+08 | -2.99752E+08 | 7.38106E+07 |
| 0 | 83105 | 7 | -1.49091E+08 | -2.90434E+08 | 1.15796E+07 | 8.84164E+05 | 3.04939E+05 | 4.65 | -1.48149E+08 | -2.91376E+08 | 7.16139E+07 |
| 0 | 83105 | 8 | -1.44759E+08 | -2.82409E+08 | -1.15847E+07 | 5.05236E+05 | 1.74251E+05 | -4.78 | -1.43791E+08 | -2.83377E+08 | 6.97930E+07 |
| 0 | 83105 | 9 | -1.38160E+08 | -2.76650E+08 | -1.12062E+07 | -6.04034E-10 | -2.08325E-10 | -4.60 | -1.37259E+08 | -2.77551E+08 | 7.01458E+07 |

**Figure 83: Element and ply ID of critical element from .f06 file**

Table 30 shows the margin of safety and critical mode for the major Meridian wing components of Wing Design II.

**Table 30: Critical modes and Margin of safety of Meridian wing components**

| Meridian Component | Margin of Safety | Critical Mode |
|---|---|---|
| Upper Skin | +0.54 | Longitudinal Compression |
| Lower Skin | +0.50 | Shear |
| Front Spar | +0.059 | Transverse Compression |
| Rear Spar | +0.50 | Transverse Compression |
| Ribs | +1.16 | Shear |
| Leading Edge | +0.33 | Shear |

#### 4.3.7.3. Fairing and Pylon Structure

Three potential load cases (Load Case 3, 4 and 5) were defined for structural analysis of the fairing-pylon structure and analyzed to determine critical load case. It was necessary to begin the study with the fairing-pylon structure load cases, to find the reaction loads for the Meridian wing sizing. Structural analysis was done for fairing-pylon structure to accomplish the following objectives:

- Preliminary sizing of the fairing and pylon structure, and propose a potential structural design.
- Determine the critical load case and design structure for that critical load case with positive margin of safety and factor of safety of 1.5.
- Come up with the initial composite layups for each component and estimate the total structure weight.
- Determine the reaction loads at the pylon spar and Meridian wing intersection, and use those reaction loads during structural analysis of Meridian wing.

Since the fairing and pylon structure have different laminate thickness, they are documented separately to distinguish their critical load case and critical component.

**Fairing Structure**

The critical load case for the fairing structure was determined to be Load Case 2. It was found that the fairing spar (critical element at the top of the rear spar cap) was most critical in longitudinal tension (layer - 1, material - fiberglass, orientation - 0°), where the M.S. of +0.07 was achieved with factor of safety of 1.5. Figure 84 shows the tensile stress distribution in the fairing spar with the critical region boxed. Figure 85 shows an enlarged view of critical region with the critical element highlighted, and Figure 89 shows the critical element and ply ID with its critical tensile stress from the .f06 file. Note that only most critical component of fairing and pylon structure are documented and all other components are provided in Appendix C- Fairing and Pylon Structure.

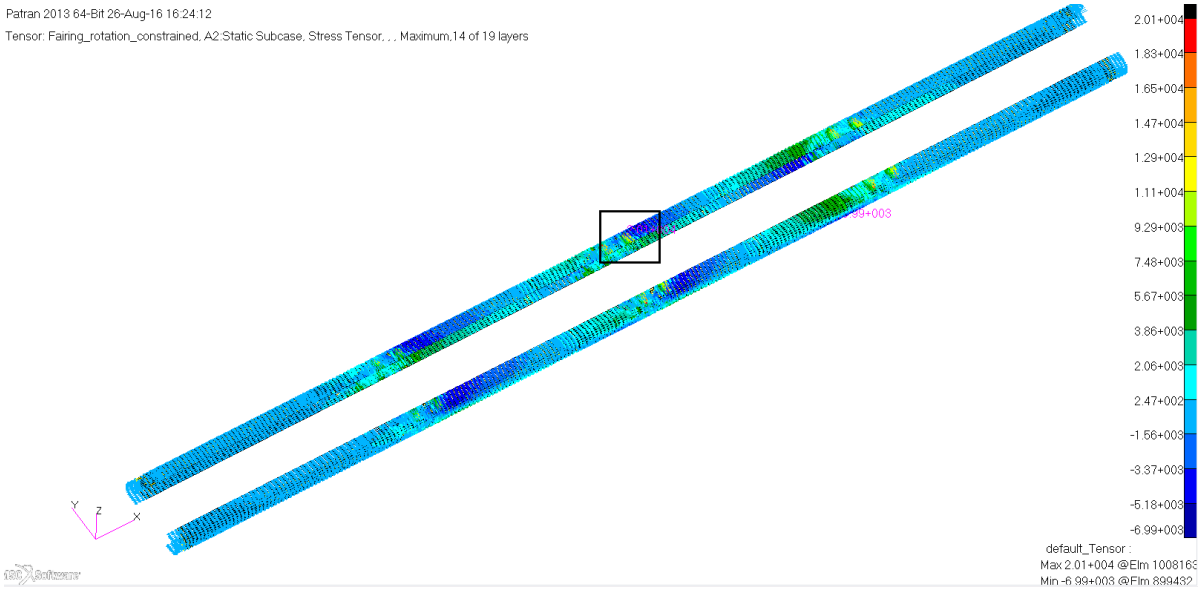


**Figure 84: Fairing spar tensile stress distribution**

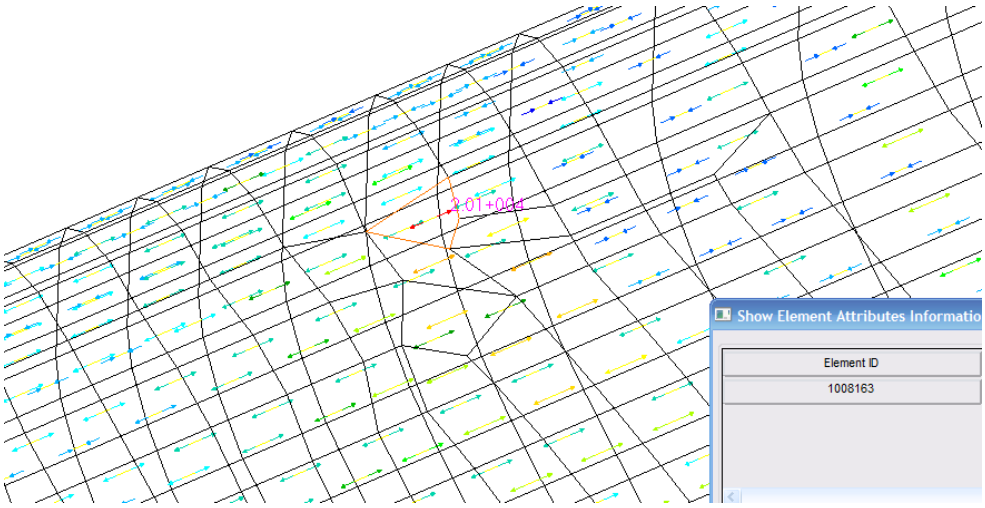


**Figure 85: Enlarged view of the critical tensile stress region**

The corresponding margin of safety for critical tensile stress of fairing spar is computed as follow:

$$MS = \frac{\sigma_{allowable}}{FS * \sigma_{actual}} - 1 = \frac{32.1\ ksi}{1.5 * 20.1\ ksi} - 1 = +0.07$$

| | | | | | | | | | | | | | |
|---|---|---|---|---|---|---|---|---|---|---|---|---|---|
| 0 | 1008162 | 11 | -4.59423E+03 | -2.25427E+03 | 5.83458E+02 | 4.20086E+03 | -4.69098E+03 | 76.75 | -2.11686E+03 | -4.73164E+03 | 1.30739E+03 | | |
| 0 | 1008162 | 12 | -3.02496E+03 | -1.28581E+03 | 4.73188E+02 | 4.33719E+03 | -4.84698E+03 | 75.72 | -1.16540E+03 | -3.14537E+03 | 9.89986E+02 | | |
| 0 | 1008162 | 13 | -1.45569E+03 | -3.17337E+02 | 3.62919E+02 | 4.43259E+03 | -4.95791E+03 | 73.74 | -2.11479E+02 | -1.56155E+03 | 6.75037E+02 | | |
| 0 | 1008162 | 14 | 1.13572E+02 | 6.51131E+02 | 2.52650E+02 | 4.48706E+03 | -5.02376E+03 | 68.39 | 7.51234E+02 | 1.34686E+01 | 3.68883E+02 | | |
| 0 | 1008162 | 15 | 2.59947E+04 | 2.08099E+04 | -2.45266E+03 | -2.06415E-04 | 3.57968E-05 | -21.71 | 2.69711E+04 | 1.98335E+04 | 3.56877E+03 | | |
| 0 | 1008163 | 1 | 2.01420E+04 | 1.25814E+04 | 1.71491E+03 | 5.97719E+02 | 6.91887E+02 | 12.20 | 2.05128E+04 | 1.22106E+04 | 4.15109E+03 | | |
| 0 | 1008163 | 2 | 1.85094E+04 | 1.15737E+04 | 1.60000E+03 | 1.15373E+03 | 1.33593E+03 | 12.38 | 1.88607E+04 | 1.12224E+04 | 3.81917E+03 | | |
| 0 | 1008163 | 3 | 1.68768E+04 | 1.05660E+04 | 1.48510E+03 | 1.66803E+03 | 1.93213E+03 | 12.60 | 1.72088E+04 | 1.02340E+04 | 3.48743E+03 | | |
| 0 | 1008163 | 4 | 1.52442E+04 | 9.55827E+03 | 1.37020E+03 | 2.14063E+03 | 2.48048E+03 | 12.87 | 1.55572E+04 | 9.24531E+03 | 3.15594E+03 | | |
| 0 | 1008163 | 5 | 1.36116E+04 | 8.55057E+03 | 1.25529E+03 | 2.57151E+03 | 2.98099E+03 | 13.19 | 1.39059E+04 | 8.25633E+03 | 2.82478E+03 | | |
| 0 | 1008163 | 6 | 1.19791E+04 | 7.54287E+03 | 1.14039E+03 | 2.96069E+03 | 3.43365E+03 | 13.60 | 1.22550E+04 | 7.26688E+03 | 2.49408E+03 | | |
| 0 | 1008163 | 7 | 1.03465E+04 | 6.53517E+03 | 1.02549E+03 | 3.30816E+03 | 3.83846E+03 | 14.14 | 1.06049E+04 | 6.27676E+03 | 2.16406E+03 | | |
| 1 | MSC.NASTRAN JOB CREATED ON 05-JUL-16 AT 14:10:23 | | | | | | | | JULY 27, 2016 MSC Nastran 3/14/14 | | PAGE 14078 | | |
| | FAIRING_ROTATION_FIXED | | | | | | | | | | | | |
| 0 | | | | | | | | | | SUBCASE 1 | | | |

S T R E S S E S I N L A Y E R E D C O M P O S I T E E L E M E N T S ( Q U A D 4 )

| | ELEMENT ID | PLY ID | STRESSES IN FIBER AND MATRIX DIRECTIONS NORMAL-1 | NORMAL-2 | SHEAR-12 | INTER-LAMINAR STRESSES SHEAR XZ-MAT | SHEAR YZ-MAT | PRINCIPAL STRESSES (ZERO SHEAR) ANGLE | MAJOR | MINOR | MAX SHEAR |
|---|---|---|---|---|---|---|---|---|---|---|---|
| 0 | 1008163 | 8 | 8.71389E+03 | 5.52746E+03 | 9.10582E+02 | 3.61392E+03 | 4.19544E+03 | 14.87 | 8.95575E+03 | 5.28560E+03 | 1.83507E+03 |
| 0 | 1008163 | 9 | 7.08130E+03 | 4.51976E+03 | 7.95679E+02 | 3.87797E+03 | 4.50456E+03 | 15.93 | 7.30834E+03 | 4.29273E+03 | 1.50781E+03 |
| 0 | 1008163 | 10 | 5.44872E+03 | 3.51206E+03 | 6.80775E+02 | 4.10032E+03 | 4.76585E+03 | 17.55 | 5.66408E+03 | 3.29670E+03 | 1.18369E+03 |
| 0 | 1008163 | 11 | 3.81613E+03 | 2.50435E+03 | 5.65872E+02 | 4.28095E+03 | 4.97928E+03 | 20.39 | 4.02650E+03 | 2.29399E+03 | 8.66257E+02 |

**Figure 86: Fairing spar critical tensile stress and an element ID from .f06 file**

Buckling analysis was also performed for the fairing-pylon structure, and it was found that first buckling mode occurs at load factor of 1.58 in the fairing bottom skin, as shown in Figure 87. For the factor of safety of 1.5, the M.S. corresponding to the first buckling mode is found to be +0.06, and comparing to the M.S. of fairing skin +0.14 from linear static analysis, the buckling stress from buckling analysis is determined to be the most critical for fairing skin.

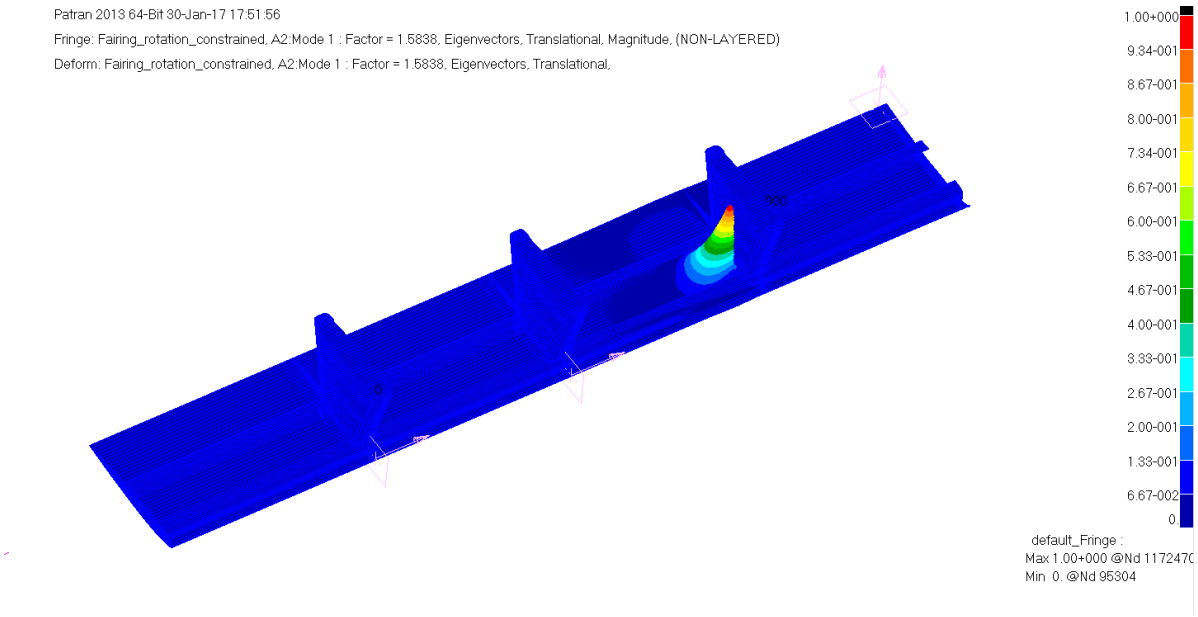


**Figure 87: Buckling analysis for load case 4 (first mode)**

The margin of safety for critical buckling stress in bottom skin of fairing structure is computed as follow:

$$MS = \frac{Buckling\ Load\ Factor}{F.S.} - 1 = \frac{1.58}{1.5} - 1 = +0.06$$

## Pylon Structure

Load Case 2 was determined to be the critical load case for both the fairing and pylon. The pylon skin was found to be most critical in shear stress, and the M.S. of +0.02 was achieved with factor of safety of 1.5. Figure 88 shows the shear stress distribution in pylon skin with critical region boxed. Figure 89 shows an enlarged view of critical region with critical element highlighted, and Figure 90 shows the critical element and ply ID with its critical shear stress from the .f06 file.

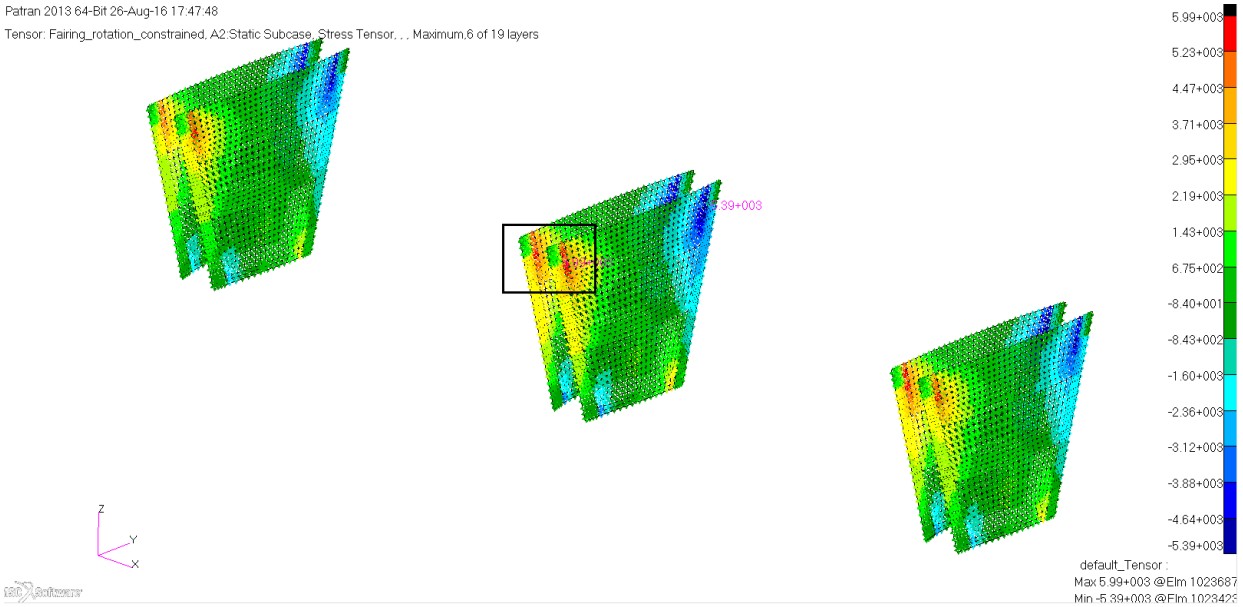


**Figure 88: Pylon skin shear stress distribution**

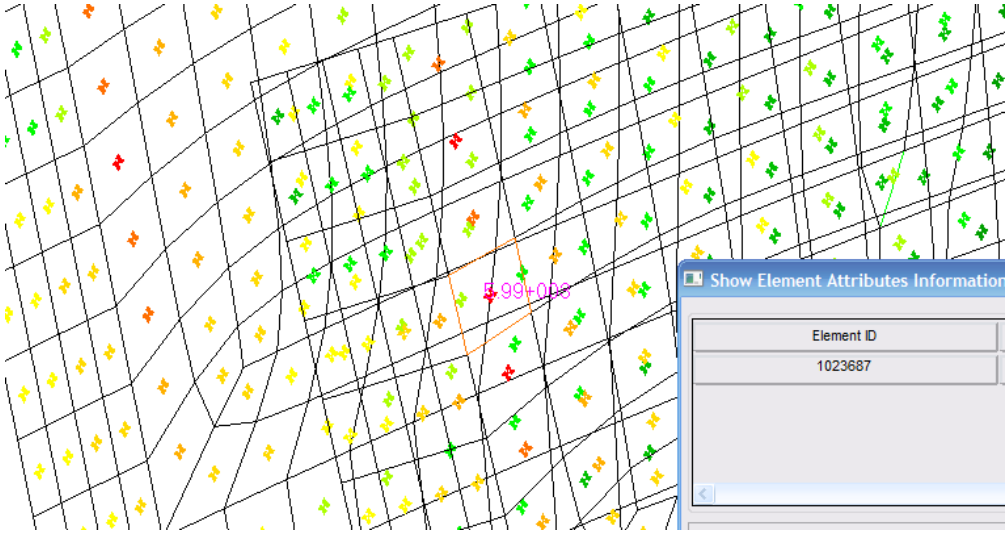


**Figure 89: Enlarged view of the critical shear stress region**

S T R E S S E S  I N  L A Y E R E D  C O M P O S I T E  E L E M E N T S  ( Q U A D 4 )

| | ELEMENT ID | PLY ID | STRESSES IN FIBER AND MATRIX DIRECTIONS NORMAL-1 | NORMAL-2 | SHEAR-12 | INTER-LAMINAR STRESSES SHEAR XZ-MAT | SHEAR YZ-MAT | PRINCIPAL STRESSES (ZERO SHEAR) ANGLE | MAJOR | MINOR | MAX SHEAR |
|---|---|---|---|---|---|---|---|---|---|---|---|
| 0 | 1023685 | 5 | -6.59630E+02 | -2.13262E+03 | 5.16883E+03 | -1.67057E+00 | 2.29032E+00 | 40.95 | 3.82491E+03 | -6.61716E+03 | 5.22104E+03 |
| 0 | 1023685 | 6 | -5.60160E+02 | -2.15974E+03 | 5.15513E+03 | -8.95373E-01 | 1.22754E+00 | 40.59 | 3.85686E+03 | -6.57675E+03 | 5.21680E+03 |
| 0 | 1023685 | 7 | -4.60690E+02 | -2.18685E+03 | 5.14143E+03 | -1.32055E-14 | 1.88259E-14 | 40.24 | 3.88960E+03 | -6.53714E+03 | 5.21337E+03 |
| 0 | 1023686 | 1 | -2.48900E+03 | -1.26206E+03 | 4.86013E+03 | 2.55593E+00 | 7.37192E+00 | 48.60 | 3.02317E+03 | -6.77423E+03 | 4.89870E+03 |
| 0 | 1023686 | 2 | -2.44107E+03 | -1.37409E+03 | 4.87695E+03 | 4.76880E+00 | 1.37544E+01 | 48.12 | 2.99846E+03 | -6.81362E+03 | 4.90604E+03 |
| 0 | 1023686 | 3 | -2.39315E+03 | -1.48612E+03 | 4.89376E+03 | 6.63862E+00 | 1.91474E+01 | 47.65 | 2.97510E+03 | -6.85436E+03 | 4.91473E+03 |
| 0 | 1023686 | 4 | -1.42254E+01 | -1.43533E+01 | 3.81157E+01 | 6.63862E+00 | 1.91474E+01 | 44.95 | 2.38264E+01 | -5.24051E+01 | 3.81158E+01 |
| 0 | 1023686 | 5 | -1.87069E+03 | -2.70735E+03 | 5.07706E+03 | 4.76880E+00 | 1.37544E+01 | 42.64 | 2.80524E+03 | -7.38328E+03 | 5.09426E+03 |
| 0 | 1023686 | 6 | -1.82276E+03 | -2.81938E+03 | 5.09387E+03 | 2.55593E+00 | 7.37192E+00 | 42.21 | 2.79712E+03 | -7.43926E+03 | 5.11819E+03 |
| 0 | 1023686 | 7 | -1.77484E+03 | -2.93141E+03 | 5.11069E+03 | 3.76963E-14 | 1.13058E-13 | 41.77 | 2.79018E+03 | -7.49642E+03 | 5.14330E+03 |
| 0 | 1023687 | 1 | -3.07706E+03 | -1.61583E+03 | 5.51915E+03 | 1.74482E+00 | 1.24000E+01 | 48.77 | 3.22086E+03 | -7.91374E+03 | 5.56730E+03 |
| 0 | 1023687 | 2 | -3.35447E+03 | -1.78284E+03 | 5.55044E+03 | 3.25545E+00 | 2.31357E+01 | 49.03 | 3.03714E+03 | -8.17445E+03 | 5.60580E+03 |
| 0 | 1023687 | 3 | -3.63189E+03 | -1.94986E+03 | 5.58174E+03 | 4.53190E+00 | 3.22071E+01 | 49.28 | 2.85387E+03 | -8.43561E+03 | 5.64474E+03 |
| 0 | 1023687 | 4 | -2.92891E+01 | -2.43842E+01 | 4.39790E+01 | 4.53190E+00 | 3.22071E+01 | 46.60 | 1.72107E+01 | -7.08839E+01 | 4.40473E+01 |
| 0 | 1023687 | 5 | -6.65598E+03 | -3.77049E+03 | 5.92288E+03 | 3.25545E+00 | 2.31357E+01 | 51.84 | 8.82827E+02 | -1.13093E+04 | 6.09606E+03 |
| 0 | 1023687 | 6 | -6.93339E+03 | -3.93750E+03 | 5.95417E+03 | 1.74482E+00 | 1.24000E+01 | 52.06 | 7.04255E+02 | -1.15752E+04 | 6.13970E+03 |
| 0 | 1023687 | 7 | -7.21081E+03 | -4.10452E+03 | 5.98546E+03 | 2.57336E-14 | 1.90170E-13 | 52.27 | 5.26027E+02 | -1.18414E+04 | 6.18369E+03 |
| 0 | 1023688 | 1 | -4.88017E+03 | -4.68649E+02 | 5.24276E+03 | -6.79372E-01 | 9.36204E+00 | 56.41 | 3.01347E+03 | -8.36229E+03 | 5.68788E+03 |
| 0 | 1023688 | 2 | -4.91084E+03 | -5.08599E+02 | 5.21457E+03 | -1.26756E+00 | 1.74675E+01 | 56.44 | 2.95038E+03 | -8.36981E+03 | 5.66009E+03 |
| 0 | 1023688 | 3 | -4.94150E+03 | -5.48549E+02 | 5.18638E+03 | -1.76456E+00 | 2.43164E+01 | 56.48 | 2.88729E+03 | -8.37734E+03 | 5.63232E+03 |
| 0 | 1023688 | 4 | -2.43391E+01 | -1.45498E+01 | 3.84774E+01 | -1.76456E+00 | 2.43164E+01 | 48.62 | 1.93430E+01 | -5.82319E+01 | 3.87875E+01 |
| 0 | 1023688 | 5 | -5.27575E+03 | -9.84044E+02 | 4.87905E+03 | -1.26756E+00 | 1.74675E+01 | 56.87 | 2.20019E+03 | -8.45998E+03 | 5.33009E+03 |
| 0 | 1023688 | 6 | -5.30641E+03 | -1.02399E+03 | 4.85086E+03 | -6.79372E-01 | 9.36204E+00 | 56.91 | 2.13721E+03 | -8.46762E+03 | 5.30242E+03 |

**Figure 90: Pylon skin critical shear stress and an element ID from .f06 file**

The corresponding margin of safety for critical shear stress of pylon skin is computed as follow:

$$MS = \frac{\tau_{allowable}}{F.S.* \ \tau_{actual}} - 1 = \frac{9.2 \ ksi}{1.5 * 5.99 \ ksi} - 1 = +0.02$$

Summary of the critical load case, margin of safety (MS) and critical mode along with the weight added by each component of fairing-pylon structure is tabulated in the Table 31. It is found that the fairing structure is most critical in buckling in fairing skin, the pylon structure is most critical in shear in the pylon skin. The total weight added by the fairing and pylon structure is determined to be 38.4 lbs per wing.

**Table 31: Summary of the load cases**

| Component | Critical load Case | Margin of Safety (MS) | Critical Mode | Weight of the component per wing (lbs) |
|---|---|---|---|---|
| Fairing Skin | Case 4 | +0.06 | Buckling | 16.7 |
| Fairing Spar | Case 4 | +0.07 | Longitudinal Tension | 11.8 |
| Fairing Rib | Case 4 | +0.26 | Shear | 1.4 |
| Pylon Skin | Case 4 | +0.02 | Shear | 4.0 |
| Pylon Spar | Case 4 | +0.06 | Longitudinal Tension | 2.9 |
| Pylon Rib | Case 4 | +1.44 | Longitudinal Tension | 1.5 |
| **Total weight of the structure per wing (lbs)** | | | | **38.4** |

### 4.3.8. The Payload and Range Calculations

This section provides some insights on payload and range calculations of the systems studied in Section 4. Table 32**Error! Reference source not found.** shows the payload calculations for four different configurations. The first configuration is the original Meridian that carries 36 lbs of Vivaldi antennas with mounting structures and the original radar box which weighs 45 lbs. The second Meridian configuration is assumed to be flying with a new radar box, and considering the advances in RF technology, the weight of a new radar box is estimated to be 25 lbs. The Meridian system with Wing Design I and II are also assumed to carry the new radar box in addition to fixed weight (such as landing skiis, Cables/other associated electronics) and the modified antenna weight. Tail ballast weight is not added to the Wing Design II Meridian configuration, assuming additional substructure would move aircraft center of gravity backwards. The Meridian configuration with Wing Design I and II also considers the respective weight added due to modifications made for the antenna integrations. Table 33 compares the aircraft performance (range) of the systems using payload weights from Table 32. For the range calculations, the following parameters were assumed: SFC = 0.45 lbs/hp-hr [34], empty weight = 791 lbs, propeller efficiency = 0.8.

**Table 32: The payload calculation for different systems**

| **Component** | **Meridian with Vivaldi system** | **Meridian with (Vivaldi system) new radar box** | **Meridian with Wing Design I** | **Meridian with Wing Design II** |
|---|---|---|---|---|
| Landing skiis (lbs) | 55 | 55 | 55 | 55 |
| Radar box (lbs) | 45 | 25 | 25 | 25 |
| Cables/other associated electronics (lbs) | 19 | 19 | 19 | 19 |
| Tail ballast (lbs) | 10 | 10 | 10 | - |
| Weight added to wing (lbs) | - | - | 9.5 | 7.4 |
| Antenna weight (lbs) | 36 | 36 | 5.5 | 5.5 |
| Fairing-pylon weight (lbs) | - | - | - | 76.7 |
| **Total Payload weight (lbs)** | **165** | **145** | **124** | **188.6** |

In Table 33, the $W_{begin}$ and $W_{end}$ represents the weight of the Meridian before and after the flight respectively, and they were determined using the respective fuel and payload weights of these four configurations. After calculating respective Lift to Drag (L/D) ratio their range was found using Breguet range equation [36]. Since the Meridian configuration with Wing Design II

exceeded the maximum payload capacity of 165 lbs, a fuel weight of 23.4 lbs was assumed to be removed in exchange. The Meridian system with Wing Design I was considered the clean aircraft configuration as this system has embedded antenna array (with insignificant antenna weight) and adds no external drag to UAS (hence no assumed change in L/D ratio). The Meridian configuration with Wing Design I delivers maximum (clean) aircraft range of 990 nmi. Hence this clean design was used as a baseline to compare the aircraft range performances of these designs. The range of the original Meridian with Vivaldi antenna and the Meridian with new radar box were determined to be ~6% and ~4% lower than the new clean range, respectively. The range of these two systems were affected by the drag and weight of externally mounted Vivaldi antenna system. Similarly, the range of the Meridian with Wing Design II was determined to be 640.6 nmi and ~35% lower than clean range. The fairing-pylon substructure drastically degrades the Meridian range for Wing Design II configuration. The aircraft and electrical performances of Wing Design I and II are discussed further in the next section.

**Table 33: The aircraft performance (range) comparison**

| Type of system | Fuel weight, $W_f$, lbs | Payload weight, $W_p$, lbs | $W_{Begin}$, lbs | $W_{end}$, lbs | L/D | Range, nmi | Change in range, % |
|---|---|---|---|---|---|---|---|
| Meridian with Vivaldi system | 120 | 165 | 1076 | 956 | 13.65 | **932.5** | **-5.8** |
| Meridian with (Vivaldi system) new radar box | 120 | 145 | 1056 | 936 | 13.65 | **951.4** | **-3.9** |
| Meridian with Wing Design I | 120 | 124 | 1035 | 915 | 13.9 | **990** (clean) | **0** |
| Meridian with Wing Design II | 96.4 | 188.5 | 1076 | 979.5 | 11.8 | **640.6** | **-35.3** |

### 4.3.9. Summary of Designs

Two potential designs for integrating an antenna array were proposed and preliminary sizing was completed. Based on future system requirements and applications, one of these preliminary designs could be pursued. If an antenna needs to be embedded inside the wing bay for moderate aircraft and antenna performance improvement, Wing Design I approach is preferred. In this design approach, the wing-embedded eight-element dipole antenna array (without ground plane) achieves a peak gain of 9.5 dB at resonant frequencies between 200-210 MHz, with a bandwidth of 87 MHz. In this preliminary study, details of the wing were not addressed during structural analysis such as modification of the ribs to accommodate integrating array into lower wing skin, which will likely add weight to the projected estimate. Also internal wing components (cable, servos, etc.) were not included in antenna simulations which will likely degrade antenna performance to some extent. These details were left for future study. The extra weight added to the aircraft due to material modifications is estimated to be 9.5 lbs. This approach does not affect the clean aircraft range (990 nmi) significantly as there is no additional drag due to antennas, only

the added weight, and aircraft range is improved by ~6% (57.5 nmi) as compared to the aircraft range with original Vivaldi design integrated (932.5 nmi). However, for the embedded configuration the wing bay constrains the antenna size, hence selection of operating frequency for an antenna is limited. Also integration of ground plane inside wing becomes difficult for lower operating frequency, hence compromising the antenna performance (i.e. low gain compared to antenna with ground plane).

When antenna performance is the priority, the second design approach is recommended. In this approach, only antenna gain was optimized without considering its ramifications on aircraft performance. By integrating the antenna array below the wing and the using the wing skin as a ground plane, a gain improvement of almost 6 dB is achieved over the existing Vivaldi integrated configuration. In this design approach, the eight-element dipole antenna array (with ground plane) integrated below wing achieves a peak gain of 13.3 dB at a resonant frequency of about 180 MHz and has a bandwidth of 87 MHz. This design has better gain and radiation pattern, hence maximizing the antenna performance. However, this design adds significant weight and drag and decreases the aircraft range. The extra structural weight of the fairing was determined to be 76.8 lbs, and the weight added due to the additional composite material layers added to the wing is determined to be 7.4 lbs (total weight added 84.2 lbs). The fairings and pylons increase the wetted area of the aircraft, and increase the aircraft drag significantly (by 37.8 lbs). Due to this additional drag, the Meridian range is reduced to 640.6 nmi from 990 nmi (clean range)—a range reduction of 35.3% (349.4 nmi). Also comparing this range to the range with Vivaldi antenna integrated on the aircraft (932.5 nmi), the dipole array with ground plane (i.e. with fairing-pylon structure) would reduce aircraft range by 31.3% (292 nmi). In addition, the fairing-pylon structure will also increase the overall manufacturing cost. This design should only be considered in the exceptional cases, for particular mission (e.g. sounding deeper into ice up to 5 km) where antenna performance is of highest importance and aircraft performance is a secondary goal. These two wing design performances are compared in Table 34.

It is important to note that the designs presented herein are considered preliminary designs that were developed to provide insight for a future antenna design. Several design and analysis details have been left for future studies, but these details could significantly impact the performance of the system. In structural analysis of Wing Design I, ribs were not modified (so that ribs hop over the array) for array integration, which will change the load path for lower wing skin and add more weight, and these modifications are left for future detailed study. The wing is likely to flex more for an embedded design, the current array performances do not include the wing flexure effects. The wing flexure will cause deformation of the ground plane and degrade electrical performance of arrays, and it is likely that a compensation method would be required. Also, the antenna and array simulations have not included any internal wing components (such as servos, cables, etc.), which will likely result in electrical performance degradation. The Wing Design II study did not consider its effect on the aircraft dynamics and control, but the heavy substructure will shift the CG location and change the stability and control derivatives. The impact of the fairing on stability and control needs to be assessed further to confirm the validity of the design. Also, runway implications due to fairing-pylon substructure integration are not studied. The added weight and drag of the fairing will result in extended runway for take-off and landing, hence also need to be

investigated further, especially considering the remote field operations of the vehicle. Although the height of Vivaldi antenna and fairing-wing offset are about ~15 in, the tip strike angle will decrease (estimated to reduce by ~2°) for the Wing Design II configuration due to the extended fairing structure. Trade-offs between reducing the antenna offset from the wing and tip-strike angle should be investigated further in future study.

The two designs demonstrate the trade-off between aircraft structural and antenna performance (or electrical performance), as shown in Table 34. The first design approach improves the aircraft structural performance, and while the antenna performance is not optimized, it is an improvement over the Vivaldi design. The second design approach compromises the aircraft structural performance but delivers maximum antenna performance. Both designs require further detailed analysis, based on application and priority, one of these design could be pursued.

**Table 34: Summary of wing designs**

| Component | Wing Design I (Dipole array without GP) | Wing Design II (Dipole array with GP) |
|---|---|---|
| Four-element gain, dB | 6.5 | 10.34 |
| Four-element bandwidth, MHz | 88 | 83 |
| Four-element Beamwidth | ~25° | ~22° |
| Eight-element gain, dB | 9.5 | 13.3 |
| Eight -element bandwidth, MHz | 87 | 87 |
| Four-element Beamwidth | ~10° | ~10° |
| Added weight, lbs | 9.5 | 7.4 |
| Added drag, lbs | 0 | 37.8 |
| Expected range, nmi | 990 | 640.6 |

# 5. Sensor Driven Preliminary Wing-Sizing

## 5.1. Overview of Study Parameters

On the outset of developing the new antenna concept for the Meridian wing, it was expected that an optimal embedded design could be determined; however, considering the dimensional constraints of the wing and lower operating frequency of the antenna, two compromising designs were determined. From the antenna study of Section 4, it was understood that the ground plane has a key role in antenna performance, and this Meridian antenna design case study motivated the following study that will provide a baseline for sensor-driven preliminary wing design. This study will be a vital tool for future vehicle design, particularly for UAS as the purpose of these vehicles is to carry sensors. If UAS-installed sensors do not meet operating requirements, there is little value for operating the vehicle.

This study shows how wing-integrated antenna gain and resonant frequency are affected by wing parameters such as span, chord, and thickness-to-chord ratio, assuming that the wing acts as a ground plane for the sensor. It is noted that the relationships derived in this section are for the ground plane (conductive) portion of the wing. If the wing is not fully conductive, the relationships will need to be modified appropriately. These wing ground plane parameters are studied at four different resonating frequencies—100 MHz, 200 MHz, 1 GHz, and 2 GHz, to ensure trends obtained are independent of frequency. The varying wing ground plane parameters are expressed as a percentage of wavelength for easy comparison of the results, and to demonstrate that the results are in fact frequency agnostic. Parametric analyses were completed using ANSYS HFSS [21] software, and with over 400 simulations the relationships between the wing ground plane parameters and antenna performance were determined. The half-wavelength dipole antenna was used as the candidate antenna for this study due to its low profile features and basic design. Therefore, the findings of this section are applicable to dipole antennas (half wavelength) only. Figure 91 shows a schematic of the planar dipole. In the beginning of the study, four antennas were tuned to the operating frequency by varying the arm length, and a ground plane that extended by one wavelength (λ) from each side of dipole antenna was created at a quarter-wavelength offset (0.25λ). The widths of the dipoles were maintained at a constant 5% of the wavelength (λ) for all operating frequencies, and due to the width and ground plane, the antennas typically resonated at a total length of 0.41λ rather than 0.5λ.

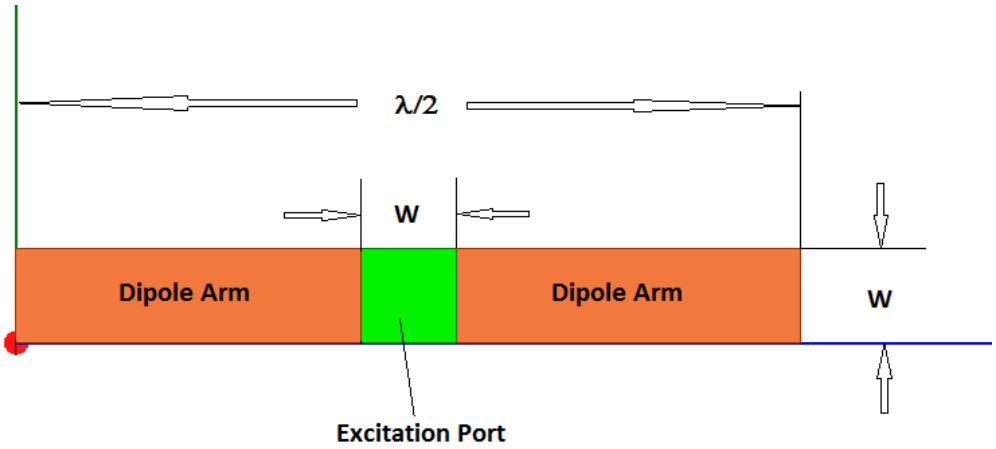


**Figure 91: Schematics of planar Dipole antenna**

## 5.2. Wing Ground Plane Span Study

In this section, the effects of wing ground plane span on antenna performance were studied. A dipole antenna was simulated with a ground plane representing a metallic wing skin offset from the antenna—representing either the upper wing skin acting as the ground plane for an antenna embedded in lower skin, or the lower wing acting as a ground plane by mounting an antenna at a specific offset from the wing. Then a parametric analysis was conducted by varying the spanwise length of the ground plane. Figure 92 shows the parameters used to define the parametric simulations. Initially, the spanwise length of the ground plane was set to L+0.1λ, then the distance from the edge of the antenna to the edge of the ground plane, d, was stepped from 5-100% of the resonant wavelength, λ, by the step size of 0.05λ. The chordwise width of the ground plane was kept constant at a total width of (W+2λ), where W is the width of an antenna which is assumed to be equal to 10% of wavelength for better return loss properties. Also, an offset distance of λ/4 was maintained between the ground plane and the antenna, as shown in Figure 93. From well-known antenna theory [35], the forward-radiated field and reflected field will add constructively at λ/4 ground plane spacing.

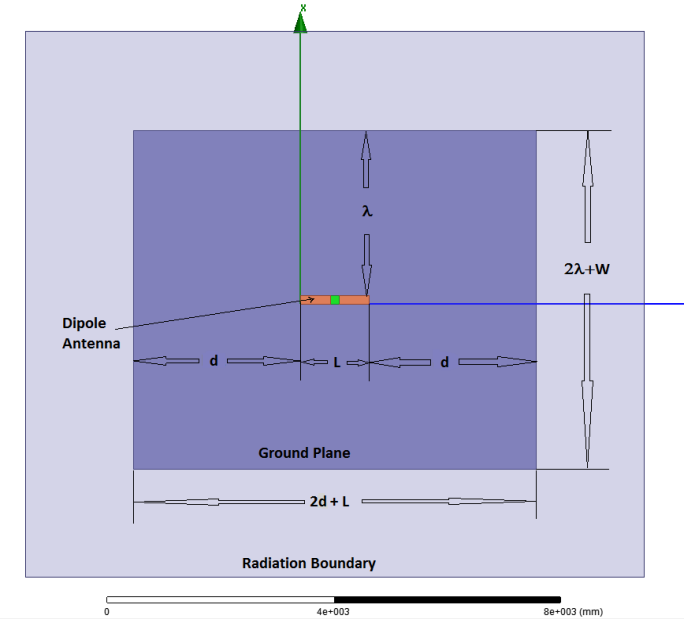


**Figure 92: Geometric definitions for the wing span study.**

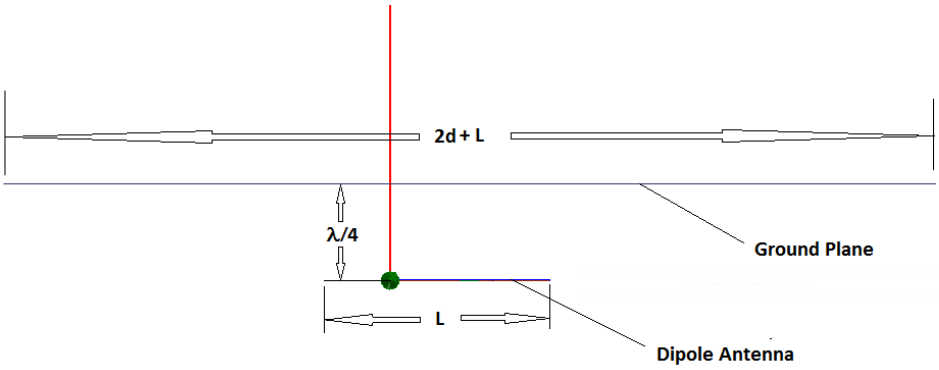


**Figure 93: Ground plane offset defined for the wing span study.**

From the parametric analysis, frequency shift and realized gain at nadir are plotted against the ground plane length extension parameter, d, on the two y-axes plot, as shown in Figure 94, for the four desired operating frequencies. The frequency shift, $f_0$, is defined in Eq. (1), where $f_d$ is resonant frequency for corresponding d, and f is the original specified operating frequency.

$$f_0 = \frac{(f_d - f)}{f} * 100 \tag{1}$$

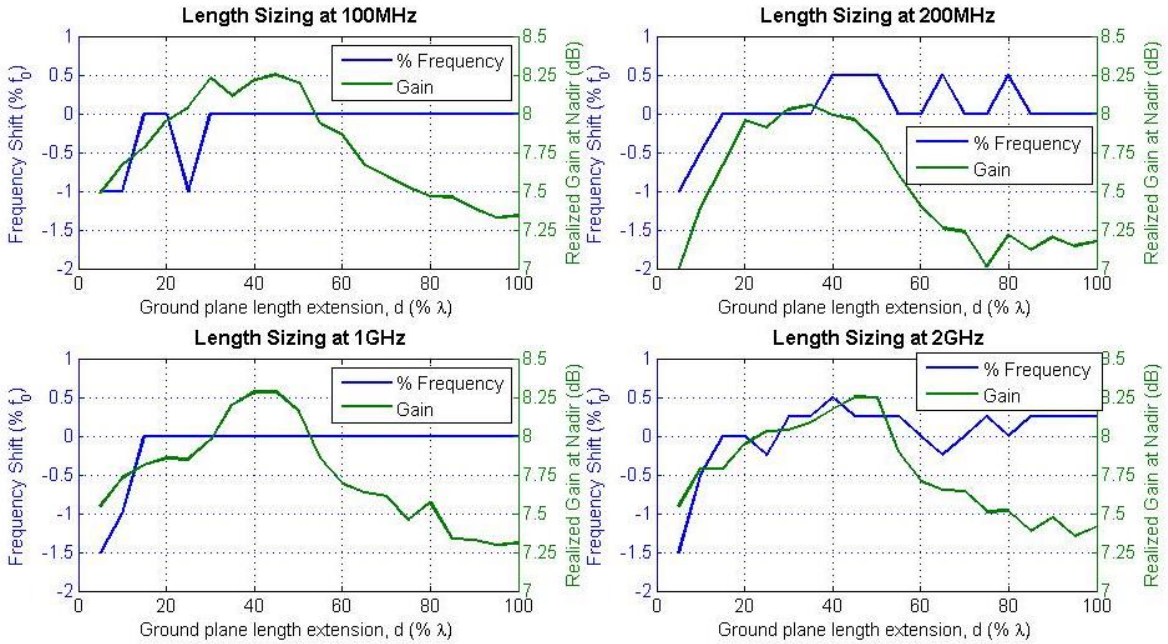


**Figure 94: Ground plane length extension vs frequency shift and realized gain at nadir plot for all operating frequencies.**

From Figure 94, it can be concluded that when d is greater than 15% of its respective wavelength, the antenna typically resonates within ±0.5% of the corresponding operating frequency. Also it is noticed that maximum gain was typically achieved when d was ~0.5λ, and to achieve gain within 0.5 dB of the maximum gain the ground plane length extension should be kept within 0.10-0.60 λ.

It can be seen from Figure 94 that the realized gain at nadir begins to decrease after 0.5λ, hence the simulation for 100 MHz was extended to 5λ to examine the trends at a much larger scale. Figure 95 shows the simulation results for an extended ground plane length, and as the plot shows a local maximum gain is achieved when the length extension parameter, d, is at 50%, 137.5%, 262.5%, and 375% of the wavelength. It is also noticed that the magnitude of the local maximum gain decreases as d increases. It can be concluded that when d is about 50% of the wavelength, maximum gain without any frequency shift is achieved.

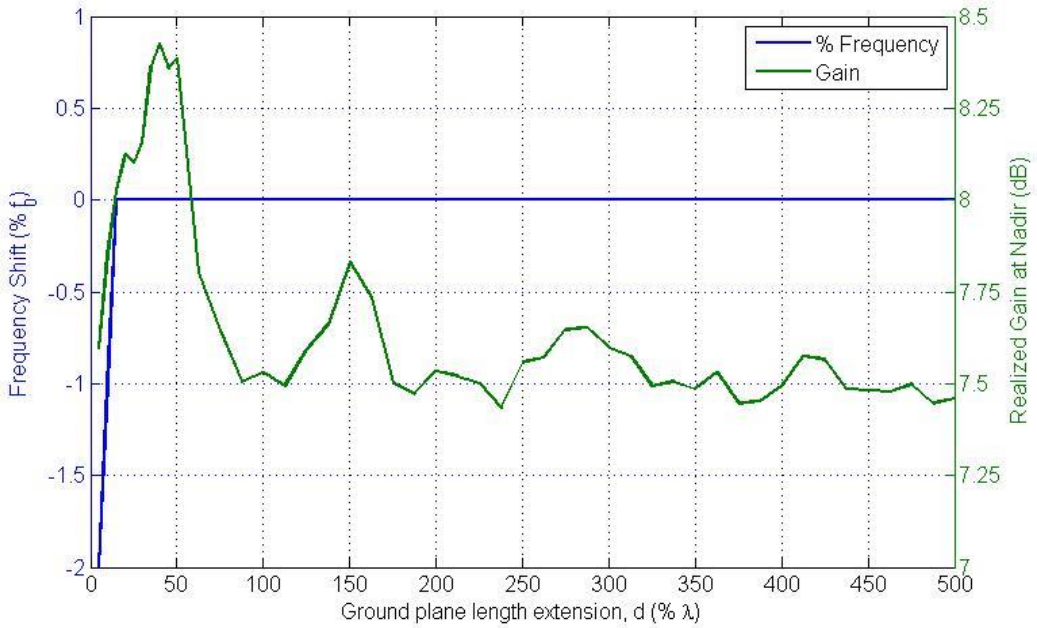


**Figure 95: Ground plane length extension up to 5λ vs frequency shift and realized gain at nadir plot at 100 MHz.**

To summarize the results obtained from the ground plane sizing study, a relationship between the antenna performance and aircraft wing sizing was developed to suggest a span size that will maximize antenna performance. Again it is noted that this relationship assumes the entire wing planform is acting as a ground plane. This relationship should be modified for 'b' if this is not the case. It was found that when d is ~0.5λ maximum gain is achieved. Although Figure 95 shows that other values of d can produce local maximum gain, since these values are much larger than 0.5λ, it would be suggested to add more antenna elements to increase total array gain rather than extend the ground plane unnecessarily. Therefore, the ground plane span relationship was determined using the minimum ideal value of d. From antenna array theory, ideal element center-to-center spacing is λ/2 [34]. Using the ideal element spacing, ideal ground plane extension length of 0.5λ that was found from the plots in Figure 94, and an antenna length of 0.5λ, a relationship for determining the ideal wing span can be derived. Assuming a fuselage diameter, F, the wing ground plane span, b, suggested for an n-element array is given by Eq. (2).

$$b = F + (n + 2)\lambda \tag{2}$$

A schematic of the geometry associated with Eq. (2) for a three dipole element array is shown in Figure 96. For any desired operating frequency, a given number of dipole elements in the array, and an approximate fuselage width, an ideal span can be determined from Eq. (2). During the preliminary sizing of the wing, this equation could be used after locating a wing-loading and power-loading design point, as described in [36]. It is noted that the gain sensitivity to the ground plane length is on the order of 0.75 dB, which is a relatively small change in the antenna performance and is likely due to the orientation of the pattern nulls directed along this axis and/or larger initial ground plane length. It can be shown in the following sections that antenna performance is much more sensitive to other wing geometric parameters.

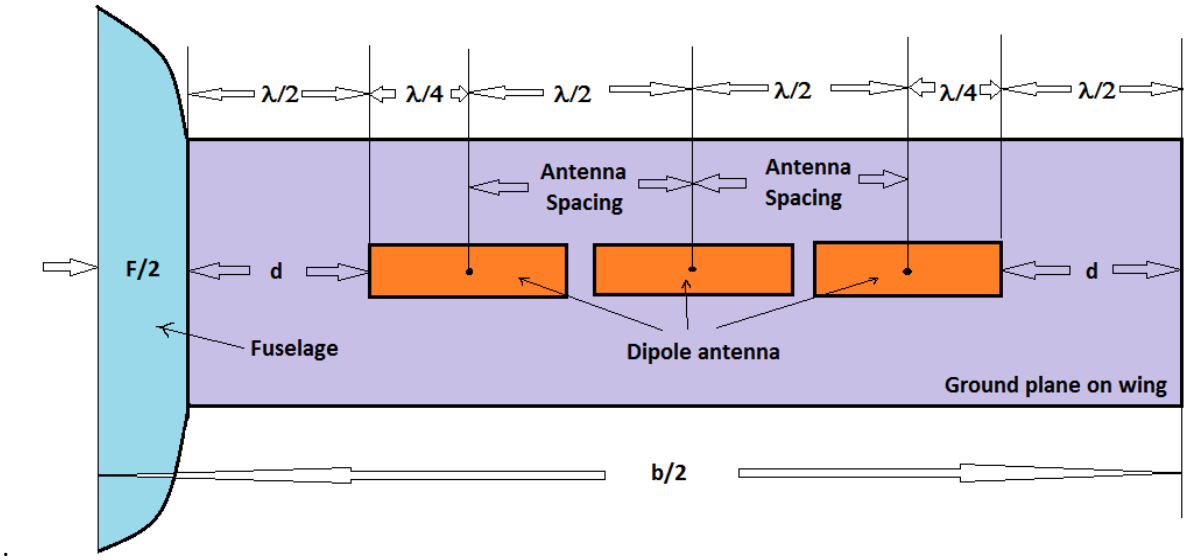


**Figure 96: Geometric definition for wing (ground plane) length calculation.**

## 5.3. Wing Ground Plane Chord Study

For the wing chord study, the antenna-ground plane offset (λ/4) and the length of the ground plane (L+2λ) was maintained while the ground plane width extension parameter was varied. Initially the width of the ground plane was set to be equal to the width of the antenna plus 0.05λ on either side of the antenna (W+0.1λ). The ground plane width extension, d, was then varied up to one wavelength with increments of 0.05λ. The geometry associated with the chord sizing study is shown in Figure 97 and Figure 98.

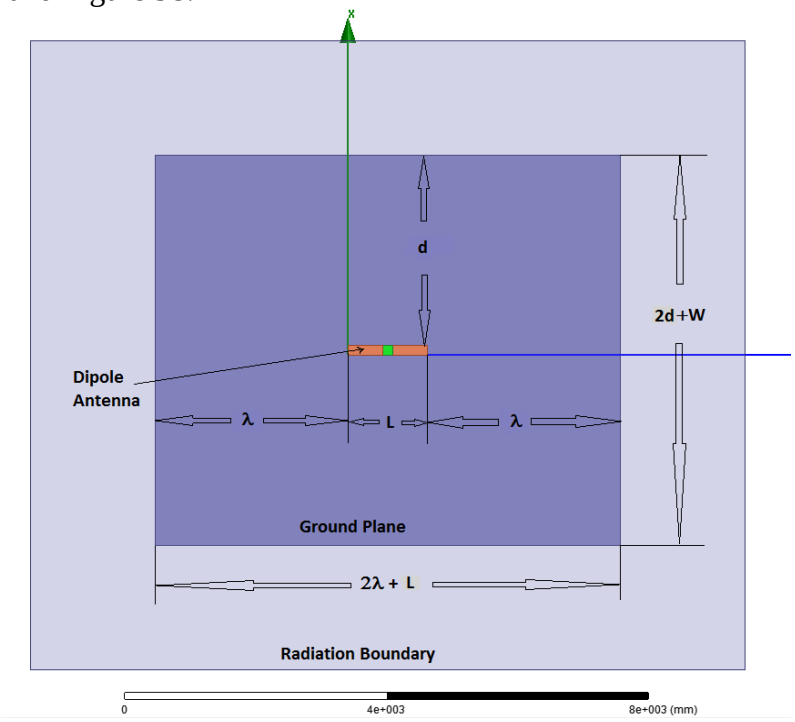


**Figure 97: Simulation setup defined for the wing chord study.**

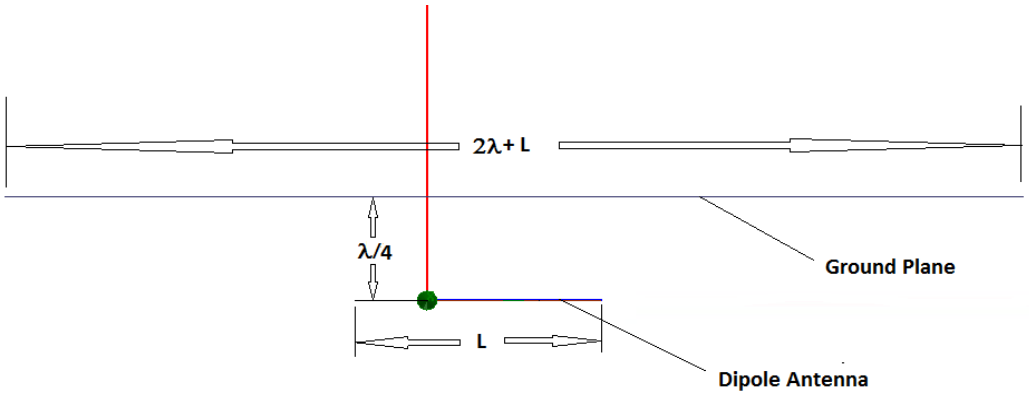


**Figure 98: Ground plane offset defined for the wing chord study.**

The frequency shifts and realized gain at nadir of the antennas are plotted against ground plane width extension d in Figure 65. It can be concluded that when the d is greater than 0.2λ, the antenna typically has no frequency shift. It can also be concluded that when d is about 0.5λ, the maximum gain is obtained while resonating at the desired operating frequency. When the ground plane extension is greater than 25% of a wavelength, the difference from maximum gain value is found to be less than 1 dB.

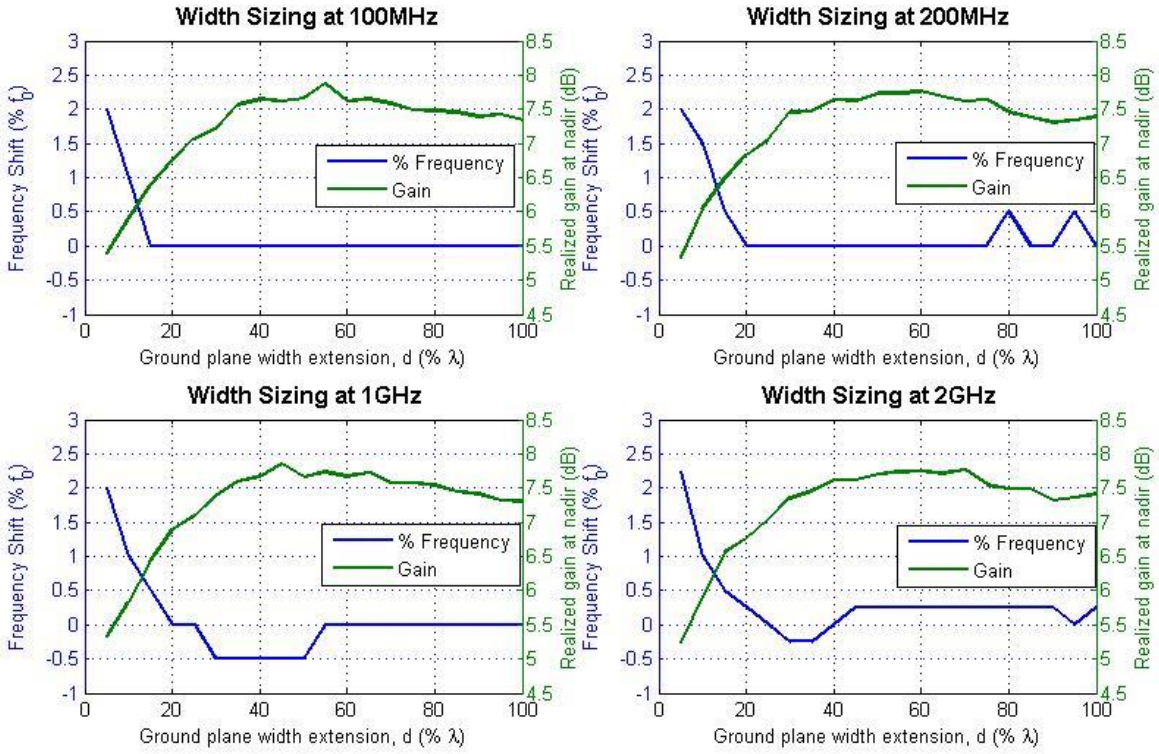


**Figure 99: Ground plane width extension parameter (d) vs frequency shift and realized gain at nadir plot for all operating frequencies.**

The chord of a ground plane, c, that optimizes the antenna performance can be found from Figure 99. Assuming a fully conductive center chord, the ideal chord is found by setting the ground plane width extension parameter to half the wavelength (i.e. d=0.5λ). In addition, the area of the wing chord occupied by control surfaces (ailerons), high lift devices (flaps) and leading edge was omitted from the effective ground plane as moving control surfaces and/or high lift devices will affect the antenna radiation pattern. Also the leading edge surface ahead of a front spar is typically curved, which will affect its effectiveness. The control surface span is typically about 30% of the wing chord [36], and the leading edge surface is assumed to be 20% of the wing chord, as shown in Figure 100. The ideal ground plane chord length, c, required for optimum dipole array performance in terms of antenna wavelength, λ, and antenna width, W, is derived in the Eq. (3).

$$c = 0.2c + 0.3c + 2 * \frac{\lambda}{2} + W \tag{3}$$

Rewriting the ground plane chord length (c),

$$c = 2(\lambda + W) \tag{4}$$

The geometry associated with Eqs. (3) and Eqs. (4), for a three dipole element array is shown in Figure 100. From Figure 99, a minimum ground plane width extension of d=0.25λ is recommended to achieve gain within 1 dB of the maximum value. Thus the recommended minimum chord size is given by the Eq. (5).

$$c_{min} = 2\left(\frac{\lambda}{2} + W\right) \tag{5}$$

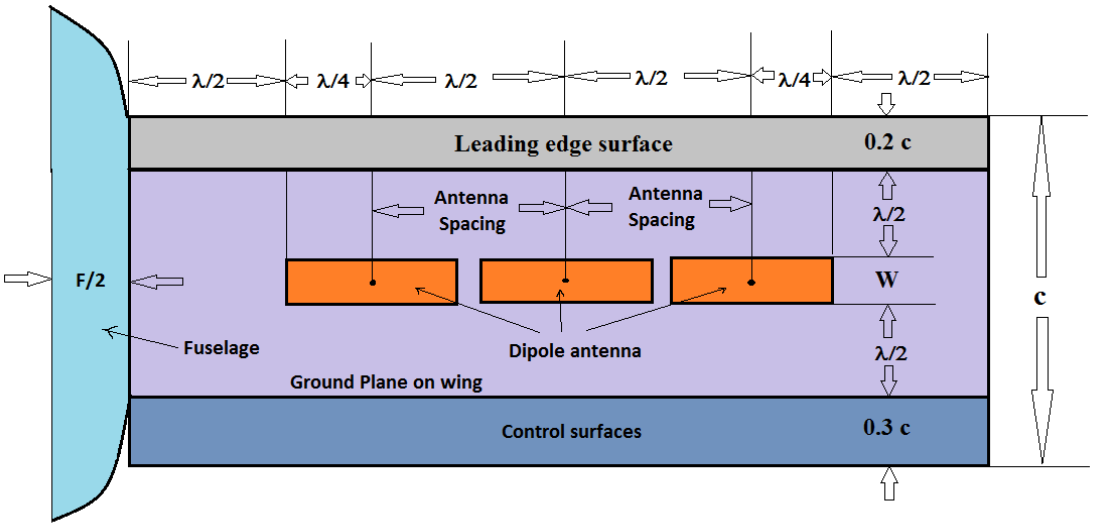


**Figure 100: Wing chord geometry associated with Eq. (3) and Eq. (4).**

After determining the wing-loading and power-loading design point, Eq. (4) and (5) can be used to estimate the wing chord. Similarly, an ideal range of ground plane aspect ratios could be determined from Eq. (2) and Eq. (4). From Figure 94 and Figure 99 it can also be seen that the antenna gain is more sensitive to the ground plane width than the length, which again is likely due to the orientation of the pattern nulls or due to the higher length to width ratio. While determining the ground plane aspect ratio this sensitivity should be observed.

## 5.4. Wing Ground Plane Height Study

For the wing height study, the ground plane length was set to (2λ+L), and ground plane width was set to (2λ+W), to eliminate the ground plane edge effects and to isolate the effect of the offset. The offset distance, h, between the antenna and the ground plane is then varied from 5 to 50 % of a wavelength (λ). A schematic of the design used for the ground plane offset study is shown in Figure 101 and Figure 102.

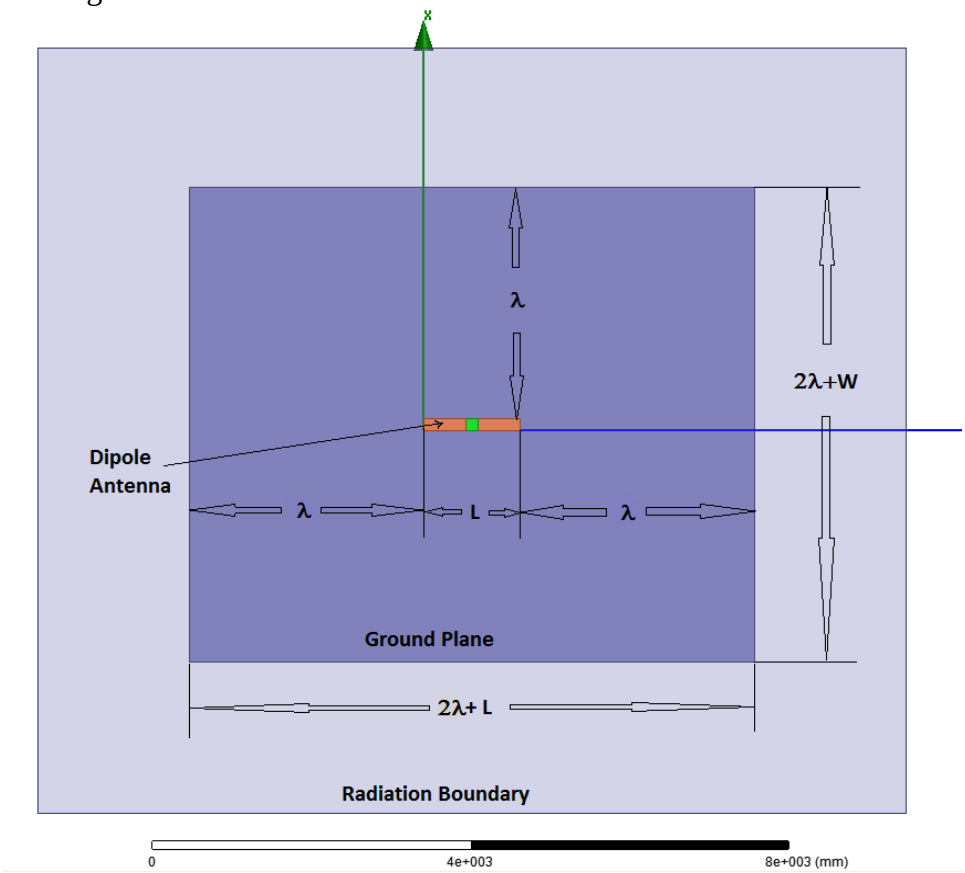


**Figure 101: Simulation setup defined for the wing height study**

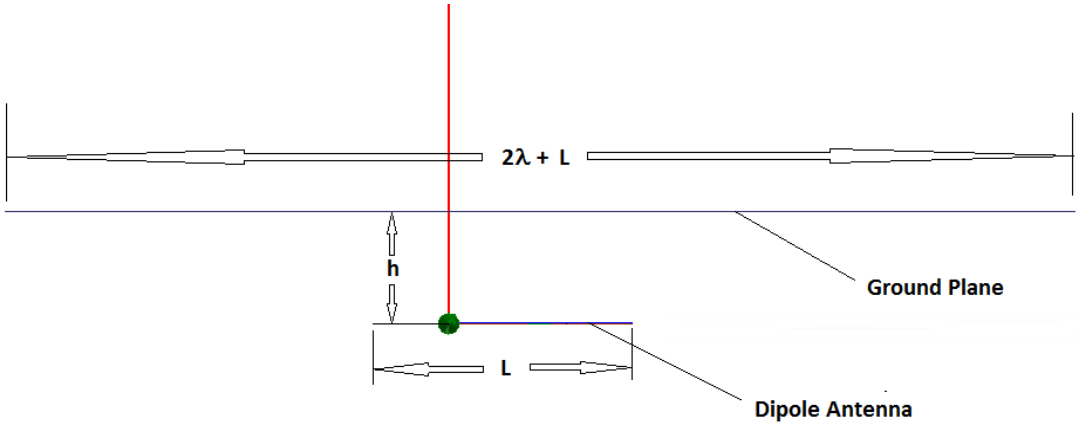


**Figure 102: Ground plane offset defined for the wing offset study.**

The frequency shift, $f_0$, is given by Eq. (1), and it is plotted against ground plane offset distance, h, as shown in Figure 103. From this plot it can be seen that the antenna resonates at the desired operating frequency when antenna-ground plane offset is within the range of 20-25% of wavelength. The gain of the dipole antennas at nadir is plotted against the ground plane offset in Figure 104, as well as the azimuth angle of maximum gain. This plot helps illustrate the change in the shape of the antenna radiation pattern as the maximum gain shifts from nadir to angles off nadir (i.e. resulting in a scalloped pattern) and back again.

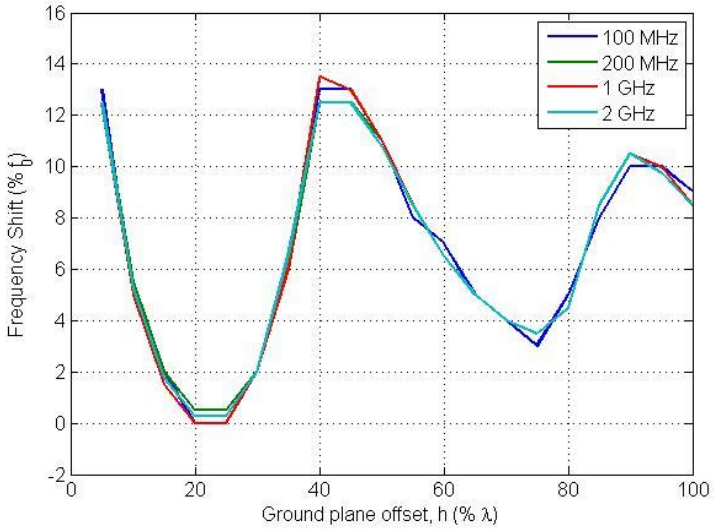


**Figure 103: Frequency shift vs ground plane offset, h (%λ)**

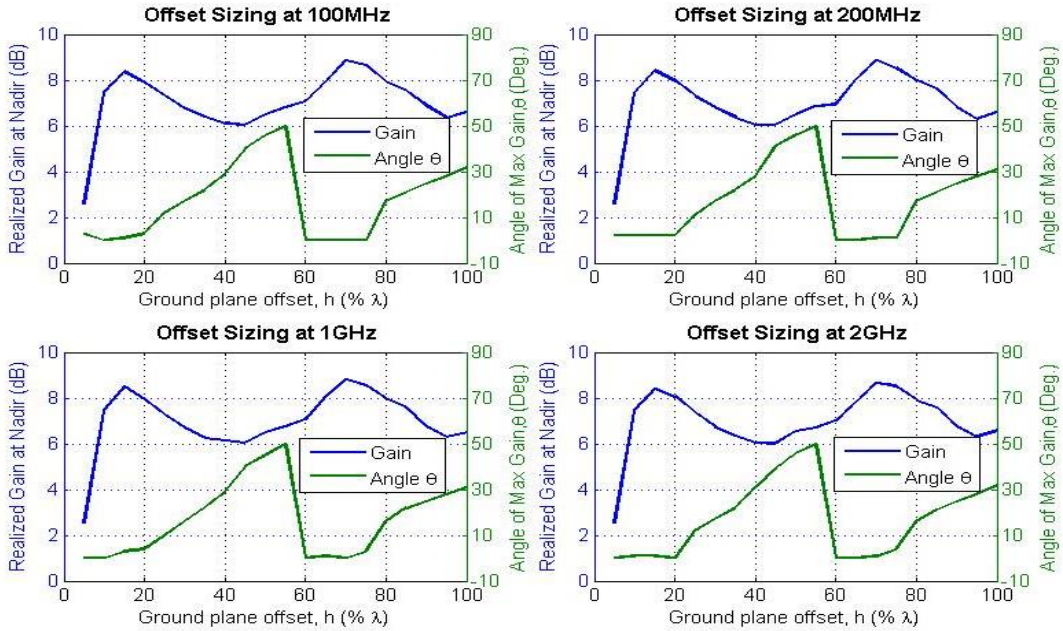


**Figure 104: Ground plane offset (h) vs realized gain at nadir and angle of max gain plot for all operating frequencies.**

From Figure 104, it can be concluded that to maximize gain at nadir an antenna-ground plane offset of 0.15λ is required. This is a somewhat surprising result as the antenna theory suggests that ideal antenna-ground plane spacing is 0.25λ. The ground plane offset range was extended up to two wavelengths to further study the antenna performance with respect to offset. Figure 105 shows the relationship between the realized gain at nadir and ground plane offset, from which it can be concluded that when the offset distance is about 15%, 70%, 125%, 175% of a wavelength, a local maximum gain at nadir can be achieved. When the ground plane offset represents the thickness of the airfoil (dipole antennas could be embedded into the lower wing skin or externally at an offset to the antenna), it is typically necessary to keep the offset, h, as small as possible. This way dipole array would need thinner airfoil section or smaller substructure, either way the smaller offset saves overall weight. Hence it is recommended that the minimum antenna-ground plane offset should be maintained at 15% of wavelength (λ), as given by Eq. (6).

$$h_{min} = 0.15\lambda \tag{6}$$

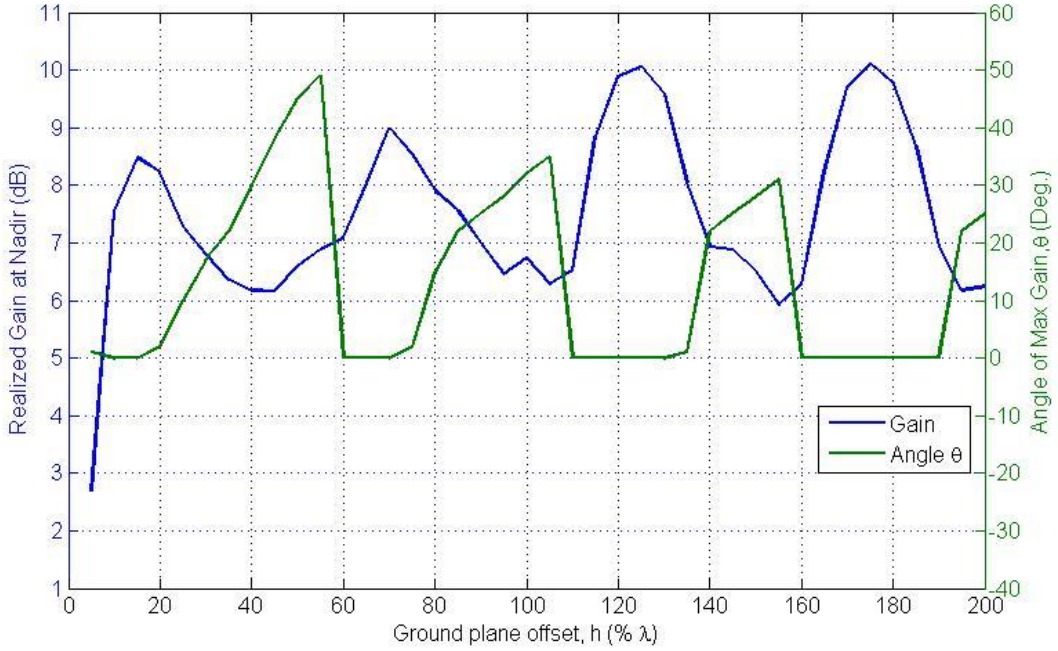


**Figure 105: Ground plane offset up to 2 wavelength vs realized gain at nadir and angle of maximum gain for all operating frequencies.**

To determine the antenna performance sensitivity to simultaneous changes in ground plane offset and ground plane width, a parametric analysis of 224 simulations was performed. In this parametric analysis, the ground plane offset was varied from 0.05-1λ and the ground plane width extension was varied from 0.10-1λ for operating frequency of 100 MHz. Figure 106 shows the 3D plot where the maximum gain is plotted against the ground plane width and antenna-ground plane offset. From Figure 105 and Figure 106 it can be noticed that the ground plane-antenna offset should be kept within 10-25% of the wavelength or 65-80% of the wavelength, for the gain to be within 1 dB of the local maximum gain. From Figure 106, it can be seen that this relationship holds

true for all ground plane width extensions analyzed. From this observation, it could be concluded that a dipole antenna array could be embedded in the lower wing skin and the upper skin could be used as a ground plane, so long as 0.5C~λ. This is based on airfoil t/c ratios typically being on the order of 8-25%.

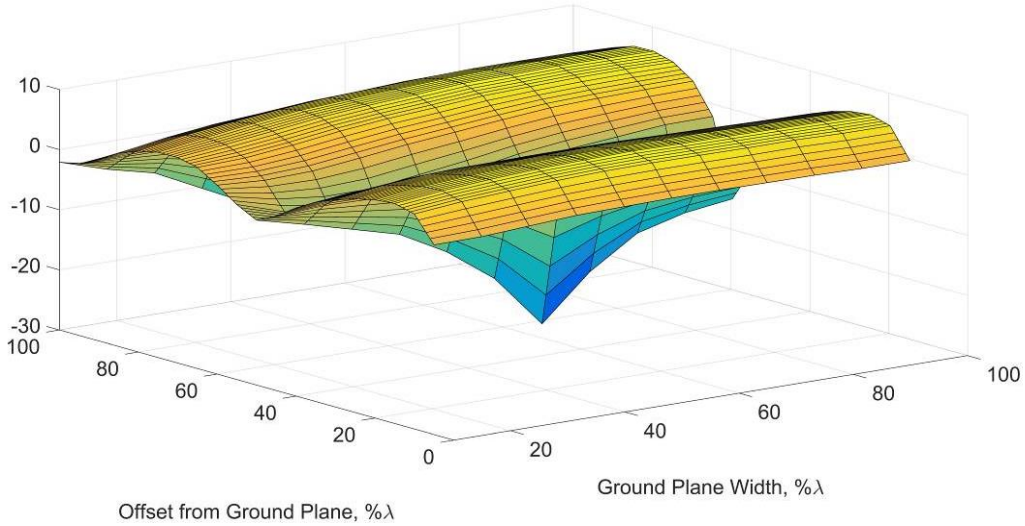


**Figure 106: 3D plot showing gain relationship to ground plane width and offset.**

## 5.5. Application of Sensor Study

To verify the trends obtained for the ground plane effect on antenna performance in the presence of coupling, a four element array composed of the modified dipole antenna described in Section 3 and a ground plane of varying size was simulated using HFSS. In Section 3.1.2, it was determined that the modified dipole antenna with ground plane resonates at a frequency of 175 MHz. The array of four modified dipole antenna elements has an element spacing of 31.2" (792.5 mm), similar to that shown in Figure 96.

### 5.5.1. Wing Span Trend Comparison

Initially, the spanwise length of the ground plane was set to 4L (~124 in), then this ground plane length was extended on either side by the following values of d (Figure 96): 15%, 50% and 75% of the resonant wavelength. The chordwise width of the ground plane was kept constant at W+λ (73 in) for optimal array performance as concluded in Section 5.2. An offset distance of λ/4 (16.9 in) was maintained between the ground plane and the dipole array. A parametric analysis was performed and the normalized gain (normalized to its corresponding maximum gain) was plotted for both array and the single antenna results from Section 5.2 for comparison in Figure 107.

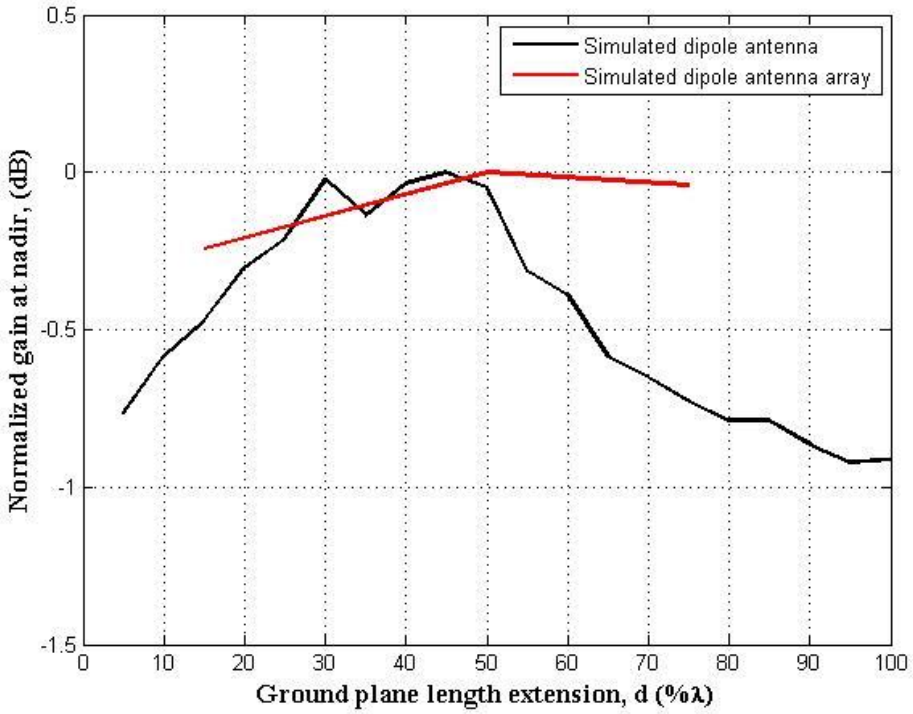


**Figure 107: Comparing the ground plane length extension vs normalized gain at nadir plots of simulated dipole antenna and simulated dipole antenna array**

While the normalized gain trend for the array in Figure 107 does not follow the exact trend of the single element, the maximum gain does occur when the extension, d, is ~0.5λ, as was found for the single element. Also similar to the single element results, the array gain is not very sensitive to the length extension parameter, which is obvious by a gain variation of less than 0.25 dB. The single element gain variation was on the order of ±0.5 dB, and it is not surprising that the array was even less sensitive to the length extension as largely only the end elements are being effected.

The level of similarity between the individual element and array results was actually a surprising find. Little mismatch between trends can be noticed, the reason might be that the ground plane design equations do not consider the cross-coupling between the elements, and it was expected that the results would be different. Also, only end elements of the array are affected due to ground plane length extension, hence array performance seems to be less affected. The fact that the individual dipole element results and the dipole array results agree so well, speaks toward the robustness of the derived equations and greatly extends their use.

### 5.5.2. Wing Chord Trend Comparison

For the wing chord study, the antenna-ground plane offset was set to be λ/4 (16.9 in), and the length of the ground plane was set to be 4L+λ (~192 in) (i.e. ground plane on either side of an array is extended by d = 0.5λ). Both parameters were kept constant while only the wing chord extension parameter was varied. Initially, the width of the ground plane was set equal to that of the antenna width (W = 5.51”), then the ground plane width extension parameter was set to 5%, 25%, 50% and 90% of the resonating wavelength, for the parametric analysis. The results for the

normalized gain of the array are plotted against d along with the results for the single element found in Section 5.3 in Figure 108.

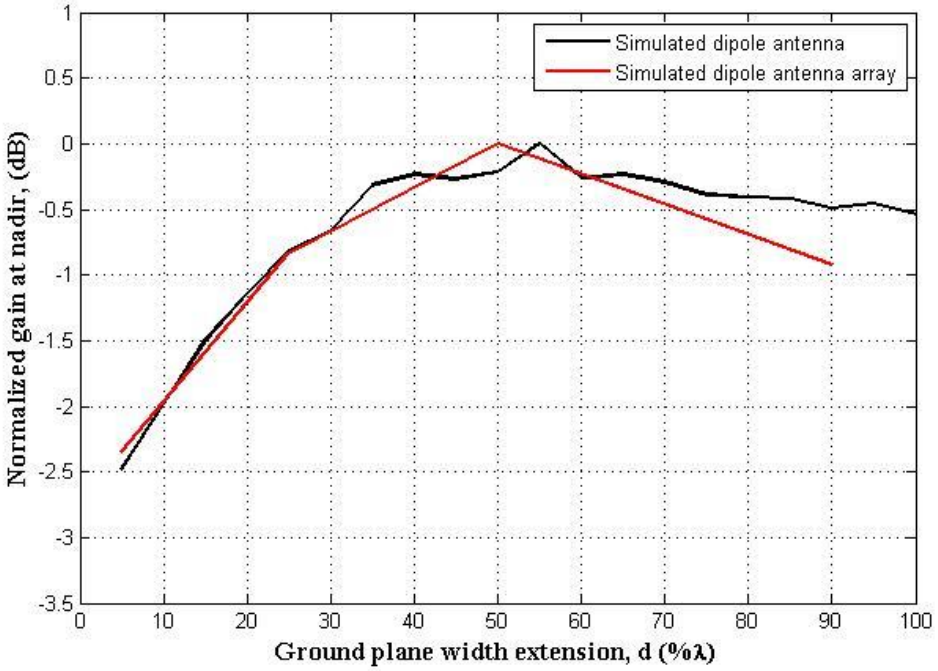


**Figure 108: Comparing the ground plane width extension vs normalized gain at nadir plots of simulated dipole antenna and simulated dipole antenna array**

From Figure 108 it can be seen that both the array and single element have very similar trends. More importantly when d is about 50% of the wavelength, the maximum gain at nadir is achieved which confirms the relation found for the estimation of wing chord in Eq. (4) is valid. The dipole array trend almost matches with single dipole antenna trend for ground plane width extension, whereas for ground plane length extension, these trends do not match well. In this case all the antenna elements are affected by the variation in the width extension. It can be noted that for the trends match well despite the existence of the coupling and proves that the derived equations are robust and valid.

### 5.5.3. Wing Offset Trend Comparison

In this study, the ground plane length was set to 4L+λ (~192 in) and the ground plane width was set to W+λ (73 in). For this study, the offset distance, h (Figure 102), between the antenna array and the ground plane was set to 5%, 10%, 15% and 30% of the resonating wavelength. From this parametric analysis, the trend for the simulated dipole antenna array is found where the normalized gain at nadir is plotted against the ground plane offset parameter (h), along with the similar trend found for the simulated dipole antenna from Section 5.4, as shown in Figure 109.

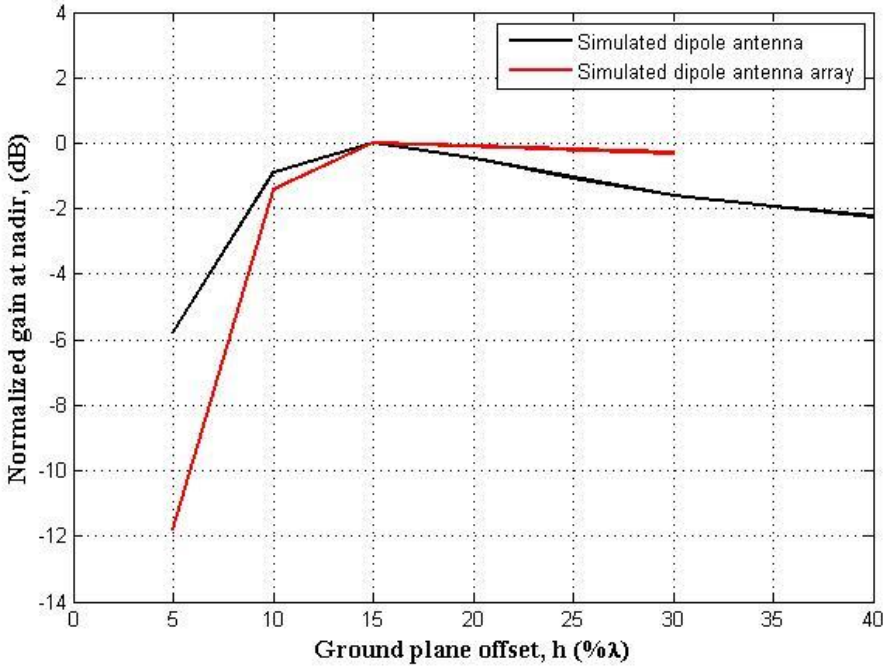


**Figure 109: Comparing the ground plane offset vs normalized gain at nadir plots of simulated dipole antenna and simulated dipole antenna array**

From Figure 109, it can be concluded that both trends are similar; optimal antenna array performance is achieved when the antenna-ground plane offset is about 15% of its resonating wavelength. The variation seen in the trends is likely caused by the cross-coupling between the antenna elements and also this offset variation affects the performance of all dipole elements hence degrading the overall array performance. However this study provides similar trend which validates relation given for the minimum offset distance by Eq. 6.

At the end of this study, to view the antenna array sensitivity to ground plane offset and width, a parametric analysis of 16 simulations was performed, where the ground plane width extension was set to 5%, 25%, 50% and 90% of resonating wavelength, and the ground plane offset was set to 5%, 10%, 15% and 30% of the resonating wavelength. The ground plane length was kept constant at 4L+λ (~192 in). The trends obtained from the parametric analysis were plotted in Figure 110, where it can be noticed that the realized gain at nadir increases significantly with ground plane offset, meaning the ground plane offset is the most sensitive parameter. From Figure 110 it can be concluded that the ground plane offset of 15% of wavelength, the ground plane width and length extension of 50% wavelength, results in the maximum realized gain for a dipole antenna array, which confirms that all the relations found in Section 5.2, 5.3 and 5.4, for the wing span, wing chord and wing height, are valid and reasonable.

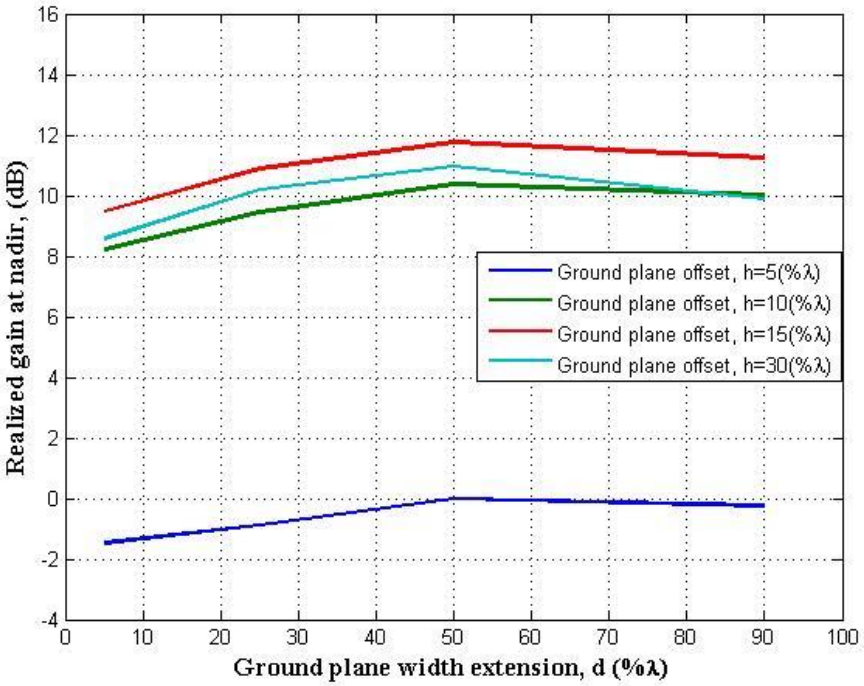


**Figure 110: Comparing the ground plane width extension vs realized gain at nadir plots at different ground plane offsets for simulated dipole antenna array**

# 6. Conclusions and Recommendations

## 6.1. Conclusions

For an existing remote sensing platform, two antenna array designs were developed and proposed. One of the designs consisted of an embedded dipole antenna array and required the material of the wing to be a low-loss dielectric. The second design consisted of an antenna array externally-mounted to the original (but slightly modified) carbon fiber wing. The following conclusions are made about these designs:

1) For a wing-embedded antenna array design, it is required for the wing materials to largely be limited to low-loss dielectric materials. When major wing components are made up of material with low dielectric constants (such as fiberglass), a dipole antenna array could be embedded into the lower wing skin. This design offers both improved electrical (~2.5dB increase in gain) and vehicle performance (~6% increase in range) over the Vivaldi design, but the antenna array is only expected to radiate half of the power in the nadir direction as compared to the dipole array with a ground plane.
2) The dipole antenna array with a ground plane offers almost 6 dB greater element gain over the Vivaldi design. However, this superior electrical performance comes at the expense of about 31% of aircraft range. Since the ratio of the received power to the transmitted power is proportional to square of the gain (by the Friis equation); for an antenna acting as a transmitter and receiver, the gain is doubled (i.e. about 12 dB improvement in total received power) in decibel (dB) scale. Hence a ground plane significantly optimizes the array performance, while it severely compromises aircraft performance. For any future development of an improved MCoRDS system for Meridian, it is necessary to work with radar and data processing engineers to better understand whether this tradeoff between electrical and aircraft performance is really necessary.

The above conclusions are based on a preliminary design analysis, and detailed design studies are necessary to better estimate the expected realized system performance. In the structural analysis of Wing Design I, ribs were not modified (so that ribs hopped over the array) for array integration, which will change the load path for lower wing skin and add more weight. These modifications are left for future detailed studies. The wing is likely to flex more with an embedded design, but the current array performances do not include the wing flexure effects. The wing flexure will cause deformation of the ground plane and degrade electrical performance of arrays, and it is likely that a compensation method would be required. Also, the antenna and array simulations have not included any internal wing components (such as servos, cables, etc.), which will likely result in electrical performance degradation. The Wing Design II study did not consider its effect on the aircraft dynamics and control, as the heavy substructure will shift the CG location and change the stability and control derivatives. The impact of the fairing on stability and control needs to be assessed further to confirm the validity of the design. Also, runway implications due to fairing-pylon substructure integration are not studied. The added weight and drag of the fairing will result in extended runways for take-off and landing, and hence needs to be investigated further, especially considering the remote field operations of the vehicle. Although the height of Vivaldi antenna and fairing-wing offset are about ~15 in, the tip strike angle will decrease (estimated to

reduce by ~2°) for the Wing Design II configuration due to the extended fairing structure. Trade-offs between reducing the antenna offset from the wing and tip-strike angle should be investigated further in future studies.

Keeping in mind the key role of a ground plane (i.e. lower wing skin) in array performance, a sensor-driven preliminary wing-sizing study was conducted for a simple planar dipole antenna. Numerical relationships were derived for an ideal wing ground plane span, wing chord, and airfoil thickness (t/c ratio), such that they maximize dipole array performance. The relationships derived are for the ground plane (conductive) portion of the wing, and if the wing is not fully conductive the relationships will need to be modified appropriately. The following are the conclusions related to this study:

3) During the wing sizing, while following the preliminary sizing approach from [36], the wing span and wing chord relations are intended to be used after a wing-loading and power-loading design point is selected. The wing ground plane span and chord (see Eq. (2) and Eq. (5)) are related to the wing area, and hence they can be chosen such that they deliver optimal antenna performance. The wing thickness-chord ratio (t/c) would determine whether an array could be embedded into the wing or will be held at an offset from wing with a custom fairing structure. An antenna array could be embedded in the lower wing skin while the upper skin could be used as a ground plane, so long as $0.5C \sim \lambda$. This conclusion is based on airfoil t/c ratios typically being on the order of 8-25%.
4) It is noticed that the dipole antenna is very sensitive to antenna-ground plane offset; a shift of $0.05\lambda$ in offset varied the peak gain by ~2 dB. The sensitivity of antenna is moderate to the change in ground plane width; a shift of $0.05\lambda$ in parameter d varied the peak gain by ~0.5 dB. The antenna is least sensitive to the change in ground plane length; a shift of $0.05\lambda$ in parameter d varied the peak gain by ~0.3 dB.

To verify the relations derived for a planar dipole, an array of modified antennas was simulated to verify its performance against wing span, wing chord and an airfoil thickness. A similar trend was found for the dipole antenna array, confirming the ground plane relationship for wing span, wing chord and wing height developed in the Sections 5.2, 5.3 and 5.4 are reasonable. From this study it can be concluded that the relationships developed for the single dipole antenna can be extended to entire dipole arrays, which greatly extends their use. However, it is cautioned against using these relationships for other antenna types without validation.

## 6.2. Recommendations

The author has the following recommendations:

1) If Wing Design I is to be pursued in the future, the antenna array integration into the lower wing skin needs to be finalized. If the dipole array is to be integrated onto the lower wing skin, the structural analysis of this design with rib cut needs to be done, so that ribs hop over the array. This FEM modification will change the load path for the wing skin and add extra weight to structure. Similarly, if antennas are to be embedded into the skin, the load bearing effects on the antenna need to be analyzed. Furthermore, for this design the change

in array performance due to the wing flexure needs to be studied. Finally, the effects of internal and external interferers, such as cables, actuators, servos, landing gear, skis, etc., on the dipole array performance will need to be investigated, as they will likely result in performance degradation.

2) For Wing Design II (fairing-pylon antenna design), the stability and control analysis for the Meridian UAS needs to be done, as the fairing may significantly affect handling qualities. As the Meridian operates in remote fields, the effects of the fairing on aircraft take-off performance also need to be studied and taken into account, and will likely require longer runways. Also, the tip strike angle need to be verified to see whether it is acceptable.
3) The quarter-wave patch antenna was found to be very sensitive to feed height, which is not an ideal design attribute considering the vehicle dynamics. It is possible that the antenna could be designed to be more robust by using novel manufacturing or design techniques. It is recommended that should this design be further pursued, these new techniques be investigated.
4) From the offset sizing, it seems that an offset of about 15% between the ground plane and array may also offer similar results as 25% offset; hence, an extended study of antenna coupling is recommended. This way the resulting degradation could be added to derived equation from Section 5.4 for better absolute performance estimation.
5) Similar trends were found for the dipole antenna array and generic dipole antenna, which validates (or confirms) the wing span, wing chord and wing height relations developed for the ground plane portion of the wing, in the section 5.2, 5.3, and 5.4. However, a more thorough simulation using smaller steps is recommended to develop more accurate trends.
6) The cross coupling between adjacent antennas need to be studied further as wing design equations do not consider cross-coupling. While the full array simulations verified the ideal ground plane parameters (suggested in the sizing equations), the purpose of further examining the coupling is to determine if actual array performance could be predicted from the simulation of one or two elements. In addition, ideal antenna spacing for an array could be found, which could then be added to the derived wing sizing equations for better estimation of actual antenna performance.
7) For this study, the lower skin was assumed to be flat, since Meridian used a Clark Y airfoil. But in future studies, the curvature of the typical airfoil shapes need to be investigated, as it may affect the radiation pattern and directivity.

# 7. Reference


1. J. Gregory, "Projections of sea level rise," *Climate Change 2013- The Physical Science Basis: Contributions of Working Group I to the Fifth Assessment Report of the Intergovernmental Panel on Climate Change*, Chapter 13, sea level change, 2013.
2. Thomas, R., E. Frederick, W. Krabill, S. Manizade and C. Martin. "Progressive increase in ice loss from Greenland," *Geophysical Research Letters*, 33(10), L10503, published on 27 May 2006. (10.1029/2006GL026075).
3. Donovan, W. R., "The Design of an Uninhabited Air Vehicle for Remote Sensing in the Cryosphere," *M.S. Thesis*, Department of Aerospace Engineering, University of Kansas, Lawrence, KS, 2007.
4. "High Strength Glass Fibers*," AGY*, 2006, www.agy.com/wp-content/uploads/2014/03/High_Strength_Glass_Fibers-Technical.pdf, accessed on Oct 2015.
5. Donovan, W. R., Mueller, D.M., Runge, E. and Liu, W. "Structural Design, Analysis, and Testing of Vivaldi Ground Penetrating Radar Antennas for the Meridian UAS", Department of Aerospace Engineering, University of Kansas, Lawrence, KS 66045, 10 April 2008.
6. "Drag Coefficient," *Engineering Toolbox*, www.engineeringtoolbox.com/drag-coefficient-d_627.html, accessed on Nov 2015.
7. Rodríguez-Morales, F., S. Gogineni, C. J. Leuschen, J. D. Paden, J. Li, C. S. Lewis, B.Panzer, D. Gomez-G. Alvestegui, A. Patel, K. Byers, R. Crowe, K. Player, R. D. Hale, E. J. Arnold, L. Smith, C. M. Gifford, D. Braaten, and C. Panton, "An Advanced Multifrequency Radar Instrumentation Suite for Polar Research," *IEEE Transactions on Geoscience and Remote Sensing*, vol. 52, no. 5, 2014.
8. Panzer, B., "Development of an electrically small Vivaldi antenna: The CReSIS Aerial Vivaldi (CAV-A)," Department of Aerospace Engineering, University of Kansas, Lawrence, KS 66045, 2004.
9. "Unmanned in Antarctica," *sUAS News the business of drones,* www.suasnews.com/2014/01/unmanned-in-antarctica/, 28 January 2014, [ACCESS DATE].
10. Gogineni, S., et al., "An improved coherent radar depth sounder," J. Glaciol., vol. 44, no. 148, pp. 659-669, 1998.
11. Arnold, E., J., "Development and Improvement of Airborne Remote Sensing Radar Platforms", *Ph.D. Dissertation*, Department of Aerospace Engineering, University of Kansas, 2013.
12. Kelly, B., et al., "A Summary of Current Instrumentation for Polar Glaciology and Geophysics Research (IPGGR)," *The Conference Center at the Maritime Institute*, MD, October 2014.
13. Jane's All the World Aircraft, 1984-1985, Jane's Publishing Incorporated, 13th Floor, 135 W 50th St, New York, NY, 10020.
14. Hale, R., Miller, H., Gogineni, S., Rodriguez-Morales, F., Leuschen, C., Paden, J., Li, J., Binder, T., Steinhage, D., Gehrmann, M. and Braaten, D. (2016), "Multi-Channel Ultra-Wideband Radar Sounder and Imager," *IGARSS 2016*, Beijing, 10 - 16 July 2016.
15. Yan, S., "Systems simulation helps design antennas for the first unmanned aircraft system used to measure polar ice sheets," University of Kansas, 2014.

16. Mohammad S. Sharawi, Daniel N. Aloi, Osamah A. Rawashdeh, "Design and Implementation of Embedded Printed Antenna Arrays in Small UAV Wing Structures," *IEEE Transactions on Antennas and Propagation*, Vol. 58, NO. 8, August 2010.
17. Neidhoefer, J., J. Ryan, and B. Leahy, "Cooperative Multi-Disciplinary Design of Integral Load Bearing Antennas in Small UAVs," AIAA Aerospace Sciences Meeting and Exhibit, Orlando, FL, 2009.
18. Richard L. Chaney, Douglas R. Hackler, Dale G. Wilson, Brian N. Meek, "Advanced Conformal Load-Bearing Antenna Structures," *American Semiconductor*, Inc., Boise, ID, USA.
19. Chi Sang You, Woonbong Hwang, "Design of load-bearing antenna structures by embedding technology of microstrip antenna in composite sandwich structure," Department of Mechanical Engineering, Pohang University of Science and Technology, Pohang, Republic of Korea.
20. "Transmitting Antenna Characteristics at VHF and UHF," *International Telecommunication Union*, pp. 10, 1995, www.itu.int/dms_pubrec/itu-r/rec/bs/R-REC-BS.1195-0-199510-S!!PDF-E.pdf.
21. HFSS, High Frequency Structure Simulator, Software Package, Ansys, Ver. 15.0.7, Canonsburg, PA, 2014.
22. R. Joshi and A. Harish, "A Modified Bow-Tie Antenna for Dual Band Applications," *IEEE Antennas and Wireless Propagation Letters*, vol. 6, pp. 468–471, Oct. 2007.
23. Byers, K. J. "Integration of a 15-Element, VHF Bow-Tie Antenna Array into an Aerodynamic Fairing on a NASA P-3 Aircraft," Department of Electrical Engineering, University of Kansas, Lawrence, KS 66045, 2011.
24. Constantine A. Balanis, "Microstrip Antennas," *Antenna Theory Analysis and Design*, 3rd edition, John Wiley, 2005.
25. Thomas Sørensen Yassin, "Development and Manufacturing of Direct Antenna Integrated RF Front-End for Ice Sounding Radar," chapter 12 'Antenna,' 31 August 2006.
26. NX Unigraphics, an advanced high-end CAD/CAM/CAE software, *originally developed by Unigraphics and updated by Siemens PLM Software*, 2011.
27. MIL-HDBK-5J, *Department of Defense Handbook: Metallic Materials and Elements for Aerospace Vehicle Structures* (31 Jan 2003) [S/S by Mmpds-01]
28. Evonik Industries, (March 6, 2017), '*Product information - ROHACELL 71 HF*,' accessed on Sept 15, 2016, from http://www.pronatindustries.com/wp-content/uploads/2014/12/ROHACELL-HF-Product-Information-datasheet.pdf.
29. Military Handbook - MIL-HDBK-17-2F: Composite Materials Handbook, *Volume 2 - Polymer Matrix Composites Materials Properties*. U.S. Department of Defense, 2002.
30. Clarkson, E., NIAR, Hexcel 8552 IM7 Unidirectional Prepreg 190 gsm and 35% RC Qualification Statistical Analysis Report, 2012 'http://www.niar.wichita.edu/coe/NCAMP_Documents/Hexcel%208552/NCP-RP-2009-028%20Rev%20A%20HEXCEL%208552%20IM7%20Uni%2011.16.12%20FINAL%20SAR.pdf'
31. Donovan, W. R., Hale, R. D., & Liu, W., (2008). "Design and Structural Analysis of the Meridian Unmanned Aircraft," *AIAA-2008-2261*, 49th AIAA/ASME/ASCE/AHS/ASC Structures, Structural Dynamics, and Materials Conference, 7 - 10 Apr, Schaumburg, IL.
32. XFLR5, An airfoil, wing and plane analysis tool, *SourceForge*, v6.12, 2016.
33. "Turbulence Modeling Resource: 2DN00: 2d NACA 0012 Airfoil Validation Case," *NASA Langley Research Center*, last updated 31 August 2016, http://turbmodels.larc.nasa.gov/naca0012_val.html.

34. Underwood, S. C., “Performance and Emission Characteristics of an Aircraft Turbo Diesel Engine using JET-A Fuel,” *M.S. Thesis*, Department of Aerospace Engineering, University of Kansas, Lawrence, KS, 2005.
35. C.A. Balanis, Antenna Theory, *Analysis and Design*, 3rd ed., Hoboken, NJ, Wiley, 2005.
36. Roskam, J., Airplane Design I-VII, 2nd ed., DARcorporation, Lawrence, KS, 2003
37. Byers, K.J., et al., “A Modified Wideband Dipole Antenna for an Airobrne VHF Ice-Penentrating Radar,” *IEEE Transactions on Instrumentation and Measurement*, Vol. 61, No. 5, May 2012.
38. XFLR5, [An airfoil, wing and plane analysis tool], *SourceForge*, v6.12, 2016, http://www.xflr5.com/xflr5.htm.
39. Sadraey, M. H., Aircraft Performance Analysis, VDM Verlag Dr. Müller, New Hampshire, 2009, Chap 3.

# Appendix A - Wing Design I

This section includes the critical stress region of each individual wing component of Wing Design I, which includes; upper skin, lower skin, front spar, rear spar, wing rib and wing leading edge. The material of all the critical layer of the components in this section is fiberglass cloth, with 0° orientations. For the margin of safety calculations, the allowable stresses are taken from Table 26.

## 1. Upper Skin

Load Case 1 is determined to be the critical load case for upper skin. The upper skin was found to be most critical in longitudinal compression in the inboard section of the wing. Figure 111 shows the maximum longitudinal compressive stress distribution with the critical region highlighted, and Figure 112 shows the critical region enlarged with the critical element number in that region. As the .f06 screen capture in Figure 113 shows, the maximum longitudinal compression in the upper skin is -18.1 ksi (-125 MPa) in layer 5.

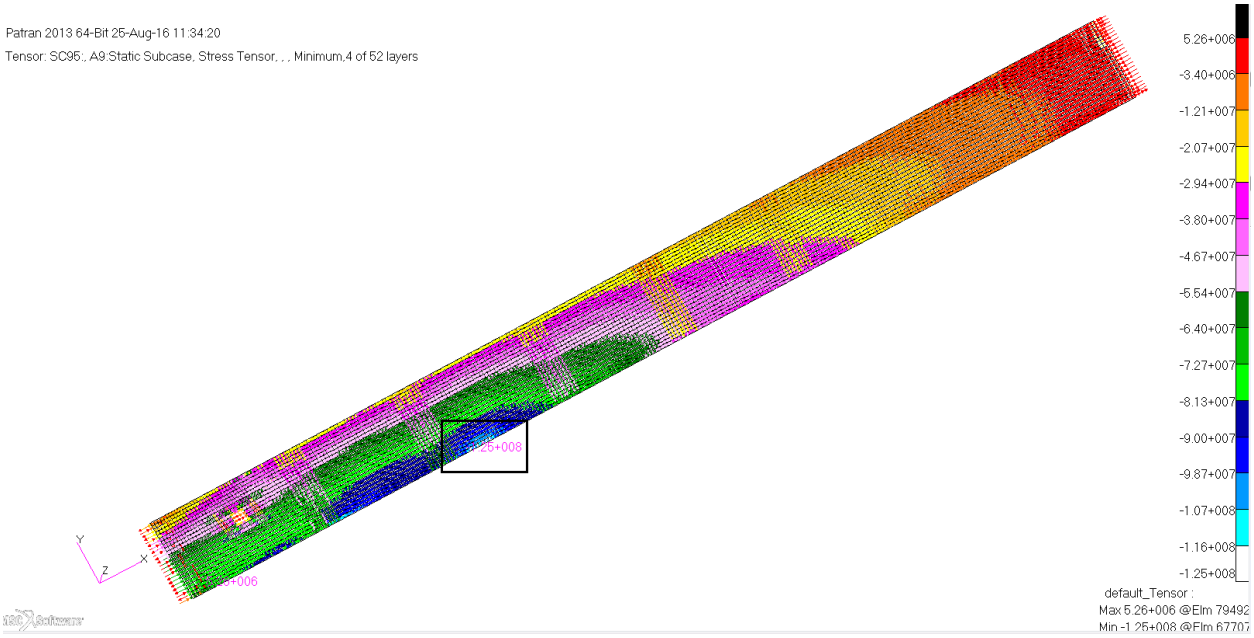


**Figure 111: Upper skin maximum longitudinal compression stress plot**

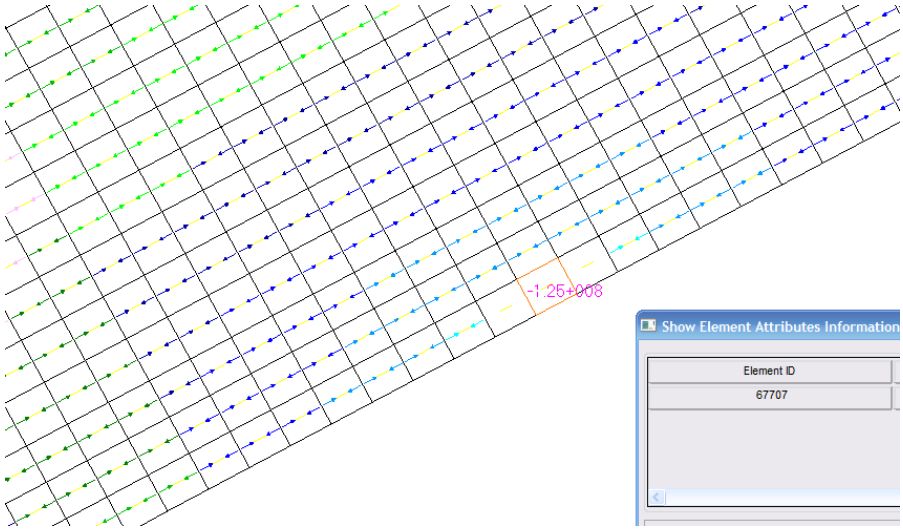


***Figure 112:*** **Upper skin compression critical region**

S T R E S S E S  I N  L A Y E R E D  C O M P O S I T E  E L E M E N T S  ( Q U A D 4 )

| | ELEMENT ID | PLY ID | STRESSES IN FIBER AND MATRIX DIRECTIONS NORMAL-1 | NORMAL-2 | SHEAR-12 | INTER-LAMINAR STRESSES SHEAR XZ-MAT | SHEAR YZ-MAT | PRINCIPAL STRESSES (ZERO SHEAR) ANGLE | MAJOR | MINOR | MAX SHEAR |
|---|---|---|---|---|---|---|---|---|---|---|---|
| 0 | 67704 | 3 | -2.36180E+07 | 1.11718E+07 | 3.84409E+06 | 7.70890E-12 | 2.64227E-10 | 83.77 | 1.15914E+07 | -2.40377E+07 | 1.78146E+07 |
| 0 | 67705 | 1 | 5.29881E+06 | 3.35564E+06 | 2.52484E+06 | 5.65128E+03 | 4.60909E+04 | 34.48 | 7.03255E+06 | 1.62190E+06 | 2.70532E+06 |
| 0 | 67705 | 2 | 4.93533E+06 | 1.51882E+06 | 2.56535E+06 | 5.65128E+03 | 4.60909E+04 | 28.17 | 6.30915E+06 | 1.45002E+05 | 3.08207E+06 |
| 0 | 67705 | 3 | 4.57186E+06 | -3.18010E+05 | 2.60586E+06 | 3.55594E-11 | 2.87531E-10 | 23.41 | 5.70019E+06 | -1.44634E+06 | 3.57327E+06 |
| 0 | 67706 | 1 | -5.22342E+07 | 1.48280E+07 | 2.06705E+07 | 5.28504E+03 | -5.83102E+03 | 74.17 | 2.06873E+07 | -5.80935E+07 | 3.93904E+07 |
| 0 | 67706 | 2 | -5.25393E+07 | 1.41182E+07 | 2.06849E+07 | 7.92756E+03 | -8.74654E+03 | 74.09 | 2.00153E+07 | -5.84364E+07 | 3.92259E+07 |
| 0 | 67706 | 3 | -5.28443E+07 | 1.34083E+07 | 2.06993E+07 | 7.92756E+03 | -8.74654E+03 | 74.00 | 1.93437E+07 | -5.87796E+07 | 3.90617E+07 |
| 0 | 67706 | 4 | -5.31493E+07 | 1.26985E+07 | 2.07137E+07 | 5.28504E+03 | -5.83102E+03 | 73.91 | 1.86724E+07 | -5.91232E+07 | 3.88978E+07 |
| 0 | 67706 | 5 | -5.34543E+07 | 1.19886E+07 | 2.07281E+07 | 1.78591E-11 | -1.85446E-11 | 73.82 | 1.80015E+07 | -5.94672E+07 | 3.87344E+07 |
| 0 | 67707 | 1 | -6.57417E+07 | 4.12353E+06 | -1.01057E+06 | -6.07526E+02 | 5.18456E+04 | -89.17 | 4.13814E+06 | -6.57563E+07 | 3.49472E+07 |
| 0 | 67707 | 2 | -6.66034E+07 | 3.98835E+06 | -1.05719E+06 | -1.19727E+03 | 1.02174E+05 | -89.14 | 4.00418E+06 | -6.66193E+07 | 3.53117E+07 |
| 0 | 67707 | 3 | -3.07006E+03 | -7.23352E+02 | 0.0 | -1.19727E+03 | 1.02174E+05 | 90.00 | -7.23352E+02 | -3.07006E+03 | 1.17335E+03 |
| 0 | 67707 | 4 | -1.23779E+08 | -4.98017E+06 | -4.15019E+06 | -6.07526E+02 | 5.18456E+04 | -88.00 | -4.83536E+06 | -1.23924E+08 | 5.95441E+07 |
| 0 | 67707 | 5 | -1.24641E+08 | -5.11534E+06 | -4.19681E+06 | -8.21985E-12 | 1.60339E-10 | -87.99 | -4.96816E+06 | -1.24788E+08 | 5.99098E+07 |
| 0 | 67708 | 1 | -9.03117E+07 | 1.76842E+07 | 1.55915E+07 | 1.15424E+04 | -4.24851E+03 | 81.95 | 1.98901E+07 | -9.25176E+07 | 5.62039E+07 |
| 0 | 67708 | 2 | -9.07963E+07 | 1.66611E+07 | 1.55557E+07 | 1.73136E+04 | -6.37276E+03 | 81.93 | 1.88677E+07 | -9.30029E+07 | 5.59353E+07 |
| 0 | 67708 | 3 | -9.12809E+07 | 1.56380E+07 | 1.55199E+07 | 1.73136E+04 | -6.37276E+03 | 81.91 | 1.78453E+07 | -9.34881E+07 | 5.56667E+07 |
| 0 | 67708 | 4 | -9.17655E+07 | 1.46150E+07 | 1.54841E+07 | 1.15424E+04 | -4.24851E+03 | 81.88 | 1.68229E+07 | -9.39734E+07 | 5.53982E+07 |
| 0 | 67708 | 5 | -9.22501E+07 | 1.35919E+07 | 1.54482E+07 | 3.90039E-11 | -1.35117E-11 | 81.86 | 1.58006E+07 | -9.44588E+07 | 5.51297E+07 |

***Figure 113:*** **Upper skin .f06 for critical compressive element**

The margin of safety for the compressive stress of the wing upper skin is given by,

$$M.S. = \frac{\sigma_{Allowable}}{FS * \sigma_{Actual}} - 1 = \frac{-37\ ksi}{1.5 * -18.1\ ksi} - 1 = \mathbf{0.36}$$

## 2. Lower Skin

Load Case 1 is determined to be the critical load case for lower skin. The lower skin was found to be most critical in longitudinal tension in the inboard section of the wing. Figure 114 shows the maximum longitudinal tensile stress distribution with the critical region highlighted, and Figure 115 shows the critical region enlarged with the critical element number in that region. As the .f06 screen capture in Figure 116 shows, the maximum longitudinal tension in the lower skin is 19.9 ksi (137 MPa) in layer 4.

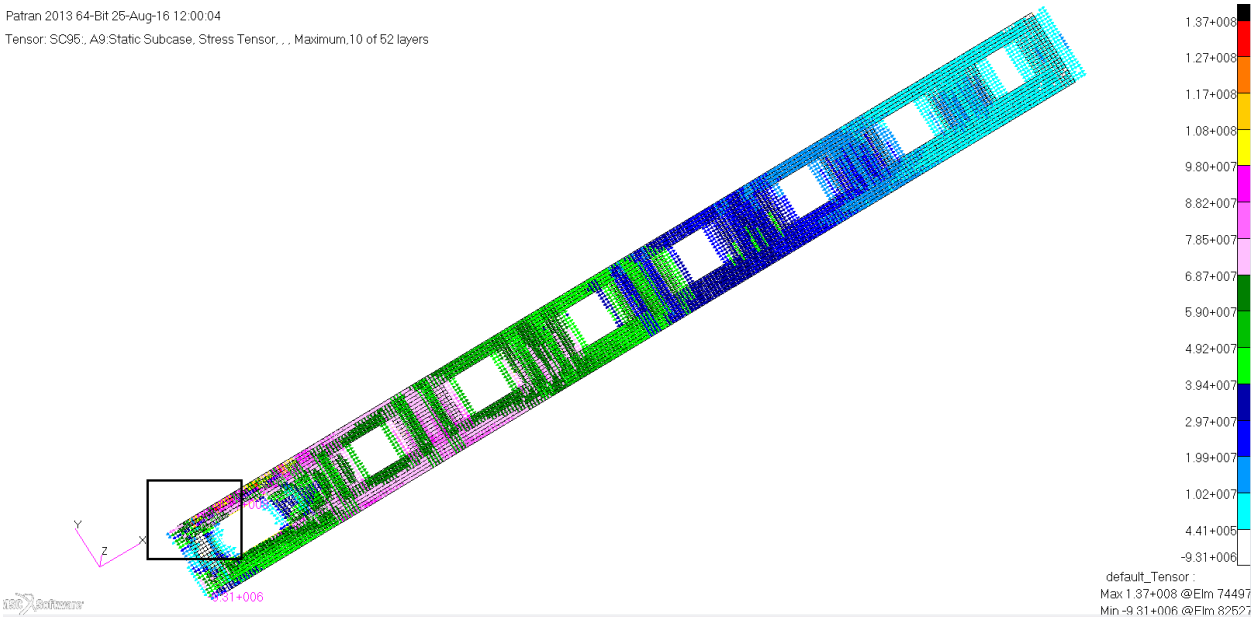


**Figure 114: Lower skin maximum longitudinal tension stress plot**

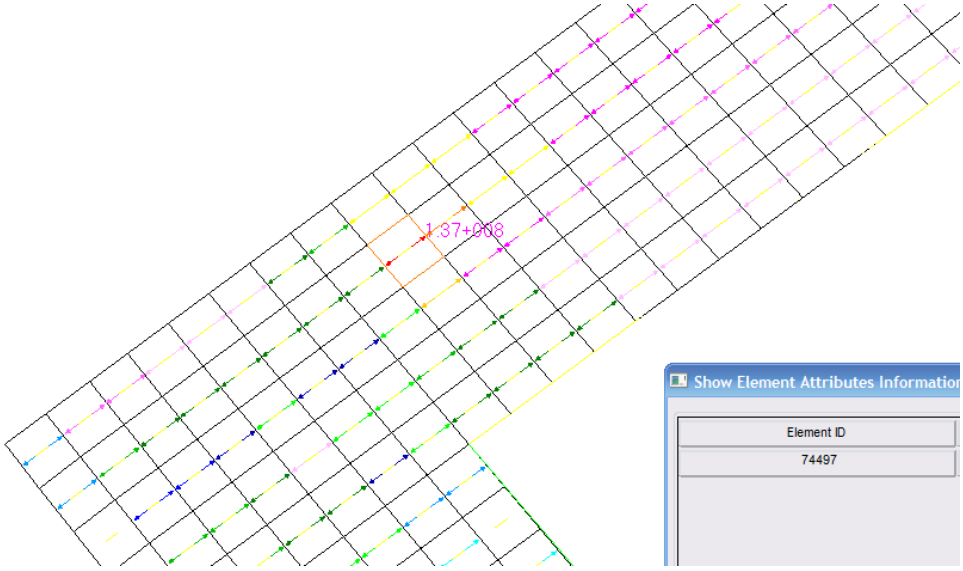


**Figure 115: Lower skin tension critical region**

S T R E S S E S  I N  L A Y E R E D  C O M P O S I T E  E L E M E N T S  ( Q U A D 4 )

| | ELEMENT ID | PLY ID | STRESSES IN FIBER AND MATRIX DIRECTIONS NORMAL-1 | NORMAL-2 | SHEAR-12 | INTER-LAMINAR STRESSES SHEAR XZ-MAT | SHEAR YZ-MAT | PRINCIPAL STRESSES (ZERO SHEAR) ANGLE | MAJOR | MINOR | MAX SHEAR |
|---|---|---|---|---|---|---|---|---|---|---|---|
| 0 | 74494 | 5 | 6.54898E+07 | 1.26021E+07 | 7.17582E+06 | -1.40751E-02 | 7.80210E-03 | 7.59 | 6.64461E+07 | 1.16458E+07 | 2.74002E+07 |
| 0 | 74495 | 1 | 6.20924E+06 | -1.98681E+07 | 1.49671E+06 | -5.37759E+04 | -2.72589E+03 | 3.27 | 6.29486E+06 | -1.99537E+07 | 1.31243E+07 |
| 0 | 74495 | 2 | 4.25227E+06 | -2.13316E+07 | 1.50430E+06 | -1.01463E+05 | -5.14440E+03 | 3.35 | 4.34042E+06 | -2.14198E+07 | 1.28801E+07 |
| 0 | 74495 | 3 | 2.29531E+06 | -2.27951E+07 | 1.51189E+06 | -1.43060E+05 | -7.25552E+03 | 3.44 | 2.38608E+06 | -2.28859E+07 | 1.26360E+07 |
| 0 | 74495 | 4 | 3.38347E+05 | -2.42587E+07 | 1.51947E+06 | -1.78569E+05 | -9.05926E+03 | 3.52 | 4.31857E+05 | -2.43522E+07 | 1.23920E+07 |
| 0 | 74495 | 5 | 6.37177E+07 | 1.46662E+07 | 1.13768E+07 | -2.30820E-02 | -1.03532E-03 | 12.44 | 6.62279E+07 | 1.21560E+07 | 2.70359E+07 |
| 0 | 74496 | 1 | 7.74296E+06 | -2.50702E+07 | 1.71958E+06 | -7.87933E+04 | 9.48557E+03 | 2.99 | 7.83283E+06 | -2.51601E+07 | 1.64964E+07 |
| 0 | 74496 | 2 | 5.53771E+06 | -2.62948E+07 | 1.73466E+06 | -1.48665E+05 | 1.79015E+04 | 3.11 | 5.63196E+06 | -2.63890E+07 | 1.60105E+07 |
| 0 | 74496 | 3 | 3.33247E+06 | -2.75193E+07 | 1.74973E+06 | -2.09614E+05 | 2.52478E+04 | 3.24 | 3.43138E+06 | -2.76182E+07 | 1.55248E+07 |
| 0 | 74496 | 4 | 1.12722E+06 | -2.87439E+07 | 1.76481E+06 | -2.61642E+05 | 3.15245E+04 | 3.37 | 1.23112E+06 | -2.88478E+07 | 1.50395E+07 |
| 0 | 74496 | 5 | 5.96942E+07 | 6.03244E+06 | 1.35172E+07 | -3.38201E-02 | 3.60270E-03 | 13.37 | 6.29068E+07 | 2.81985E+06 | 3.00435E+07 |
| 0 | 74497 | 1 | 1.16828E+08 | -8.10647E+06 | 5.13308E+06 | -8.19172E+04 | 3.92926E+04 | 2.35 | 1.17038E+08 | -8.31701E+06 | 6.26776E+07 |
| 0 | 74497 | 2 | 1.23540E+08 | -5.15588E+06 | 5.83794E+06 | -1.09223E+05 | 5.23901E+04 | 2.59 | 1.23804E+08 | -5.42016E+06 | 6.46121E+07 |
| 0 | 74497 | 3 | 1.30252E+08 | -2.20530E+06 | 6.54280E+06 | -8.19172E+04 | 3.92926E+04 | 2.82 | 1.30574E+08 | -2.52770E+06 | 6.65509E+07 |
| 0 | 74497 | 4 | 1.36964E+08 | 7.45290E+05 | 7.24766E+06 | 0.0 | 0.0 | 3.04 | 1.37348E+08 | 3.60755E+05 | 6.84938E+07 |
| 0 | 74498 | 1 | 1.06901E+08 | -1.24462E+07 | 5.43435E+06 | -2.42576E+04 | 4.56870E+04 | 2.60 | 1.07147E+08 | -1.26931E+07 | 5.99203E+07 |
| 0 | 74498 | 2 | 1.10518E+08 | -7.18740E+06 | 6.25302E+06 | -3.23434E+04 | 6.09160E+04 | 3.03 | 1.10849E+08 | -7.51865E+06 | 5.91840E+07 |
| 0 | 74498 | 3 | 1.14136E+08 | -1.92863E+06 | 7.07170E+06 | -2.42576E+04 | 4.56870E+04 | 3.47 | 1.14565E+08 | -2.35791E+06 | 5.84615E+07 |
| 0 | 74498 | 4 | 1.17753E+08 | 3.33014E+06 | 7.89037E+06 | 0.0 | 0.0 | 3.93 | 1.18295E+08 | 2.78860E+06 | 5.77531E+07 |

**Figure 116: Lower skin .f06 for critical tensile element**

The margin of safety for the tensile stress of the wing lower skin is given by,

$$M.S. = \frac{\sigma_{Allowable}}{FS * \sigma_{Actual}} - 1 = \frac{32.1\ ksi}{1.5 * 19.9\ ksi} - 1 = \mathbf{0.08}$$

### 3. Wing Front Spar

Load Case 1 is determined to be the critical load case for front spar of the wing. The front spar was found to be most critical in longitudinal compression in the inboard section of the wing. Figure 117 shows the maximum longitudinal compressive stress distribution with the critical region highlighted, and Figure 118 shows the critical region enlarged with the critical element number in that region. As the .f06 screen capture in Figure 119 shows, the maximum longitudinal compression in the front spar is -162 MPa in layer 47.

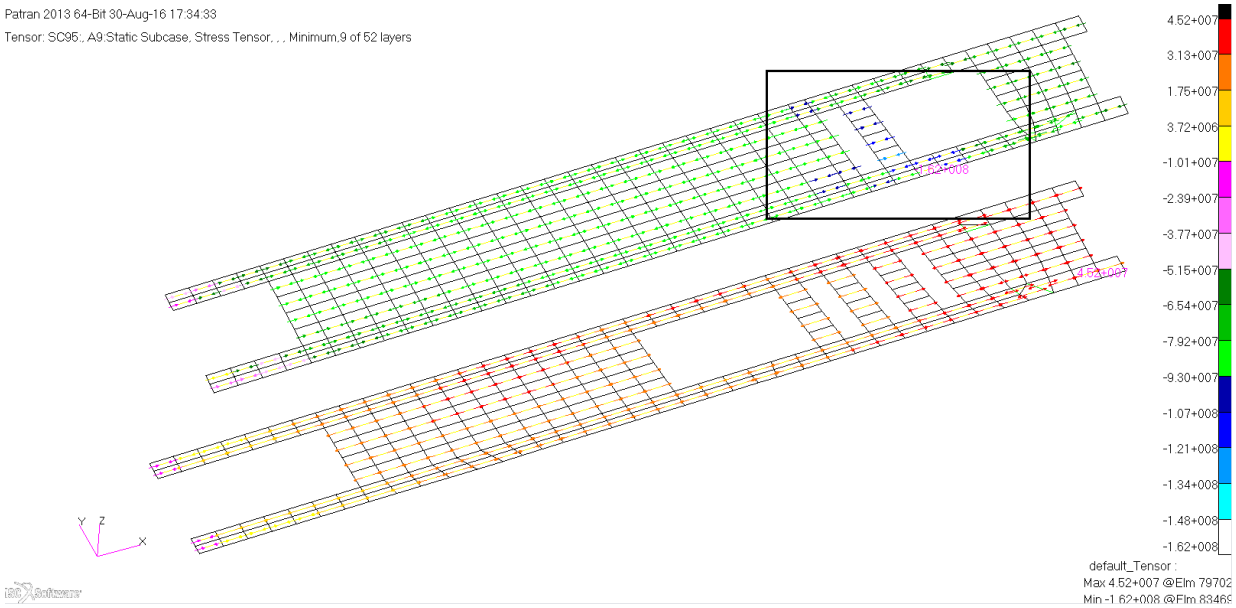


**Figure 117: Front spar maximum longitudinal compression stress plot**

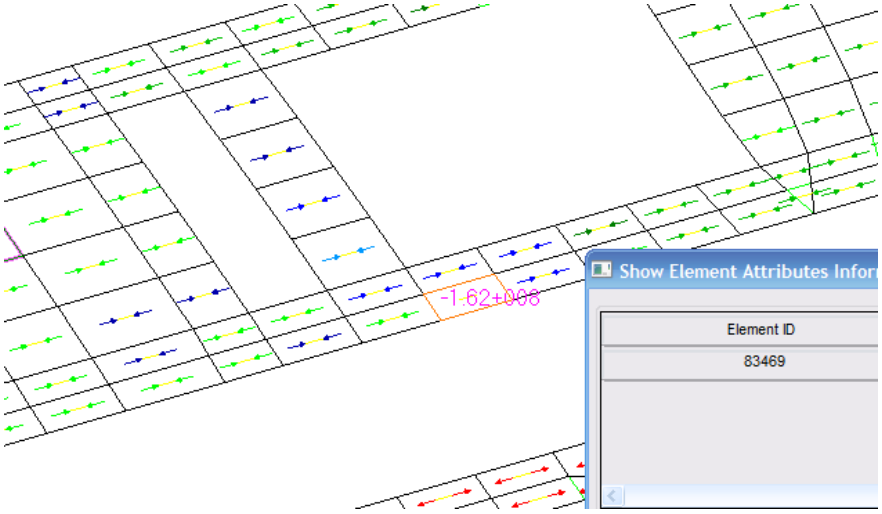


**Figure 118: Front spar compression critical region**

S T R E S S E S  I N  L A Y E R E D  C O M P O S I T E  E L E M E N T S  ( Q U A D 4 )

| | ELEMENT ID | PLY ID | STRESSES IN FIBER AND MATRIX DIRECTIONS NORMAL-1 | NORMAL-2 | SHEAR-12 | INTER-LAMINAR STRESSES SHEAR XZ-MAT | SHEAR YZ-MAT | PRINCIPAL STRESSES (ZERO SHEAR) ANGLE | MAJOR | MINOR | MAX SHEAR |
|---|---|---|---|---|---|---|---|---|---|---|---|
| 0 | 83469 | 43 | -4.06086E+08 | -3.12947E+07 | -1.00572E-03 | -6.06271E+06 | -6.67996E+06 | -90.00 | -3.12947E+07 | -4.06086E+08 | 1.87395E+08 |
| 0 | 83469 | 44 | -4.12545E+08 | -3.19592E+07 | -1.02321E-03 | -4.88727E+06 | -6.50779E+06 | -90.00 | -3.19592E+07 | -4.12545E+08 | 1.90293E+08 |
| 0 | 83469 | 45 | -2.52851E+08 | -2.63662E+07 | -1.23409E+07 | -2.87840E+06 | -3.81423E+06 | -86.89 | -2.56957E+07 | -2.53522E+08 | 1.13913E+08 |
| 0 | 83469 | 46 | -2.63300E+08 | -3.24464E+07 | -1.27412E+07 | -7.11844E+05 | -9.09233E+05 | -86.85 | -3.17454E+07 | -2.64001E+08 | 1.16128E+08 |
| 0 | 83469 | 47 | -1.62072E+08 | -6.72524E+07 | -8.99644E+06 | -1.61323E-07 | -3.64029E-08 | -84.63 | -6.64064E+07 | -1.62918E+08 | 4.82560E+07 |
| 0 | 83470 | 1 | -2.99840E+07 | 1.68970E+07 | -4.47252E+06 | 9.58438E+05 | -7.25430E+04 | -84.60 | 1.73198E+07 | -3.04069E+07 | 2.38634E+07 |
| 0 | 83470 | 2 | 1.83554E+07 | 1.40242E+08 | -6.26171E+06 | 3.87552E+06 | -3.04318E+05 | -87.07 | 1.40563E+08 | 1.80345E+07 | 6.12642E+07 |
| 0 | 83470 | 3 | 1.25057E+07 | 1.34742E+08 | -5.97848E+06 | 6.58028E+06 | -5.19223E+05 | -87.21 | 1.35034E+08 | 1.22140E+07 | 6.14100E+07 |
| 0 | 83470 | 4 | -1.08457E+08 | -1.07011E+04 | -4.89942E-04 | 8.16292E+06 | -5.32960E+05 | -90.00 | -1.07011E+04 | -1.08457E+08 | 5.42230E+07 |
| 0 | 83470 | 5 | -1.12058E+08 | -5.22127E+05 | -4.77561E-04 | 9.67762E+06 | -5.46108E+05 | -90.00 | -5.22127E+05 | -1.12058E+08 | 5.57679E+07 |
| 0 | 83470 | 6 | -1.15659E+08 | -1.03355E+06 | -4.65180E-04 | 1.11244E+07 | -5.58665E+05 | -90.00 | -1.03355E+06 | -1.15659E+08 | 5.73127E+07 |
| 0 | 83470 | 7 | -1.19260E+08 | -1.54498E+06 | -4.52798E-04 | 1.25032E+07 | -5.70634E+05 | -90.00 | -1.54498E+06 | -1.19260E+08 | 5.88575E+07 |
| 0 | 83470 | 8 | -1.22861E+08 | -2.05641E+06 | -4.40417E-04 | 1.38142E+07 | -5.82012E+05 | -90.00 | -2.05641E+06 | -1.22861E+08 | 6.04024E+07 |
| 0 | 83470 | 9 | -4.41387E+07 | 4.02897E+06 | -3.44188E+06 | 1.44251E+07 | -6.28257E+05 | -85.93 | 4.27367E+06 | -4.43834E+07 | 2.43285E+07 |
| 0 | 83470 | 10 | -1.31514E+08 | -3.28525E+06 | -4.10668E-04 | 1.55728E+07 | -6.38219E+05 | -90.00 | -3.28525E+06 | -1.31514E+08 | 6.41142E+07 |
| 0 | 83470 | 11 | -1.35115E+08 | -3.79668E+06 | -3.98287E-04 | 1.66526E+07 | -6.47591E+05 | -90.00 | -3.79668E+06 | -1.35115E+08 | 6.56591E+07 |

**Figure 119: Front spar .f06 for critical compressive element**

The margin of safety for the compressive stress of the front spar is given by,

$$M.S. = \frac{\sigma_{Allowable}}{FS * \sigma_{Actual}} - 1 = \frac{-255\ MPa}{1.5 * -162\ MPa} - 1 = \mathbf{0.05}$$

### 4. Wing Rear Spar

Load Case 1 is determined to be the critical load case for the rear spar. The rear spar was found to be most critical in longitudinal tension in the inboard section of the wing. Figure 120 shows the maximum longitudinal tensile stress distribution with the critical region highlighted, and Figure 121 shows the critical region enlarged with the critical element number in that region. As the .f06 screen capture in Figure 122 shows, the maximum longitudinal tension in the rear spar is 19.1 ksi (132 MPa) in layer 10.

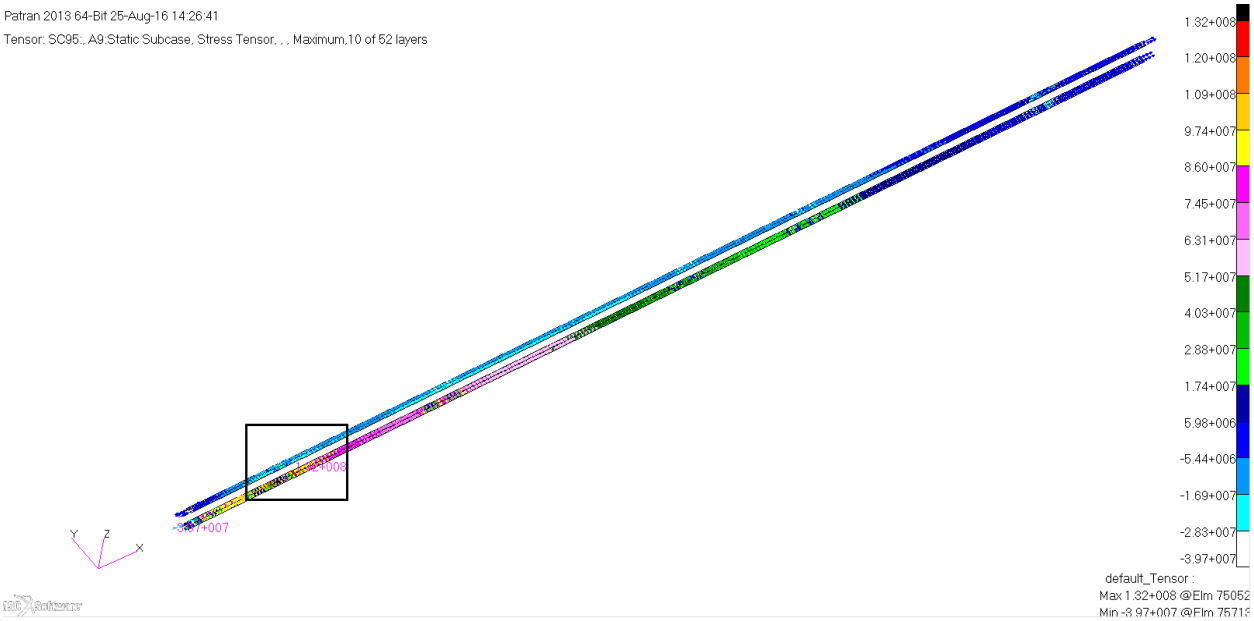


***Figure 120:*** **Rear spar maximum longitudinal tension stress plot**

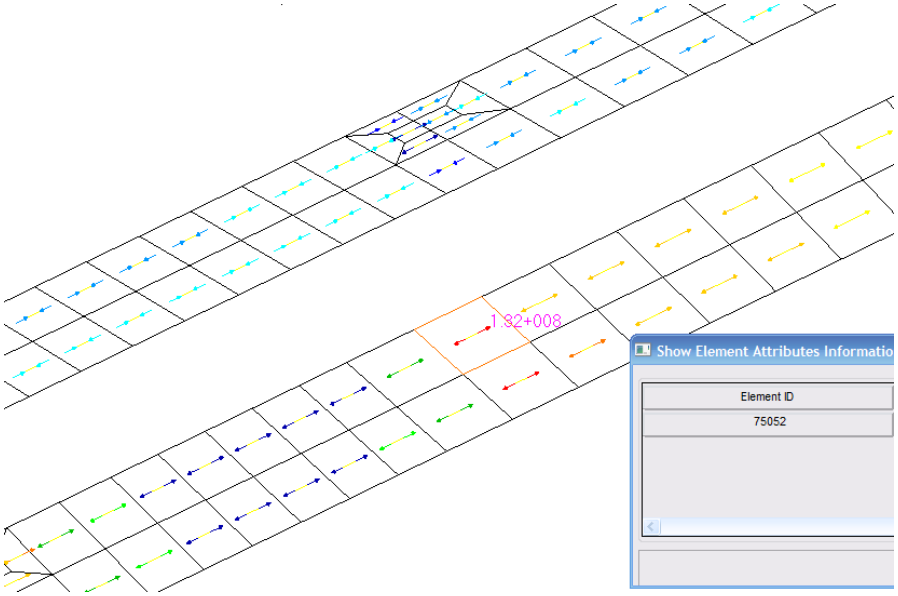


***Figure 121:*** **Rear spar tension critical region**

| | | | | | | | | | | | | |
|---|---|---|---|---|---|---|---|---|---|---|---|---|
| 0 | 75052 | 1 | 8.45550E+07 | -4.60382E+06 | 2.11320E+06 | -6.03884E+05 | 2.07574E+05 | 1.36 | 8.46050E+07 | -4.65388E+06 | 4.46295E+07 |
| 0 | 75052 | 2 | 8.97918E+07 | -3.30646E+06 | 9.30802E+05 | -1.07357E+06 | 3.69021E+05 | 0.57 | 8.98011E+07 | -3.31576E+06 | 4.65584E+07 |
| 0 | 75052 | 3 | 9.50286E+07 | -2.00909E+06 | -2.51600E+05 | -1.40906E+06 | 4.84340E+05 | -0.15 | 9.50293E+07 | -2.00974E+06 | 4.85195E+07 |
| 0 | 75052 | 4 | 1.00265E+08 | -7.11718E+05 | -1.43400E+06 | -1.61036E+06 | 5.53532E+05 | -0.81 | 1.00286E+08 | -7.32079E+05 | 5.05089E+07 |
| 0 | 75052 | 5 | 1.05502E+08 | 5.85650E+05 | -2.61641E+06 | -1.67745E+06 | 5.76596E+05 | -1.43 | 1.05567E+08 | 5.20443E+05 | 5.25235E+07 |
| 0 | 75052 | 6 | 1.10739E+08 | 1.88302E+06 | -3.79881E+06 | -1.61036E+06 | 5.53532E+05 | -2.00 | 1.10871E+08 | 1.75061E+06 | 5.45604E+07 |
| 0 | 75052 | 7 | 1.15976E+08 | 3.18039E+06 | -4.98121E+06 | -1.40906E+06 | 4.84340E+05 | -2.52 | 1.16195E+08 | 2.96084E+06 | 5.66173E+07 |
| 0 | 75052 | 8 | 1.21213E+08 | 4.47776E+06 | -6.16361E+06 | -1.07357E+06 | 3.69021E+05 | -3.01 | 1.21537E+08 | 4.15322E+06 | 5.86920E+07 |

1 THIS IS A DEFAULT SUBCASE. AUGUST 19, 2016 MSC Nastran 3/14/14 PAGE 11159

0 SUBCASE 95

S T R E S S E S I N L A Y E R E D C O M P O S I T E E L E M E N T S ( Q U A D 4 )

| | ELEMENT ID | PLY ID | STRESSES IN FIBER AND MATRIX DIRECTIONS NORMAL-1 | NORMAL-2 | SHEAR-12 | INTER-LAMINAR STRESSES SHEAR XZ-MAT | SHEAR YZ-MAT | PRINCIPAL STRESSES (ZERO SHEAR) ANGLE | MAJOR | MINOR | MAX SHEAR |
|---|---|---|---|---|---|---|---|---|---|---|---|
| 0 | 75052 | 9 | 1.26450E+08 | 5.77513E+06 | -7.34602E+06 | -6.03884E+05 | 2.07574E+05 | -3.47 | 1.26895E+08 | 5.32958E+06 | 6.07828E+07 |
| 0 | 75052 | 10 | 1.31686E+08 | 7.07249E+06 | -8.52842E+06 | -3.37760E-09 | 1.08333E-09 | -3.90 | 1.32267E+08 | 6.49153E+06 | 6.28879E+07 |
| 0 | 75053 | 1 | 6.33631E+06 | 1.97865E+06 | 1.26426E+06 | -5.67272E+04 | -1.68354E+05 | 15.06 | 6.67653E+06 | 1.63842E+06 | 2.51906E+06 |
| 0 | 75053 | 2 | 6.21054E+06 | -5.89013E+05 | 1.16392E+06 | -1.09143E+05 | -3.24005E+05 | 9.45 | 6.40426E+06 | -7.82730E+05 | 3.59350E+06 |
| 0 | 75053 | 3 | 6.08478E+06 | -3.15667E+06 | 1.06359E+06 | -1.57249E+05 | -4.66952E+05 | 6.48 | 6.20561E+06 | -3.27750E+06 | 4.74156E+06 |
| 0 | 75053 | 4 | 5.95902E+06 | -5.72433E+06 | 9.63255E+05 | -2.01043E+05 | -5.97196E+05 | 4.68 | 6.03791E+06 | -5.80322E+06 | 5.92056E+06 |
| 0 | 75053 | 5 | 5.83326E+06 | -8.29199E+06 | 8.62920E+05 | -2.40526E+05 | -7.14736E+05 | 3.48 | 5.88578E+06 | -8.34451E+06 | 7.11515E+06 |
| 0 | 75053 | 6 | 5.70750E+06 | -1.08596E+07 | 7.62586E+05 | -2.75699E+05 | -8.19573E+05 | 2.63 | 5.74253E+06 | -1.08947E+07 | 8.31860E+06 |

**Figure 122: Rear spar .f06 for critical tensile element**

The margin of safety for the tensile stress of the rear spar is given by,

$$M.S. = \frac{\sigma_{Allowable}}{FS * \sigma_{Actual}} - 1 = \frac{32.1\ ksi}{1.5 * 19.1\ ksi} - 1 = \mathbf{0.12}$$

## 5. Wing Rib

Load Case 1 is determined to be the critical load case for wing rib. The wing rib was found to be most critical in transverse compression in the inboard section of the wing. Figure 123 shows the maximum transverse compressive stress distribution with the critical region highlighted, and Figure 124 shows the critical region enlarged with the critical element number in that region. As the .f06 screen capture in Figure 125 shows, the maximum transverse compression in the wing rib is -7.4 ksi (-50.6 MPa) in layer 1.


**Figure 123: Rib maximum transverse compression stress plot**

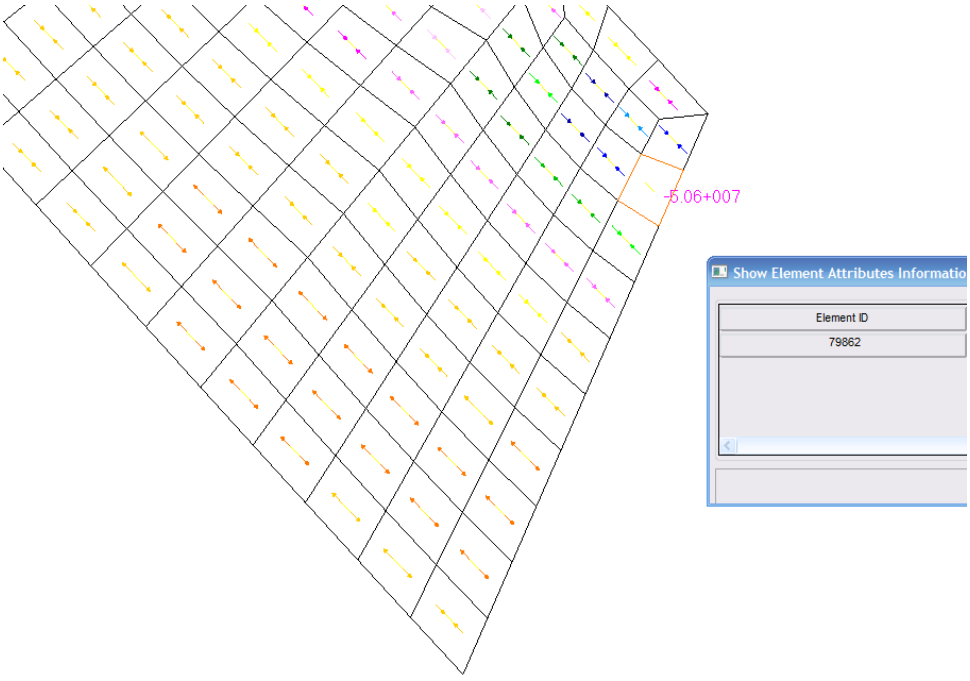


**Figure 124: Rib compression critical region**

| | STRESSES IN LAYERED COMPOSITE ELEMENTS (QUAD4) | | | | | | | | | |
|---|---|---|---|---|---|---|---|---|---|---|
| | ELEMENT ID | PLY ID | STRESSES IN FIBER AND MATRIX DIRECTIONS NORMAL-1 | NORMAL-2 | SHEAR-12 | INTER-LAMINAR STRESSES SHEAR XZ-MAT | SHEAR YZ-MAT | PRINCIPAL STRESSES (ZERO SHEAR) ANGLE | MAJOR | MINOR | MAX SHEAR |
| 0 | 79860 | 5 | -5.78321E+07 | -5.53535E+06 | -8.08878E+06 | 1.66098E+04 | -6.66390E+04 | -81.41 | -4.31284E+06 | -5.90546E+07 | 2.73709E+07 |
| 0 | 79860 | 6 | -5.89814E+07 | -5.60262E+06 | -8.23716E+06 | 1.70318E-10 | -6.91233E-10 | -81.42 | -4.36041E+06 | -6.02236E+07 | 2.79316E+07 |
| 0 | 79861 | 1 | 4.10799E+06 | -5.42383E+06 | 6.97159E+06 | 2.30277E+04 | -2.77554E+04 | 27.82 | 7.78702E+06 | -9.10286E+06 | 8.44494E+06 |
| 0 | 79861 | 2 | -2.82321E+05 | -3.01993E+05 | 5.09537E+04 | 2.30277E+04 | -2.77554E+04 | 39.54 | -2.40262E+05 | -3.44051E+05 | 5.18944E+04 |
| 0 | 79861 | 3 | 2.18427E+06 | -5.13602E+06 | 6.35407E+06 | 2.36987E-11 | -8.39588E-11 | 30.03 | 5.85699E+06 | -8.80874E+06 | 7.33287E+06 |
| 0 | 79862 | 1 | -1.56419E+07 | -5.06458E+07 | -7.89601E+06 | -3.02914E+04 | -5.58895E+04 | -12.14 | -1.39432E+07 | -5.23445E+07 | 1.92007E+07 |
| 0 | 79862 | 2 | -4.52339E+05 | -5.33333E+05 | -6.38188E+04 | -3.02914E+04 | -5.58895E+04 | -28.80 | -4.17253E+05 | -5.68420E+05 | 7.55833E+04 |
| 0 | 79862 | 3 | -1.15605E+07 | -4.37203E+07 | -8.79420E+06 | -3.11741E-11 | -1.69063E-10 | -14.34 | -9.31282E+06 | -4.59680E+07 | 1.83276E+07 |
| 0 | 79863 | 1 | -5.60961E+07 | -4.51339E+06 | 1.05220E+07 | 1.85063E+05 | -3.00639E+05 | 78.90 | -2.44964E+06 | -5.81598E+07 | 2.78551E+07 |
| 0 | 79863 | 2 | -3.77270E+07 | 8.92354E+07 | 1.53121E+07 | 6.78159E+05 | -1.14153E+06 | 83.22 | 9.10559E+07 | -3.95476E+07 | 6.53017E+07 |
| 0 | 79863 | 3 | -4.18664E+07 | 8.01667E+07 | 1.53205E+07 | 1.04875E+06 | -1.77351E+06 | 82.95 | 8.20607E+07 | -4.37604E+07 | 6.29106E+07 |
| 0 | 79863 | 4 | -6.17028E+07 | -1.49197E+07 | 1.05378E+07 | 1.13073E+06 | -1.90669E+06 | 77.87 | -1.26556E+07 | -6.39668E+07 | 2.56556E+07 |
| 0 | 79863 | 5 | -6.31890E+07 | -1.76783E+07 | 1.05420E+07 | 1.18538E+06 | -1.99547E+06 | 77.57 | -1.53550E+07 | -6.55124E+07 | 2.50787E+07 |
| 0 | 79863 | 6 | -6.46753E+07 | -2.04370E+07 | 1.05462E+07 | 1.21271E+06 | -2.03987E+06 | 77.25 | -1.80514E+07 | -6.70609E+07 | 2.45047E+07 |

**Figure 125: Rib .f06 for critical compressive element**

The margin of safety for the compressive stress of the wing rib is given by,

$$M.S. = \frac{\sigma_{Allowable}}{FS * \sigma_{Actual}} - 1 = \frac{-31.6\ ksi}{1.5 * -7.4\ ksi} - 1 = \mathbf{1.87}$$

### 6. Wing Leading Edge

Load Case 1 is determined to be the critical load case for wing leading edge. The leading edge was found to be most critical in shear in the inboard section of the wing. Figure 126 shows the maximum shear stress distribution with the critical region highlighted, and Figure 127 shows the critical region enlarged with the critical element number in that region. As the .f06 screen capture in Figure 128 shows, the maximum shear in the leading edge is 5.3 ksi (36.7 MPa) in layer 2.

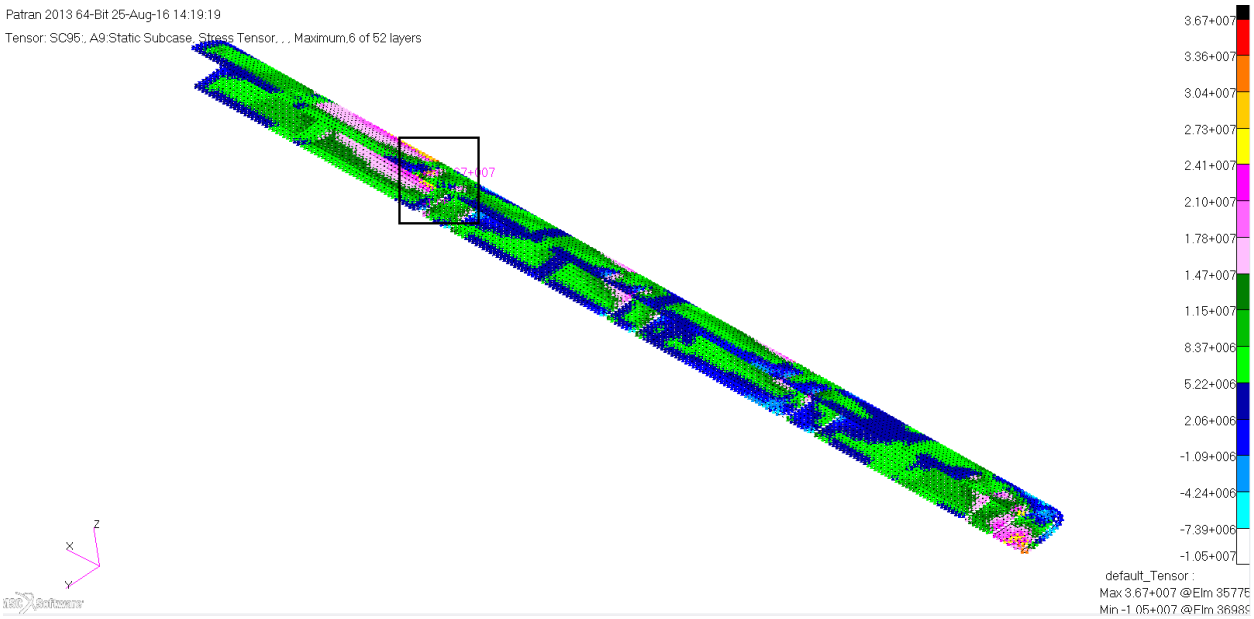


**Figure 126: Leading edge maximum shear stress plot**

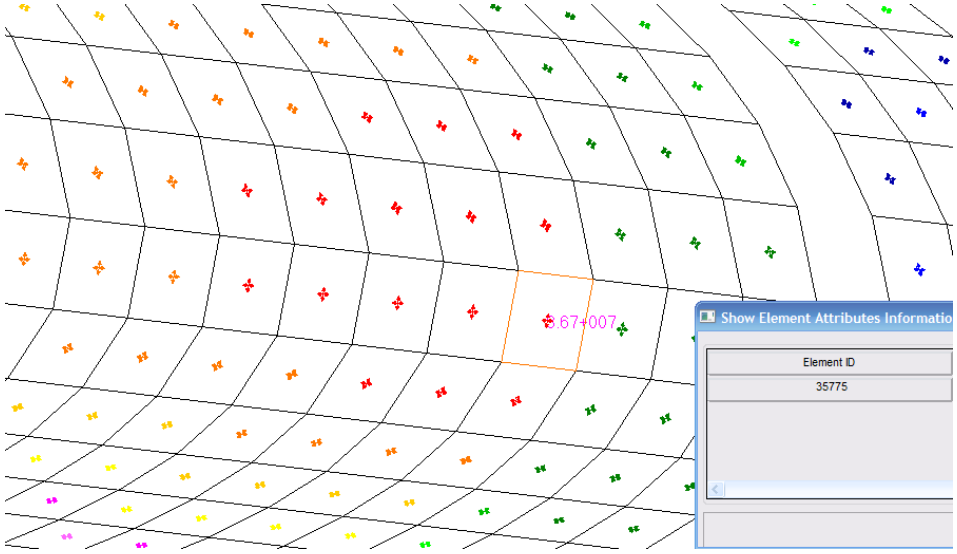


**Figure 127: Leading edge shear critical region**

S T R E S S E S  I N  L A Y E R E D  C O M P O S I T E  E L E M E N T S  ( Q U A D 4 )

| | ELEMENT ID | PLY ID | STRESSES IN FIBER AND MATRIX DIRECTIONS NORMAL-1 | NORMAL-2 | SHEAR-12 | INTER-LAMINAR STRESSES SHEAR XZ-MAT | SHEAR YZ-MAT | PRINCIPAL STRESSES (ZERO SHEAR) ANGLE | MAJOR | MINOR | MAX SHEAR |
|---|---|---|---|---|---|---|---|---|---|---|---|
| 0 | 35770 | 8 | -4.08105E+07 | -1.57278E+06 | 6.46421E-05 | 3.21485E+04 | 1.18801E+05 | 90.00 | -1.57278E+06 | -4.08105E+07 | 1.96189E+07 |
| 0 | 35770 | 9 | -1.49848E+07 | -1.40548E+06 | 7.18137E+05 | 5.25158E-11 | -9.26001E-11 | 86.98 | -1.36761E+06 | -1.50227E+07 | 6.82754E+06 |
| 0 | 35771 | 1 | 4.57384E+07 | 4.70397E+06 | 3.24201E+07 | -1.29617E+05 | -5.35058E+04 | 28.84 | 6.35881E+07 | -1.31457E+07 | 3.83669E+07 |
| 0 | 35771 | 2 | 4.55419E+07 | -4.16533E+05 | 3.18050E+07 | 0.0 | 0.0 | 27.08 | 6.18005E+07 | -1.66751E+07 | 3.92378E+07 |
| 0 | 35772 | 1 | -1.30663E+07 | 5.21219E+06 | 2.15128E+06 | 4.26165E+03 | -1.49184E+05 | 83.38 | 5.46198E+06 | -1.33161E+07 | 9.38903E+06 |
| 0 | 35772 | 2 | -1.37942E+07 | 2.35134E+06 | 2.30874E+06 | 5.68220E+03 | -1.98912E+05 | 82.02 | 2.67499E+06 | -1.41178E+07 | 8.39641E+06 |
| 0 | 35772 | 3 | -1.45221E+07 | -5.09519E+05 | 2.46619E+06 | 4.26165E+03 | -1.49184E+05 | 80.30 | -8.81443E+04 | -1.49434E+07 | 7.42765E+06 |
| 0 | 35772 | 4 | -1.52499E+07 | -3.37038E+06 | 2.62364E+06 | 0.0 | 0.0 | 78.08 | -2.81674E+06 | -1.58036E+07 | 6.49342E+06 |
| 0 | 35773 | 1 | 3.61661E+07 | 9.24845E+06 | 3.48283E+07 | -9.80340E+04 | -3.69858E+04 | 34.44 | 6.00456E+07 | -1.46310E+07 | 3.73383E+07 |
| 0 | 35773 | 2 | 3.47254E+07 | -1.21728E+06 | 3.48807E+07 | 0.0 | 0.0 | 31.37 | 5.59922E+07 | -2.24841E+07 | 3.92382E+07 |
| 0 | 35774 | 1 | -1.52004E+07 | 1.13283E+06 | 2.97893E+06 | -2.00185E+04 | -5.89475E+04 | 79.98 | 1.65917E+06 | -1.57267E+07 | 8.69295E+06 |
| 0 | 35774 | 2 | -1.47246E+07 | 2.08636E+06 | 3.19486E+06 | -2.66913E+04 | -7.85967E+04 | 79.59 | 2.67305E+06 | -1.53113E+07 | 8.99218E+06 |
| 0 | 35774 | 3 | -1.42489E+07 | 3.03989E+06 | 3.41080E+06 | -2.00185E+04 | -5.89475E+04 | 79.23 | 3.68845E+06 | -1.48974E+07 | 9.29294E+06 |
| 0 | 35774 | 4 | -1.37731E+07 | 3.99342E+06 | 3.62673E+06 | 0.0 | 0.0 | 78.90 | 4.70523E+06 | -1.44849E+07 | 9.59507E+06 |
| 0 | 35775 | 1 | 1.56478E+07 | 1.22558E+07 | 3.64353E+07 | -2.44993E+04 | 4.00323E+04 | 43.67 | 5.04265E+07 | -2.25229E+07 | 3.64747E+07 |
| 0 | 35775 | 2 | 1.38888E+07 | 1.71490E+05 | 3.67404E+07 | 0.0 | 0.0 | 39.71 | 4.44052E+07 | -3.03449E+07 | 3.73751E+07 |
| 0 | 35777 | 1 | -2.04225E+07 | 4.67509E+06 | 6.80650E+06 | -2.06835E+04 | -2.41996E+02 | 75.76 | 6.40217E+06 | -2.21496E+07 | 1.42759E+07 |
| 0 | 35777 | 2 | -1.89430E+07 | 8.03614E+06 | 7.41375E+06 | 0.0 | 0.0 | 75.60 | 9.93918E+06 | -2.08460E+07 | 1.53926E+07 |
| 0 | 35778 | 1 | -7.22398E+06 | 7.68792E+06 | 3.66440E+07 | 5.32485E+04 | 9.78746E+04 | 50.75 | 3.76268E+07 | -3.71629E+07 | 3.73949E+07 |
| 0 | 35778 | 2 | -7.85615E+06 | 4.16398E+06 | 3.65442E+07 | 0.0 | 0.0 | 49.67 | 3.51891E+07 | -3.88812E+07 | 3.70351E+07 |

**Figure 128: Leading edge .f06 for critical shear element**

The margin of safety for the shear stress of the wing leading edge is given by,

$$M.S. = \frac{\tau_{Allowable}}{FS * \ \tau_{Actual}} - 1 = \frac{9.2\ ksi}{1.5 * 5.3\ ksi} - 1 = \mathbf{0.15}$$

# Appendix B - Wing Design II

This section includes the critical stress region of each individual wing component of Wing Design II, which includes; upper skin, lower skin, front spar, rear spar, wing rib and wing leading edge. The material of all the critical layer of the components in this section is carbon fiber cloth, with 0° orientations. For the margin of safety calculations, the allowable stresses are taken from Table 27.

### 1. Upper Skin

Load Case 2 is determined to be the critical load case for upper skin. The upper skin was found to be most critical in longitudinal compression in the inboard section of the wing. Figure 129 shows the maximum longitudinal compressive stress distribution with the critical region highlighted, and Figure 130 shows the critical region enlarged with the critical element number in that region. As the .f06 screen capture in Figure 131shows, the maximum longitudinal compression in the upper skin is -35.5 ksi (-245 MPa) in layer 5.

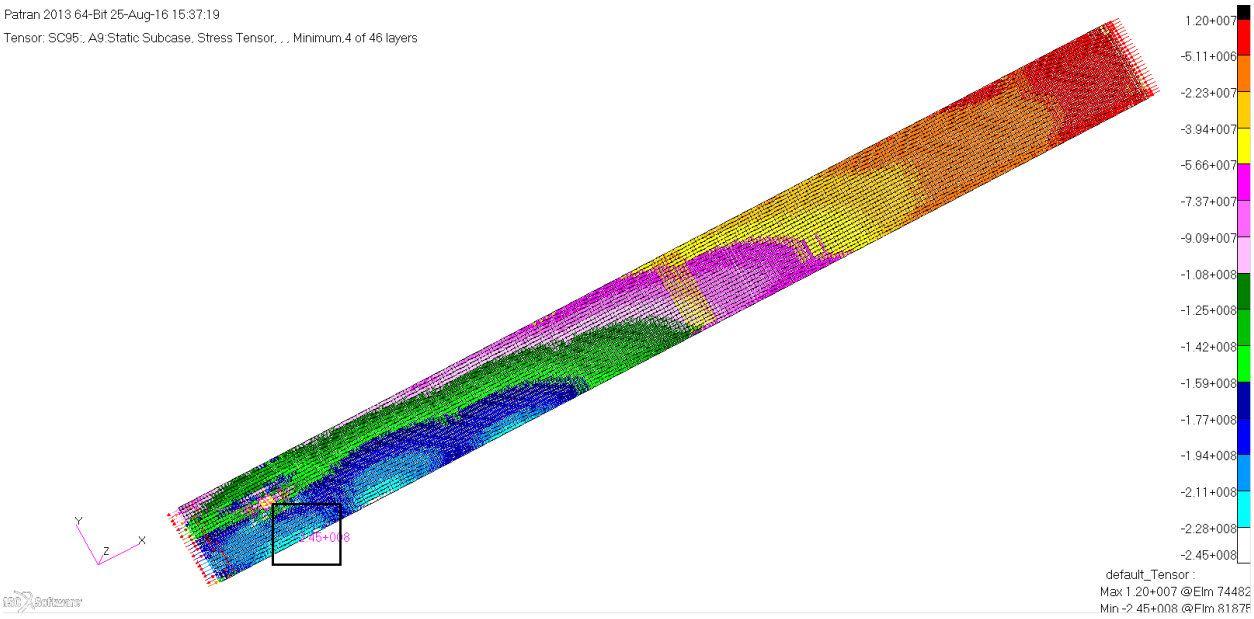


**Figure 129: Upper skin maximum longitudinal compression stress plot**

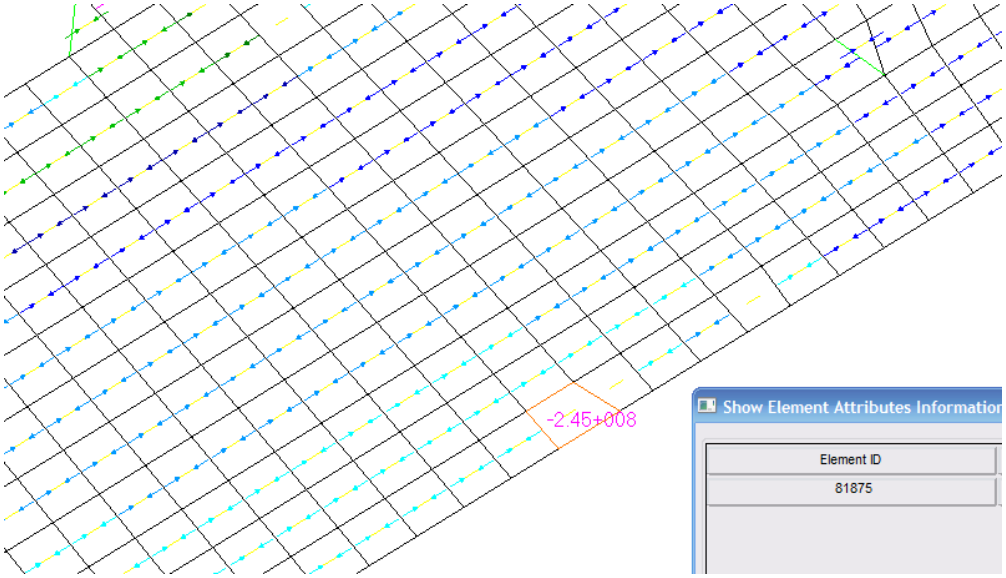


**Figure 130: Upper skin compression critical region**

S T R E S S E S  I N  L A Y E R E D  C O M P O S I T E  E L E M E N T S  ( Q U A D 4 )

| | ELEMENT ID | PLY ID | STRESSES IN FIBER AND MATRIX DIRECTIONS NORMAL-1 | NORMAL-2 | SHEAR-12 | INTER-LAMINAR STRESSES SHEAR XZ-MAT | SHEAR YZ-MAT | PRINCIPAL STRESSES (ZERO SHEAR) ANGLE | MAJOR | MINOR | MAX SHEAR |
|---|---|---|---|---|---|---|---|---|---|---|---|
| 0 | 81874 | 7 | -1.92123E+08 | 3.40207E+06 | -7.87242E+06 | -6.98004E+05 | 2.02005E+06 | -87.70 | 3.71853E+06 | -1.92439E+08 | 9.80789E+07 |
| 0 | 81874 | 8 | -1.45335E+08 | -4.73967E+07 | 1.62358E+07 | -3.98860E+05 | 1.15431E+06 | 80.83 | -4.47753E+07 | -1.47957E+08 | 5.15907E+07 |
| 0 | 81874 | 9 | -1.49805E+08 | -4.69383E+07 | 1.59223E+07 | 4.76856E-10 | -1.38004E-09 | 81.40 | -4.45301E+07 | -1.52213E+08 | 5.38416E+07 |
| 0 | 81875 | 1 | -1.65807E+08 | -2.83522E+07 | 1.12754E+07 | 2.50771E+03 | 8.14776E+04 | 85.34 | -2.74334E+07 | -1.66726E+08 | 6.96463E+07 |
| 0 | 81875 | 2 | -1.67392E+08 | -2.76655E+07 | 1.09947E+07 | 4.91540E+03 | 1.59705E+05 | 85.53 | -2.68056E+07 | -1.68252E+08 | 7.07230E+07 |
| 0 | 81875 | 3 | -1.95121E+03 | -2.89112E+02 | 0.0 | 4.91540E+03 | 1.59705E+05 | 90.00 | -2.89112E+02 | -1.95121E+03 | 8.31049E+02 |
| 0 | 81875 | 4 | -2.43675E+08 | 5.39196E+06 | -2.51564E+06 | 2.50771E+03 | 8.14776E+04 | -89.42 | 5.41736E+06 | -2.43701E+08 | 1.24559E+08 |
| 0 | 81875 | 5 | -2.45260E+08 | 6.07861E+06 | -2.79627E+06 | 9.98306E-12 | 6.48716E-11 | -89.36 | 6.10972E+06 | -2.45291E+08 | 1.25700E+08 |
| 0 | 81877 | 1 | -4.05873E+07 | -7.31950E+07 | 2.16395E+07 | 6.36259E+05 | -7.05123E+04 | 26.50 | -2.97972E+07 | -8.39851E+07 | 2.70940E+07 |
| 0 | 81877 | 2 | -3.52036E+08 | 4.36385E+06 | 2.79932E+06 | 1.28934E+06 | -7.78661E+04 | 89.55 | 4.38584E+06 | -3.52058E+08 | 1.78222E+08 |
| 0 | 81877 | 3 | -3.52219E+08 | 4.13718E+06 | 2.72928E+06 | 1.91662E+06 | -8.49293E+04 | 89.56 | 4.15808E+06 | -3.52240E+08 | 1.78199E+08 |
| 0 | 81877 | 4 | -3.52402E+08 | 3.91051E+06 | 2.65923E+06 | 2.51807E+06 | -9.17017E+04 | 89.57 | 3.93035E+06 | -3.52422E+08 | 1.78176E+08 |
| 0 | 81877 | 5 | -3.52585E+08 | 3.68384E+06 | 2.58919E+06 | 3.09372E+06 | -9.81835E+04 | 89.58 | 3.70265E+06 | -3.52604E+08 | 1.78153E+08 |
| 0 | 81877 | 6 | -4.76574E+07 | -7.49687E+07 | 2.10398E+07 | 3.57091E+06 | -1.51068E+05 | 28.51 | -3.62301E+07 | -8.63959E+07 | 2.50829E+07 |
| 0 | 81877 | 7 | -3.53280E+08 | 2.82248E+06 | 2.32302E+06 | 4.04847E+06 | -1.56445E+05 | 89.63 | 2.83764E+06 | -3.53295E+08 | 1.78066E+08 |

***Figure 131:*** **Upper skin .f06 for critical compressive element**

The margin of safety for the compressive stress of the wing upper skin is given by,

$$M.S. = \frac{\sigma_{Allowable}}{FS * \sigma_{Actual}} - 1 = \frac{-82\ ksi}{1.5 * -35.5\ ksi} - 1 = \mathbf{0.54}$$

## 2. Lower Skin

Load Case 2 is determined to be the critical load case for lower skin. The lower skin was found to be most critical in shear in the inboard section of the wing. Figure 132 shows the maximum shear stress distribution with the critical region highlighted, and Figure 133 shows the critical region enlarged with the critical element number in that region. As the .f06 screen capture in Figure 134 shows, the maximum shear in the lower skin is 6 ksi (41 MPa) in layer 10.

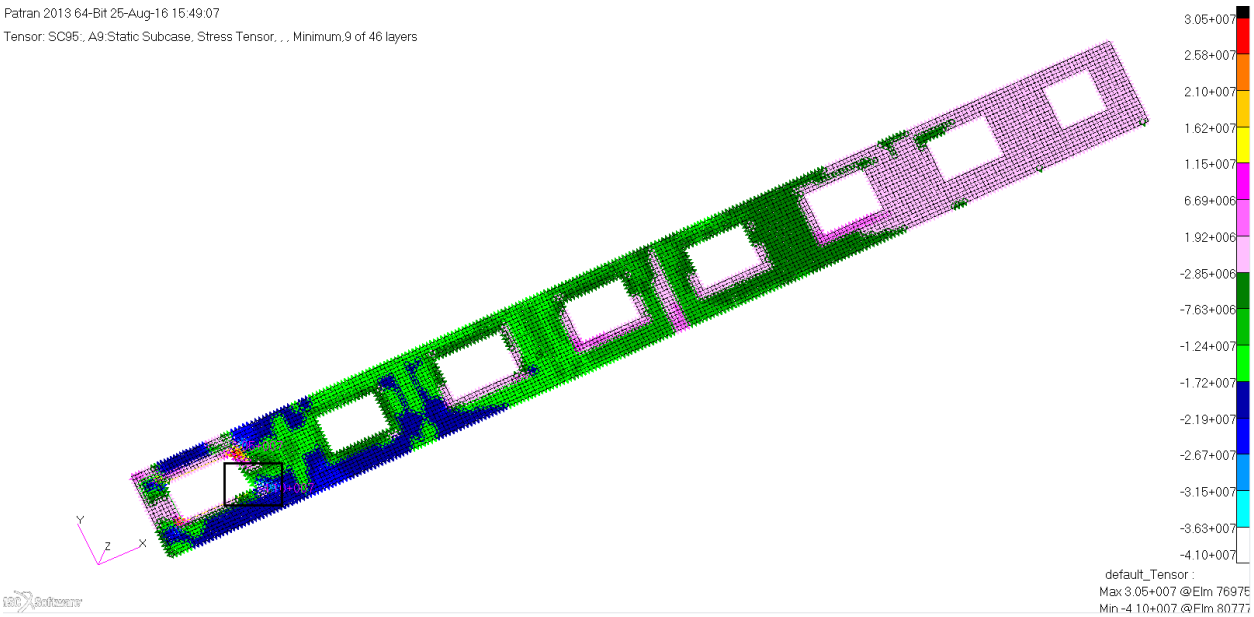


**Figure 132: Lower skin maximum shear stress plot**

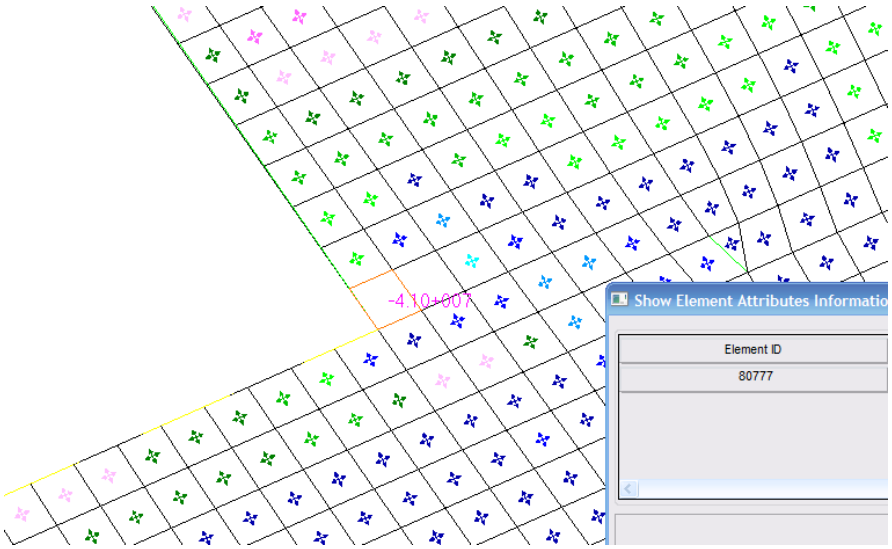


**Figure 133: Lower skin shear critical region**

| | | | | | | | | | | | | |
|---|---|---|---|---|---|---|---|---|---|---|---|---|
| 0 | 80777 | 1 | 5.39685E+07 | 2.28666E+07 | -3.78782E+07 | 1.52770E+03 | -6.21900E+04 | -33.84 | 7.93637E+07 | -2.52859E+06 | 4.09462E+07 |
| 0 | 80777 | 2 | 5.52685E+07 | 1.85551E+07 | -3.82280E+07 | 2.71591E+03 | -1.10560E+05 | -32.18 | 7.93187E+07 | -5.49512E+06 | 4.24069E+07 |
| 0 | 80777 | 3 | 5.65685E+07 | 1.42436E+07 | -3.85778E+07 | 3.56463E+03 | -1.45110E+05 | -30.63 | 7.94071E+07 | -8.59504E+06 | 4.40011E+07 |
| 0 | 80777 | 4 | 5.78685E+07 | 9.93205E+06 | -3.89276E+07 | 4.07386E+03 | -1.65840E+05 | -29.19 | 7.96149E+07 | -1.18144E+07 | 4.57147E+07 |
| 0 | 80777 | 5 | 5.91685E+07 | 5.62053E+06 | -3.92774E+07 | 4.24361E+03 | -1.72750E+05 | -27.86 | 7.99293E+07 | -1.51403E+07 | 4.75348E+07 |
| 0 | 80777 | 6 | 6.04684E+07 | 1.30901E+06 | -3.96272E+07 | 4.07386E+03 | -1.65840E+05 | -26.63 | 8.03384E+07 | -1.85610E+07 | 4.94497E+07 |
| 0 | 80777 | 7 | 6.17684E+07 | -3.00251E+06 | -3.99770E+07 | 3.56463E+03 | -1.45110E+05 | -25.49 | 8.08317E+07 | -2.20658E+07 | 5.14488E+07 |
| 0 | 80777 | 8 | 6.30684E+07 | -7.31402E+06 | -4.03268E+07 | 2.71591E+03 | -1.10560E+05 | -24.45 | 8.13998E+07 | -2.56454E+07 | 5.35226E+07 |
| 0 | 80777 | 9 | 6.43684E+07 | -1.16255E+07 | -4.06766E+07 | 1.52770E+03 | -6.21900E+04 | -23.48 | 8.20343E+07 | -2.92914E+07 | 5.56629E+07 |
| 0 | 80777 | 10 | 6.56684E+07 | -1.59371E+07 | -4.10264E+07 | 6.49437E-12 | -2.64375E-10 | -22.58 | 8.27278E+07 | -3.29965E+07 | 5.78621E+07 |

1 THIS IS A DEFAULT SUBCASE. AUGUST 8, 2016 MSC Nastran 3/14/14 PAGE 12568

0 SUBCASE 95

S T R E S S E S I N L A Y E R E D C O M P O S I T E E L E M E N T S ( Q U A D 4 )

| ELEMENT ID | PLY ID | STRESSES IN FIBER AND MATRIX DIRECTIONS NORMAL-1 | NORMAL-2 | SHEAR-12 | INTER-LAMINAR STRESSES SHEAR XZ-MAT | SHEAR YZ-MAT | PRINCIPAL STRESSES (ZERO SHEAR) ANGLE | MAJOR | MINOR | MAX SHEAR |
|---|---|---|---|---|---|---|---|---|---|---|
| 0 80778 | 1 | 1.30550E+08 | 3.52946E+06 | -3.60894E+06 | -2.01723E+04 | 2.62339E+04 | -1.63 | 1.30653E+08 | 3.42700E+06 | 6.36129E+07 |
| 0 80778 | 2 | 1.30512E+08 | 2.03431E+06 | -3.86327E+06 | -3.58619E+04 | 4.66381E+04 | -1.72 | 1.30628E+08 | 1.91824E+06 | 6.43550E+07 |
| 0 80778 | 3 | 1.30474E+08 | 5.39152E+05 | -4.11760E+06 | -4.70687E+04 | 6.12124E+04 | -1.81 | 1.30604E+08 | 4.08797E+05 | 6.50978E+07 |
| 0 80778 | 4 | 1.30436E+08 | -9.56002E+05 | -4.37193E+06 | -5.37928E+04 | 6.99571E+04 | -1.90 | 1.30581E+08 | -1.10131E+06 | 6.58412E+07 |

**Figure 134: Lower skin .f06 for critical shear element**

The margin of safety for the shear stress of the wing lower skin is given by,

$$M.S. = \frac{\tau_{Allowable}}{FS * \tau_{Actual}} - 1 = \frac{13\ ksi}{1.5 * 6\ ksi} - 1 = \mathbf{0.50}$$

### 3. Wing Front Spar

Load Case 2 is determined to be the critical load case for front spar. The front spar was found to be most critical in transverse compression in the inboard section of the wing. Figure 135 shows the maximum transverse compressive stress distribution with the critical region highlighted, and Figure 136 shows the critical region enlarged with the critical element number in that region. As the .f06 screen capture in Figure 137 shows, the maximum transverse compression in the front spar is -51.6 ksi (-356 MPa) in layer 9.

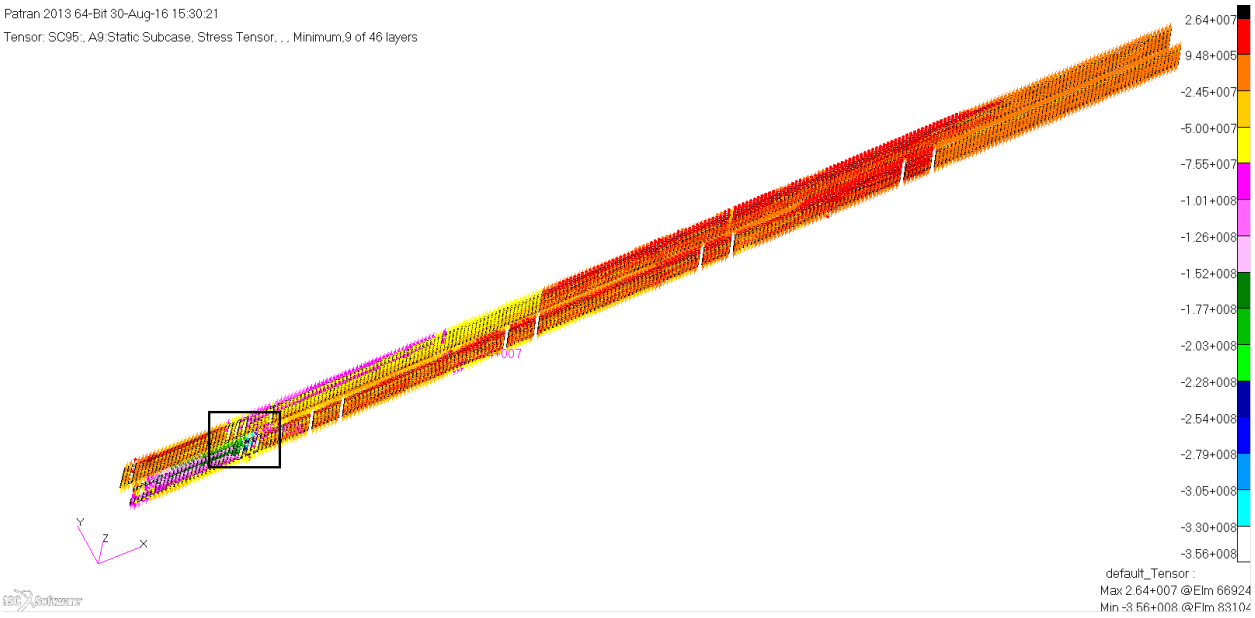


**Figure 135: Front spar maximum transverse compression stress plot**

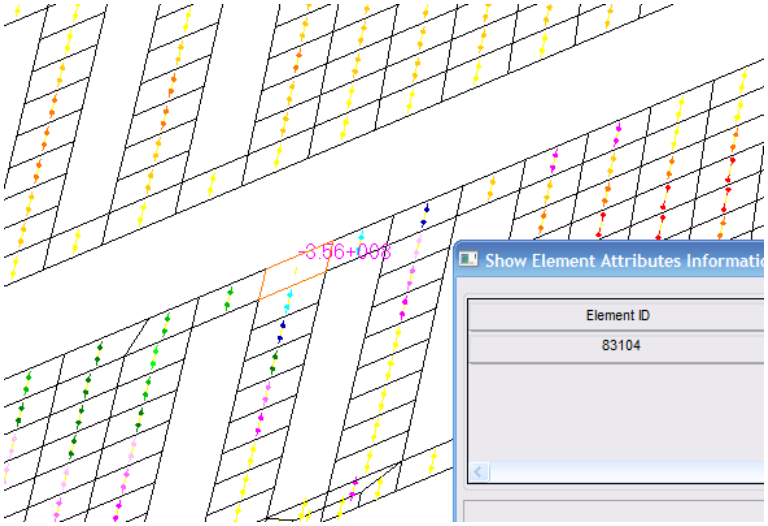


**Figure 136: Front spar compression critical region**

| | | | | | | | | | | | |
|---|---|---|---|---|---|---|---|---|---|---|---|
| 0 | 83104 | 6 | -2.16314E+08 | -1.66696E+08 | 2.78121E+07 | -2.66862E+06 | 1.73847E+06 | 65.87 | -1.54236E+08 | -2.28775E+08 | 3.72693E+07 |
| 0 | 83104 | 7 | -2.16675E+08 | -1.60230E+08 | 2.83342E+07 | -1.81618E+06 | 1.18315E+06 | 67.44 | -1.48461E+08 | -2.28444E+08 | 3.99917E+07 |
| 0 | 83104 | 8 | -1.49341E+07 | -3.55865E+08 | 5.35533E+06 | -1.03782E+06 | 6.76084E+05 | 0.90 | -1.48500E+07 | -3.55949E+08 | 1.70549E+08 |
| 0 | 83104 | 9 | -8.79654E+06 | -3.55896E+08 | 5.93317E+06 | 1.24076E-09 | -8.08291E-10 | 0.98 | -8.69514E+06 | -3.55998E+08 | 1.73651E+08 |
| 0 | 83105 | 1 | -1.90950E+08 | -3.22718E+08 | -1.42347E+07 | 5.05236E+05 | 1.74251E+05 | -6.10 | -1.89430E+08 | -3.24238E+08 | 6.74044E+07 |
| 0 | 83105 | 2 | -1.84351E+08 | -3.16960E+08 | -1.38561E+07 | 8.84164E+05 | 3.04939E+05 | -5.90 | -1.82919E+08 | -3.18392E+08 | 6.77366E+07 |
| 0 | 83105 | 3 | -1.64860E+08 | -3.24094E+08 | 1.12951E+07 | 1.29916E+06 | 4.48066E+05 | 4.04 | -1.64063E+08 | -3.24891E+08 | 8.04141E+07 |
| 0 | 83105 | 4 | -1.60918E+08 | -3.15679E+08 | 1.13662E+07 | 1.50665E+06 | 5.19629E+05 | 4.18 | -1.60087E+08 | -3.16509E+08 | 7.82109E+07 |
| 0 | 83105 | 5 | -1.56975E+08 | -3.07264E+08 | 1.14373E+07 | 1.50665E+06 | 5.19629E+05 | 4.33 | -1.56110E+08 | -3.08129E+08 | 7.60096E+07 |

1 THIS IS A DEFAULT SUBCASE. AUGUST 8, 2016 MSC Nastran 3/14/14 PAGE 13242

0 SUBCASE 95

S T R E S S E S I N L A Y E R E D C O M P O S I T E E L E M E N T S ( Q U A D 4 )

| ELEMENT ID | PLY ID | STRESSES IN FIBER AND MATRIX DIRECTIONS NORMAL-1 | NORMAL-2 | SHEAR-12 | INTER-LAMINAR STRESSES SHEAR XZ-MAT | SHEAR YZ-MAT | PRINCIPAL STRESSES (ZERO SHEAR) ANGLE | MAJOR | MINOR | MAX SHEAR |
|---|---|---|---|---|---|---|---|---|---|---|
| 0 83105 | 6 | -1.53033E+08 | -2.98849E+08 | 1.15084E+07 | 1.29916E+06 | 4.48066E+05 | 4.49 | -1.52130E+08 | -2.99752E+08 | 7.38106E+07 |
| 0 83105 | 7 | -1.49091E+08 | -2.90434E+08 | 1.15796E+07 | 8.84164E+05 | 3.04939E+05 | 4.65 | -1.48149E+08 | -2.91376E+08 | 7.16139E+07 |
| 0 83105 | 8 | -1.44759E+08 | -2.82409E+08 | -1.15847E+07 | 5.05236E+05 | 1.74251E+05 | -4.78 | -1.43791E+08 | -2.83377E+08 | 6.97930E+07 |
| 0 83105 | 9 | -1.38160E+08 | -2.76650E+08 | -1.12062E+07 | -6.04034E-10 | -2.08325E-10 | -4.60 | -1.37259E+08 | -2.77551E+08 | 7.01458E+07 |
| 0 83106 | 1 | -3.34979E+08 | -1.48569E+08 | -3.81017E+06 | -2.05701E+05 | 7.68897E+05 | -88.83 | -1.48491E+08 | -3.35057E+08 | 9.32829E+07 |
| 0 83106 | 2 | -3.31114E+08 | -1.43584E+08 | -3.52728E+06 | -3.59976E+05 | 1.34557E+06 | -88.92 | -1.43517E+08 | -3.31180E+08 | 9.38312E+07 |
| 0 83106 | 3 | -2.13758E+08 | -2.52089E+08 | -1.59673E+07 | -5.28935E+05 | 1.97713E+06 | -19.90 | -2.07978E+08 | -2.57869E+08 | 2.49456E+07 |

***Figure 137:*** **Front spar .f06 for critical compressive element**

The margin of safety for the compressive stress of the front spar is given by,

$$M.S. = \frac{\sigma_{Allowable}}{FS * \sigma_{Actual}} - 1 = \frac{-82\ ksi}{1.5 * -51.6\ ksi} - 1 = \mathbf{0.059}$$

### 4. Wing Rear Spar

Load Case 2 is determined to be the critical load case for rear spar. The rear spar was found to be most critical in transverse compression in the inboard section of the wing. Figure 138 shows the maximum transverse compressive stress distribution with the critical region highlighted, and Figure 139 shows the critical region enlarged with the critical element number in that region. As the .f06 screen capture in Figure 140 shows, the maximum transverse compression in the rear spar is -36.4 ksi (-251 MPa) in layer 1.

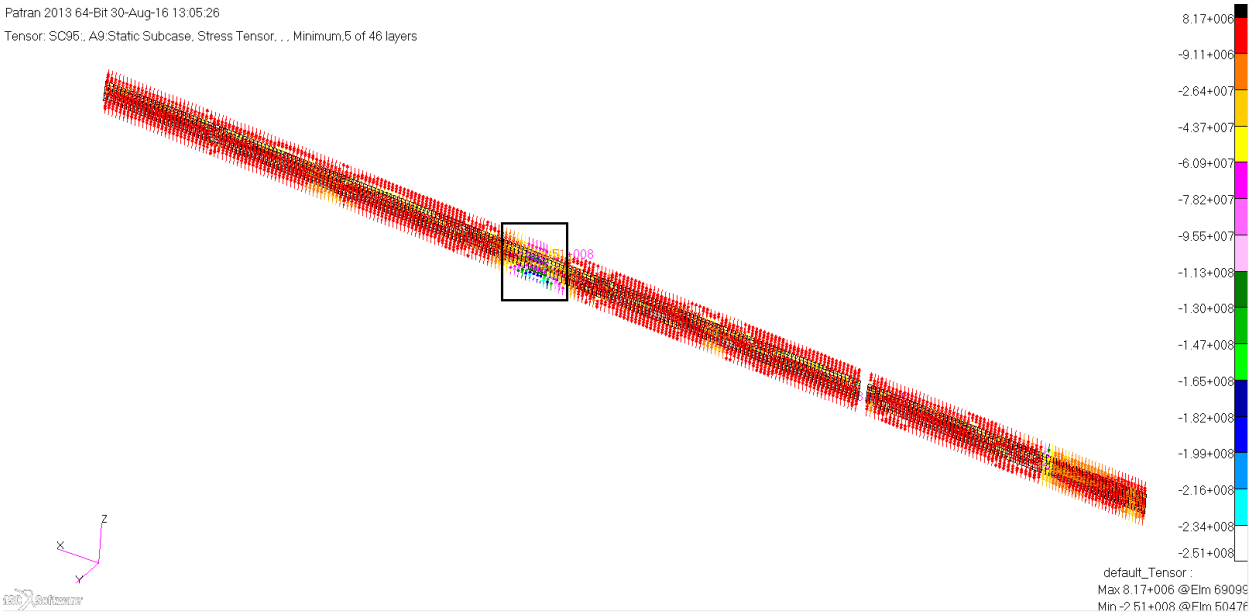


**Figure 138: Rear spar maximum transverse compression stress plot**

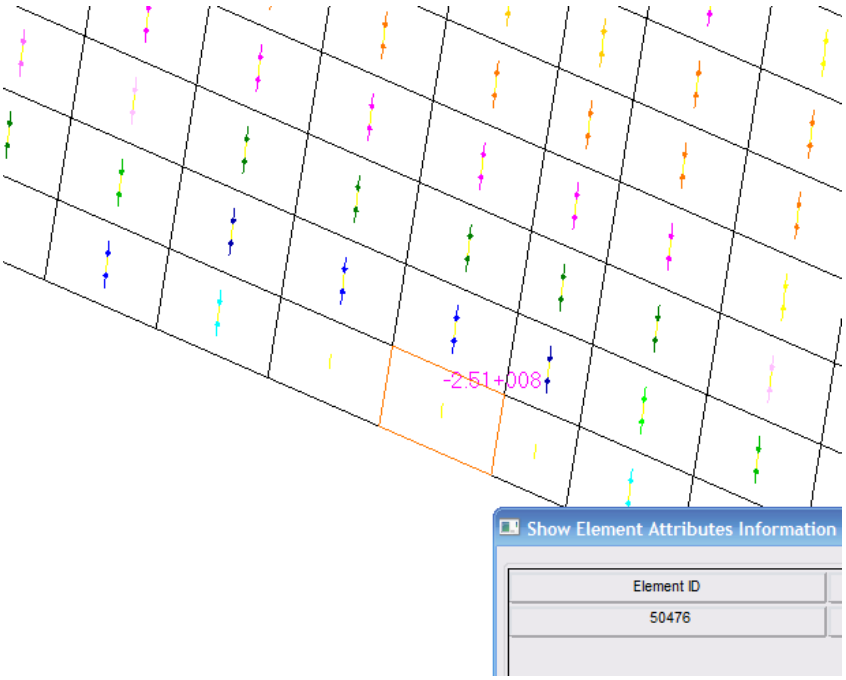


**Figure 139: Rear spar compression critical region**

S T R E S S E S  I N  L A Y E R E D  C O M P O S I T E  E L E M E N T S  ( Q U A D 4 )

| | ELEMENT ID | PLY ID | STRESSES IN FIBER AND MATRIX DIRECTIONS NORMAL-1 | NORMAL-2 | SHEAR-12 | INTER-LAMINAR STRESSES SHEAR XZ-MAT | SHEAR YZ-MAT | PRINCIPAL STRESSES (ZERO SHEAR) ANGLE | MAJOR | MINOR | MAX SHEAR |
|---|---|---|---|---|---|---|---|---|---|---|---|
| 0 | 50474 | 2 | 1.71314E+06 | -6.69549E+07 | -1.54037E+07 | 1.25643E+05 | 2.32533E+06 | -12.08 | 5.01022E+06 | -7.02520E+07 | 3.76311E+07 |
| 0 | 50474 | 3 | 1.39954E+07 | -4.58680E+06 | -1.49615E+07 | 1.25643E+05 | 2.32533E+06 | -29.08 | 2.23159E+07 | -1.29074E+07 | 1.76117E+07 |
| 0 | 50474 | 4 | 2.62776E+07 | 5.77813E+07 | -1.45193E+07 | 8.37619E+04 | 1.55022E+06 | -68.67 | 6.34521E+07 | 2.06068E+07 | 2.14227E+07 |
| 0 | 50474 | 5 | 3.85598E+07 | 1.20149E+08 | -1.40770E+07 | 1.39335E-10 | 2.57874E-09 | -80.48 | 1.22510E+08 | 3.61993E+07 | 4.31553E+07 |
| 0 | 50475 | 1 | -6.04820E+06 | -1.88161E+08 | -1.67994E+07 | 1.01576E+05 | 1.62457E+06 | -5.23 | -4.51146E+06 | -1.89698E+08 | 9.25931E+07 |
| 0 | 50475 | 2 | 7.13848E+06 | -9.71242E+07 | -1.59836E+07 | 1.52363E+05 | 2.43685E+06 | -8.52 | 9.53376E+06 | -9.95195E+07 | 5.45266E+07 |
| 0 | 50475 | 3 | 2.03252E+07 | -6.08751E+06 | -1.51678E+07 | 1.52363E+05 | 2.43685E+06 | -24.48 | 2.72303E+07 | -1.29926E+07 | 2.01114E+07 |
| 0 | 50475 | 4 | 3.35118E+07 | 8.49492E+07 | -1.43520E+07 | 1.01576E+05 | 1.62457E+06 | -75.42 | 8.86827E+07 | 2.97783E+07 | 2.94522E+07 |
| 0 | 50475 | 5 | 4.66985E+07 | 1.75986E+08 | -1.35362E+07 | 1.68968E-10 | 2.70241E-09 | -84.09 | 1.77388E+08 | 4.52965E+07 | 6.60457E+07 |
| 0 | 50476 | 1 | 2.57728E+06 | -2.50992E+08 | -1.76163E+07 | 1.35626E+05 | 1.71842E+06 | -3.96 | 3.79530E+06 | -2.52210E+08 | 1.28003E+08 |
| 0 | 50476 | 2 | 1.32156E+07 | -1.29179E+08 | -1.63751E+07 | 2.03439E+05 | 2.57764E+06 | -6.48 | 1.50744E+07 | -1.31038E+08 | 7.30560E+07 |
| 0 | 50476 | 3 | 2.38539E+07 | -7.36540E+06 | -1.51338E+07 | 2.03439E+05 | 2.57764E+06 | -22.06 | 2.99857E+07 | -1.34973E+07 | 2.17415E+07 |
| 0 | 50476 | 4 | 3.44922E+07 | 1.14448E+08 | -1.38925E+07 | 1.35626E+05 | 1.71842E+06 | -80.42 | 1.16793E+08 | 3.21471E+07 | 4.23230E+07 |
| 0 | 50476 | 5 | 4.51305E+07 | 2.36261E+08 | -1.26513E+07 | 2.25610E-10 | 2.85854E-09 | -86.23 | 2.37095E+08 | 4.42967E+07 | 9.63992E+07 |
| 0 | 50477 | 1 | 6.81600E+07 | -3.78306E+07 | -3.89698E+06 | -4.14914E+04 | -1.70614E+06 | -2.10 | 6.83031E+07 | -3.79737E+07 | 5.31384E+07 |
| 0 | 50477 | 2 | 6.17069E+07 | -3.01785E+07 | -3.58388E+06 | -7.37625E+04 | -3.03314E+06 | -2.23 | 6.18465E+07 | -3.03180E+07 | 4.60823E+07 |
| 0 | 50477 | 3 | 5.52539E+07 | -2.25264E+07 | -3.27079E+06 | -9.68133E+04 | -3.98099E+06 | -2.40 | 5.53912E+07 | -2.26637E+07 | 3.90274E+07 |

**Figure 140: Rear spar .f06 for critical compressive element**

The margin of safety for the compressive stress of the rear spar is given by,

$$M.S. = \frac{\sigma_{Allowable}}{FS * \sigma_{Actual}} - 1 = \frac{-82\ ksi}{1.5 * -36.4\ ksi} - 1 = \mathbf{0.5}$$

## 5. Wing Rib

Load Case 2 is determined to be the critical load case for wing rib. The wing rib was found to be most critical in shear in the inboard section of the wing. Figure 141 shows the maximum shear stress distribution with the critical region highlighted, and Figure 142 shows the critical region enlarged with the critical element number in that region. As the .f06 screen capture in Figure 143 shows, the maximum shear in the wing rib is 4.1 ksi (28.5 MPa) in layer 3.


**Figure 141: Rib maximum shear stress plot**

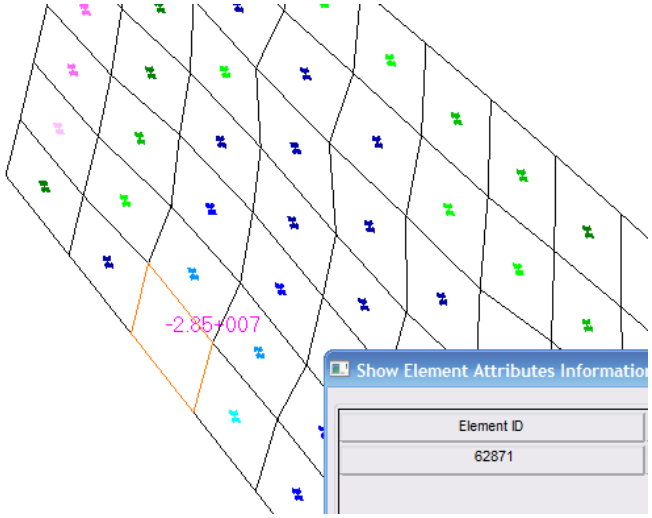


***Figure 142:*** **Rib shear critical region**

S T R E S S E S  I N  L A Y E R E D  C O M P O S I T E  E L E M E N T S  ( Q U A D 4 )

| | ELEMENT ID | PLY ID | STRESSES IN FIBER AND MATRIX DIRECTIONS NORMAL-1 | NORMAL-2 | SHEAR-12 | INTER-LAMINAR STRESSES SHEAR XZ-MAT | SHEAR YZ-MAT | PRINCIPAL STRESSES (ZERO SHEAR) ANGLE | MAJOR | MINOR | MAX SHEAR |
|---|---|---|---|---|---|---|---|---|---|---|---|
| 0 | 62868 | 2 | 1.66949E+07 | 1.62069E+07 | -7.57762E+06 | -1.32822E+06 | 6.88977E+04 | -44.08 | 2.40324E+07 | 8.86934E+06 | 7.58155E+06 |
| 0 | 62868 | 3 | 2.17658E+07 | 3.19520E+07 | -9.04090E+06 | -1.53463E+06 | 7.96045E+04 | -59.70 | 3.72357E+07 | 1.64821E+07 | 1.03768E+07 |
| 0 | 62868 | 4 | 9.93190E+07 | -2.47852E+07 | -1.76561E+06 | -1.37245E+06 | 7.11917E+04 | -0.81 | 9.93441E+07 | -2.48103E+07 | 6.20772E+07 |
| 0 | 62868 | 5 | 1.18371E+08 | -2.30213E+07 | -2.66906E+06 | -7.08997E+05 | 3.67772E+04 | -1.08 | 1.18421E+08 | -2.30717E+07 | 7.07466E+07 |
| 0 | 62868 | 6 | 3.69787E+07 | 7.91871E+07 | -1.34307E+07 | -2.11749E-02 | 1.09839E-03 | -73.76 | 8.30983E+07 | 3.30675E+07 | 2.50154E+07 |
| 0 | 62869 | 1 | 6.59950E+06 | -3.27572E+07 | -2.13570E+07 | -7.06954E+04 | 6.96448E+03 | -23.67 | 1.59618E+07 | -4.21195E+07 | 2.90406E+07 |
| 0 | 62869 | 2 | -4.34568E+04 | -7.06570E+04 | -1.19106E+05 | -7.06954E+04 | 6.96448E+03 | -41.74 | 6.28231E+04 | -1.76937E+05 | 1.19880E+05 |
| 0 | 62869 | 3 | -1.36043E+07 | -3.53711E+07 | -2.39510E+07 | -1.99563E-10 | 1.96597E-11 | -32.78 | 1.82005E+06 | -5.07955E+07 | 2.63078E+07 |
| 0 | 62870 | 1 | 1.08096E+07 | 2.05237E+07 | -4.40138E+06 | -8.62018E+05 | 9.30140E+05 | -68.91 | 2.22213E+07 | 9.11199E+06 | 6.55466E+06 |
| 0 | 62870 | 2 | 1.69670E+07 | 2.81364E+07 | -6.72533E+06 | -1.40196E+06 | 1.51275E+06 | -64.85 | 3.12935E+07 | 1.38099E+07 | 8.74179E+06 |
| 0 | 62870 | 3 | 2.31244E+07 | 3.57490E+07 | -9.04928E+06 | -1.61983E+06 | 1.74784E+06 | -62.45 | 4.04700E+07 | 1.84034E+07 | 1.10333E+07 |
| 0 | 62870 | 4 | 1.03508E+08 | -3.08642E+07 | -1.19171E+06 | -1.44864E+06 | 1.56312E+06 | -0.51 | 1.03518E+08 | -3.08748E+07 | 6.71965E+07 |
| 0 | 62870 | 5 | 1.24121E+08 | -3.77076E+07 | -1.31488E+06 | -7.48358E+05 | 8.07498E+05 | -0.47 | 1.24132E+08 | -3.77183E+07 | 8.09251E+07 |
| 0 | 62870 | 6 | 4.15967E+07 | 5.85868E+07 | -1.60211E+07 | -2.23505E-02 | 2.41168E-02 | -58.97 | 6.82258E+07 | 3.19577E+07 | 1.81340E+07 |
| 0 | 62871 | 1 | -1.36886E+07 | -3.12274E+07 | -2.50924E+07 | -1.00891E+05 | 7.97941E+03 | -35.37 | 4.12272E+06 | -4.90387E+07 | 2.65807E+07 |
| 0 | 62871 | 2 | -9.36735E+04 | -9.69626E+04 | -1.40994E+05 | -1.00891E+05 | 7.97941E+03 | -44.67 | 4.56857E+04 | -2.36322E+05 | 1.41004E+05 |
| 0 | 62871 | 3 | -4.53738E+07 | -3.52261E+07 | -2.85418E+07 | -2.84800E-10 | 2.25247E-11 | -50.04 | -1.13107E+07 | -6.92893E+07 | 2.89893E+07 |
| 0 | 62872 | 1 | 3.38629E+07 | 8.21382E+06 | -5.61875E+06 | -2.05049E+06 | 4.64510E+04 | -11.83 | 3.50397E+07 | 7.03696E+06 | 1.40014E+07 |
| 0 | 62872 | 2 | 4.82298E+07 | 4.97586E+06 | -4.65240E+06 | -3.64532E+06 | 8.25796E+04 | -6.07 | 4.87245E+07 | 4.48110E+06 | 2.21217E+07 |
| 0 | 62872 | 3 | 6.25967E+07 | 1.73789E+06 | -3.68605E+06 | -4.78448E+06 | 1.08386E+05 | -3.45 | 6.28191E+07 | 1.51545E+06 | 3.06518E+07 |
| 0 | 62872 | 4 | 7.69636E+07 | -1.50007E+06 | -2.71970E+06 | -5.46798E+06 | 1.23869E+05 | -1.98 | 7.70577E+07 | -1.59422E+06 | 3.93260E+07 |

**Figure 143: Rib .f06 for critical shear element**

The margin of safety for the shear stress of the wing rib is given by,

$$M.S. = \frac{\tau_{Allowable}}{FS * \tau_{Actual}} - 1 = \frac{13\ ksi}{1.5 * 4.1\ ksi} - 1 = \mathbf{1.16}$$

## 6. Wing Leading Edge

Load Case 2 is determined to be the critical load case for wing leading edge. The leading edge was found to be most critical in shear in the inboard section of the wing. Figure 144shows the maximum shear stress distribution with the critical region highlighted, and Figure 145 shows the critical region enlarged with the critical element number in that region. As the .f06 screen capture in Figure 146 shows, the maximum shear in the leading edge is 6.7 ksi (46.2 MPa) in layer 2.

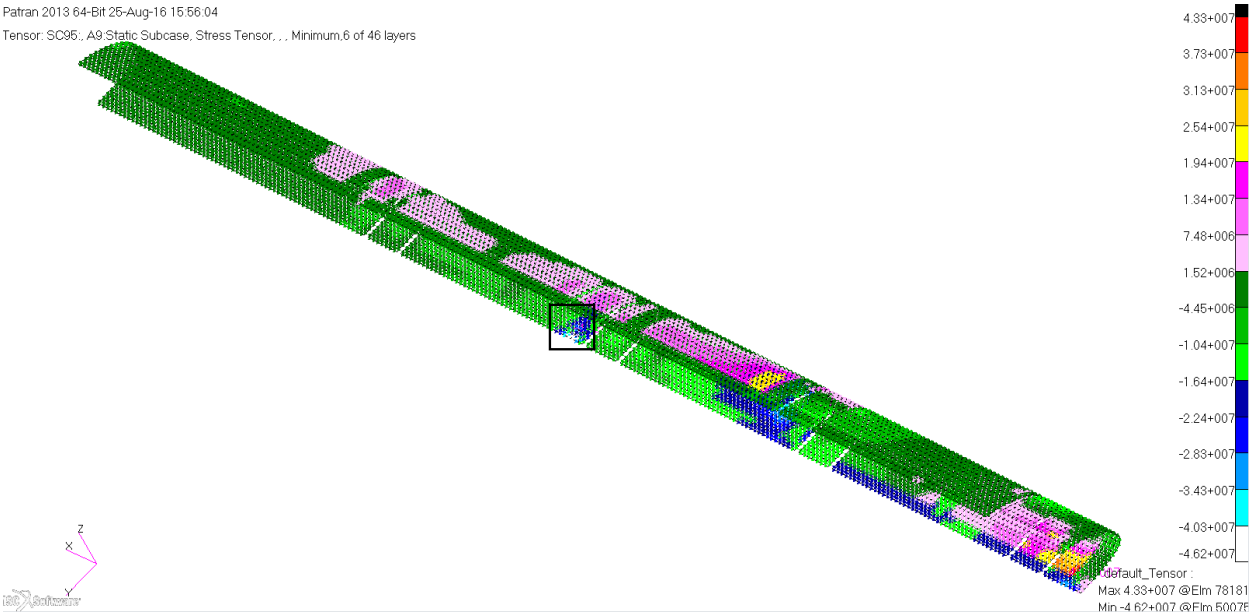


**Figure 144: Leading edge maximum shear stress plot**

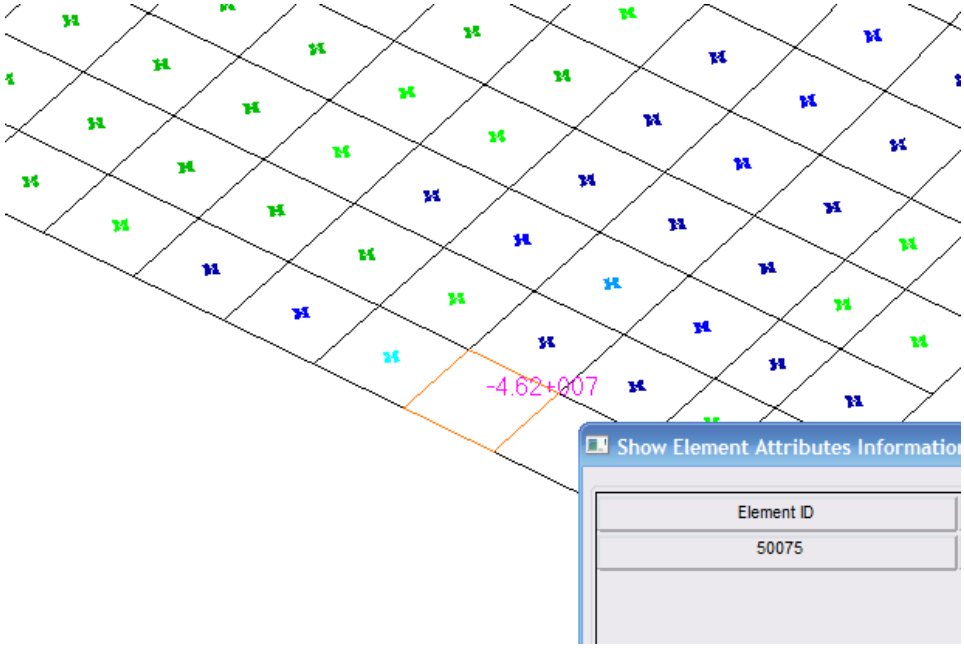


**Figure 145: Leading edge shear critical region**

```
0     50074    17   1.19860E+08  1.84918E+07  1.10076E+06  -3.27360E+04  7.76848E+05    0.62  1.19872E+08  1.84799E+07  5.06962E+07
0     50074    18   1.21298E+08  2.06018E+07  1.10379E+06  -1.68992E+04  7.09311E+05    0.63  1.21310E+08  2.05897E+07  5.03603E+07
0     50074    19   9.74694E+07  8.51316E+07  3.78032E+06  -1.10319E-10  2.15369E-10   15.75  9.85355E+07  8.40654E+07  7.23505E+06
0     50075     1  -2.00737E+08 -2.12765E+08 -4.62202E+07   2.93338E+04 -8.44025E+06  -41.29 -1.60141E+08 -2.53360E+08  4.66098E+07
0     50075     2   6.01906E+07 -1.78844E+08  1.15007E+05   4.53966E+04 -1.30620E+07    0.03  6.01907E+07 -1.78844E+08  1.19518E+08
0     50075     3   5.40922E+07  1.22102E+08 -7.88027E+05   2.93338E+04 -8.44025E+06  -89.34  1.22111E+08  5.40831E+07  3.40139E+07
0     50075     4   2.25531E+08  2.45510E+08  3.17446E+07   0.0          0.0          53.73  2.68800E+08  2.02241E+08  3.32793E+07
1   THIS IS A DEFAULT SUBCASE.                                                 AUGUST   8, 2016  MSC Nastran  3/14/14   PAGE  6090

0                                                                                                                    SUBCASE 95

                                S T R E S S E S   I N   L A Y E R E D   C O M P O S I T E   E L E M E N T S   ( Q U A D 4 )
   ELEMENT  PLY  STRESSES IN FIBER AND MATRIX DIRECTIONS    INTER-LAMINAR  STRESSES  PRINCIPAL STRESSES (ZERO SHEAR)       MAX
     ID      ID    NORMAL-1     NORMAL-2     SHEAR-12     SHEAR XZ-MAT  SHEAR YZ-MAT  ANGLE    MAJOR        MINOR        SHEAR
0     50076    1   9.31124E+07  7.53743E+07 -1.89173E+07   1.20168E+05 -2.91056E+06  -32.44  1.05137E+08  6.33501E+07  2.08932E+07
0     50076    2   1.08119E+08 -3.22150E+07  5.22089E+05   1.85970E+05 -4.50435E+06    0.21  1.08121E+08 -3.22169E+07  7.01690E+07
0     50076    3   2.02430E+07 -3.69216E+07 -4.57174E+05   1.20168E+05 -2.91056E+06   -0.46  2.02466E+07 -3.69253E+07  2.85860E+07
0     50076    4  -6.31162E+07 -4.61451E+07  2.20105E+06   0.0          0.0          82.73 -4.58642E+07 -6.33970E+07  8.76638E+06
0     50077    1   1.46796E+08  1.50669E+08 -5.41548E+05   7.34043E+04  2.39079E+06  -82.19  1.50744E+08  1.46722E+08  2.01100E+06
0     50077    2  -1.78514E+08 -1.96961E+08 -3.02727E+07   0.0          0.0          -36.53 -1.56091E+08 -2.19384E+08  3.16465E+07
```

**Figure 146: Leading edge .f06 for critical shear element**

The margin of safety for the shear stress of the is given by,

$$M.S. = \frac{\tau_{Allowable}}{FS * \tau_{Actual}} - 1 = \frac{13\ ksi}{1.5 * 6.7\ ksi} - 1 = \mathbf{0.33}$$

# Appendix C - Fairing and Pylon Structure

The fairing structure and pylon structure was analyzed for linear static analysis and buckling analysis. This section includes the critical stress region of each individual fairing and pylon structure component, which includes; skin, spar and rib components of each. The material of all the critical layer of the components in this section is fiberglass cloth, with 0° orientations. For the margin of safety calculations, the allowable stresses are taken from Table 26.

## 1. Fairing Skin

Load Case 4 is determined to be the critical load case for fairing skin. The fairing skin was found to be most critical in transverse tension in the mid-board section of the fairing lower skin. Figure 147 shows the maximum transverse tensile stress distribution with the critical region highlighted, and Figure 148 shows the critical region enlarged with the critical element number in that region. As the .f06 screen capture in Figure 149 shows, the maximum transverse tension in the fairing skin is 18 ksi in layer 5.

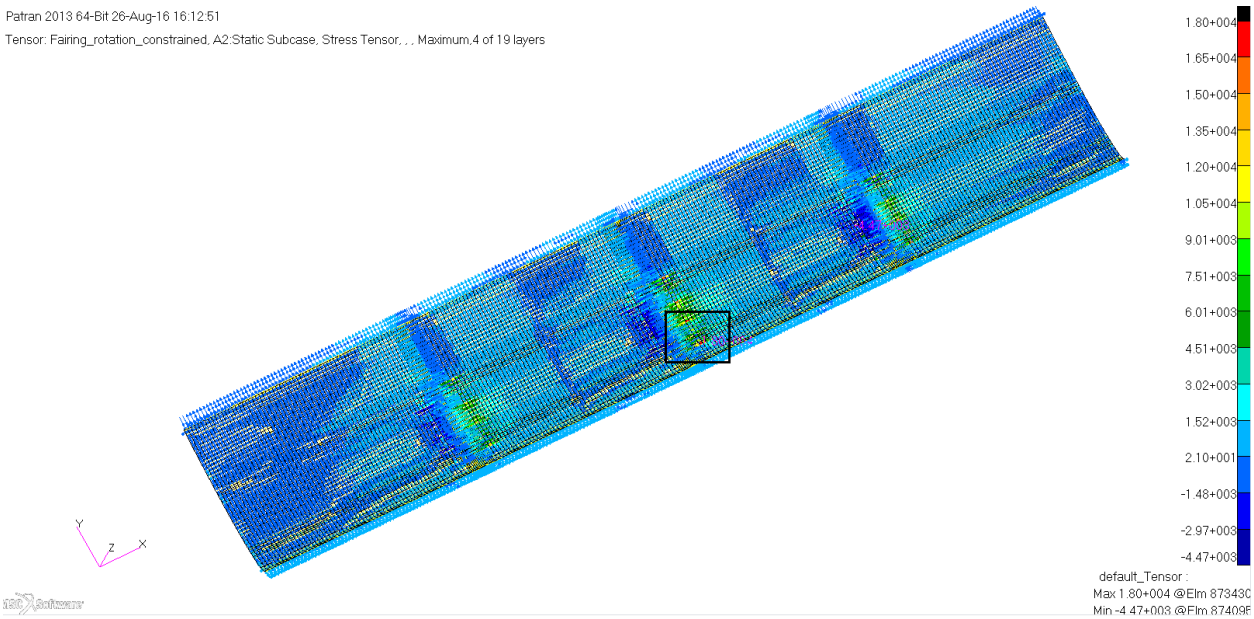


**Figure 147: Fairing skin maximum transverse tension stress plot**

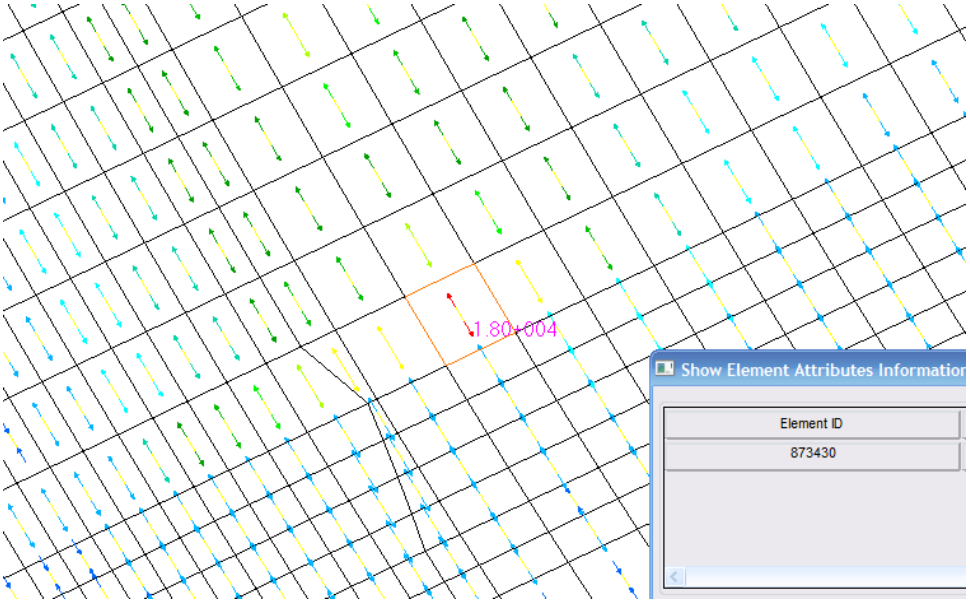


***Figure 148:*** **Fairing skin tension critical region**

S T R E S S E S  I N  L A Y E R E D  C O M P O S I T E  E L E M E N T S  ( Q U A D 4 )

| | ELEMENT ID | PLY ID | STRESSES IN FIBER AND MATRIX DIRECTIONS NORMAL-1 | NORMAL-2 | SHEAR-12 | INTER-LAMINAR STRESSES SHEAR XZ-MAT | SHEAR YZ-MAT | PRINCIPAL STRESSES (ZERO SHEAR) ANGLE | MAJOR | MINOR | MAX SHEAR |
|---|---|---|---|---|---|---|---|---|---|---|---|
| 0 | 873429 | 5 | 1.83594E+03 | 8.94211E+03 | 5.52107E+02 | -7.91491E-16 | -2.19596E-14 | 85.58 | 8.98475E+03 | 1.79330E+03 | 3.59573E+03 |
| 0 | 873430 | 1 | -2.27733E+03 | -5.45086E+03 | -6.65043E+02 | -6.75038E+00 | 5.22027E+01 | -11.37 | -2.14360E+03 | -5.58459E+03 | 1.72049E+03 |
| 0 | 873430 | 2 | -1.87942E+03 | -3.63376E+03 | -6.48603E+02 | -1.24543E+01 | 9.63126E+01 | -18.24 | -1.66567E+03 | -3.84752E+03 | 1.09092E+03 |
| 0 | 873430 | 3 | 1.56349E+01 | 2.98446E+01 | -4.27380E+00 | -1.24543E+01 | 9.63126E+01 | -74.49 | 3.10310E+01 | 1.44485E+01 | 8.29122E+00 |
| 0 | 873430 | 4 | 2.45818E+03 | 1.61744E+04 | -4.69394E+02 | -6.75038E+00 | 5.22027E+01 | -88.04 | 1.61904E+04 | 2.44213E+03 | 6.87413E+03 |
| 0 | 873430 | 5 | 2.85609E+03 | 1.79914E+04 | -4.52954E+02 | -1.18247E-13 | 1.02158E-12 | -88.29 | 1.80050E+04 | 2.84254E+03 | 7.58122E+03 |
| 0 | 873431 | 1 | 4.62787E+01 | 1.65515E+03 | -1.66912E+03 | -9.91364E+00 | 3.77700E+01 | -57.87 | 2.70357E+03 | -1.00214E+03 | 1.85285E+03 |
| 0 | 873431 | 2 | 1.37891E+02 | 2.27634E+03 | -1.44415E+03 | -1.82904E+01 | 6.96846E+01 | -63.26 | 3.00400E+03 | -5.89773E+02 | 1.79689E+03 |
| 0 | 873431 | 3 | 1.57803E+01 | 2.77577E+01 | -1.66643E+00 | -1.82904E+01 | 6.96846E+01 | -82.23 | 2.79852E+01 | 1.55528E+01 | 6.21624E+00 |
| 0 | 873431 | 4 | 1.13656E+03 | 9.04789E+03 | 1.00822E+03 | -9.91364E+00 | 3.77700E+01 | 82.85 | 9.17436E+03 | 1.01009E+03 | 4.08213E+03 |
| 0 | 873431 | 5 | 1.22817E+03 | 9.66908E+03 | 1.23319E+03 | -1.73659E-13 | 7.39141E-13 | 81.86 | 9.84556E+03 | 1.05170E+03 | 4.39693E+03 |
| 0 | 873432 | 1 | 3.01519E+02 | 5.77748E+03 | -1.48780E+03 | -4.14234E+00 | 2.60821E+01 | -75.74 | 6.15560E+03 | -7.66017E+01 | 3.11610E+03 |

**Figure 149: Fairing skin.f06 for critical tensile element**

The margin of safety for the tensile stress of the fairing skin is given by,

$$M.S. = \frac{\sigma_{Allowable}}{FS * \sigma_{Actual}} - 1 = \frac{30.8\ ksi}{1.5 * 18\ ksi} - 1 = \mathbf{0.14}$$

## 2. Fairing Spar

Load Case 4 is determined to be the critical load case for fairing spar. The fairing spar was found to be most critical in longitudinal tension in the mid-board section of the fairing. Figure 150 shows the maximum longitudinal tensile stress distribution with the critical region highlighted, and Figure 151 shows the critical region enlarged with the critical element number in that region. As the .f06 screen capture in Figure 152 shows, the maximum longitudinal tension in the fairing spar is 20.1 ksi in layer 1.

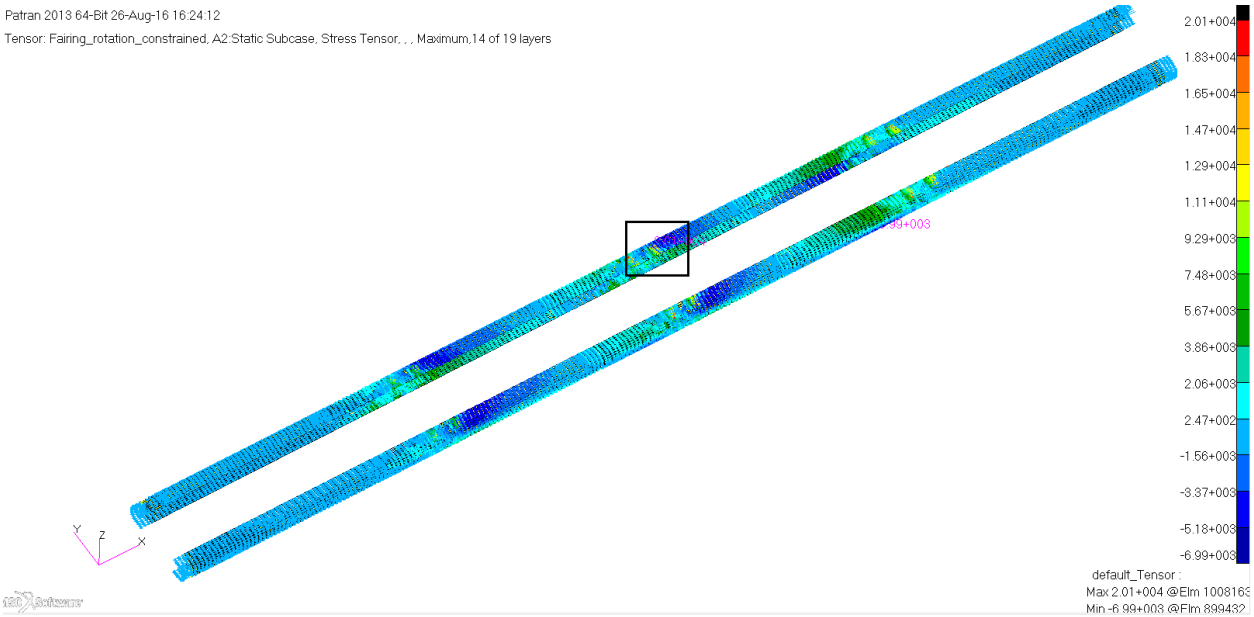


**Figure 150: Fairing spar maximum longitudinal tension stress plot**

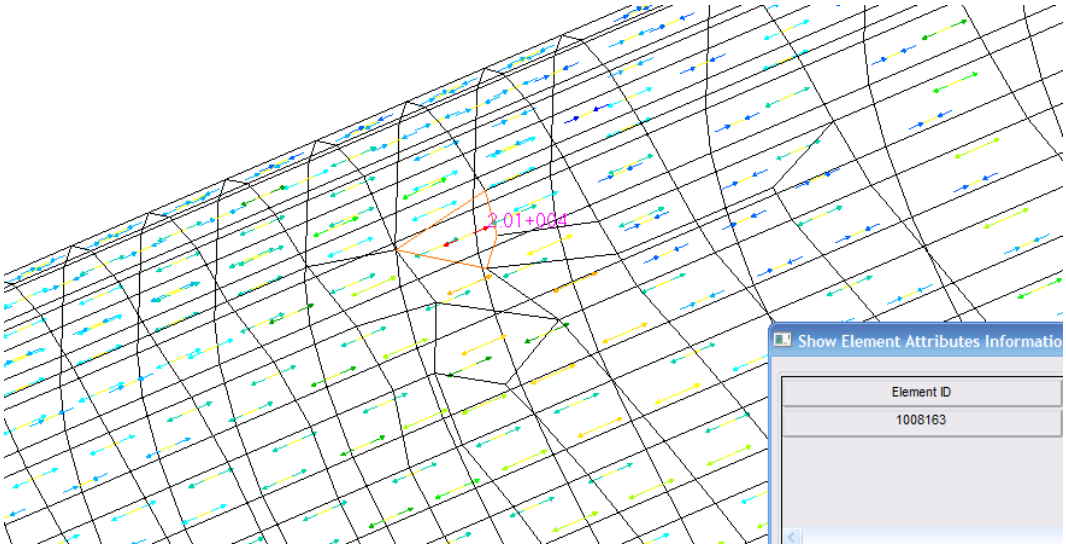


**Figure 151: Fairing spar tension critical region**

| | | | | | | | | | | | | |
|---|---|---|---|---|---|---|---|---|---|---|---|---|
| 0 | 1008162 | 11 | -4.59423E+03 | -2.25427E+03 | 5.83458E+02 | 4.20086E+03 | -4.69098E+03 | 76.75 | -2.11686E+03 | -4.73164E+03 | 1.30739E+03 |
| 0 | 1008162 | 12 | -3.02496E+03 | -1.28581E+03 | 4.73188E+02 | 4.33719E+03 | -4.84698E+03 | 75.72 | -1.16540E+03 | -3.14537E+03 | 9.89986E+02 |
| 0 | 1008162 | 13 | -1.45569E+03 | -3.17337E+02 | 3.62919E+02 | 4.43259E+03 | -4.95791E+03 | 73.74 | -2.11479E+02 | -1.56155E+03 | 6.75037E+02 |
| 0 | 1008162 | 14 | 1.13572E+02 | 6.51131E+02 | 2.52650E+02 | 4.48706E+03 | -5.02376E+03 | 68.39 | 7.51234E+02 | 1.34686E+01 | 3.68883E+02 |
| 0 | 1008162 | 15 | 2.59947E+04 | 2.08099E+04 | -2.45266E+03 | -2.06415E-04 | 3.57968E-05 | -21.71 | 2.69711E+04 | 1.98335E+04 | 3.56877E+03 |
| 0 | 1008163 | 1 | 2.01420E+04 | 1.25814E+04 | 1.71491E+03 | 5.97719E+02 | 6.91887E+02 | 12.20 | 2.05128E+04 | 1.22106E+04 | 4.15109E+03 |
| 0 | 1008163 | 2 | 1.85094E+04 | 1.15737E+04 | 1.60000E+03 | 1.15373E+03 | 1.33593E+03 | 12.38 | 1.88607E+04 | 1.12224E+04 | 3.81917E+03 |
| 0 | 1008163 | 3 | 1.68768E+04 | 1.05660E+04 | 1.48510E+03 | 1.66803E+03 | 1.93213E+03 | 12.60 | 1.72088E+04 | 1.02340E+04 | 3.48743E+03 |
| 0 | 1008163 | 4 | 1.52442E+04 | 9.55827E+03 | 1.37020E+03 | 2.14063E+03 | 2.48048E+03 | 12.87 | 1.55572E+04 | 9.24531E+03 | 3.15594E+03 |
| 0 | 1008163 | 5 | 1.36116E+04 | 8.55057E+03 | 1.25529E+03 | 2.57151E+03 | 2.98099E+03 | 13.19 | 1.39059E+04 | 8.25633E+03 | 2.82478E+03 |
| 0 | 1008163 | 6 | 1.19791E+04 | 7.54287E+03 | 1.14039E+03 | 2.96069E+03 | 3.43365E+03 | 13.60 | 1.22550E+04 | 7.26688E+03 | 2.49408E+03 |
| 0 | 1008163 | 7 | 1.03465E+04 | 6.53517E+03 | 1.02549E+03 | 3.30816E+03 | 3.83846E+03 | 14.14 | 1.06049E+04 | 6.27676E+03 | 2.16406E+03 |

1 MSC.NASTRAN JOB CREATED ON 05-JUL-16 AT 14:10:23 JULY 27, 2016 MSC Nastran 3/14/14 PAGE 14078
FAIRING_ROTATION_FIXED

0 SUBCASE 1

S T R E S S E S I N L A Y E R E D C O M P O S I T E E L E M E N T S ( Q U A D 4 )

| | ELEMENT ID | PLY ID | STRESSES IN FIBER AND MATRIX DIRECTIONS NORMAL-1 | NORMAL-2 | SHEAR-12 | INTER-LAMINAR STRESSES SHEAR XZ-MAT | SHEAR YZ-MAT | PRINCIPAL STRESSES (ZERO SHEAR) ANGLE | MAJOR | MINOR | MAX SHEAR |
|---|---|---|---|---|---|---|---|---|---|---|---|
| 0 | 1008163 | 8 | 8.71389E+03 | 5.52746E+03 | 9.10582E+02 | 3.61392E+03 | 4.19544E+03 | 14.87 | 8.95575E+03 | 5.28560E+03 | 1.83507E+03 |
| 0 | 1008163 | 9 | 7.08130E+03 | 4.51976E+03 | 7.95679E+02 | 3.87797E+03 | 4.50456E+03 | 15.93 | 7.30834E+03 | 4.29273E+03 | 1.50781E+03 |
| 0 | 1008163 | 10 | 5.44872E+03 | 3.51206E+03 | 6.80775E+02 | 4.10032E+03 | 4.76585E+03 | 17.55 | 5.66408E+03 | 3.29670E+03 | 1.18369E+03 |
| 0 | 1008163 | 11 | 3.81613E+03 | 2.50435E+03 | 5.65872E+02 | 4.28095E+03 | 4.97928E+03 | 20.39 | 4.02650E+03 | 2.29399E+03 | 8.66257E+02 |

**Figure 152: Fairing spar.f06 for critical tensile element**

The margin of safety for the tensile stress of the fairing spar is given by,

$$M.S. = \frac{\sigma_{Allowable}}{FS * \sigma_{Actual}} - 1 = \frac{32.1\ ksi}{1.5 * 20.1\ ksi} - 1 = \mathbf{0.06}$$

### 3. Fairing Rib

Load Case 4 is determined to be the critical load case for fairing rib. The fairing rib was found to be most critical in shear in the mid-board section of the fairing. Figure 153 shows the maximum shear stress distribution with the critical region highlighted, and Figure 154 shows the critical region enlarged with the critical element number in that region. As the .f06 screen capture in Figure 155 shows, the maximum shear in the fairing rib is 4.87 ksi in layer 1.

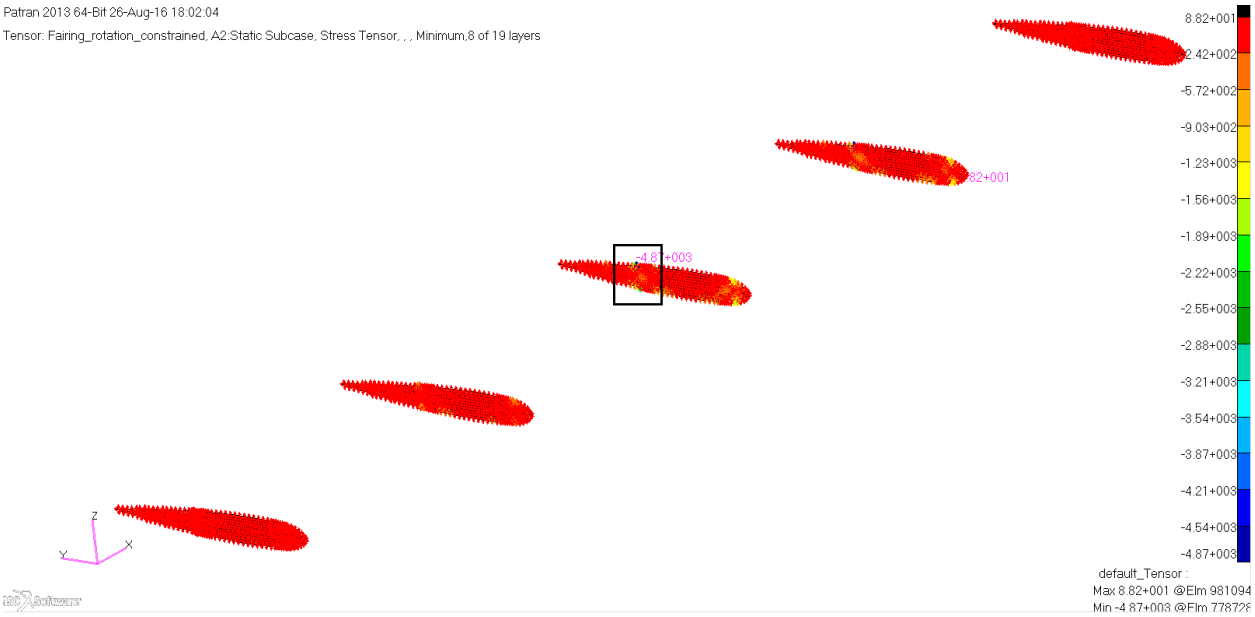


**Figure 153: Fairing rib maximum shear stress plot**

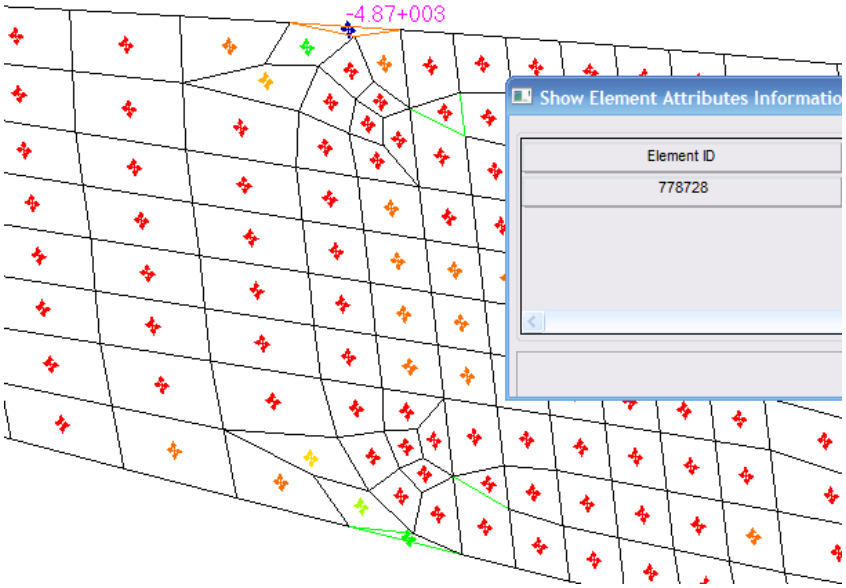


**Figure 154: Fairing rib shear critical region**

| | | | STRESSES IN LAYERED COMPOSITE ELEMENTS (TRIA3) | | | | | | | | | |
|---|---|---|---|---|---|---|---|---|---|---|---|---|
| | ELEMENT ID | PLY ID | STRESSES IN FIBER AND MATRIX DIRECTIONS NORMAL-1 | NORMAL-2 | SHEAR-12 | INTER-LAMINAR STRESSES SHEAR XZ-MAT | SHEAR YZ-MAT | PRINCIPAL STRESSES (ZERO SHEAR) ANGLE | MAJOR | MINOR | MAX SHEAR |
| 0 | 778697 | 1 | -1.19092E+02 | -1.90601E+02 | 1.28473E+02 | -1.60532E+00 | 1.56093E+02 | 37.22 | -2.14910E+01 | -2.88202E+02 | 1.33355E+02 |
| 0 | 778697 | 2 | -8.79257E+01 | -1.36111E+02 | 9.23950E+01 | -2.75197E+00 | 2.67589E+02 | 37.69 | -1.65340E+01 | -2.07503E+02 | 9.54846E+01 |
| 0 | 778697 | 3 | -5.67596E+01 | -8.16216E+01 | 5.63172E+01 | -3.43997E+00 | 3.34486E+02 | 38.78 | -1.15178E+01 | -1.26863E+02 | 5.76728E+01 |
| 0 | 778697 | 4 | -2.55936E+01 | -2.71318E+01 | 2.02394E+01 | -3.66930E+00 | 3.56785E+02 | 43.91 | -6.10873E+00 | -4.66167E+01 | 2.02540E+01 |
| 0 | 778697 | 5 | 5.57250E+00 | 2.73579E+01 | -1.58385E+01 | -3.43997E+00 | 3.34486E+02 | -62.26 | 3.56878E+01 | -2.75737E+00 | 1.92226E+01 |
| 0 | 778697 | 6 | 3.67386E+01 | 8.18477E+01 | -5.19163E+01 | -2.75197E+00 | 2.67589E+02 | -56.74 | 1.15897E+02 | 2.68917E+00 | 5.66040E+01 |
| 0 | 778697 | 7 | 6.79046E+01 | 1.36338E+02 | -8.79941E+01 | -1.60532E+00 | 1.56093E+02 | -55.62 | 1.96534E+02 | 7.70852E+00 | 9.44125E+01 |
| 0 | 778697 | 8 | 9.90707E+01 | 1.90827E+02 | -1.24072E+02 | 2.37735E-16 | 2.42663E-14 | -55.15 | 2.77232E+02 | 1.26665E+01 | 1.32283E+02 |
| 0 | 778717 | 1 | -2.12927E+02 | -7.47945E+02 | -2.31402E+02 | -3.27164E+01 | -1.78643E+02 | -20.43 | -1.26730E+02 | -8.34142E+02 | 3.53706E+02 |
| 0 | 778717 | 2 | -1.56656E+02 | -5.34055E+02 | -1.64063E+02 | -5.60853E+01 | -3.06245E+02 | -20.50 | -9.53066E+01 | -5.95404E+02 | 2.50049E+02 |
| 0 | 778717 | 3 | -1.00384E+02 | -3.20165E+02 | -9.67247E+01 | -7.01066E+01 | -3.82807E+02 | -20.68 | -6.38789E+01 | -3.56670E+02 | 1.46395E+02 |
| 0 | 778717 | 4 | -4.41118E+01 | -1.06275E+02 | -2.93861E+01 | -7.47803E+01 | -4.08327E+02 | -21.70 | -3.24195E+01 | -1.17967E+02 | 4.27740E+01 |
| 0 | 778717 | 5 | 1.21601E+01 | 1.07615E+02 | 3.79525E+01 | -7.01066E+01 | -3.82807E+02 | 70.75 | 1.20865E+02 | -1.09034E+00 | 6.09778E+01 |
| 0 | 778717 | 6 | 6.84320E+01 | 3.21505E+02 | 1.05291E+02 | -5.60853E+01 | -3.06245E+02 | 70.12 | 3.59582E+02 | 3.03547E+01 | 1.64614E+02 |
| 0 | 778717 | 7 | 1.24704E+02 | 5.35394E+02 | 1.72630E+02 | -3.27164E+01 | -1.78643E+02 | 69.97 | 5.98317E+02 | 6.17813E+01 | 2.68268E+02 |
| 0 | 778717 | 8 | 1.80976E+02 | 7.49284E+02 | 2.39968E+02 | 4.84504E-15 | -2.77718E-14 | 69.91 | 8.37055E+02 | 9.32048E+01 | 3.71925E+02 |
| 0 | 778728 | 1 | -8.06002E+03 | -8.48652E+03 | -4.86566E+03 | -1.52258E+02 | -4.85525E+03 | -43.75 | -3.40294E+03 | -1.31436E+04 | 4.87033E+03 |
| 0 | 778728 | 2 | -5.75199E+03 | -6.08903E+03 | -3.48257E+03 | -2.61014E+02 | -8.32329E+03 | -43.61 | -2.43387E+03 | -9.40715E+03 | 3.48664E+03 |
| 0 | 778728 | 3 | -3.44397E+03 | -3.69153E+03 | -2.09948E+03 | -3.26267E+02 | -1.04041E+04 | -43.31 | -1.46463E+03 | -5.67087E+03 | 2.10312E+03 |
| 0 | 778728 | 4 | -1.13594E+03 | -1.29404E+03 | -7.16383E+02 | -3.48018E+02 | -1.10977E+04 | -41.85 | -4.94259E+02 | -1.93572E+03 | 7.20731E+02 |
| 0 | 778728 | 5 | 1.17208E+03 | 1.10346E+03 | 6.66710E+02 | -3.26267E+02 | -1.04041E+04 | 43.53 | 1.80536E+03 | 4.70179E+02 | 6.67592E+02 |
| 0 | 778728 | 6 | 3.48011E+03 | 3.50096E+03 | 2.04980E+03 | -2.61014E+02 | -8.32329E+03 | 45.15 | 5.54036E+03 | 1.44070E+03 | 2.04983E+03 |
| 0 | 778728 | 7 | 5.78813E+03 | 5.89845E+03 | 3.43289E+03 | -1.52258E+02 | -4.85525E+03 | 45.46 | 9.27663E+03 | 2.40995E+03 | 3.43334E+03 |

**Figure 155: Fairing rib .f06 for critical shear element**

The margin of safety for the shear stress of the fairing rib is given by,

$$M.S. = \frac{\tau_{Allowable}}{FS * \tau_{Actual}} - 1 = \frac{9.2\ ksi}{1.5 * 4.87\ ksi} - 1 = \mathbf{0.26}$$

## 4. Pylon Skin

Load Case 4 is determined to be the critical load case for pylon skin. The pylon skin was found to be most critical in shear in the mid-board section of the pylon. Figure 156 shows the maximum shear stress distribution with the critical region highlighted, and Figure 157 shows the critical region enlarged with the critical element number in that region. As the .f06 screen capture Figure 158 shows, the maximum shear in the pylon skin is 5.99 ksi in layer 7.

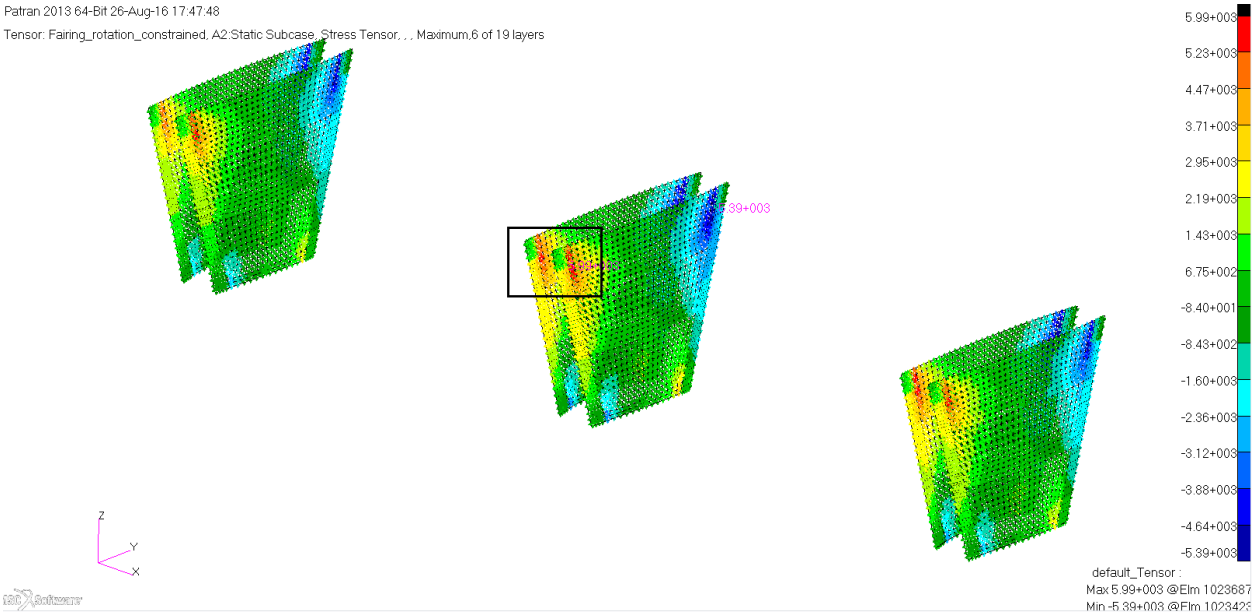


**Figure 156: Pylon skin maximum shear stress plot**

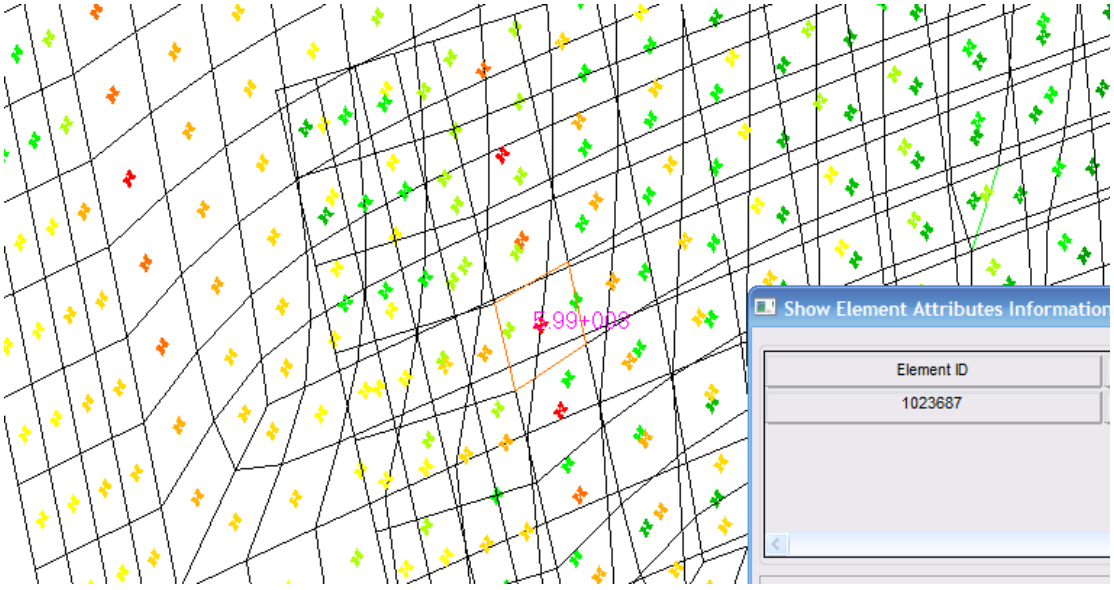


***Figure 157:*** **Pylon skin shear critical region**

S T R E S S E S  I N  L A Y E R E D  C O M P O S I T E  E L E M E N T S  ( Q U A D 4 )

| | ELEMENT ID | PLY ID | STRESSES IN FIBER AND MATRIX DIRECTIONS NORMAL-1 | NORMAL-2 | SHEAR-12 | INTER-LAMINAR STRESSES SHEAR XZ-MAT | SHEAR YZ-MAT | PRINCIPAL STRESSES (ZERO SHEAR) ANGLE | MAJOR | MINOR | MAX SHEAR |
|---|---|---|---|---|---|---|---|---|---|---|---|
| 0 | 1023685 | 5 | -6.59630E+02 | -2.13262E+03 | 5.16883E+03 | -1.67057E+00 | 2.29032E+00 | 40.95 | 3.82491E+03 | -6.61716E+03 | 5.22104E+03 |
| 0 | 1023685 | 6 | -5.60160E+02 | -2.15974E+03 | 5.15513E+03 | -8.95373E-01 | 1.22754E+00 | 40.59 | 3.85686E+03 | -6.57675E+03 | 5.21680E+03 |
| 0 | 1023685 | 7 | -4.60690E+02 | -2.18685E+03 | 5.14143E+03 | -1.32055E-14 | 1.88259E-14 | 40.24 | 3.88960E+03 | -6.53714E+03 | 5.21337E+03 |
| 0 | 1023686 | 1 | -2.48900E+03 | -1.26206E+03 | 4.86013E+03 | 2.55593E+00 | 7.37192E+00 | 48.60 | 3.02317E+03 | -6.77423E+03 | 4.89870E+03 |
| 0 | 1023686 | 2 | -2.44107E+03 | -1.37409E+03 | 4.87695E+03 | 4.76880E+00 | 1.37544E+01 | 48.12 | 2.99846E+03 | -6.81362E+03 | 4.90604E+03 |
| 0 | 1023686 | 3 | -2.39315E+03 | -1.48612E+03 | 4.89376E+03 | 6.63862E+00 | 1.91474E+01 | 47.65 | 2.97510E+03 | -6.85436E+03 | 4.91473E+03 |
| 0 | 1023686 | 4 | -1.42254E+01 | -1.43533E+01 | 3.81157E+01 | 6.63862E+00 | 1.91474E+01 | 44.95 | 2.38264E+01 | -5.24051E+01 | 3.81158E+01 |
| 0 | 1023686 | 5 | -1.87069E+03 | -2.70735E+03 | 5.07706E+03 | 4.76880E+00 | 1.37544E+01 | 42.64 | 2.80524E+03 | -7.38328E+03 | 5.09426E+03 |
| 0 | 1023686 | 6 | -1.82276E+03 | -2.81938E+03 | 5.09387E+03 | 2.55593E+00 | 7.37192E+00 | 42.21 | 2.79712E+03 | -7.43926E+03 | 5.11819E+03 |
| 0 | 1023686 | 7 | -1.77484E+03 | -2.93141E+03 | 5.11069E+03 | 3.76963E-14 | 1.13058E-13 | 41.77 | 2.79018E+03 | -7.49642E+03 | 5.14330E+03 |
| 0 | 1023687 | 1 | -3.07706E+03 | -1.61583E+03 | 5.51915E+03 | 1.74482E+00 | 1.24000E+01 | 48.77 | 3.22086E+03 | -7.91374E+03 | 5.56730E+03 |
| 0 | 1023687 | 2 | -3.35447E+03 | -1.78284E+03 | 5.55044E+03 | 3.25545E+00 | 2.31357E+01 | 49.03 | 3.03714E+03 | -8.17445E+03 | 5.60580E+03 |
| 0 | 1023687 | 3 | -3.63189E+03 | -1.94986E+03 | 5.58174E+03 | 4.53190E+00 | 3.22071E+01 | 49.28 | 2.85387E+03 | -8.43561E+03 | 5.64474E+03 |
| 0 | 1023687 | 4 | -2.92891E+01 | -2.43842E+01 | 4.39790E+01 | 4.53190E+00 | 3.22071E+01 | 46.60 | 1.72107E+01 | -7.08839E+01 | 4.40473E+01 |
| 0 | 1023687 | 5 | -6.65598E+03 | -3.77049E+03 | 5.92288E+03 | 3.25545E+00 | 2.31357E+01 | 51.84 | 8.82827E+02 | -1.13093E+04 | 6.09606E+03 |
| 0 | 1023687 | 6 | -6.93339E+03 | -3.93750E+03 | 5.95417E+03 | 1.74482E+00 | 1.24000E+01 | 52.06 | 7.04255E+02 | -1.15752E+04 | 6.13970E+03 |
| 0 | 1023687 | 7 | -7.21081E+03 | -4.10452E+03 | 5.98546E+03 | 2.57336E-14 | 1.90170E-13 | 52.27 | 5.26027E+02 | -1.18414E+04 | 6.18369E+03 |
| 0 | 1023688 | 1 | -4.88017E+03 | -4.68649E+02 | 5.24276E+03 | -6.79372E-01 | 9.36204E+00 | 56.41 | 3.01347E+03 | -8.36229E+03 | 5.68788E+03 |
| 0 | 1023688 | 2 | -4.91084E+03 | -5.08599E+02 | 5.21457E+03 | -1.26756E+00 | 1.74675E+01 | 56.44 | 2.95038E+03 | -8.36981E+03 | 5.66009E+03 |
| 0 | 1023688 | 3 | -4.94150E+03 | -5.48549E+02 | 5.18638E+03 | -1.76456E+00 | 2.43164E+01 | 56.48 | 2.88729E+03 | -8.37734E+03 | 5.63232E+03 |
| 0 | 1023688 | 4 | -2.43391E+01 | -1.45498E+01 | 3.84774E+01 | -1.76456E+00 | 2.43164E+01 | 48.62 | 1.93430E+01 | -5.82319E+01 | 3.87875E+01 |
| 0 | 1023688 | 5 | -5.27575E+03 | -9.84044E+02 | 4.87905E+03 | -1.26756E+00 | 1.74675E+01 | 56.87 | 2.20019E+03 | -8.45998E+03 | 5.33009E+03 |
| 0 | 1023688 | 6 | -5.30641E+03 | -1.02399E+03 | 4.85086E+03 | -6.79372E-01 | 9.36204E+00 | 56.91 | 2.13721E+03 | -8.46762E+03 | 5.30242E+03 |

**Figure 158: Pylon skin .f06 for critical shear element**

The margin of safety for the shear stress of the pylon skin is given by,

$$M.S. = \frac{\tau_{Allowable}}{FS * \tau_{Actual}} - 1 = \frac{9.2\ ksi}{1.5 * 5.99\ ksi} - 1 = \mathbf{0.02}$$

## 5. Pylon Spar

Load Case 4 is determined to be the critical load case for pylon spar. The pylon spar was found to be most critical in longitudinal tension in the outboard section of the pylon. Figure 159 shows the maximum longitudinal tensile stress distribution with the critical region highlighted, and Figure 160 shows the critical region enlarged with the critical element number in that region. As the .f06 screen capture in Figure 161 shows, the maximum longitudinal tension in pylon spar is 20.2 ksi in layer 1.

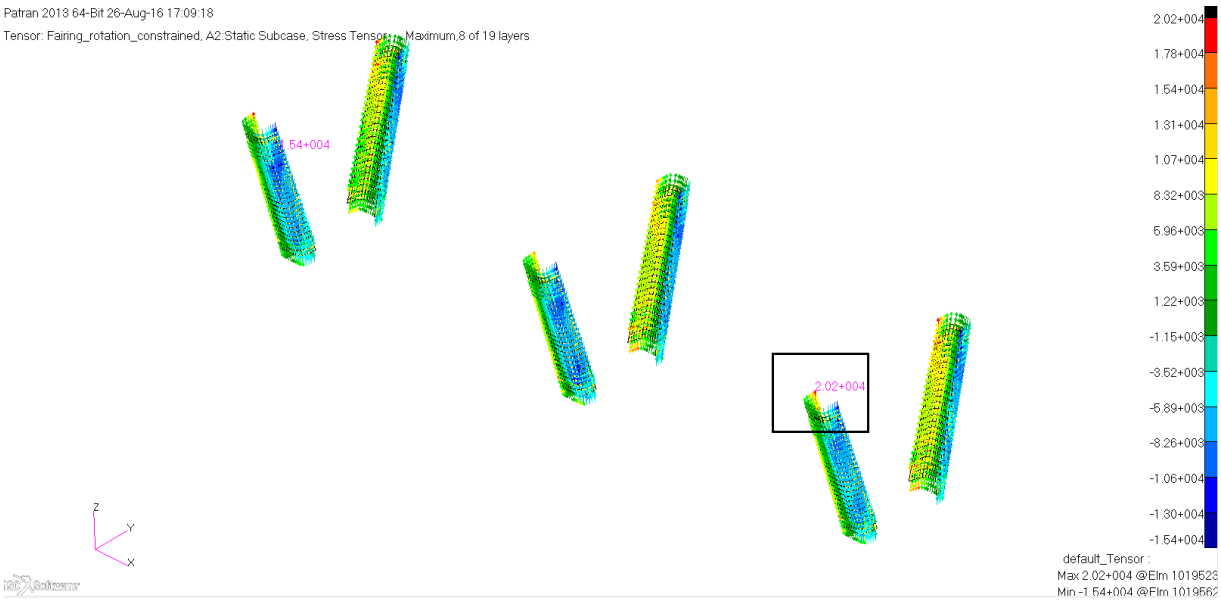


**Figure 159: Pylon spar maximum longitudinal tension stress plot**

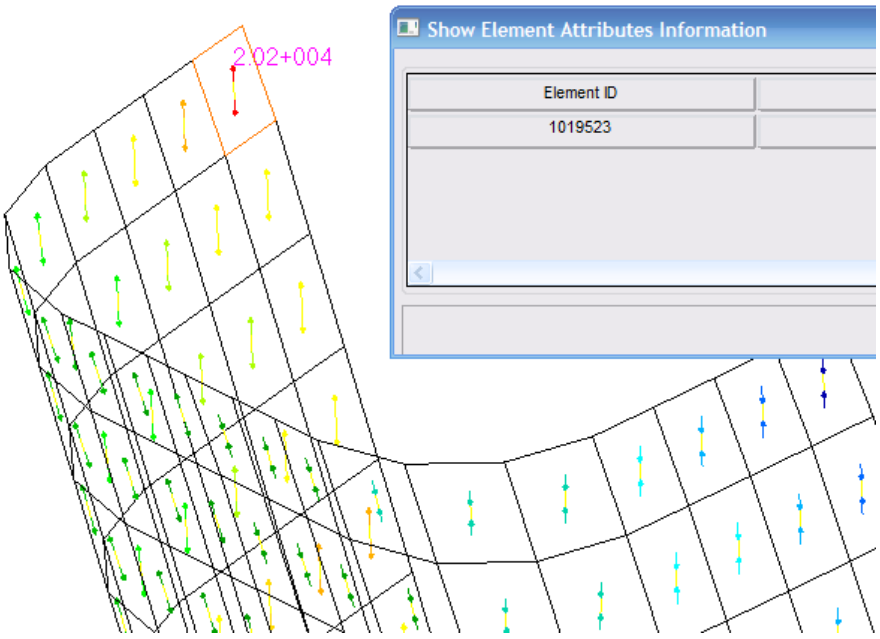


**Figure 160: Pylon spar tension critical region**

S T R E S S E S  I N  L A Y E R E D  C O M P O S I T E  E L E M E N T S  ( Q U A D 4 )

| | ELEMENT ID | PLY ID | STRESSES IN FIBER AND MATRIX DIRECTIONS NORMAL-1 | NORMAL-2 | SHEAR-12 | INTER-LAMINAR STRESSES SHEAR XZ-MAT | SHEAR YZ-MAT | PRINCIPAL STRESSES (ZERO SHEAR) ANGLE | MAJOR | MINOR | MAX SHEAR |
|---|---|---|---|---|---|---|---|---|---|---|---|
| 0 | 1019520 | 8 | 7.85354E+03 | 7.03726E+02 | 2.98775E+03 | -4.77308E-16 | 9.94894E-16 | 19.94 | 8.93767E+03 | -3.80406E+02 | 4.65904E+03 |
| 0 | 1019521 | 1 | 9.46805E+03 | 6.21573E+02 | 2.76198E+03 | 3.58259E+00 | 5.40009E+00 | 15.99 | 1.02596E+04 | -1.69934E+02 | 5.21475E+03 |
| 0 | 1019521 | 2 | 9.30768E+03 | 6.16382E+02 | 2.77980E+03 | 6.14158E+00 | 9.25730E+00 | 16.30 | 1.01207E+04 | -1.96645E+02 | 5.15867E+03 |
| 0 | 1019521 | 3 | 9.14730E+03 | 6.11190E+02 | 2.79761E+03 | 7.67698E+00 | 1.15716E+01 | 16.62 | 9.98248E+03 | -2.23981E+02 | 5.10323E+03 |
| 0 | 1019521 | 4 | 8.98693E+03 | 6.05998E+02 | 2.81543E+03 | 8.18878E+00 | 1.23431E+01 | 16.95 | 9.84489E+03 | -2.51964E+02 | 5.04843E+03 |
| 0 | 1019521 | 5 | 8.82656E+03 | 6.00807E+02 | 2.83324E+03 | 7.67698E+00 | 1.15716E+01 | 17.28 | 9.70798E+03 | -2.80615E+02 | 4.99430E+03 |
| 0 | 1019521 | 6 | 8.66618E+03 | 5.95615E+02 | 2.85106E+03 | 6.14158E+00 | 9.25730E+00 | 17.62 | 9.57175E+03 | -3.09955E+02 | 4.94085E+03 |
| 0 | 1019521 | 7 | 8.50581E+03 | 5.90424E+02 | 2.86887E+03 | 3.58259E+00 | 5.40009E+00 | 17.97 | 9.43624E+03 | -3.40008E+02 | 4.88812E+03 |
| 0 | 1019521 | 8 | 8.34544E+03 | 5.85232E+02 | 2.88669E+03 | -5.30553E-16 | 8.39497E-16 | 18.32 | 9.30146E+03 | -3.70796E+02 | 4.83613E+03 |
| 0 | 1019522 | 1 | 9.71387E+03 | 6.24647E+02 | 2.56300E+03 | 5.72693E+00 | 2.67135E+00 | 14.71 | 1.03868E+04 | -4.82557E+01 | 5.21751E+03 |
| 0 | 1019522 | 2 | 9.56001E+03 | 5.93309E+02 | 2.58324E+03 | 9.81760E+00 | 4.57945E+00 | 14.97 | 1.02510E+04 | -9.76595E+01 | 5.17432E+03 |
| 0 | 1019522 | 3 | 9.40616E+03 | 5.61971E+02 | 2.60349E+03 | 1.22720E+01 | 5.72432E+00 | 15.24 | 1.01156E+04 | -1.47511E+02 | 5.13158E+03 |
| 0 | 1019522 | 4 | 9.25230E+03 | 5.30633E+02 | 2.62373E+03 | 1.30901E+01 | 6.10594E+00 | 15.52 | 9.98076E+03 | -1.97821E+02 | 5.08929E+03 |
| 0 | 1019522 | 5 | 9.09845E+03 | 4.99294E+02 | 2.64398E+03 | 1.22720E+01 | 5.72432E+00 | 15.79 | 9.84634E+03 | -2.48602E+02 | 5.04747E+03 |
| 0 | 1019522 | 6 | 8.94459E+03 | 4.67956E+02 | 2.66422E+03 | 9.81760E+00 | 4.57945E+00 | 16.08 | 9.71241E+03 | -2.99865E+02 | 5.00614E+03 |
| 0 | 1019522 | 7 | 8.79073E+03 | 4.36618E+02 | 2.68447E+03 | 5.72693E+00 | 2.67135E+00 | 16.36 | 9.57897E+03 | -3.51622E+02 | 4.96530E+03 |
| 0 | 1019522 | 8 | 8.63688E+03 | 4.05280E+02 | 2.70471E+03 | -8.48113E-16 | 4.15287E-16 | 16.66 | 9.44604E+03 | -4.03886E+02 | 4.92496E+03 |
| 0 | 1019523 | 1 | 2.01695E+04 | 3.68922E+03 | 1.96153E+03 | 1.54531E+01 | -6.89635E+01 | 6.69 | 2.03997E+04 | 3.45897E+03 | 8.47038E+03 |
| 0 | 1019523 | 2 | 1.96050E+04 | 3.48965E+03 | 1.94177E+03 | 2.92421E+01 | -1.30561E+02 | 6.77 | 1.98356E+04 | 3.25898E+03 | 8.28832E+03 |
| 0 | 1019523 | 3 | 1.90404E+04 | 3.29007E+03 | 1.92201E+03 | 4.13670E+01 | -1.84792E+02 | 6.86 | 1.92716E+04 | 3.05892E+03 | 8.10632E+03 |
| 0 | 1019523 | 4 | 1.84759E+04 | 3.09049E+03 | 1.90226E+03 | 5.18279E+01 | -2.31656E+02 | 6.94 | 1.87076E+04 | 2.85878E+03 | 7.92440E+03 |
| 0 | 1019523 | 5 | 1.79113E+04 | 2.89091E+03 | 1.88250E+03 | 6.06246E+01 | -2.71155E+02 | 7.04 | 1.81437E+04 | 2.65857E+03 | 7.74255E+03 |
| 0 | 1019523 | 6 | 1.73468E+04 | 2.69134E+03 | 1.86275E+03 | 6.77572E+01 | -3.03287E+02 | 7.13 | 1.75798E+04 | 2.45828E+03 | 7.56078E+03 |
| 0 | 1019523 | 7 | 1.67823E+04 | 2.49176E+03 | 1.84299E+03 | 7.32258E+01 | -3.28053E+02 | 7.23 | 1.70161E+04 | 2.25790E+03 | 7.37910E+03 |
| 0 | 1019523 | 8 | 1.62177E+04 | 2.29218E+03 | 1.82323E+03 | 7.70302E+01 | -3.45453E+02 | 7.34 | 1.64525E+04 | 2.05743E+03 | 7.19752E+03 |

**Figure 161: Pylon spar .f06 for critical tensile element**

The margin of safety for the tensile stress of the pylon spar is given by,

$$M.S. = \frac{\sigma_{Allowable}}{FS * \sigma_{Actual}} - 1 = \frac{32.1\ ksi}{1.5 * 20.2\ ksi} - 1 = \mathbf{0.06}$$

### 6. Pylon Rib

Load Case 4 is determined to be the critical load case for pylon rib. The pylon rib was found to be most critical in longitudinal tension in the outboard section of the pylon. Figure 162 shows the maximum longitudinal tensile stress distribution with the critical region highlighted, and Figure 163 shows the critical region enlarged with the critical element number in that region. As the .f06

screen capture in Figure 164 shows, the maximum longitudinal tension in the pylon rib is 8.79 ksi in layer 1.

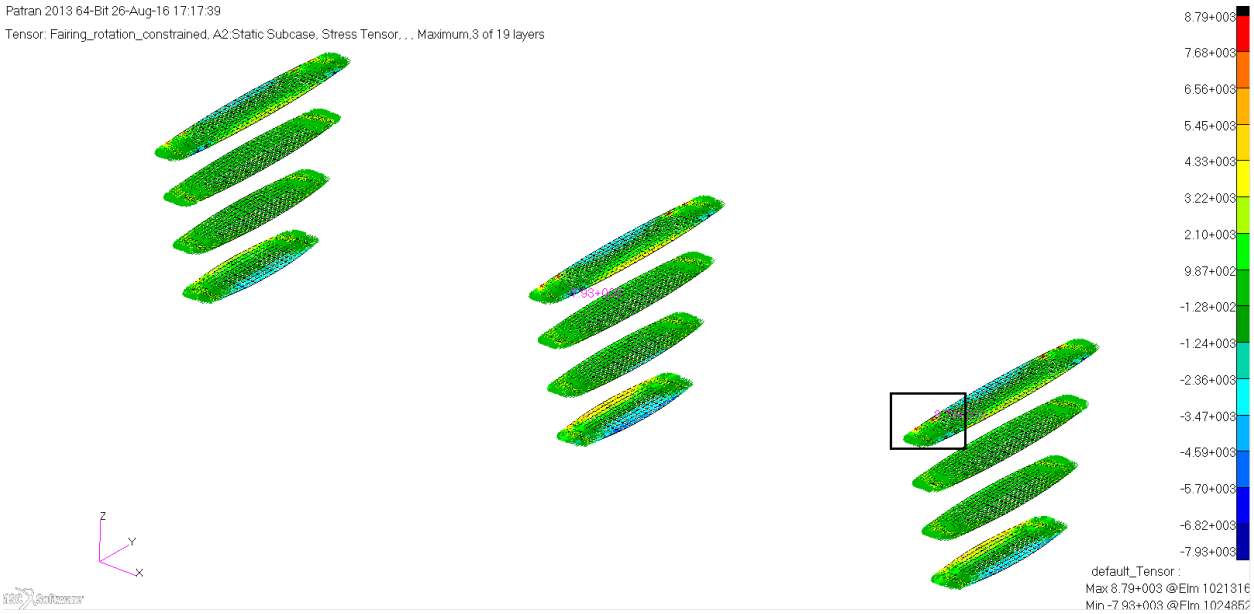


**Figure 162: Pylon rib maximum longitudinal tension stress plot**

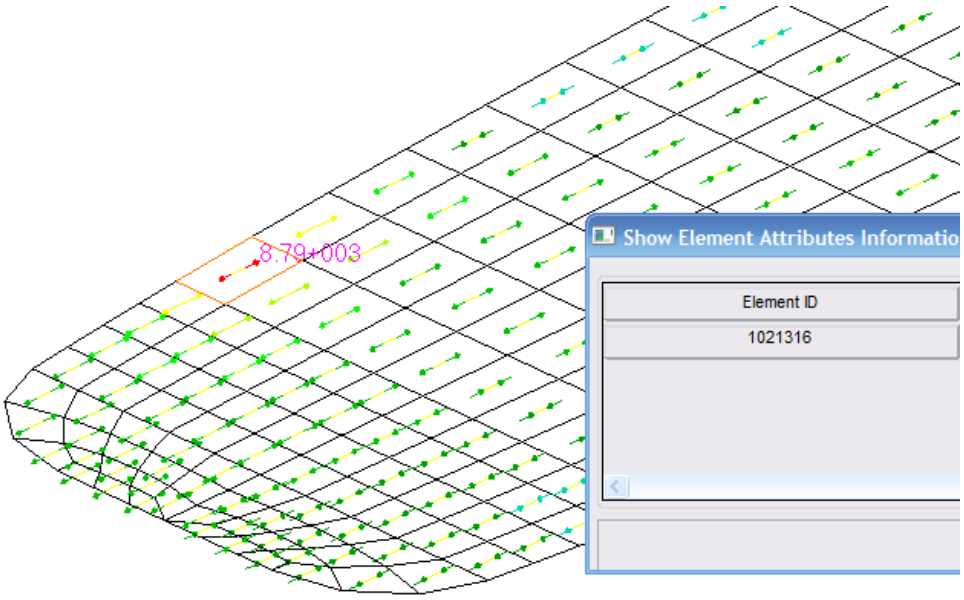


**Figure 163: Pylon rib tension critical region**

S T R E S S E S  I N  L A Y E R E D  C O M P O S I T E  E L E M E N T S  ( Q U A D 4 )

| | ELEMENT ID | PLY ID | STRESSES IN FIBER AND MATRIX DIRECTIONS NORMAL-1 | NORMAL-2 | SHEAR-12 | INTER-LAMINAR STRESSES SHEAR XZ-MAT | SHEAR YZ-MAT | PRINCIPAL STRESSES (ZERO SHEAR) ANGLE | MAJOR | MINOR | MAX SHEAR |
|---|---|---|---|---|---|---|---|---|---|---|---|
| 0 | 1021315 | 1 | 2.38258E+03 | 4.27928E+02 | -6.83679E+02 | 2.98043E+01 | 5.62701E+00 | -17.49 | 2.59797E+03 | 2.12533E+02 | 1.19272E+03 |
| 0 | 1021315 | 2 | 2.06178E+03 | 4.80827E+02 | -5.77271E+02 | 4.47064E+01 | 8.44051E+00 | -18.07 | 2.25013E+03 | 2.92480E+02 | 9.78823E+02 |
| 0 | 1021315 | 3 | 1.74098E+03 | 5.33726E+02 | -4.70863E+02 | 4.47064E+01 | 8.44051E+00 | -18.98 | 1.90291E+03 | 3.71796E+02 | 7.65557E+02 |
| 0 | 1021315 | 4 | 1.42018E+03 | 5.86625E+02 | -3.64455E+02 | 2.98043E+01 | 5.62701E+00 | -20.58 | 1.55705E+03 | 4.49750E+02 | 5.53652E+02 |
| 0 | 1021315 | 5 | 1.09938E+03 | 6.39525E+02 | -2.58047E+02 | -3.86205E-15 | 7.65426E-16 | -24.15 | 1.21507E+03 | 5.23829E+02 | 3.45622E+02 |
| 0 | 1021316 | 1 | 8.79236E+03 | 7.77907E+02 | -6.41851E+02 | 3.96639E+01 | 1.21210E+01 | -4.55 | 8.84344E+03 | 7.26828E+02 | 4.05830E+03 |
| 0 | 1021316 | 2 | 8.27551E+03 | 5.75696E+02 | -5.55200E+02 | 5.94959E+01 | 1.81815E+01 | -4.10 | 8.31534E+03 | 5.35869E+02 | 3.88974E+03 |
| 0 | 1021316 | 3 | 7.75867E+03 | 3.73486E+02 | -4.68548E+02 | 5.94959E+01 | 1.81815E+01 | -3.62 | 7.78828E+03 | 3.43878E+02 | 3.72220E+03 |
| 0 | 1021316 | 4 | 7.24183E+03 | 1.71275E+02 | -3.81896E+02 | 3.96639E+01 | 1.21210E+01 | -3.08 | 7.26239E+03 | 1.50708E+02 | 3.55584E+03 |
| 0 | 1021316 | 5 | 6.72498E+03 | -3.09354E+01 | -2.95244E+02 | -5.13967E-15 | 1.64879E-15 | -2.50 | 6.73786E+03 | -4.38135E+01 | 3.39084E+03 |
| 0 | 1021317 | 1 | 1.65987E+02 | 4.69697E+01 | -2.77727E+02 | -5.65449E-01 | -5.76721E+00 | -38.95 | 3.90508E+02 | -1.77552E+02 | 2.84030E+02 |
| 0 | 1021317 | 2 | 1.54112E+02 | 7.23461E+01 | -1.70966E+02 | -8.48173E-01 | -8.65082E+00 | -38.28 | 2.89015E+02 | -6.25569E+01 | 1.75786E+02 |
| 0 | 1021317 | 3 | 1.42238E+02 | 9.77225E+01 | -6.42051E+01 | -8.48173E-01 | -8.65082E+00 | -35.44 | 1.87934E+02 | 5.20265E+01 | 6.79537E+01 |
| 0 | 1021317 | 4 | 1.30364E+02 | 1.23099E+02 | 4.25556E+01 | -5.65449E-01 | -5.76721E+00 | 42.56 | 1.69442E+02 | 8.40209E+01 | 4.27103E+01 |
| 0 | 1021317 | 5 | 1.18489E+02 | 1.48475E+02 | 1.49316E+02 | 7.32711E-17 | -7.84498E-16 | 47.87 | 2.83549E+02 | -1.65849E+01 | 1.50067E+02 |

**Figure 164: Pylon rib .f06 for critical tensile element**

The margin of safety for the tensile stress of the pylon rib is given by,

$$M.S. = \frac{\sigma_{Allowable}}{FS * \ \sigma_{Actual}} - 1 = \frac{32.1\ ksi}{1.5 * 8.79\ ksi} - 1 = \mathbf{1.4}$$